④

Department of the Navy

OFFICE OF NAVAL RESEARCH

Mechanics Division

Arlington, Virginia 22217

AD-A200 806

Final Report

# FRICTION PHENOMENON IN CONTACT STRESS PROBLEMS

D. Post and J. N. Reddy

Department of Engineering Science and Mechanics

Virginia Polytechnic Institute and State University

Blacksburg, VA 24061

DTIC
ELECTE
OCT 1 9 1988
H

1

88 8 31 087

## ABSTRACT

Numerical, experimental, and hybrid combinations of these methods, were used to study plane contact problems.

The experimental program used moire interferometry to determine in-plane displacement fields near the contact boundaries of pin-loaded aluminum and graphite-epoxy plates. The experiments closely modeled two dimensional behavior and introduced zero-thickness gratings (for the aluminum plate). The experimental data were reduced by means of a localized hybrid analysis which used the experimental displacement data as input to a finite element analysis of selected zones of interest.

The stress distributions obtained were generally consistent with those of published analytical and experimental studies but the detailed frictional phenomena were found to be very localized and somewhat irregular.

The composite plate program featured a failure analysis based upon the experimentally determined stress distributions. These distributions were combined with a maximum stress failure criterion to predict the mode and location of the failure. The results of an earlier experiment were used to assess the accuracy of a general finite element algorithm for plane elastic problems. On the basis of this comparison refinements to the solution methodology were made. Specifically this involved the introduction of both static and dynamic co-efficients of friction. Values for these were deduced from the experiment and closer agreement between experimental and numerical stress distributions was obtained.

Further program reorganization was performed to improve the computational efficiency. An algorithm is also presented (but not implemented) to allow for severe deformation and cracking. This is based upon the Eulerian-Lagrangian description of deformation.

2

# REPORT DOCUMENTATION PAGE

| 1a. REPORT SECURITY CLASSIFICATION | 1b RESTRICTIVE MARKINGS |
|---|---|
| 2a. SECURITY CLASSIFICATION AUTHORITY | 3 DISTRIBUTION/AVAILABILITY OF REPORT |
| 2b. DECLASSIFICATION / DOWNGRADING SCHEDULE | |
| 4 PERFORMING ORGANIZATION REPORT NUMBER(S) | 5 MONITORING ORGANIZATION REPORT NUMBER(S) |

| 6a. NAME OF PERFORMING ORGANIZATION | 6b OFFICE SYMBOL (If applicable) | 7a NAME OF MONITORING ORGANIZATION |
|---|---|---|
| Virginia Polytechnic Institute and State Univ. | | Office of Naval Research |

| 6c. ADDRESS (City, State, and ZIP Code) | 7b ADDRESS (City, State, and ZIP Code) |
|---|---|
| Blacksburg, Virginia 24061 | Mechanics Division (Code 430)<br>800 N. Quincy Street<br>Arlington, VA 22217 |

| 8a. NAME OF FUNDING / SPONSORING ORGANIZATION | 8b OFFICE SYMBOL (If applicable) | 9 PROCUREMENT INSTRUMENT IDENTIFICATION NUMBER |
|---|---|---|
| ONR | | N 00014-84-K-0052 |

| 8c. ADDRESS (City, State, and ZIP Code) | 10 SOURCE OF FUNDING NUMBERS | | | |
|---|---|---|---|---|
| | PROGRAM ELEMENT NO | PROJECT NO | TASK NO | WORK UNIT ACCESSION NO |
| | | | | |

11 TITLE (Include Security Classification)

FRICTION PHENOMENON IN CONTACT STRESS PROBLEMS

12 PERSONAL AUTHOR(S)
Post, D. and Reddy, J. N.

| 13a. TYPE OF REPORT | 13b. TIME COVERED | 14 DATE OF REPORT (Year, Month, Day) | 15 PAGE COUNT |
|---|---|---|---|
| FINAL | FROM _____ TO _____ | 1988-7-1 | 201 |

16 SUPPLEMENTARY NOTATION

matrix crack..., composite plates, Aluminum... ... ...

| 17 | COSATI CODES | | 18 SUBJECT TERMS (Continue on reverse if necessary and identify by block number) |
|---|---|---|---|
| FIELD | GROUP | SUB-GROUP | Contact, moire interferometry, fringe patterns, hybrid techniques elasto-plastic analysis, Eulerian-Lagrangian Formulation, finite element analysis, stick and slip, updated Lagrangian description. |
| | | | |
| | | | |
| | | | |

19 ABSTRACT (Continue on reverse if necessary and identify by block number)

Numerical, experimental, and hybrid combinations of these methods, were used to study plane contact problems.

The experimental program used moire interferometry to determine in-plane displacement fields near the contact boundaries of pin-loaded aluminum and graphite-epoxy plates. The experiments closely modeled two dimensional behavior and introduced zero-thickness gratings (for the aluminum plate). The experimental data were reduced by means of a localized hybrid analysis which used the experimental displacement data as input to a finite element analysis of selected zones of interest.

The stress distributions obtained were generally consistent with those of published analytical and experimental studies but the detailed frictional phenomena were found to be very localized and somewhat irregular.

(CONTINUED ON REVERSE SIDE)

| 20 DISTRIBUTION AVAILABILITY OF ABSTRACT | 21 ABSTRACT SECURITY CLASSIFICATION |
|---|---|
| ☒ UNCLASSIFIED/UNLIMITED ☐ SAME AS RPT ☐ DTIC USERS | |
| 22a NAME OF RESPONSIBLE INDIVIDUAL | 22b TELEPHONE (Include Area Code) | 22c OFFICE SYMBOL |

**DD FORM 1473,** 84 MAR
83 APR edition may be used until exhausted
All other editions are obsolete

19. ABSTRACT (CONT'D)

The composite plate program featured a failure analysis based upon the experimentally determined stress distributions. These distributions were combined with a maximum stress failure criterion to predict the mode and location of the failure. The results of an earlier experiment were used to assess the accuracy of a general finite element algorithm for plane elastic problems. On the basis of this comparison refinements to the solution methodology were made. Specifically this involved the introduction of both static and dynamic co-efficients of friction. Values for these were deduced from the experiment and closer agreement between experimental and numerical stress distributions was obtained.

Further program reorganization was performed to improve the computational efficiency. An algorithm is also presented (but not implemented) to allow for severe deformation and cracking. This is based upon the Eulerian-Lagrangian description of deformation.

A brief comparison of the latest experimental and numerical stress distributions is presented. The agreement is generally good but dependent upon assumed values of the co-efficients of friction in the case of shear stresses at the surface of contact.

A brief comparison of the latest experimental and numerical stress distributions is presented. The agreement is generally good but dependent upon assumed values of the co-efficients of friction in the case of shear stresses at the surface of contact.

# TABLE OF CONTENTS

## GENERAL INTRODUCTION

Contact stresses in pin-loaded isotropic and composite plates were determined using experimental and numerical methods. State-of-the-art moire interferometry techniques were used in the experimental program which needed much refinement before satisfactory results were obtained. These refinements or, rather, innovations appear to be, in themselves, important contributions to the literature.

The finite element method was used in a numerical analysis of the problem. Substantial development of modeling techniques was required for the contact problem. New algorithms have been devised. The results of the first series of experiments on an aluminum specimen were used to fine tune the numerical analysis and highlight the need for further refinement. A direct combination of the experimental and numerical techniques was used in a hybrid study.

In this final report attention will be focused upon the latest series of experiments and numerical analyses. They fall in two self-contained sections and will be reported as such.

The experimental program presents two new studies. The earlier investigation of the aluminum plate has been further developed to provide a closer approximation to two-dimensional behavior. In conjunction with this, shear-lag errors associated with a finite thickness of the specimen grating have been removed by the development of an etched grating on the specimen surface.

An experiment on a pin-loaded graphite-epoxy plate was also performed. This specimen was loaded beyond initial failure.

A new method of data reduction - the localized hybrid analysis - is presented. The method provided a convenient means of reducing the vast

6

amounts of data provided by the experiments. The stress distributions so obtained confirmed the general trends expected but also uncovered unexpected localized phenomena. In the case of the composite plate the stress distributions allowed a failure analysis which correctly predicted the location of matrix cracking.

The section on the numerical studies describes refinement to the algorithm for plane elastic contact problems. These include the important modification of allowing both static and dynamic coefficients of friction as opposed to the use of a single coefficient in earlier studies. This has improved the model behavior and also involved a substantial reorganization of the program methodology. Details of the iteration technique needed to establish the contact zone have also been improved and halting of the program execution has been eliminated. With these refinements, better correlation with experimental results was obtained.

The basic scheme used in the numerical study is Lagrangian. A further development for large deformation and fracture is proposed. A method based on the Euler-Lagrangian formulation is described.

Given the parallel nature of the experimental and numerical studies, it has not been possible to perform detailed comparisons of the latest series of experiments and the refined numerical studies. Some comments upon the interaction of the two approaches are made.

# EXPERIMENTAL STUDIES OF CONTACT STRESSES WITH FRICTION

D. Post,* R. Czarnek,+ J. Morton,* B. Han‡ and M. Y. Tsai‡
Department of Engineering Science and Mechanics
Virginia Polytechnic Institute and State University
Blacksburg, VA 24061

## ABSTRACT

The contact stress problem with friction has been studied experimentally for pin-loaded aluminum and graphite-epoxy composite plates. High sensitivity moire interferometry was used to provide full-field displacement data on both sides of the plate in a final series of experiments which were designed to ensure two-dimensional behavior. A further innovation was the use of an etched (zero-thickness) grating for the aluminum specimen.

The experimental data were reduced using a new approach termed the localized hybrid analysis which employed moire displacement data as input to a local region of interest which was modeled with finite elements.

The experiments verified general trends for the contact stresses in the literature but, in addition, localized phenomena were discovered. These included very high gradients in the shear stresses near the contact boundary and compressive hoop stresses which were strongly dependent upon the sign of the shear stress.

The composite specimen showed local failures in two modes - bearing and tension (matrix cracking). The location of the matrix cracking was well predicted using the calculated stress distributions and a maximum stress failure criterion.

---

\* Professor of Engineering Science and Mechanics

+ Assistant Professor of Engineering Science and Mechanics

‡ Graduate Research Assistant

8

# 1. INTRODUCTION

Experimental, and hybrid studies have been conducted for aluminum-to-aluminum contact and aluminum-to-graphite-epoxy.

The sponsored work has progressed to a satisfactory terminus. Analysis of both experimental load-increasing and load-decreasing phases of contact have been completed. Dissemination of the results has begun at the AIAA Conference in April, 1988 [1]. Several technical papers are planned to present the abundant information from these studies.

The experimental analyses were fraught with unanticipated difficulties. In the end, they were circumvented by advances in experimental science that seem, in themselves, to be significant contributions. These advances include etched aluminum high-frequency specimen gratings, load balancing using two-sided observation of the specimen, and a localized hybrid technique that can focus on any zone.

The primary object of the study was to learn the nature of frictional affects and their role in contact stress problems. A two-dimensional version of a pin-loaded plate was chosen for the study. A secondary objective was to extract engineering information on the behavior of such a joint. Matrix cracking and localized bearing failure arose as especially significant behavior of the composite plate. This report provides a description of the final experimental and analytical studies, including techniques, analyses and results.

## 2. DESIGN OF THE EXPERIMENTS

### 2.1 BACKGROUND AND CURRENT APPROACH

The experimental analysis was that of a thin plate with a circular hole, with loading along the hole boundary by a disk having an initially small clearance. Deformations were measured by moire interferometry, which is a whole-field optical method for measuring in-plane displacements, U and V, with high sensitivity [2]. Strains were determined from the displacements, and stresses were calculated using the specimen material properties.

### A. Load Balancing and Two-Sided Observation

While loading conditions for previous experiments in this series were carefully designed and executed [3,4], surprising deviations from plane stress conditions were uncovered. Equilibrium of forces was tested using stresses determined from the experiments. Equilibrium was satisfied by experimentally determined stresses at a small distance from the hole boundary -- typically 3 plate thicknesses or 1/4 the hole diameter from the boundary -- but equilibrium was not verified using stresses along the hole boundary. This must have been caused by nonuniform contact loading across the thickness of the plate.

Special provisions were made in the current experiments to adjust the loading to equalize its effect on the front and back surfaces of the specimen. The plate and pin geometry is illustrated in Fig. 1. The pin has the same thickness as the plate near the contact zone, but it is flared on the non-contact side to accept loads on opposite sides of the center plane. The loading arrangement, which is illustrated schematically in Fig. 2, was designed to permit adjustment of the forces

$P_1$ and $P_2$ as required to assure symmetrical loading across the thickness of the plate.

How was symmetry assessed? High-sensitivity moire interferometry was used to generate contour maps of the U and V displacement fields of the plate, i.e., displacement components in the x and y directions, respectively. In this work two moire interferometry systems were used together, one to display displacement fields of the front side of the specimen and the other to display displacements of the back side. Symmetry through the specimen thickness was assessed by the equality of the V displacement fields on front and back sides. The loading aparatus was adjusted to give essentially equal front and back patterns.

B. Etched Gratings

Another issue that guided the design of the experiments related to the specimen grating employed for the moire interferometry measurements. In earlier experiments of aluminum-to-aluminum contact, the specimen grating was applied by replication in the normal way [2], using an epoxy adhesive as the replicating agent. The resulting grating was 25 μm (0.001 in.) thick, and while this is a small thickness, shear lag could mask the true behavior at the contact interface. Cleanliness of the contact interface was uncertain, too, inasmuch as excess epoxy could contaminate the aluminum interface zone. To counter both problems in the current work, relatively robust specimen gratings were etched into the aluminum specimen. The shear lag was nullified by virtue of the zero-thickness grating. Subsequently the hole was bored in the plate, assuring a fresh, clean hole surface. The issue of contamination seemed important because contaminants would influence the frictional behavior,

11

altering the frictional parameters of the contact and even acting as a lubricant.

This etching method could not be extended to the study of the composite plate. The motivation was less compelling, however, since contamination of the interface by the epoxy was less serious for the graphite-epoxy specimen.

C. Hybrid Method

The method of analyzing the fringe patterns of displacement was improved, too. Two approaches were employed in previous work:

In one, the displacement gradients were determined from the fringe patterns using a method in which the fringe order at each point of interest, plus the slope of the fringe through that point, were extracted as raw data. Strains were calculated from the displacement gradients and stresses were calculated from strains and material properties [3].

In the other, a hybrid experimental/numerical method was used. Experimentally determined displacement data along the hole boundary were used in a mixed load and displacement boundary value formulation of the finite element method. For each load level, the procedure required iteration through the full load history from the initial zero load condition [5].

These methods had significant disadvantages. For the first, the measurement of fringe slopes was tedious and subject to large errors; it was particularly difficult to extract the slopes with confidence near the hole boundary, where the strains and fringe slopes changed rapidly. For the second, the iteration through the load history compounded the errors or uncertainties encountered at each load level.

The improvement for the current work was a localized hybrid method. In it, any localized region could be analyzed using experimentally determined displacements as boundary conditions for a finite element analysis. Displacement data were sufficient, eliminating the need for measured fringe slopes, and eliminating the need for iteration through the load history.

## 2.2 EXPERIMENTAL METHOD: MOIRE INTERFEROMETRY

Moire interferometry is a relatively new technique, but it has already been applied to the solution of several practical problems. An extensive review is given in Ref. [2].

Moire interferometry responds only to geometric changes of the specimen, and thus it is effective for diverse engineering materials, including the currently important anisotropic and nonlinear materials. It provides whole-field contour maps of in-plane deformation fields -- precisely the experimental counterpart to the primary output of theoretical studies by finite element methods and related computer analysis methods. The sensitivity of traditional geometric moire has been inadequate for most engineering applications, but recent developments in moire interferometry provide increased sensitivity by nearly two orders of magnitude. Now, moire interferometry offers the needed sensitivity and promises to be an important method of experimental solid mechanics.

Moire interferometry is an optical method using coherent light and featuring subwavelength sensitivity and high spatial resolution. Its principle is depicted schematically in Fig. 3. In this method, a crossed-line diffraction grating is replicated on the specimen and it

13

deforms together with the loaded specimen. A virtual reference grating created by interference of two coherent beams A and B is superimposed on the specimen grating. The specimen and reference gratings form a fringe pattern which is a contour map of $N_x$, or the in-plane specimen displacement U. Additional input beams C and D in the vertical plane (not shown) produce the fringe pattern for the V displacement field. The patterns are photographed with a camera focused on the specimen surface.

The relevant equations are

$$f = \frac{2}{\lambda} \sin\alpha \qquad (1)$$

$$U = \frac{1}{f} N_x , \qquad V = \frac{1}{f} N_y \qquad (2)$$

$$\epsilon_x = \frac{\partial U}{\partial x} = \frac{1}{f} \frac{\partial N_x}{\partial x} \qquad (3)$$

$$\epsilon_y = \frac{\partial V}{\partial y} = \frac{1}{f} \frac{\partial N_y}{\partial y} \qquad (4)$$

$$\gamma_{xy} = \frac{\partial U}{\partial y} + \frac{\partial V}{\partial x} = \frac{1}{f} \left[\frac{\partial N_x}{\partial y} + \frac{\partial N_y}{\partial x}\right] \qquad (5)$$

where f is the frequency of the virtual reference grating, $\lambda$ is the wavelength of the light employed, $\alpha$ is the angle of incidence (Fig. 3), N is the fringe order at each point in the moire pattern and $\epsilon$ and $\gamma$ are normal and shear strains, respectively. In this work, f = 2400 lines/mm (60,960 lines/in.).

The configuration of the optical system used in this work is illustrated in Fig. 4. Beams corresponding to A, B, C and D (Fig. 3) illuminate the front side of the specimen to generate the U and V

displacement fields present on the front side. At the same time, beams C' and D' (with central rays in the yz plane) illuminate the back side to generate its V field. The insert in Fig. 4 shows beams C and C' as they strike the specimen directly from the collimated beam, while another portion of each collimated beam is reflected by plane mirrors to form beams D and D'.

The laser employed here was an Argon Ion Laser operated at 150mW and wavelength 514.5 nm. The plane of polarization was parallel to the y axis. The polarizer in the camera path passed light with y polarization. This was needed to filter the elliptical polarizations created by mirror reflections in the three-dimensional paths. The two cameras were adjusted for equal magnifications of 2.2. Kodak Technical Pan sheet film, size 4x5 inches, was used. Exposure times were approximately 1/8 seconds for the aluminum specimen, and 1/16 seconds for the graphite-epoxy specimen (with its replicated grating of higher diffraction efficiency).

## 2.3  LOADING SYSTEM

The experiment was conducted on a vibration isolating optical table, with the optical equipment of Fig. 4 and the loading system of Fig. 5 mounted on the table. The loading system consisted of a sturdy steel frame, a loading and load measuring device and fixtures to engage the specimen.

The loading device utilized two lubricated wedges. When one was displaced laterally by manual operation of the loading screw, it displaced the surrounding frame upwards. The linkage attached to the specimen moved upwards, too, exerting a tensile load on the specimen.

The load was measured by means of electric resistance strain gages on the narrow legs of the loading device. The load was reacted through the pin and saddle by two cross-bars on the main frame, one behind the specimen and one in front. The front cross-bar was adjustable as shown.

The main frame was attached to a base plate containing three adjusting screws. The screws rested on the optical table and allowed rigid-body in-plane and out-of-plane rotation of the specimen relative to the optical system.

## 2.4 SPECIMEN GRATINGS

### A. On The Aluminum Plate

For the aluminum plate, the specimen gratings were etched into its surfaces before the hole was bored. First, the front and back surfaces of the specimen were polished to a smooth, bright finish by buffing with rouge. Then a positive photoresist (Shipley S1400-31 Photoresist diluted with four parts of Type A Thinner) was applied by the drag method illustrated in Fig. 6. With this method, a lens tissue is wetted with the dilute photoresist and dragged at a slow uniform velocity across the specimen. A uniform photoresist film less than a wavelength thick was achieved; uniformity was essential in order to overcome deleterious effects caused by light reflected from the bright aluminum interface.

The photoresist was exposed to a 1200 lines/mm virtual grating. The virtual grating was produced in a separate optical system that caused two collimated beams of laser light to intersect in accord with Eq. 1, where f = 1200 $\ell$/mm, $\alpha$ is the half-angle of intersection and $\lambda$ = 413 nm (using a Krypton Ion Laser). Two exposures were made on each

side, with 90 deg rotation between the exposures to produce crossed-line gratings.

The photoresist images were developed by immersion in Shipley Developer 352. The developer is a dilute solution of sodium hydroxide, which is also an etchant for aluminum. The developer first dissolved and removed the exposed zones of photoresist (zones of constructive interference of the virtual grating). Upon penetrating to the interface, the developer attacked the aluminum and so formed a crossed-line grating in the aluminum.

The specimen was then clamped between acrylic plates and the hole was machined in the specimen.

B. On The Graphite-Epoxy Plate

The conventional procedure [2] was used to produce gratings on the graphite-epoxy specimen. First, a crossed-line grating mold was prepared by exposing a high-resolution photographic plate to a 1200 ℓ/mm virtual grating. A metallic film of aluminum was formed by vacuum deposition (evaporation) on the mold. Then the g :ing was replicated on the specimen, following the steps depicted in Fig. 7. The adhesive was a room-temperature curing epoxy. After removing the mold, a thin (approximately 25 μm) highly-reflective crossed-line grating was produced on the specimen.

In this case, the hole was previously machined in the specimen. During the epoxy curing process, the excess epoxy was repeatedly cleaned from the hole boundary using a cotton swab dampened with alcohol; at the gel stage, excess epoxy was removed with a sharp tool. After the epoxy hardened, the hole boundary was scraped lightly as a final cleaning step.

17

## 3. EXPERIMENTAL PROCEDURE

### 3.1 SPECIMEN LOADING

With the specimen installed in the loading fixture (Fig. 5), an initial load of 25 pounds was applied to stabilize the aluminum specimen (a 20 pound initial load was used for the composite specimen). The optical system was adjusted to produce null fields: the U and V fields on the front side and the $V_b$ field on the back side, where the subscript denotes the back side. Because of the initial load and imperfections of specimen and reference gratings, they were not true null fields, i.e., they were not devoid of fringes, but the number of fringes across each field was minimized.

The loads were increased in a systematic sequence and the U, V and $V_b$ moire fringe patterns were photographed for each load step. Prior to recording the patterns, adjustments were made in an iterative fashion as follows. The V and $V_b$ patterns were observed on the camera screens. Any rigid-body rotation of the specimen caused by the loading was cancelled by rotation of the loading fixture through adjustments of its base. Then fringes that crossed a line segment along the y axis were counted and compared for front and back sides of the specimen. If they were not equal (within about 1/4 fringe), the load was reduced to about 50 pounds (30 pounds for the composite specimen). The lever that engaged the pin and saddle (Fig. 5) was adjusted and the load was raised again to the target value. If the fringe counts in V and $V_b$ fields were not equal, the procedure was repeated until equality was achieved. Then the moire patterns were photographed.

The load sequence is given in Fig. 8 for both specimens, for the loading and unloading phases. The large circles denote load levels at which the patterns were recorded, and the small circles indicate

18

observations in the iterative process.  At higher load levels and in the unloading phase, equal deformations of the front and back surfaces were obtained without iteration, as indicated.

## 3.2  FRINGE PATTERNS AND FRINGE ORDER EXTRACTION

The fringe patterns were enlarged and printed photographically at magnifications of about 5 times and 10 times.  Representative U and V patterns on the aluminum plate are shown in Figs. 9 and 10 for an intermediate and high load level, respectively.  Figures 11 and 12 give examples for the composite plate.  Fringe orders $N_x$ and $N_y$ were established, as illustrated in Fig. 9.  An extensive set of patterns is reproduced in Appendix I.

While the fringes on the aluminum specimen are sufficiently well delineated to extract fringe positions with high accuracy, they exhibited more optical noise than those on the composite specimen.  The noise was caused by the inferior quality of the etched gratings, compared to the replicated gratings on the composite.  Further development of the etching process is required to enhance the appearance of the fringe patterns.

The jagged boundary of the composite plate is caused by local bearing failure of the composite, with elements of the outer ply overriding the pin surface.  The failure process is discussed in subsequent sections.

Data were extracted from the fringe patterns by means of a digitizing system.  It consisted of a digitizing table, a cursor and a microcomputer.  The coordinates of fringe centers along the hole boundary and other preselected lines were measured by electromagnetic

fields built into the digitizing table. Using a magnifying lens for observation, cross-hairs of the cursor were positioned visually at the intersection of the fringe center and the preselected line, and the coordinates of the cursor were tabulated by the microcomputer. Accuracy of the digitizer was 0.001 in. on the scale of the photographic print, or 0.0001 to 0.0002 in. on the scale of the specimen.

# 4. HYBRID METHODS OF DATA REDUCTION

## 4.1 COMBINATIONS OF MOIRE INTERFEROMETRY AND FINITE ELEMENT ANALYSIS

Moire interferometry provides full-field displacement data corresponding to the in-plane components $u(x,y)$ and $v(x,y)$ on the specimen surface. In many cases the strain and stress distributions are required in the engineering analysis. The former are obtained from the appropriate derivatives:

$$\epsilon_x = \frac{\partial u}{\partial x} \, , \ \epsilon_y = \frac{\partial v}{\partial y} \ \text{and} \ \gamma_{xy} = \frac{\partial u}{\partial y} + \frac{\partial v}{\partial x} \tag{6}.$$

Once these are obtained the stress may be determined from knowledge of the material constitutive law. The differentiation required to determine the strains at some point may be performed manually (defining the gradient in a small region) or, indeed, optically [6]. A further method of reducing the moire data is to use the finite element (or even the boundary integral evaluation) method. In this section the basic principles of the finite element method will be reviewed and methods of combining moire interferometry and finite element analyses will be introduced.

The finite element method of stress analysis is well established. It allows the solution of many complex stress analysis problems through an approximate numerical technique. Structural components are discretized into a number of elements. The displacements within each element are assumed to follow known functional relations (e.g. linear, quadratic etc). The stiffness of each element is computed in terms of the co-efficients of the displacement function and the material law for the element. The stiffness of the structural component is formulated by requiring equilibrium and compatibility at the nodes of the elements.

The technique is, of course, a "stand alone" method of stress analysis. A major problem, however, can occur in the specification of the boundary conditions (forces and/or displacements). Another problem which may arise is the requirement of a very large number of elements to discretize a large body (when the real region of interest may be quite small).

A hybrid approach to the pin-loaded plate problem has been used by Heyliger [5]. In this, the moire displacement data were used around the pin/plate boundary and the uniform remote stress condition applied. Thus, when symmetry was involved, an entire half of the plate had to be discretized and analyzed.

In order to propose further hybrid approaches, let us examine some basic ideas behind the finite element method and highlight possible combinations of photomechanics data and finite element analysis. Following the notation of Reddy [7], the displacement within an element may be written as

$$u = \sum_{j=1}^{n} u_j \psi_j \tag{7}$$

and

$$v = \sum_{j=1}^{n} v_j \psi_j, \tag{8}$$

where $u_j$ and $v_j$ represent the displacement at each of the n nodes of an element and $\psi_j$ is one of n interpolation functions for a given element.

The strain within the element is, of course, obtained by differentiating the displacement components u, v. Thus, for an element

$$\{\epsilon\}_e = [D] [\psi]_e \{\Delta\}_e , \tag{9}$$

22

where [D] is the matrix of differential operators

$$[D] = \begin{bmatrix} \frac{\partial}{\partial x} & 0 \\ 0 & \frac{\partial}{\partial y} \\ \frac{\partial}{\partial y} & \frac{\partial}{\partial x} \end{bmatrix}$$

and $\{\Delta\}_e$ is a column vector containing the nodal displacements,

$$\{\Delta\}_e = [u_1 \ v_1 \ \cdots \ u_n \ v_n]^T \tag{10}$$

Thus one approach to a hybrid of moire interferometry and finite element analysis would be to use the fringe pattern data (for u and v fields) to determine the displacements of the nodes everywhere in some arbitrary region. The finite element (interpolation) analysis then gives approximate strains within each element (for chosen orders of interpolation function). That is, the finite element analysis is used as a convenient tool for differentiating the fringe (displacement) data. Of course, stresses may then be determined from the appropriate material constitutive law.

This approach may have merit in the cases where there is a regional variation in the material properties, such as plastic deformation or local failure. However, it may become tedious unless automated.

Another approach is to follow the finite element analysis more closely. After formulating element strain and stress behavior the element stiffness is related to the nodal forces and displacements by

$$[K^{(e)}] \ \{\Delta^{(e)}\} = \{F^{(e)}\} \tag{11}$$

$$\text{where } [K^{(e)}] = \int_{\Omega^{(e)}} [B^T]_e \ [C]_e \ [B]_e \ dv \tag{12}.$$

Here, $[B]_e = [D] [\psi]_e$ and $[C]_e$ is the element constitutive matrix.

Usually the integration is performed numerically using Gauss-Legendre quadrature. This consists of sampling values of a function at special points within any given element, applying weighting functions and summing over the element. These sampling points within the element are known as Gauss points. The eight-node quadrilateral element shown in Fig. 13 employs nine Gauss points. The most accurate results are those at the Gauss points but usually the nodal values are of greater interest. In the contact problem we are interested in the deformation of the surface of contact so we need the stress components at the contact boundary.

Following formulation of the element stiffnesses, the overall stiffness matrix may be assembled by incorporating requirements of nodal compatibility and equilibrium. A convenient, partitioned form, is

$$
\begin{bmatrix} [K^{11}] & [K^{12}] \\ [K^{21}] & [K^{22}] \end{bmatrix} \begin{Bmatrix} \{\Delta^1\} \\ \{\Delta^2\} \end{Bmatrix} = \begin{Bmatrix} \{F^1\} \\ \{F^2\} \end{Bmatrix} \tag{13}
$$

where $\{\Delta^1\}$ and $\{F^2\}$ represent <u>known</u> displacements and forces respectively. Terms $\{\Delta^2\}$ and $\{F^1\}$ are <u>unknown</u> displacements and forces. Thus a further local hybrid approach suggests itself. Let $\{\Delta^1\}$ be the displacements of nodes around the boundary of some arbitrary region of a pair of moire fringe patterns. These displacements are readily determined at the location of the nodes. Within the region, the resultants nodal forces $\{F^2\}$ are known (to be zero). The internal nodal displacements $\{\Delta^2\}$ are then regarded as unknown and may be calculated from

$$
\{\Delta^2\} = [K^{22}]^{-1} \{F^2\} - [K^{22}]^{-1} [K^{21}] \{\Delta^1\} \tag{14}.
$$

24

The nodal forces along the boundary of the arbitrary region are given by

$$\{F^1\} = ([K^{11}] - [K^{22}]^{-1} [K^{21}]) \{\Delta^1\} + [K^{12}] [K^{22}]^{-1} \{F^2\} \qquad (15).$$

These calculations are performed routinely in the finite element analysis.

The analysis above is presented to highlight an approach which will be termed "the localized hybrid method," and to emphasize some advantages and limitations. In the localized hybrid analysis the material behavior of all elements within the chosen region must be known even for the calculation of strains - that is, $\{\Delta^2\}$ depends upon the global and, in turn, the element stiffness matrices. This is to be contrasted with the direct interpolation approach described earlier in which strains may be calculated in regions of gross material non-linearity (provided, of course, the appropriate strain-displacement relationship is included in the formulation) . In the localized hybrid method, since the moire data are available everywhere within the region, subsequent comparisons of calculated and actual displacements can be made. This provides vital checks of the accuracy of the analysis and allows refinements to be made in the finite element mesh. Similarly the interpolation approach must satisfy the additional requirement that the internal interelement nodal forces satisfy equilibrium. The degree to which this is achieved may be used as a measure of the accuracy of the discretization or appropriateness of the interpolation functions.

Of the two approaches described above the localized hybrid method is the most useful for present purposes.

In the localized hybrid analysis a further extension is possible. In addition to specifying only the displacements of the boundary nodes,

internal nodal displacements may also be included. This is particularly useful when there are high displacement gradients and good modeling is desired without additional mesh refinement.

Before describing the application of the localized hybrid method to the contact problem, it is appropriate to demonstrate the method and examine the robustness or stability of the approach. To this end a test case (which is close to the contact problem geometry) will be described.

## 4.2 TEST CASE: LOCALIZED HYBRID ANALYSIS

There are two main reasons for performing a test case for the localized hybrid method for the contact problem. The first is that the experimental displacements at the pin/plate boundary will be input into the numerical analysis and the resulting stresses in this same region are of primary importance. We need to determine the effect of experimental error upon the accuracy of these stresses. Away from these boundary nodes, at internal nodes, it would be expected from St. Venant's Principle that the effects of errors in displacement will be attenuated. The magnitude of probable errors in displacement are easily estimated. The second objective is, then, to quantify the effect of random errors of such a magnitude upon the calculated stresses. In other words, what is the sensitivity of the technique expressed in terms of stresses?

A region representative of that used in the experiment is shown in Fig. 14. The region was first meshed and loaded as shown. The loads were chosen to produce stresses of similar orders as those in the aluminum plate experiment. The finite element analysis provided the nodal displacements, stresses and strains everywhere in the region. It will be observed that this example contains some distorted elements. Since this is a self-contained test case and our interest lies on the curved, densely meshed boundary, element distortion is not important.

Next, the calculated displacements of the nodes on the boundary of the region were input into a second finite element analysis. As expected the forces from the first analysis were reproduced in the calculation. However, suppose now that there are some errors in the input displacements at the boundary nodes. These may be of two classes.

27

In the first, there may be one relatively large error while the others are precisely known. This may correspond to a counting error in the fringe data reduction. In the second case, there may be random errors associated with each nodal displacement value. This may correspond to uncertainty in the estimation of partial fringe orders from the moire data.

In this test case, separate analyses were performed with both types of displacement errors. The magnitudes of the displacements and errors were chosen to be typical of those which might occur in the moire experiment. It is estimated that the largest interpolation error might be one quarter of a fringe order (approximately 0.0001mm in displacement). When values of displacements were modified to contain random errors in the range $-10^{-4}$ mm to $+10^{-4}$ mm and the calculation made, there is hardly any discernible effect upon the stresses calculated at the boundary (Fig. 15). That is, the points from the data containing the displacement errors are virtually superimposed upon the line from the force-input calculations.

Coarse or geometrical moire provides a much lower sensitivity than moire interferometry. To illustrate the effect of a larger random error of maximum value equivalent to 2.5 fringe orders the test case was run again. This corresponds to a similar order of interpolation error which might occur with a virtual reference grating of 240 lines/mm (still very fine by geometric moire standards). The results indicate that the general trend is preserved but there is a large fluctuation in the stress values (Fig. 16). The errors are much more significant in the shear stresses which are much lower than the normal stresses in this calculation.

Fig. 17 shows that a shear stress of the order of 5 ksi is readily determined using the localized hybrid approach in conjunction with moire interferometry with a quarter fringe order maximum error and a virtual reference grating of 2400 lines per mm. A coarser method of determining displacements would not, however, be satisfactory in this case. A further case showing a maximum shear stress of 1 ksi is presented in Fig. 18. The trend is still apparent but fluctuations are of the order of 0.25 ksi which are similar in magnitude to these in the 5 ksi example (but these fluctuations seem smaller because of the larger scale). This indicates the current limit on stresses which may be determined using the localized hybrid method. Thus, refinement of the moire experiment would be required for confident measurement of stresses below 1 ksi. This may be achieved in future experiments using carrier patterns, enhanced sensitivity, etc.

In the case of the discrete error, (in the example a large value of 5 fringe orders was used) it is seen that the St. Venant Principle clearly operates and that the resulting error is confined to within a very local region and this error is likely to be easy to detect when it occurs (Fig. 19).

## 4.3 APPLICATION OF THE LOCALIZED HYBRID METHOD TO THE CONTACT PROBLEM

In the pin-loaded plate problem, primary interest was centered on the stress distribution around the surface of contact. A secondary goal was the determination of the angular extent of the contact zone as the applied load varied. Finite element meshes were then devised for the plate in the vicinity of the contact zone only. In selecting meshes several options were available. The first, and most tempting, was to

fit the boundary nodes to the locations of the fringe centers. However, the moire experiment produces two distinct fringe patterns so that it is not possible to define a single mesh in this way. An alternative compromise is to use the denser (V) fringe pattern. This method is attractive in that it would yield the most accurate values of input nodal displacements. Practically, however, it is tedious for large numbers of load cases.

A convenient approach is to take advantage of mesh generators in the finite element programs and define regular meshes. In this case the fractional fringe orders at the nodes must be estimated. It has been shown above that even with a one quarter fringe error in interpolation excellent stress accuracy is obtained for all but the lowest stress values. Even in the case of low stress there are optical methods of enhancing the accuracy of the interpolation using carrier patterns. Some of the meshes used are shown in Figs. 20 and 21. The rules and the approach used in the selection of the meshes were those of a conventional finite element analysis. The elements employed in the analysis were eight-node isoparametric quadrilaterals. The analysis assumed plane stress conditions and the material properties used were for the aluminum, $E = 10.2 \times 10^6$ psi and $\nu = 0.34$ and, for the quasi-isotropic graphite-epoxy composite, $E_{11} = E_{22} = 7.72 \times 10^6$ psi, $G_{12} = 2.97 \times 10^6$ psi and $\nu_{12} = 0.30$.

As mentioned above moire interferometry yields separate fringe patterns for the U and V-fields. In the case of the pin-loaded plate these have very different fringe densities (Figs. 9-12). The fringe orders for the U and V displacements at the boundary nodes must be determined. Several methods were evaluated. These included estimation

of the fractional fringe orders at nodes when the mesh was plotted on transparent film and superimposed upon the fringe patterns. Another method consisted of determining the order and co-ordinates of the fringe center intersecting the boundary of the mesh using a digitizing system. Fringe orders at the boundary nodes were then obtained by linear interpolation. Both method were used successfully.

Two finite element programs were used in the data reduction. The first was based on a listing in Hinton and Owen [8]. This program provided a basic analysis but lacked pre and post-processing capabilities. The program was run on an IBM 3090 and specific (to the contact problem) mesh generation and post-processing programs were written for an IBM Personal System 2 Model 50 with the LOTUS 1-2-3 Software.

The second finite element program used (mainly for the graphite-epoxy analysis) was FINEL - a comprehensive suite developed by Denis Hitchings at Imperial College, London. The version used ran on the Apollo DN 3000 minicomputer. This program has comprehensive mesh generation capabilities and a wide selection of element types. Sophisticated post-processing is also allowed.

It should be recalled that the finite element calculations provide the best estimates of the element stresses at specific internal locations known as the "Gauss points." Thus the values of stress components around the pin/plate boundary must be extrapolated from the Gauss points to the boundary nodes. For the quadratic elements used, the stress (and strain) variations within an element are linear. Of course, for very small elements, errors associated with this can be taken as negligible. For the coarsest mesh used the distance from the nearest Gauss point to boundary node was about 0.2 plate thicknesses.

31

In the following section the stress distributions at and near the surface of contact in the pin-loaded plate will be presented for both the aluminum and composite plates.

# 5. STRESS DISTRIBUTIONS

## 5.1 INTRODUCTION

The radial, hoop and shear stresses on, and near, the surface of contact were determined from the moire data using the localized hybrid approach. The stress distributions will be presented first for the aluminum plate and then for the composite plate. The angular coordinate system and convention for a positive shear stress are shown in Fig. 22.

## 5.2 ALUMINUM PLATE

The variation of the radial stress with angular location and applied load is shown in Fig. 23. In most instances the fluctuations in stress appear to be at the same angular locations for the various load levels. This suggests that the fluctuations represent real stress variations and are not artifacts of the computations.

The variation of the hoop stress with angular location and applied load is shown in Fig. 24. It may be observed that the hoop stresses are compressive near the zone of first contact ($\theta \simeq 90^0$), the greater the load the smaller the region in compression, and that the peak compressive stress is approximately independent of load. It is also apparent that distribution of stress is not symmetric about $\theta = 90^0$. It might further be noted that the largest hoop stresses are tensile and occur at or just beyond the end of the contact region.

The shear stress distributions are shown in Fig. 25. It is immediately apparent that the variation of this stress component along the contact region is highly irregular. The variation of shear stress with applied load is also extremely non-linear. One important comment to make is that the magnitudes of the shear stresses are an order of

magnitude lower than the other two stress components. To provide some perspective on this, the three components of stress are plotted on the same axes in Figs. 26 and 27 for the 500 and 1250 lb loads, respectively.

In order to provide some insight into the rate at which the contact stresses decay with distance away from the contact region the radial, hoop and shear stresses are plotted for various locations near the contact zone in Figs. 28-30 respectively for the applied load case P = 1250 lb. It will be observed that the variation is very rapid. In the case of the hoop stress the compressive stress (at $\theta = 90^0$) becomes tensile within less than half a plate thickness from the contact point. The effect in the shear stress distribution is most striking. Within about one plate thickness the shear stresses change sign. Thus the contribution of the frictional effects to the stress near the contact zone is very localized. A small distance away the global effects of loading and geometry dominate, and the shear stress fluctuations are attenuated and the distributions become symmetric about $\theta = 90°$. The stress components become essentially independent of the frictional effects at the pin-plate boundary.

Since some publications provide stress distributions in terms of cartesian rather than polar coordinates, the cartesian components of stress are shown in Figs. 31 and 32 for the 500 and 1250 lb load cases, respectively. Also, the stress components are normalized with respect to the bearing stress p ( = P/Dt) in Fig. 33.

As noted in the description of the experimental procedure, the moire displacement data were also recorded on the unloading part of the load cycle. The stress distributions on this load-decreasing phase may be compared with those on the load-increasing phase.

34

The radial stress distributions around the pin-plate boundary are shown for the load-decreasing phase in Fig. 34. The corresponding hoop and shear stress distributions are shown in Figs. 35 and 36, respectively. Comparisons of the loading and unloading stress distributions are provided in Figs. 37 and 38. It is clear that the most pronounced difference in the loading and unloading stress distributions lies in the shear stresses - particularly for the 500 lb load case in which there has been a complete reversal in the shear stress direction. This, of course, is to be expected since the direction of relative slip or tendency to slip is reversed on unloading and this effect will be greater as the load is reduced and reach a maximum before falling to zero when the load is removed. This is apparent in Fig. 36 for the 250 lb load which has a smaller peak shear stress than the 500 lb case. Also in the 500 lb decreasing load case, observe that the maximum shear stress occurs at about $45^{\circ}$ and that the change of sign of the shear stress gives rise to an increase in the radial (compressive) stress, as required from equilibrium considerations. It should also be remarked that the magnitudes of the shear stresses are much larger on the load-decreasing phase and, indeed, the peak values in the 500 lb case approach that of the 1250 lb case. Note also in Fig. 38 that the region of negative hoop stress has been almost eliminated on the load decreasing phase.

It has been observed that during the load increasing phase the shear stress underwent a rapid transition with radial distance from the surface of contact into the plate. In the load-decreasing phase, however, this phenomenon does not occur - see Fig. 39. This is, of course, to be expected since the shear stress due to friction and that due to the unfilled hole have the same signs.

## 5.3 COMPOSITE PLATE

In the study of the stress distribution in a pin-loaded composite plate the possibility of failure mechanisms had to be taken into consideration. Indeed, a major interest in the study was the identification of the nature and location of various failure mechanisms. Thus the presentation of results from the program on the composite plate will differ from that for the aluminum plate.

The fringe patterns obtained for a load of 400 lb applied to the quasi-isotropic graphite-epoxy plate are shown in Figs. 11a-c. It is apparent that the fringes in the U-field (Fig. 11b) are much less dense than those in the V-field (Fig. 11a) and that there is a marked lack of symmetry in the U-field. There is also a local gradient on the left side of the picture (indicative of sub-surface ply damage).

The fringe patterns were analyzed using the localized hybrid approach. The meshes used are shown in Fig. 21. Meshes II and III (Fig. 21) were used to determine the contact angle more precisely and the overlap between meshes I and II (or III) provided a useful check of the sensitivity of the results to the mesh and input data.

The direct application of the localized hybrid analysis for the stress components at the surface of contact produced wide variations in the stress components near the first contact point ($\theta = 90°$) and near $\theta = 150°$ (which coincided with the local anomaly in the U-field fringe pattern (Fig. 11b). Attention (as far as the stress analysis was concerned) was then centered on regions close to but a little removed from the surface of contact. These new zones of interest were taken as circular arcs concentric with the center of the hole. On one such arc, 1.55 plate thicknesses from the surface of contact, the stress component

distributions are much smoother. These stress components are shown in Figs. 40 and 41 for the polar and cartesian coordinates respectively.

One advantage of the localized hybrid analysis is that meaningful values of stress can be obtained in regions near anomalous zones. In the case of the graphite-epoxy plate, the surface stress distributions were obtained for angles in the range 0 to 60°. These stress distributions are shown in Figs. 42-44. It will be observed that the peak hoop stress occured a little before the 0 and 180° positions.

Owing to the possibility of local bearing failure at $\theta = 90°$ it is not possible to compare the peak radial stresses in the composite and aluminum plates. There are, however, marked differences in the shear stress distributions. First, it should be remarked that the magnitudes of the shear stresses are about double (for a given load) in the case of the composite plate. The shear stress distributions are also much smoother and regular. A most important difference is, however, the change of sign of the shear stress at $\theta = 30°$. In the cases for low values of $\theta$ the shear stresses are negative. In the case of the aluminum pin this continues to be the case until the shear stress approaches zero and then changes sign as $\theta$ approaches 90°. This difference between the isotropic aluminum and the quasi-isotropic composite is curious, to say the least. Differences in the sign of shear stresses in isotropic and quasi-isotropic materials were reported in an experimental investigation by Hyer and Liu [9] without comment. This feature is not apparent in the analytical laminate studies. This point will be addressed in more detail below in a discussion of failure and contact mechanics.

# 6. DISCUSSION OF RESULTS

## 6.1 CONTACT MECHANICS

Significant regions at the pin-plate interface are shown in Fig. 45. Ideally, it would be desired to determine the extent of the contact, slip and no slip regions. The extent of the contact region is readily defined. The location around the boundary at which both the radial and shear stresses first become zero is taken as the end of the contact zone. Beyond this position the radial and shear stresses remain zero. In the present study the extent of the contact zone is then determined from the distributions of $\sigma_r$ and $\tau_{r\theta}$. Since the shear stresses are small and approach zero slowly near the end of the contact zone, precise definition is difficult, so moire confidence is placed upon the radial stress distributions. Also, it should be noted that with the experimental and numerical nature of the investigation the stresses are small and oscillatory but not exactly zero just beyond the end of the contact zone.

The contact angle increases as the applied load increases and has the value zero at zero load (representing a line or point contact). The variation of contact angle with load is shown in Fig. 46 for loading and unloading of the aluminum plate. It will be observed that for a given load the contact angle is marginally greater on the unloading phase. This is, of course, consistent with the reversed direction of the frictional forces on unloading.

The change of contact angle with load accounts largely for non-linear geometrical effects in the pin-loaded plate problem. It is observed that the contact angle increases rapidly with load at first and then more slowly as the contact angle approaches 180°. The effects of

38

this upon the variation of the peak radial contact stress are shown in Fig. 47.

For the case of the composite plate, a more approximate determination of the contact angle had to be made as a result of the local bearing failure and matrix cracking on one side of the plate. The variation of contact angle with load is presented in Fig. 48. The contact angle increases more rapidly at first and then more slowly than in the aluminum plate. This is consistent with local failure in the composite plate at very low loads.

Regions of slip are those within which a limiting frictional stress has been exceeded and there is relative displacement tangential to the surface of contact. Coulomb friction defines static and dynamic coefficients of friction for the surfaces in contact. Under limiting conditions the ratio of the shear and normal stress should be constant for the surfaces and, in the present case, equal to the co-efficient of friction. This ratio is plotted for two load cases in Fig 49. It is difficult, from this, to determine the coefficient of friction, whether slipping has occurred or even if the frictional behavior is Coulomb in nature. On the unloading phase at 500 lb it is possible that between $\theta = 35^{\circ}$ and $\theta = 60^{\circ}$ some limiting value $\mu \simeq 0.2$ is obtained. However, without knowledge of the displacement of the pin relative to the plate, this becomes a matter of conjecture. It should be noted that the extreme parts of the curves ($\theta \simeq 0$ and $\theta \simeq 180^{\circ}$) are unreliable since both the shear and radial stress approach zero in these zones.

## 6.2 STRESS DISTRIBUTIONS

There have been many analytic studies of the pin/plate contact problem. These vary greatly in complexity and often include restrictive assumptions. Unfortunately an exact comparison of the current experimentally determined stress distributions with analytical ones is difficult, if not impossible, owing to the lack of detailed information about actual conditions at the pin/plate interface, particularly the local coefficient of friction and the distribution of contact surface asperities. The analytical solutions assume Coulomb friction with some value(s) of the coefficient(s) of friction. Hyer and Klang [10] present non-dimensional stress distributions for a similar problem. The sensitivity to load and, therefore, contact angle is not indicated. Thus the results of Klang and Hyer are compared for two load levels (750 and 1250 lb) from the present study (Figs. 50 and 51). Generally, the peak stress values compare well for all stress components. The distributions show general agreement except for the shear stresses. One peculiarity of the Hyer and Klang solution is, however, the large compressive hoop stress at the first contact point ($\theta = 90°$). This phenomenon is not detected in the present study perhaps as a result of the overestimated coefficient of friction in the analytical study. The possible existence of some compressive hoop stresses is not questioned. Indeed such stresses are shown in Fig. 24. In this figure it is shown that increasing load does not affect the magnitude of this compressive stress but does reduce its extent (in the hoop direction). The existence of the compressive hoop stress may be explained by considering the Poisson expansion (in the hoop direction) of an element at the first contact point under the large compressive radial stress. This expansion

is resisted by the tractions between the pin and plate so that the hoop strains are smaller than in the unrestrained case. Hyer and Klang show that the effect is strongly dependent upon the magnitude of the coefficient of friction assumed in the analysis. In the case that $\mu$ is taken as zero the hoop stresses are always positive in the Hyer and Klang model. Experimental support for the dependence of this effect upon the sign of the frictional tractions is provided by data from the unloading phase. The reversed sign of the shear stress tends to promote positive (tensile) hoop stresses near $\theta = 90$ in Fig. 38. Another effect of this is to shift the peak compressive radial stress away from the first contact point.

A further insight into this phenomenon can be seen by considering the equilibrium equations in polar coordinates. In the absence of body forces, these are

$$\frac{\partial \sigma_r}{\partial r} + \frac{1}{r} \frac{\partial \tau_{r\theta}}{\partial \theta} + \frac{\sigma_r - \sigma_\theta}{r} = 0 \tag{16}$$

and

$$\frac{1}{r} \frac{\partial \sigma_\theta}{\partial \theta} + \frac{\partial \tau_{r\theta}}{\partial r} + \frac{2\tau_{r\theta}}{r} = 0 \tag{17}$$

The hoop stress $\sigma_\theta$ can be written as

$$\sigma_\theta = ra + b + \sigma_r \tag{18}$$

where $a = \dfrac{\partial \sigma_r}{\partial r}$ and $b = \dfrac{\partial \tau_{r\theta}}{\partial \theta}$ .

The experimentally determined stresses and stress gradients identify the relative importance of each term in the equilibrium equations. Near

41

$\theta = 90°$, $\sigma_r$ is large and compressive (negative) and a (the gradient of $\sigma_r$ in the radial direction) is positive. Depending upon the local direction of relative motion (or impending motion), b (the rate of change of shear stress along the contact interface) may be positive or negative. Of course b also depends upon the magnitude of the frictional forces. In the loading phase b is positive. So $\sigma_r$ must be negative enough to yield a compressive $\sigma_\theta$. On unloading to 500 lb, $\sigma_r$ becomes more negative (than on the loading phase), $b = 0$ and $\sigma_\theta$ is positive from which it is deduced that a must be more positive. That is, the rate of increase of the radial stress with distance from the contact boundary must be greater in the unloading case. This is consistent with the experimental observation that $\sigma_r$ is greater on the unloading phase and that the frictional effects are highly localized. Thus, depending upon the sign and magnitude of the contact tractions, negative hoop stress can occur.

The test case used in validating the localized hybrid analysis provides a convenient means of illustrating the effect of the magnitude and sign of the frictional tractions upon the hoop stress distributions. These numerically obtained results are summarized in Fig. 52. It is clearly shown that the constraint effect of frictional shear stress is responsible for the local tensile or compressive hoop stresses near $\theta = 90°$. That is, when the applied shear tractions are positive, compressive hoop stresses are created.

It has been observed above that the extent of the compressive hoop stress zone decreases as the load increases but the peak magnitude hardly changes. Qualitatively this may be explained by observing that, while the radial stress increases relatively rapidly with load, the

42

constraints due to the frictional forces increase much less rapidly. Thus the effect of the increasing radial stress promotes tensile hoop stresses and the extent of the compressive hoop stress zone is diminished.

Summarizing the stress distributions obtained in the experimental stress analysis,

(i) The greatest stresses are tensile and in the hoop direction near $\theta = 0^0$ and $180^o$. Depending upon the loading sequence (loading/unloading) the smallest hoop stresses occur at or near $\theta = 90^0$ and may be compressive. Defining the stress concentration factor (SCF) as the maximum stress (at $\theta = 0°$ and $180°$) divided by the average stress on the ligament, it may be seen that, in the case of the aluminum plate, the SCF depends upon the load and marginally upon the loading sequence and also approaches the value predicted by Frocht and Hill [11] Fig. 53.

The stress concentration factors for the composite plate show more fluctuation. Initially these are close to that for the aluminum plate but, as a result of material failure which leads to a complex load redistribution, the SCF's are up to 20% higher.

(ii) The radial stresses are large and compressive near the point of first contact ($\theta = 90°$). As pointed out above, the effects of frictional tractions are so as to produce compressive hoop stresses in this region and shift the location of the peak radial compressive stresses away from the point of first contact. This is most clearly apparent in the 1250 lb load case. In terms of the bearing stress (p), the peak radial stress is about 0.9 p compared to 1.2 p for the peak hoop stress.

43

(iii)  The shear stress distributions at the pin/plate contact surface are complex.  It has already been observed that these are typically an order of magnitude smaller than the hoop and radial stresses.  On an expanded scale in Fig. 25, fluctuations of up to 0.5 ksi are apparent.  In the case of all but the largest loads these fluctuations tend to mask the general trends.

It is important to establish whether these fluctuations represent true frictional phenomena or are artifacts of the method of stress calculation.

## 6.3  FRICTIONAL PHENOMENA

The stress components at the contact boundary in the aluminum specimen contain fluctuatons of as much as 1.5 ksi amplitude.  Away from the contact boundary, these fluctuations are attenuated.  In the case of the composite specimen (away from the failure zones) the distributions are much smoother than in the aluminum specimen.  The possible sources of these fluctuations are computational and experimental artifacts, and true localized frictional phenomena.

### (i)  Computational artifacts

The test case for the localized hybrid analysis provides a good check of the sensitivity of the numerical method.  The fact that the errors introduced in the displacements caused only small amplitude fluctuations directly associated with the input data suggests that differences between Gauss point and nodal point accuracies may be discounted.  Also, the largest error in assigning the input nodal displacements from the fringe values would give rise to a fluctuation of no more than 0.5 ksi and probably less.

The stress distributions were calculated for several load levels. The fluctuations tended to occur at fixed locations around the contact interface. This provides further support to the proposition that random errors in assigning fringe order displacement data to the boundary nodes may be discounted. More important, however, it suggests that the fluctuations are identified with the contact geometry.

The composite and aluminum specimen data were originally analyzed with different meshes and finite element programs. When both sets of data were reduced using identical procedures the results were the same. That is the fluctuations in the aluminum specimen stresses were still much greater than in the composite.

(ii) Experimental artifacts

The gratings on the aluminum and composite specimens were different. Those on the aluminum were etched and thus had zero thickness while the composite specimen had replicated gratings which had a thickness of about 0.001 in. The etched grating was used to eliminate the possibility of shear lag in the epoxy replicating medium. The presence of shear lag would cause some smoothing of fluctuations but it is very unlikely that this effect would be large enough to account for the much smoother stress distributions in the composite specimen study.

(iii) Localized frictional effects

The arguments presented above suggest that the experiment on the aluminum specimens has identified localized frictional effects which give rise to stress fluctuations of about 1 ksi. The fluctuations are large enough to mask the general trend in the contact shear stress. Moving away from the contact interface these fluctuations are rapidly

attenuated and the stress distributions become independent of the frictional effects at the interface. Thus the interfacial frictional effects are very short range and associated with small scale phenomena.

It will be observed that the stress distributions do not show exact symmetry about $\theta = 90°$. The shear stress distributions show the most pronounced lack of symmetry and the effect of this is to move the peak radial and minimum hoop stresses away from $\theta = 90°$. The fringe patterns clearly indicate a lack of symmetry in displacements. Thus the frictional effects are not symmetrical. This is, of course, consistent with a localized friction model.

The composite specimen did not show such strong localized effects. Also, the shear stress distributions were very different from those in the aluminum specimen. From $\theta = 0$ to about $\theta = 30°$, the shear stresses are negative in both cases. However, beyond $\theta = 30°$ the composite specimen has positive shear stresses on the contact interface. (It will be recalled that only a limited range of $\theta$-values were available for the composite due to local failure.) This indicates that the sign of the direction of slip or tendency to slip in the composite is reversed beyond $\theta = 30°$. The photoelastic experiments reported by Hyer and Liu [9] are much less sensitive than those presented here. The photoelastic study yielded opposite signs of shear stresses in isotropic and quasi-isotropic plates. The current investigation suggests this is only partly true. (It seems likely that the photoelastic experiment might not have been able to detect the small positive shear stresses.)

This difference between isotropic and quasi-isotropic behavior is important and has not been included in analytical studies which use laminated plate theory. One clue to the behavior of the (0/60/-60)

laminate lies in the observation that there is a plane of symmetry at $\theta$ = 30° where the shear stress changes sign. This is illustrated in Fig. 54. Another factor concerns the detailed frictional behavior of the composite and the aluminum pin. Frictional effects occur between the aluminum and the graphite fibers and between the aluminum and the epoxy matrix. The nominal fiber volume fraction is 60% but consideration should be given to the variation with $\theta$ of the area of graphite exposed to the aluminum. It may be shown that this is minimized at $\theta$ = 90° and 30° but is largest at $\theta$ = 60° where some fibers are tangential to the hole. Thus the frictional tractions in the composite will vary with angular position in a manner different from that in an isotropic material. Near $\theta$ = 60°, the greatest amount of graphite will be in contact with the aluminum. Thus any model of the frictional behavior of a pin-loaded fiber composite plate must include the variation of the co-efficients of friction with angular position. That is, the simple application of Coulomb friction will be in error.

The above arguments are specific to the (0/60/-60) lay-up but similar arguments apply to other stacking sequences. The shear stress distributions in the composite specimen are further complicated by the presence of local failure.

## 6.4  COMPOSITE PLATE, FAILURE ANALYSIS

After loading and unloading the graphite-epoxy plate, non-destructive damage evaluation techniques were employed. The ultrasonic C-scan showed no evidence of (delamination) damage. However, the penetrant enhanced X-ray investigation showed the presence of matrix cracks in the 60° and -60° plies at $\theta \simeq$ 30° and $\theta \simeq$ 150° respectively.

Note that the cracks are larger in the -60° plies which are four layers thick. There was also some evidence of bearing failure (Fig. 55).

Micrographic sections were also prepared from the specimens. These failed to show the matrix cracks so clearly defined in the radiographs but they were successful in depicting the bearing failures of the 0° plies. Fig. 56 shows fiber kink in the outer 0° ply and associated delamination (which is also apparent in the radiograph) near $\theta = 90°$.

The stress distributions obtained at the pin-plate boundary were used in a laminate analysis to determine the variation of the ply stresses with angle. In order to predict the location of matrix cracking, stresses normal to the fiber direction are plotted for each ply orientation in Figs. 57-59. It may be observed that the largest tensile stresses normal to the fiber direction occur in the 60° plies. The angular location of the peak stress increases with load and occurs at about 20° at a load of 900 lb. On the basis of a maximum stress failure criterion the location of the matrix cracks is well predicted.

At this stage it is not possible to determine the load at which the matrix cracking first occurs. The inclusion of thermal residual stresses is a very significant but unquantifiable factor. A further complication is the fact that the observed damage is that accumulated in the complete loading cycle. There is experimental evidence that matrix cracking may have occurred at very low load levels first in the thick (4 layers) -60° plies near $\theta = 150°$, rather than in the thinner (2 layers) dispersed 60° plies near $\theta = 30°$.

Further discussion follows in the section General Summary and Conclusions.

# REFERENCES

1.  Morton, J., Post, D., Han, B. and Tsai, M. Y., "Stress and Failure Analysis of a Pin-Loaded Composite Plate". Presented at 29th Structures, Structural Dynamics and Materials Conference, Williamsburg, VA, April 1988.

2.  Post, D., "Moire Interferometry," Chapter 7, Handbook of Experimental Mechanics, A. S. Kobayashi, Editor, Prentice-Hall, Englewood Cliffs, NJ, 1987.

3.  Joh, D., "An Experimental Study of the Frictional Phenomena Around the Pin Joints of Plates Using Moire Interferometry." Ph.D. Dissertation, Dept. of Engineering Science & Mechanics, Virginia Polytechnic Institute & State Univ., Blacksburg, VA, 1986.

4.  Joh, D., Czarnek, R. and Post, D., "Measurement of Micro-Slip Amplitude Around the Pin Joint of Plates Using Moire Interferometry." SPIE Proc. 814, Bellingham, WA (in press).

5.  Hyliger, P. R., "Frictional Phenomena in Planar Elastic Contact Stress Problems," Ph.D. Dissertation, Dept. of Engineering Science & Mechanics, Virginia Polytechnic Institute & State Univ., Blacksburg, VA, 1986.

6.  Post, D., Czarnek, R. and Joh, D., "Shear Strain Contours from Moire Interferometry," Experimental Mechanics, 25(3), pp. 282-287, 1985.

7.  Reddy, J. N., An Introduction to the Finite Element Method, McGraw-Hill, New York, 1984.

8.  Hinton, E. and Owen, D. R. J., Finite Element Programming, Academic Press, London, 1977.

9.  Hyer, M. W. and Liu, D., "Stresses in a Quasi-isotropic Pin-Loaded Connector Using Photoelasticity," Experimental Mechanics, 24(1), pp. 48-53, 1984.

10. Hyer, M. W. and Klang, E. C., "Contact Stresses in Pin-Loaded Orthotropic Plates," Int. J. Solids & Structures, Vol. 21, No. 9, pp. 957-975, 1985.

11. Frocht, M. M. and Hill, H. N., "Stress-Concentration Factors Around a Central Circular Hole in a Plate Loaded Through Pin in the Hole," J. Appl. Mech., Trans. ASME, 62, pp. A5-A9, 1940.

**Specimen Material**

Plate :
(1)Aluminum 7075–T6
(2)AS4–3501-6
$[0_2/60_2/-60_2]_s$

Pin :
Aluminum 7075–T6

| | in | mm |
|---|---|---|
| A | 3.0 | 76.2 |
| B | 12.7 | 323.7 |
| C | 1.5 | 38.1 |
| D | 0.751 | 19.08 |
| E | 0.75 | 19.05 |
| F | 1.061 | 26.95 |
| G | 0.061 | 1.55 |

0.001 in
Initial
Clearance
$(D_{hole} - D_{pin})$

x,U

y,V

Load

R

R

R

G

F

E

Pin

Thickness
0.061 in
(1.55 mm)

Grating

D

A

B

C

Plate
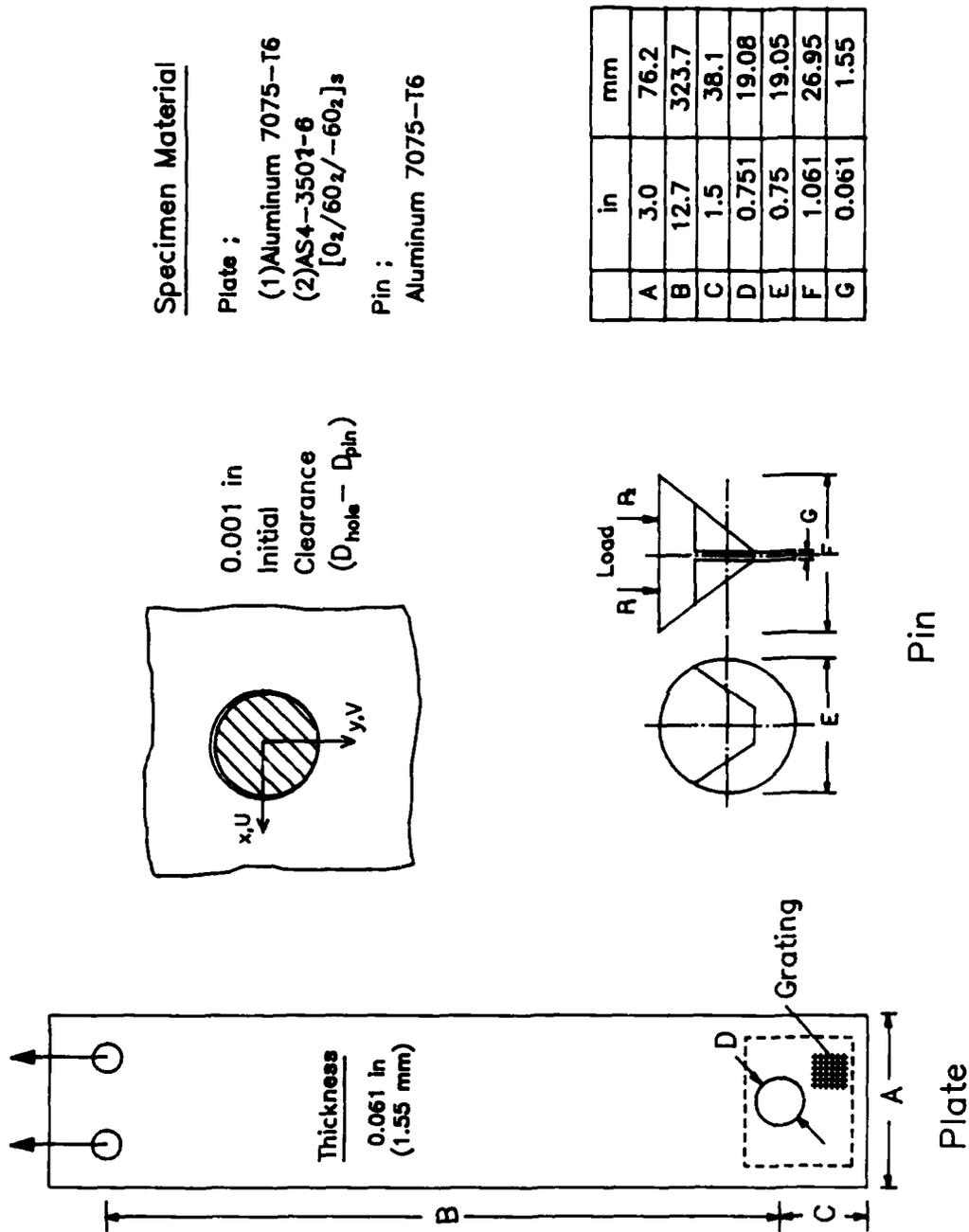
Fig. 1. Specimen geometry and specimen material.
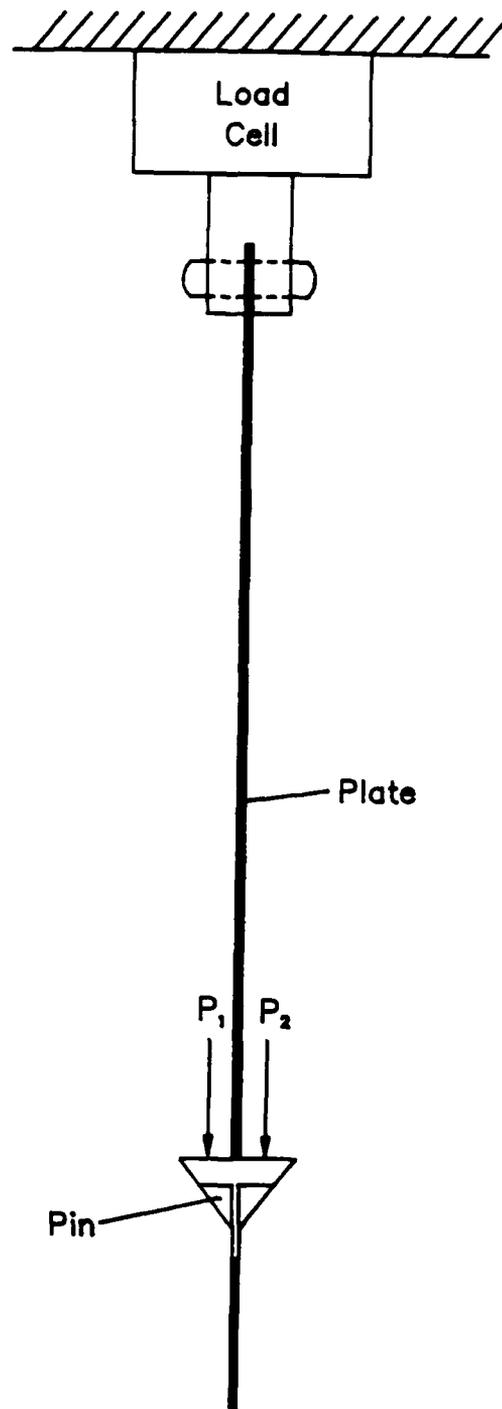
Fig. 2. Schematic diagram of the loading system.
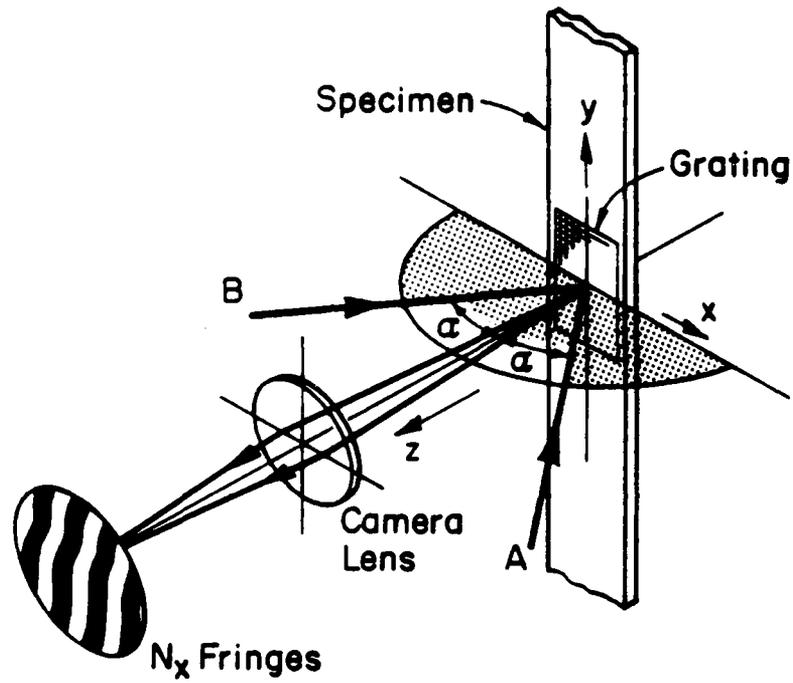
Fig. 3. Schematic diagram of moire interferometry for generating the $N_x$ fringe pattern, which depicts the U-displacement field. Corresponding beams C and D (not shown) in the yz plane generate the V-displacement field. Note that A, B, C and D represent broad beams, not merely rays.
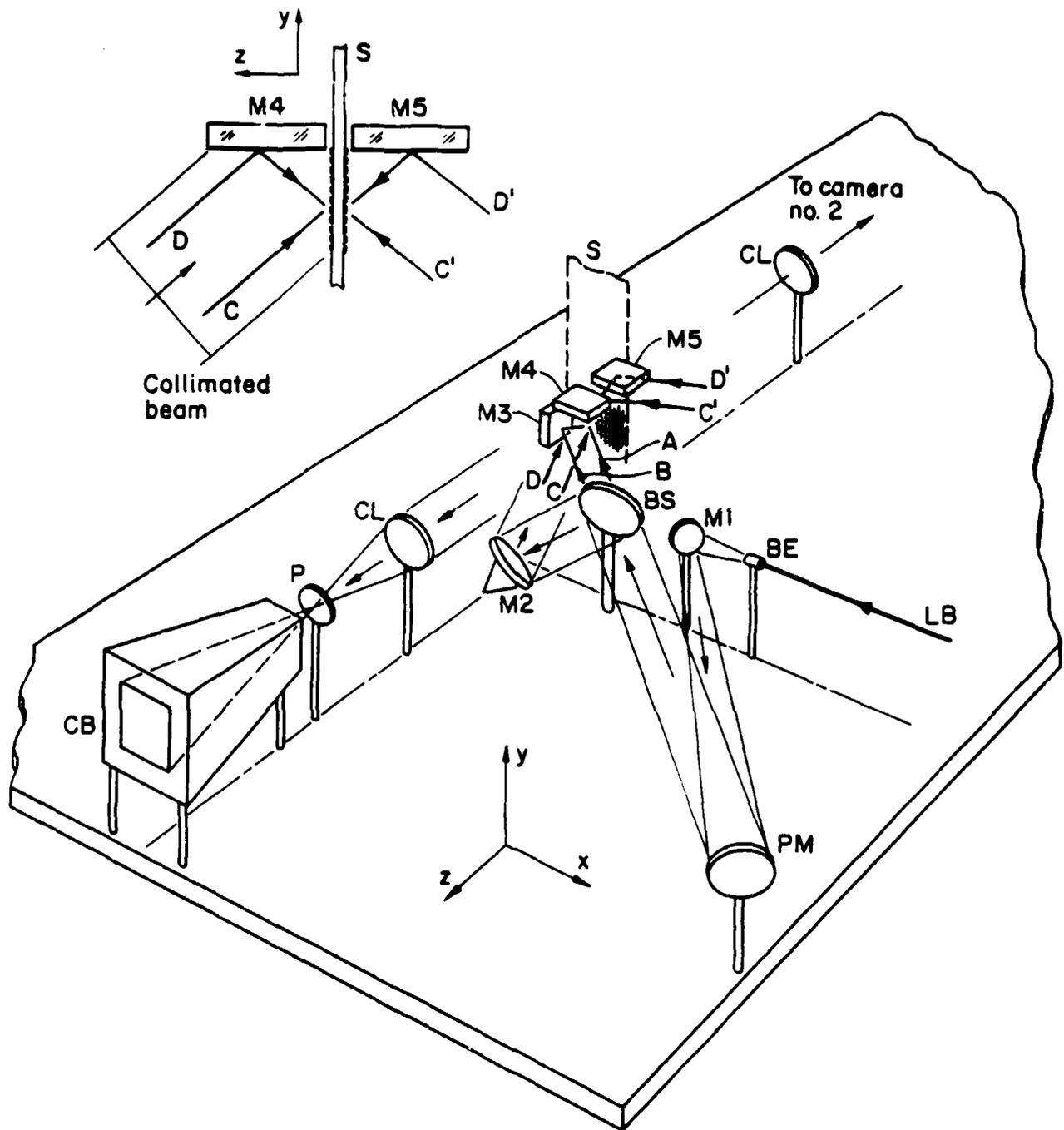
Fig. 4. Moire interferometer for 2-sided viewing of specimen.
Additional elements form collimated beams C' and D'.

| | | | |
|---|---|---|---|
| LB | – laser beam | S | – specimen and spec. grating |
| BE | – beam expander | CL | – camera lens |
| M1-M5 | – plane mirrors | P | – linear polarizer |
| PM | – parabolic mirror | CB | – camera back |
| BS | – beam splitter | | |
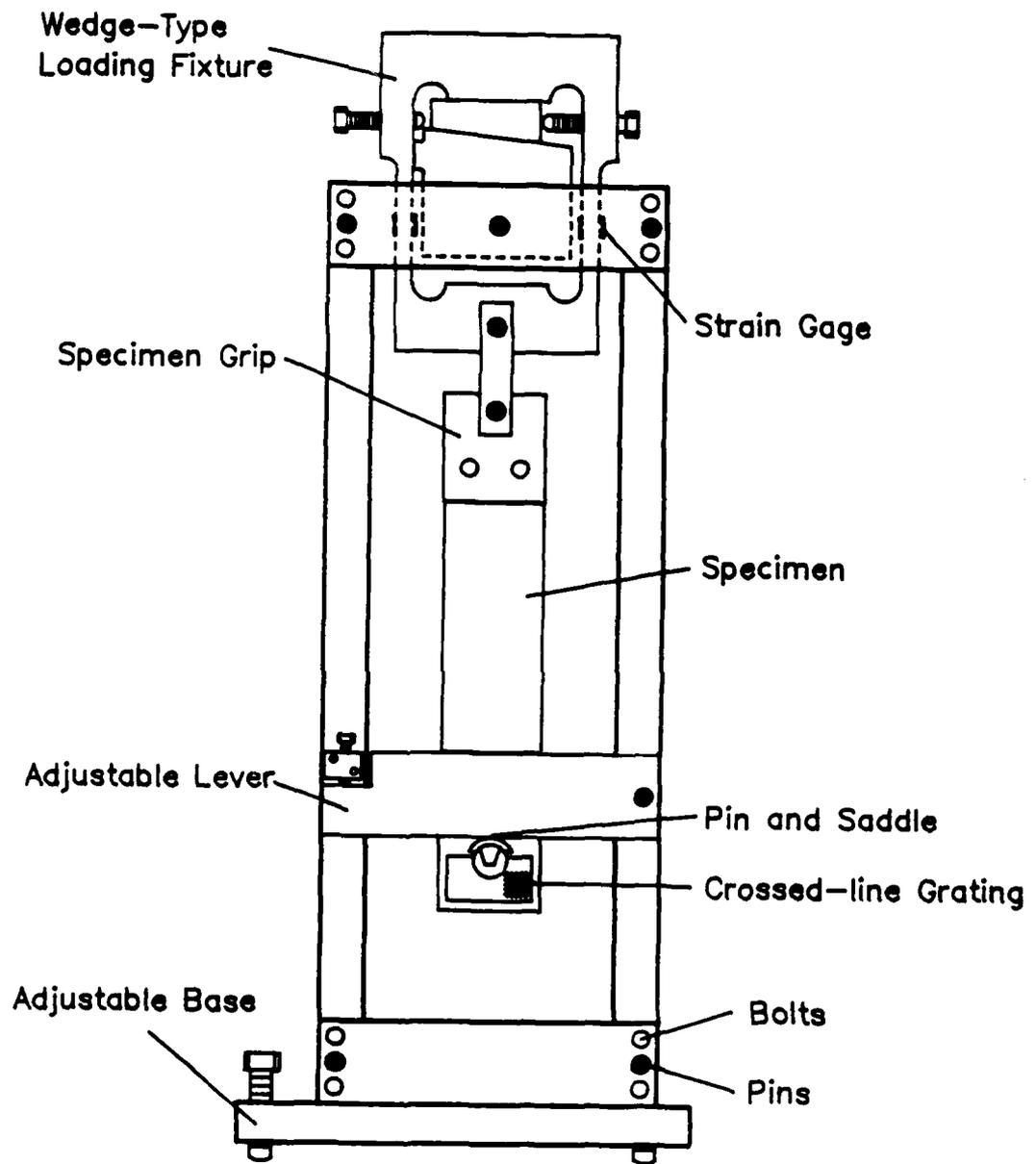
Fig. 5. Loading system.
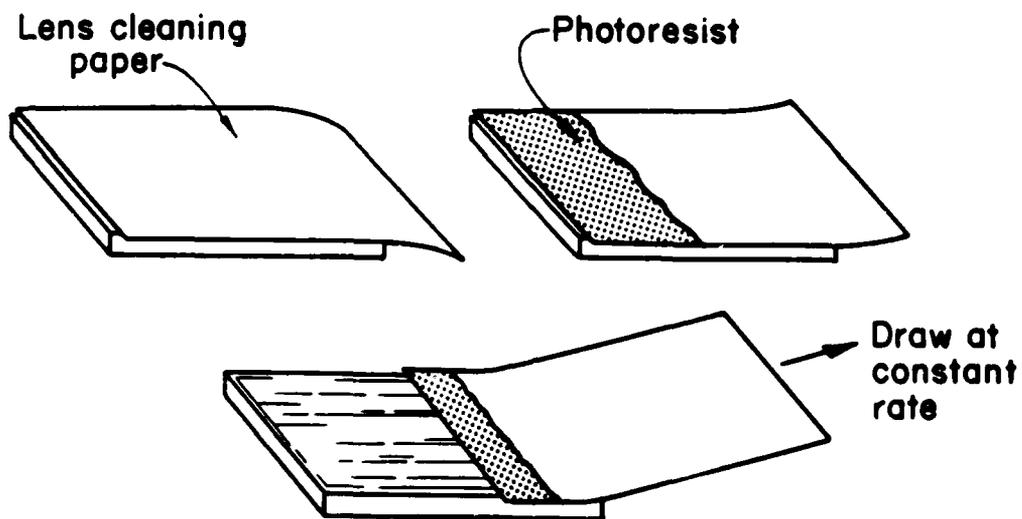
Fig. 6. Drag method for applying a uniform film of photoresist on the aluminum specimen.
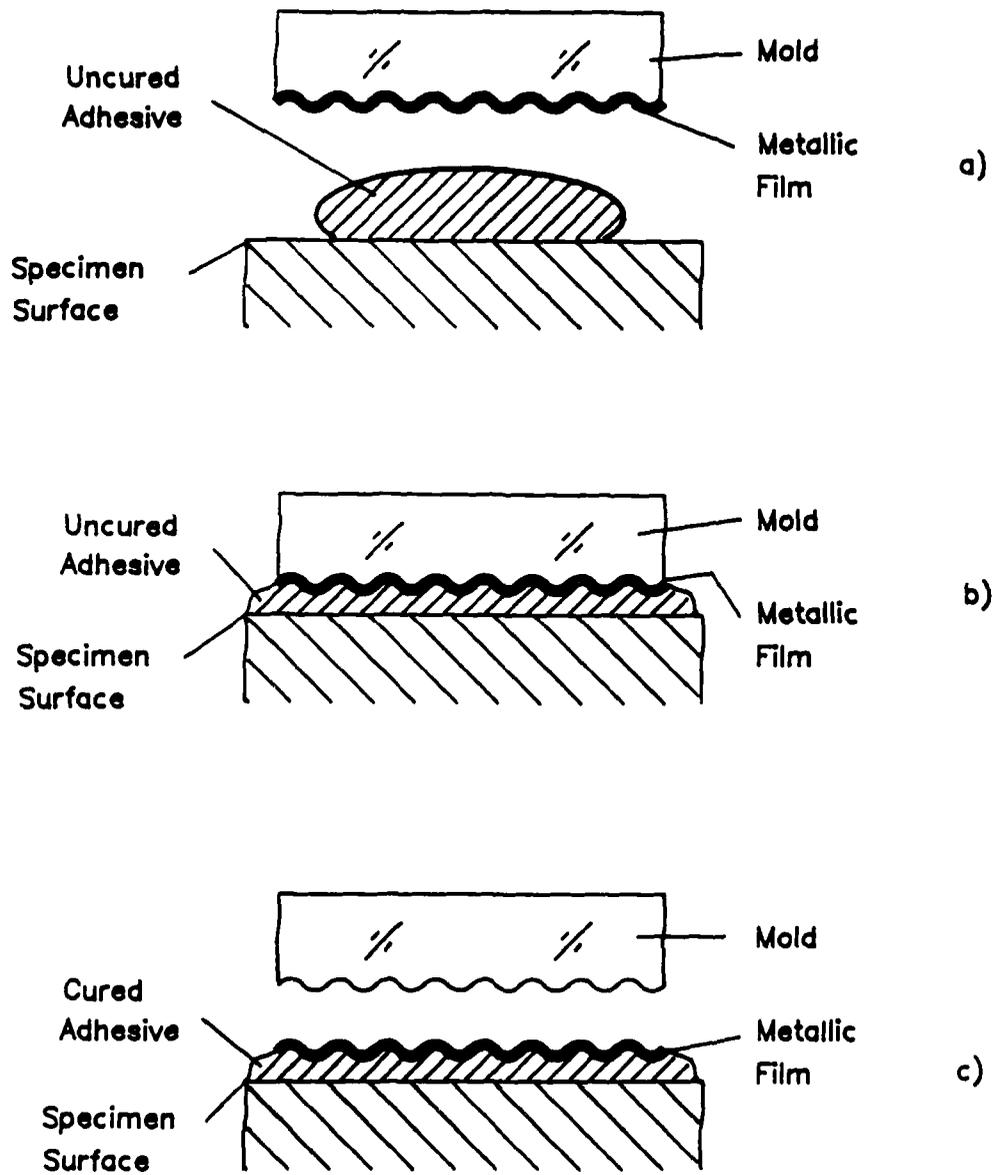
Fig. 7. Replication technique used to form gratings on the composite specimen.
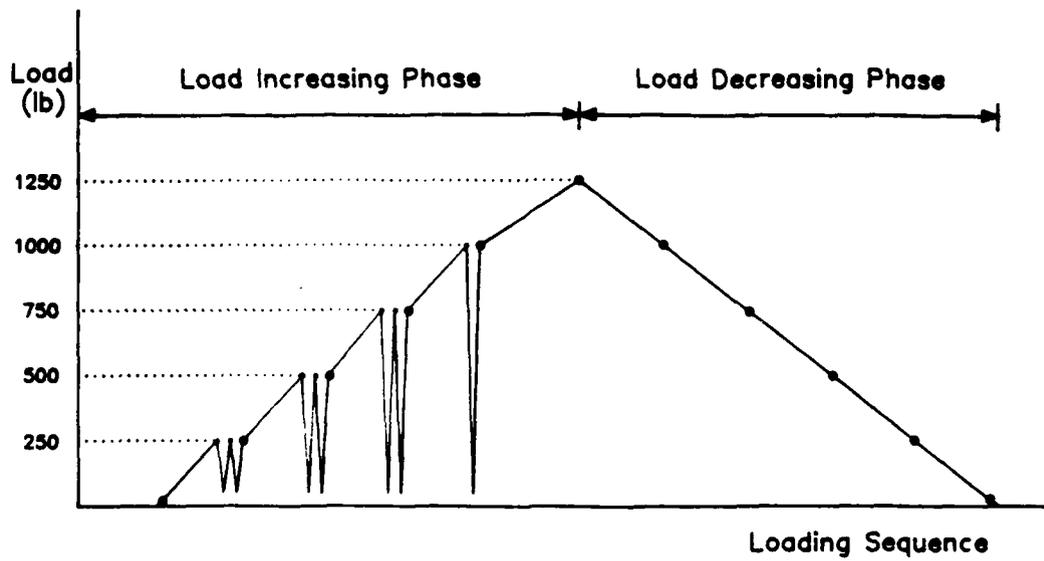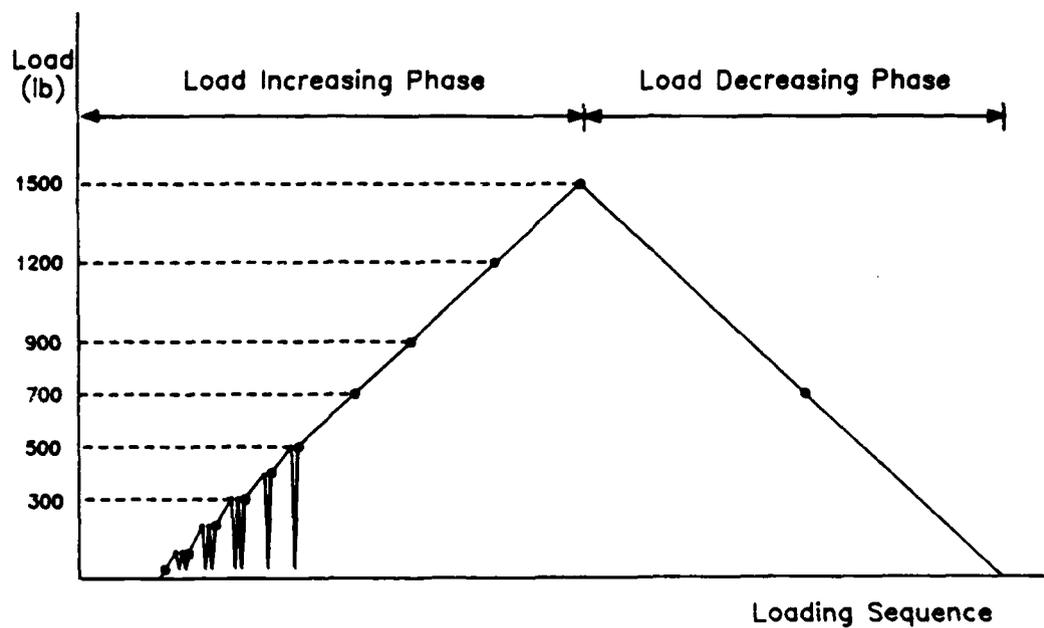
Fig. 8. Loading and unloading sequence. Small circles represent the iterative procedure for achieving plane stress conditions; larger circles indicate photographic records of fringe patterns.

Fig. 9a. $N_y$ fringe pattern, depicting the V-displacement field at the front of the aluminum specimen for the 500 lb. load.

Fig. 9b. $N_x$ fringe pattern, depicting the U-displacement field at the front of the aluminum specimen for the 500 lb. load.
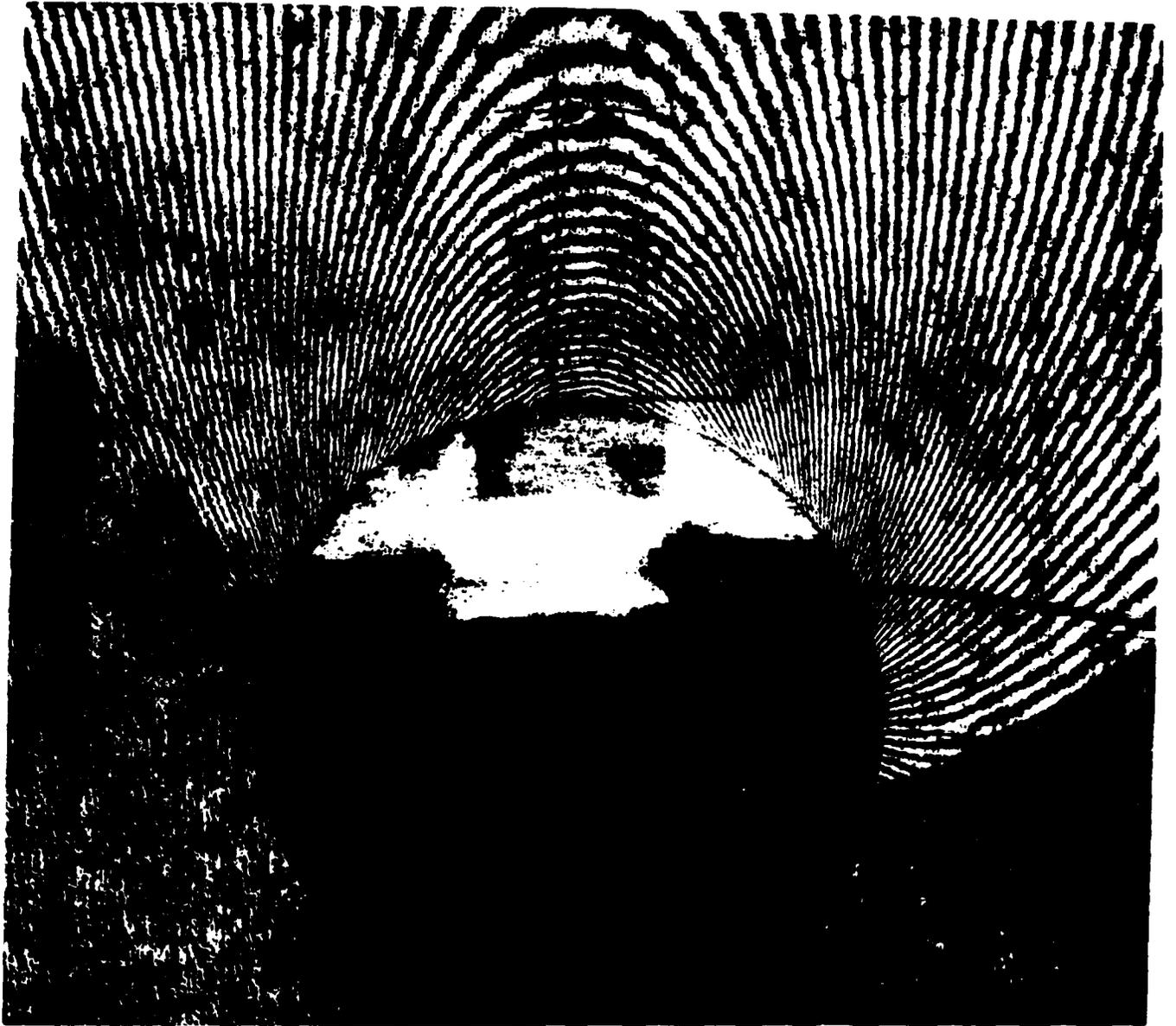
Fig. 9c. $N_y$ pattern at the back of the aluminum specimen for the 500 lb. load.
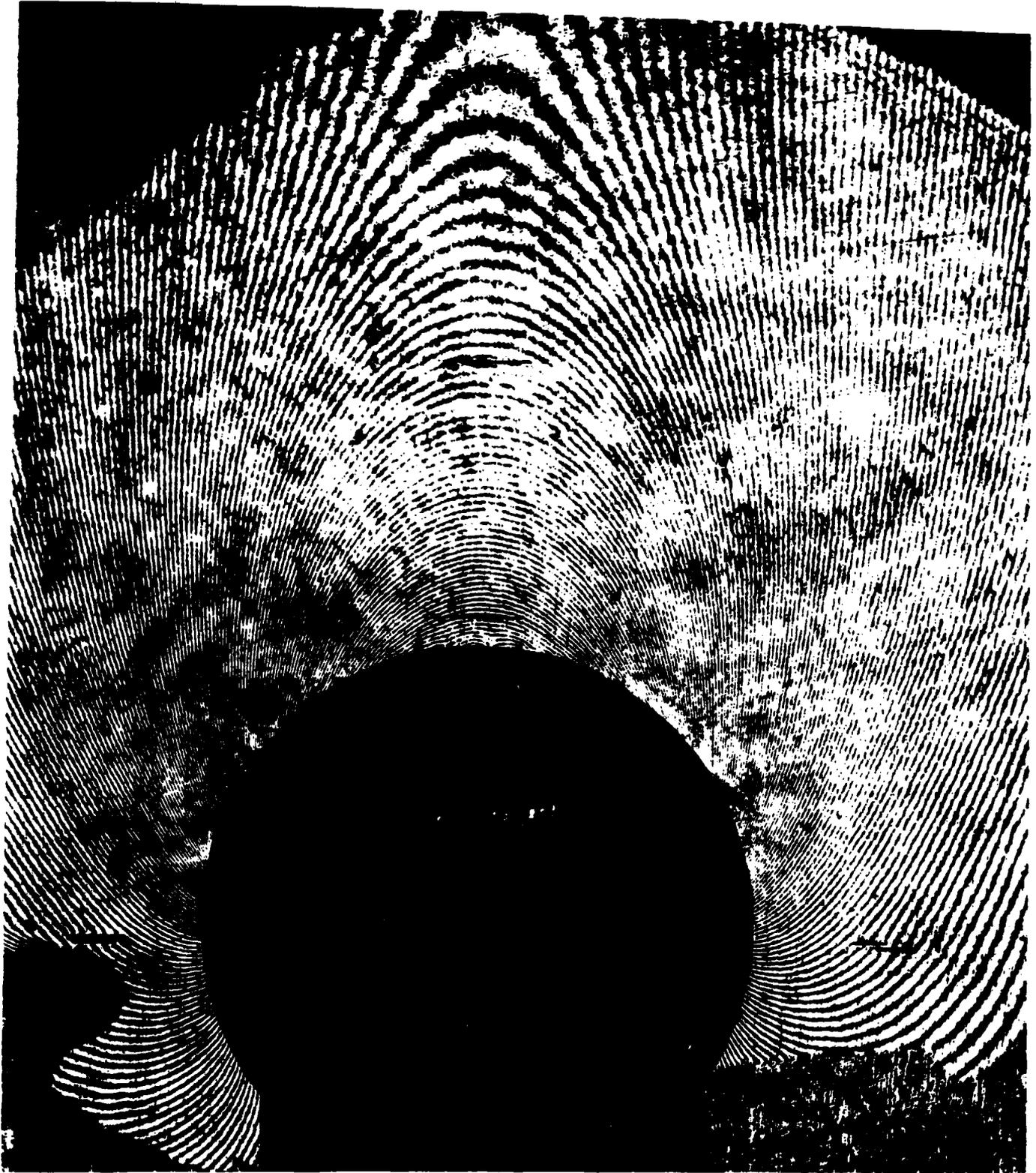
Fig. 10a. $N_y$ pattern at the front of the aluminum specimen for the 1250 lb. load.

61
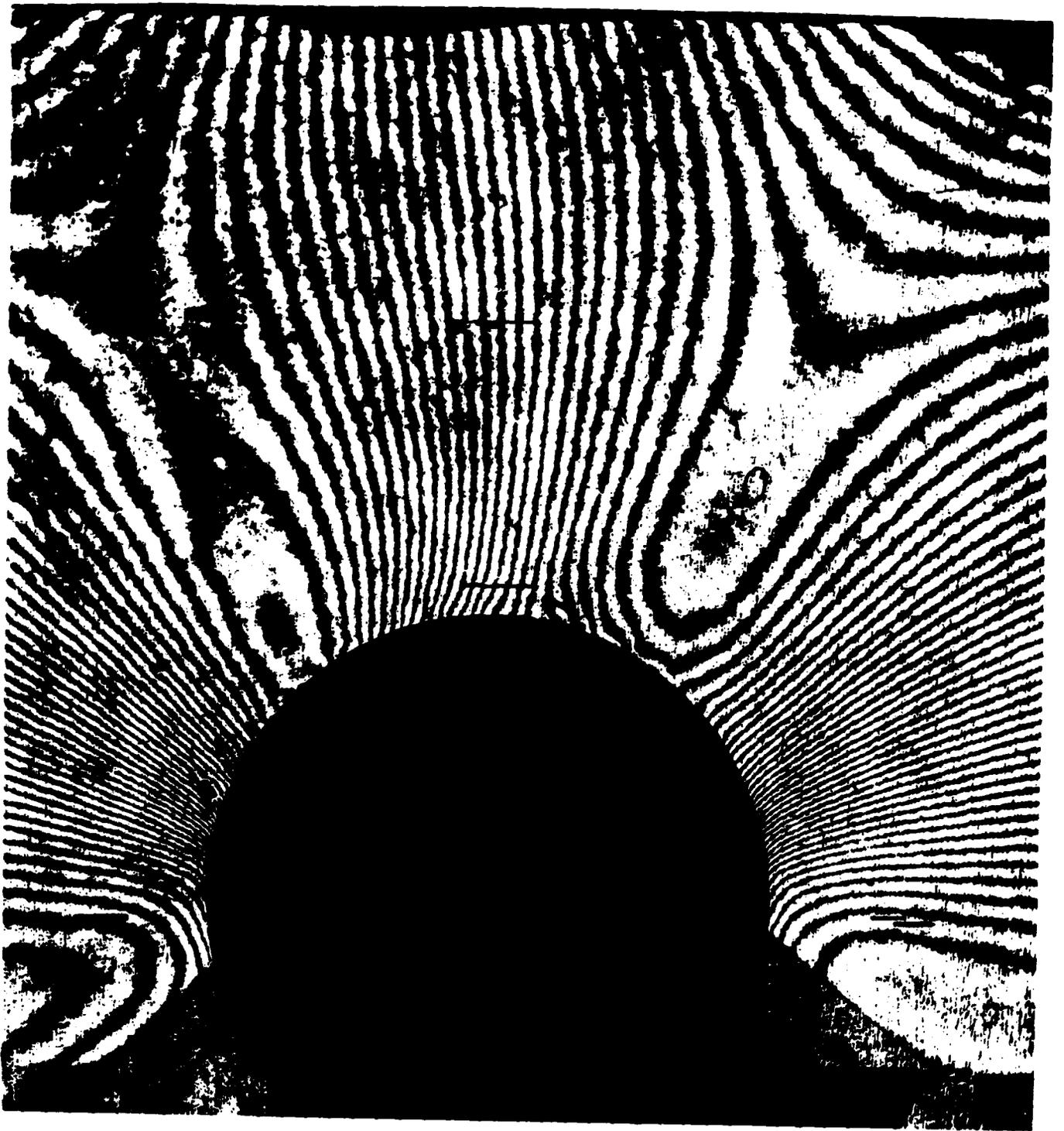
Fig. 10b. $N_x$ pattern at the front of the aluminum specimen for the 1250 lb. load.
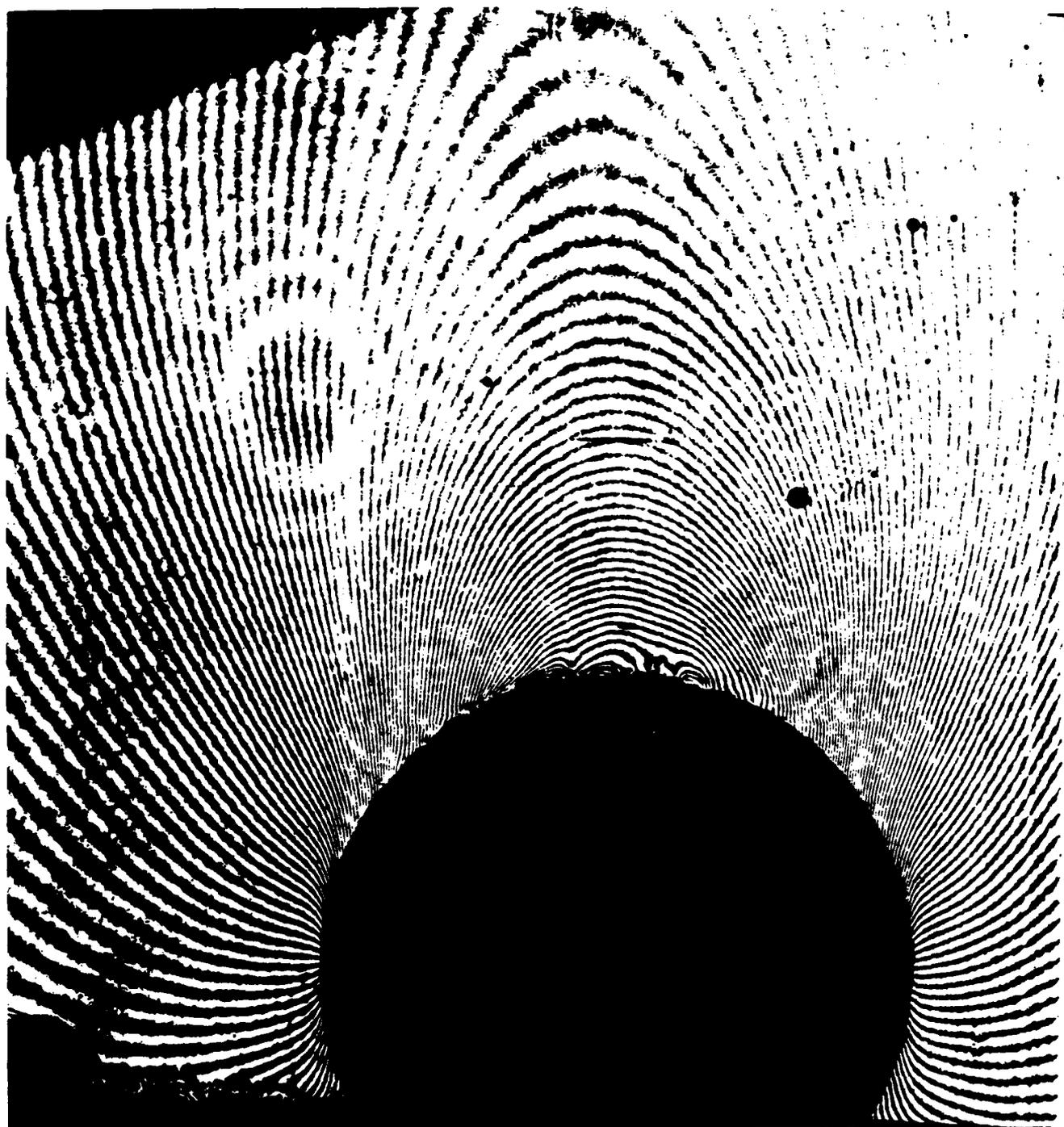
Fig. 11a.  $N_y$  fringe pattern at the front of the composite specimen for the 400 lb. load.
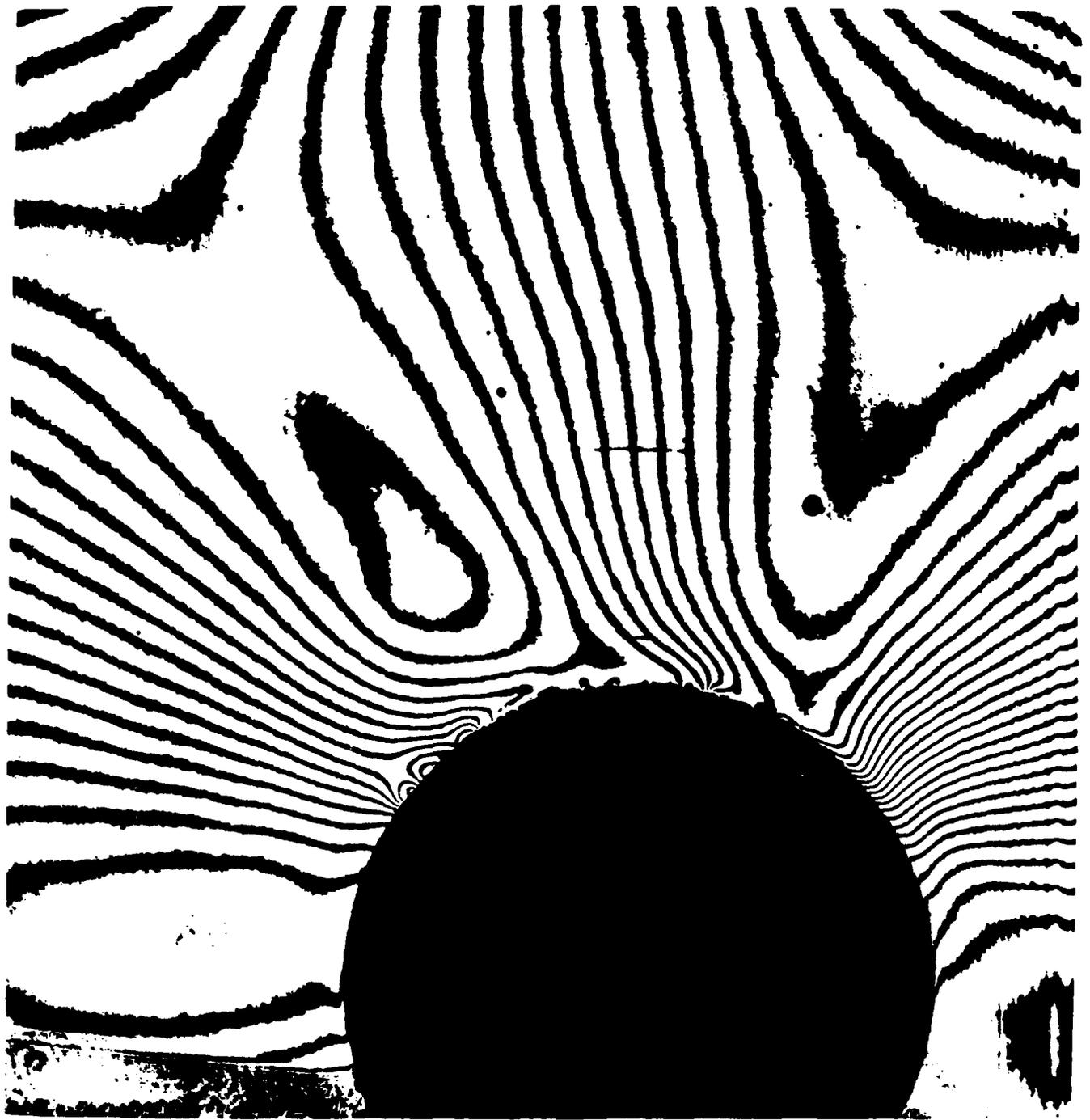
Fig. 11b.  $N_x$ fringe pattern at the front of the composite specimen for the 400 lb. load.
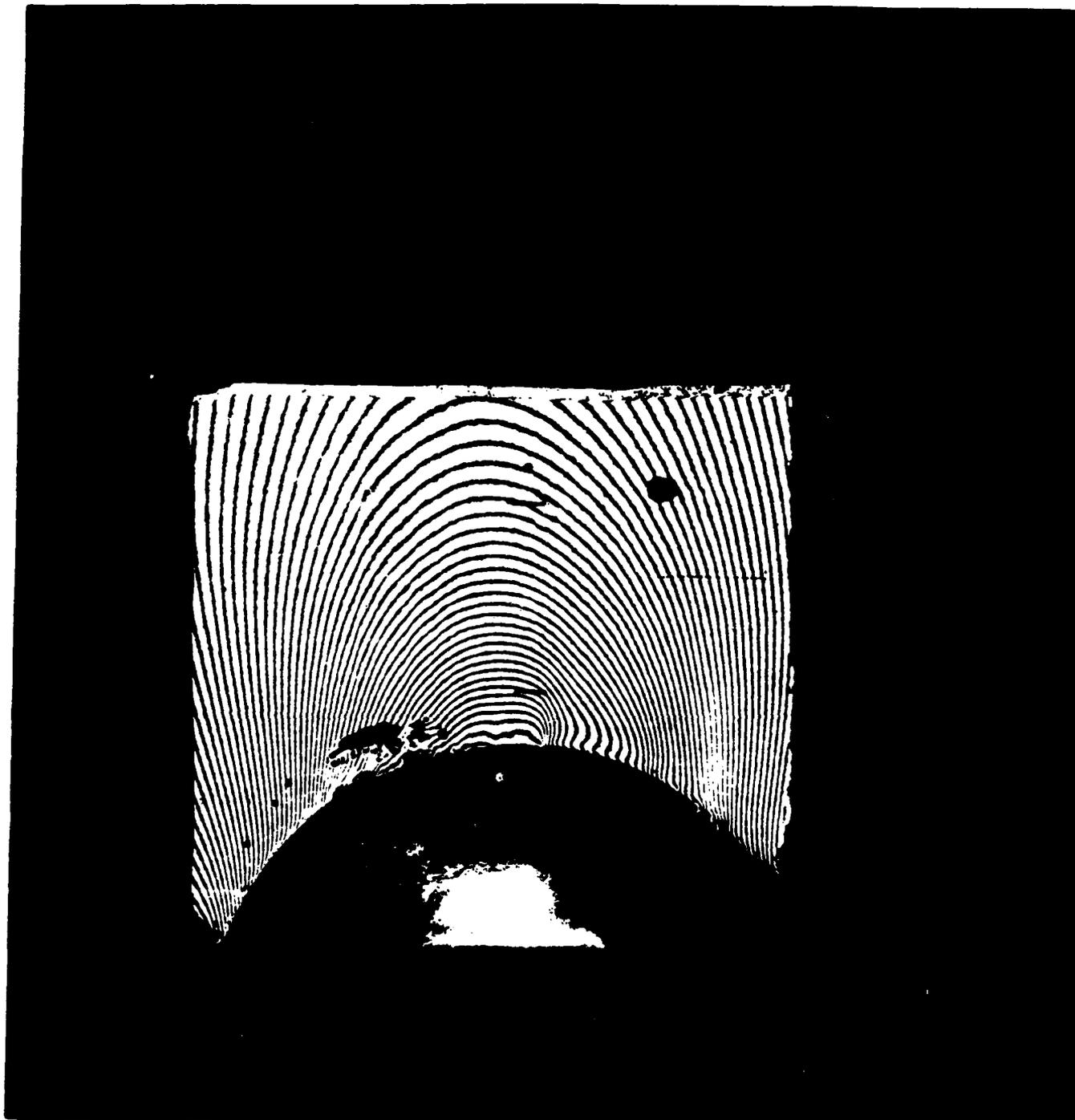
Fig. 11c. $N_y$ pattern at the back of the composite specimen for the 400 lb. load.
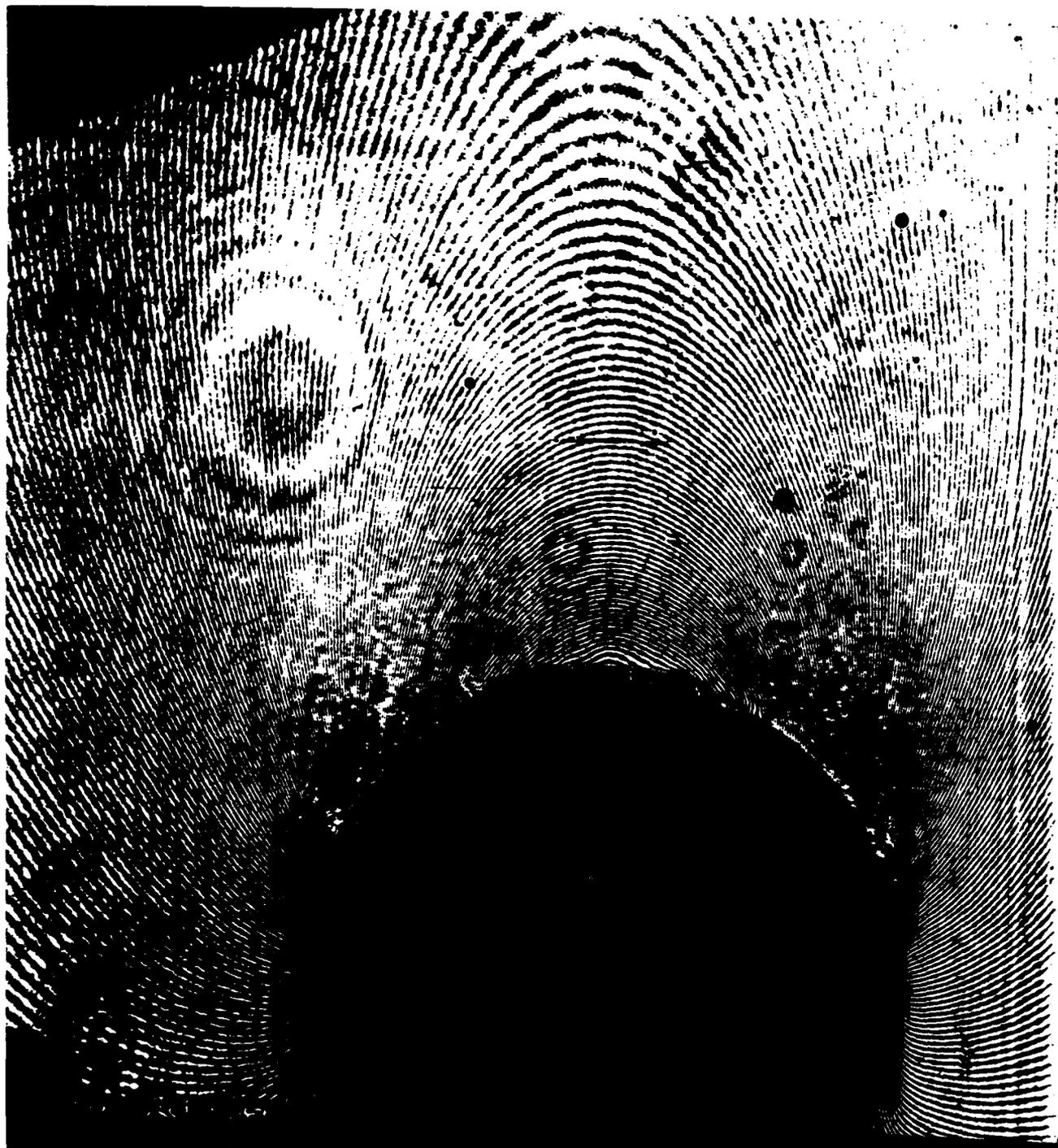
Fig. 12a. $N_y$ fringe pattern at the front of the composite specimen for the 900 lb. load.
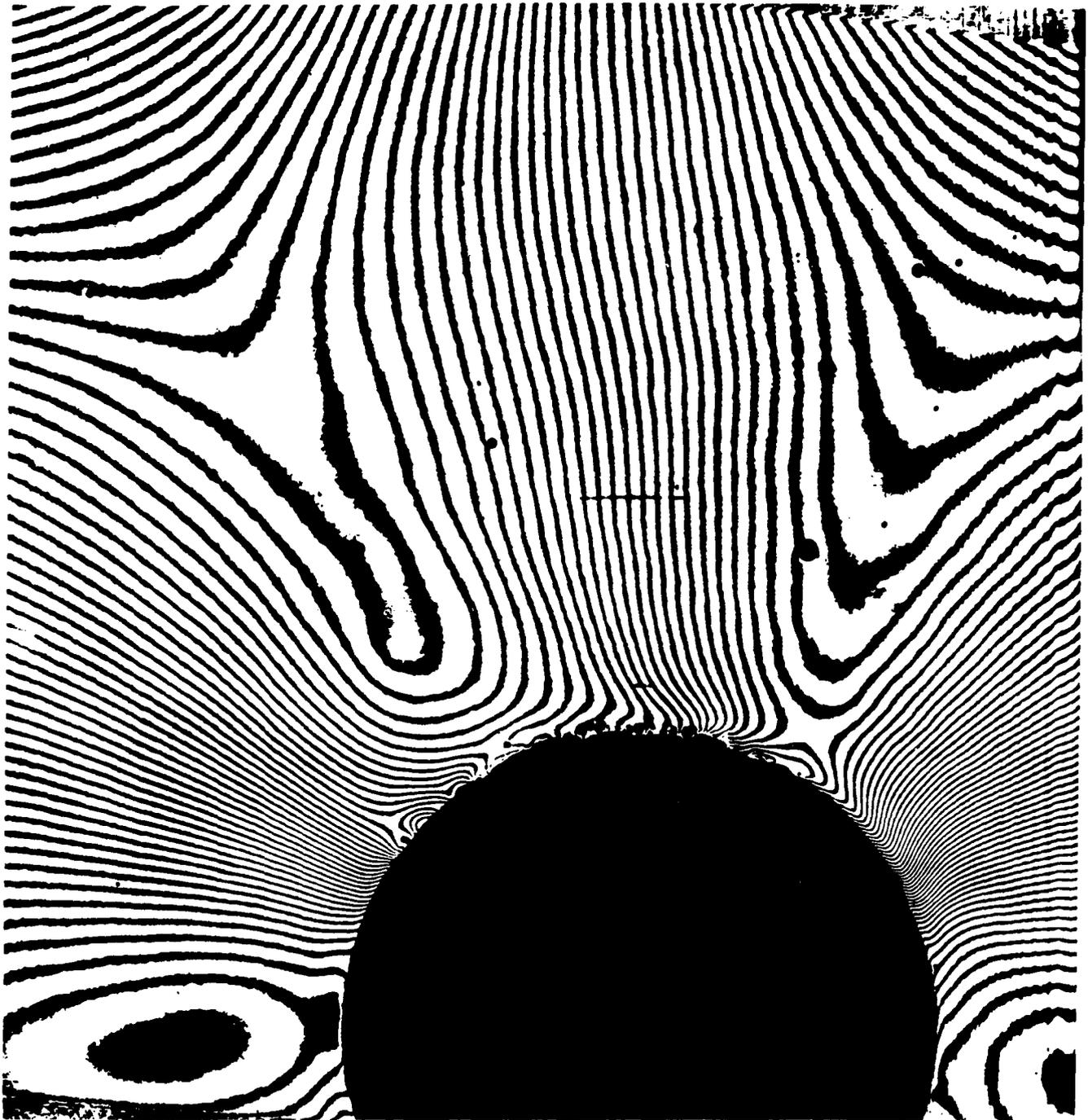
Fig. 12b.  $N_x$ fringe pattern at the front of the composite specimen for
the 900 lb. load.
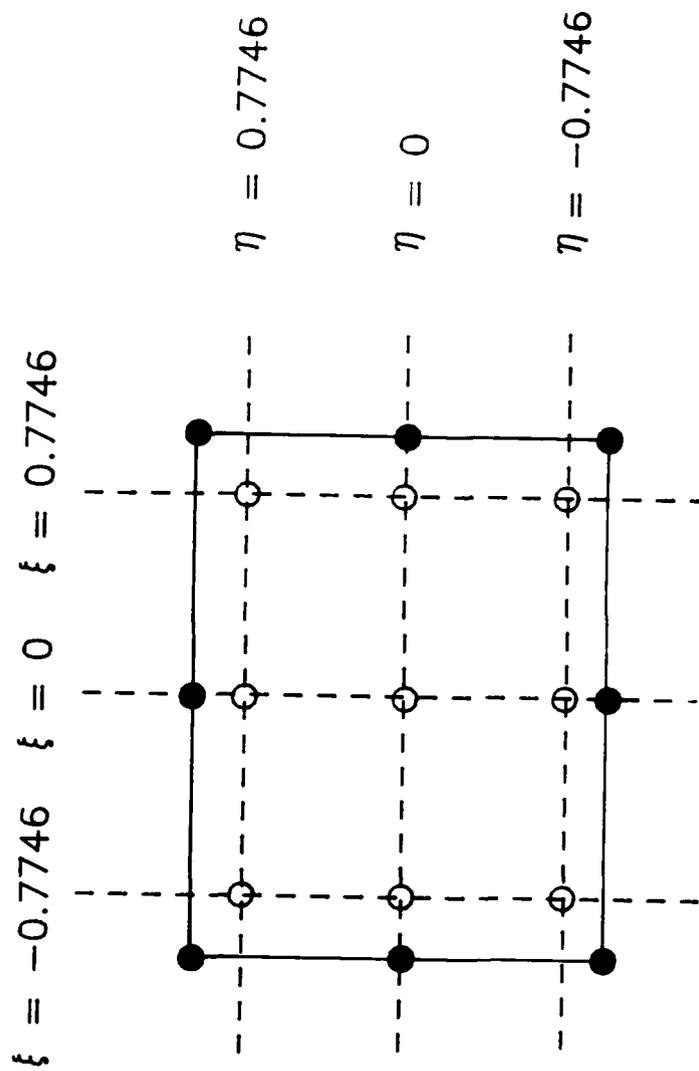
Fig. 13. Gauss point locations for an 8-node quadrilateral element.
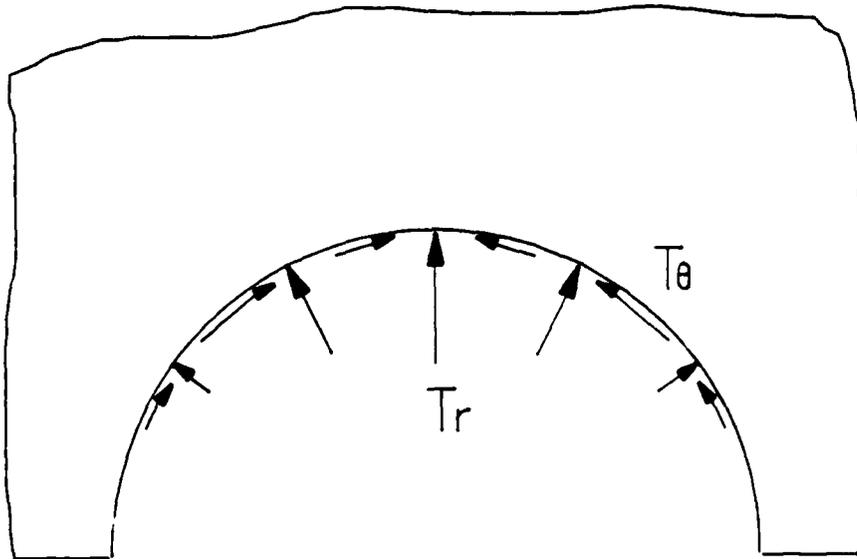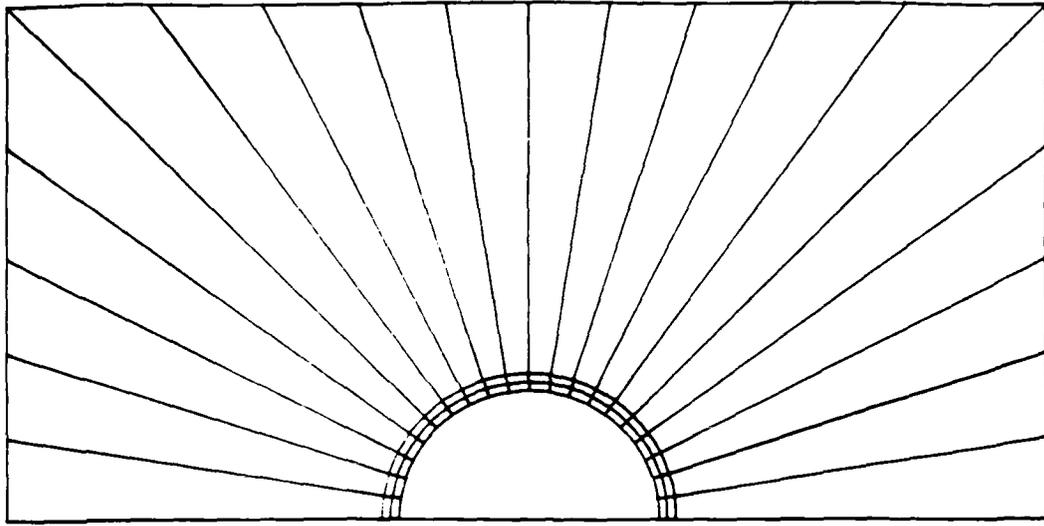
Fig. 14. Numerical model for testing the localized hybrid analysis.
The mesh is taken as representative of the region of interest in the
experiment and the loads were chosen to give typical stresses in the
contact problem.
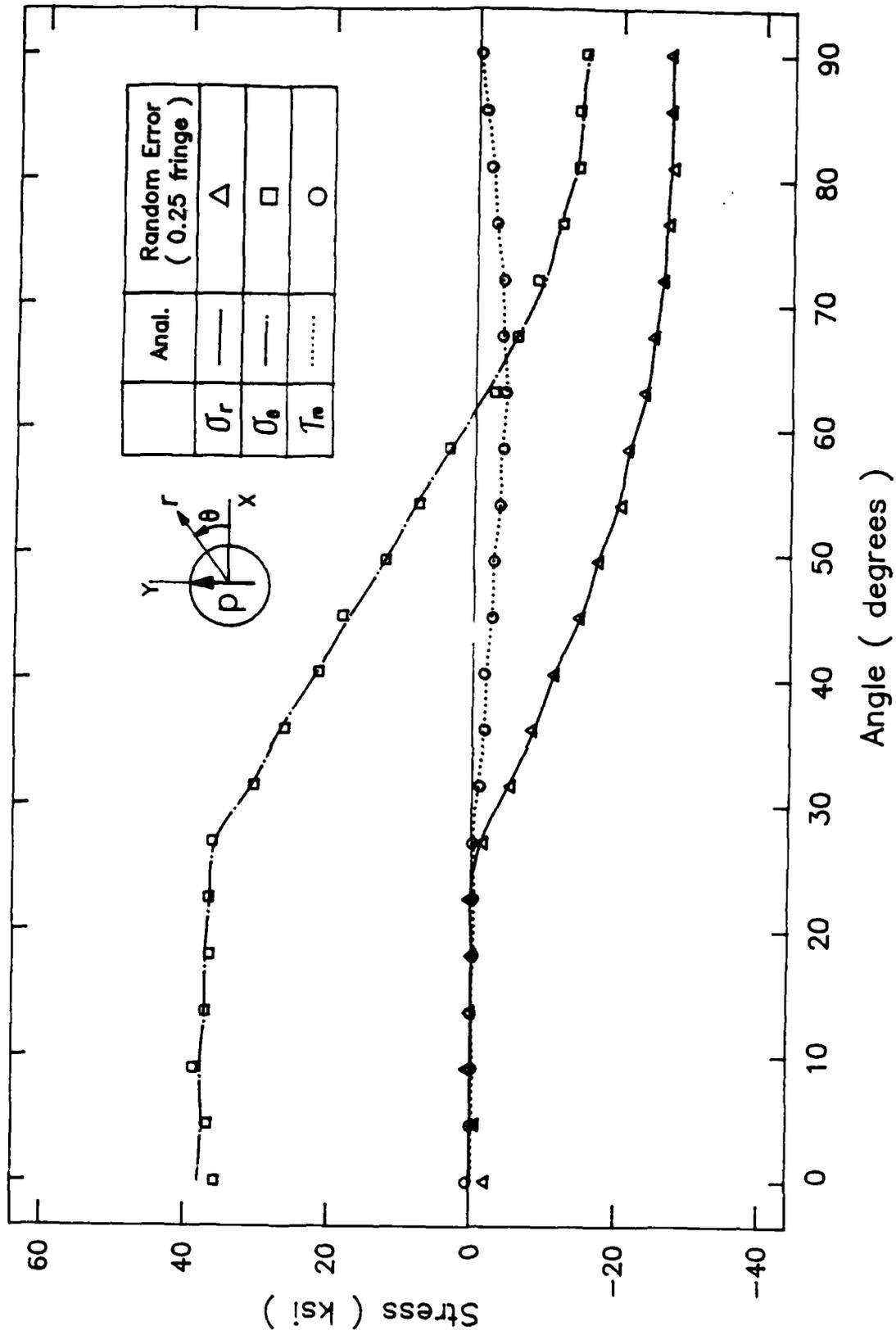
Fig. 15. Comparison of stresses for load input case and a displacement
input case with random errors of maximum value corresponding to one
quarter fringe order.

70
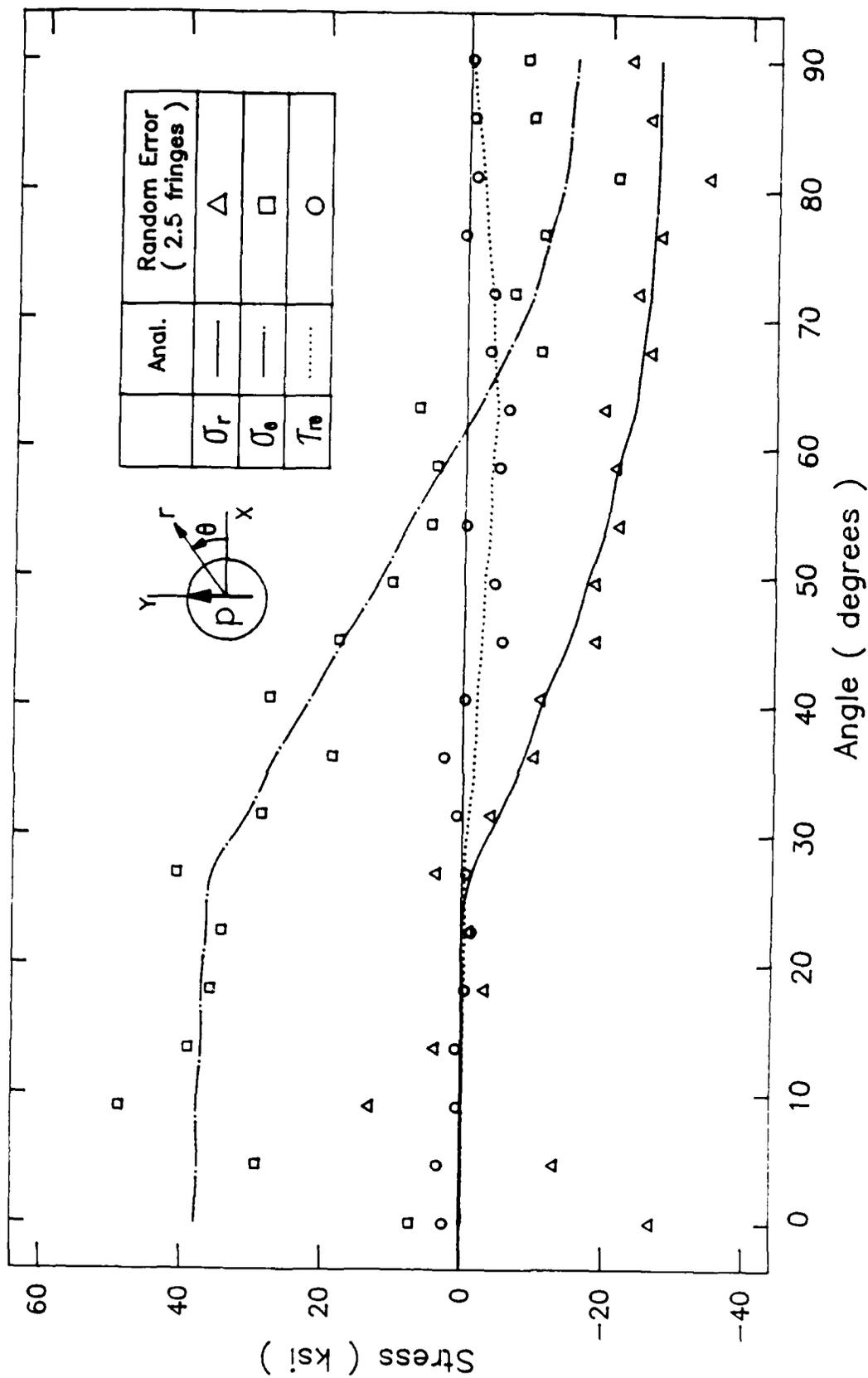
Fig. 16. Comparison of stresses for load input case and a displacement
input case with random errors of maximum value corresponding to 2.5
fringe orders.

71
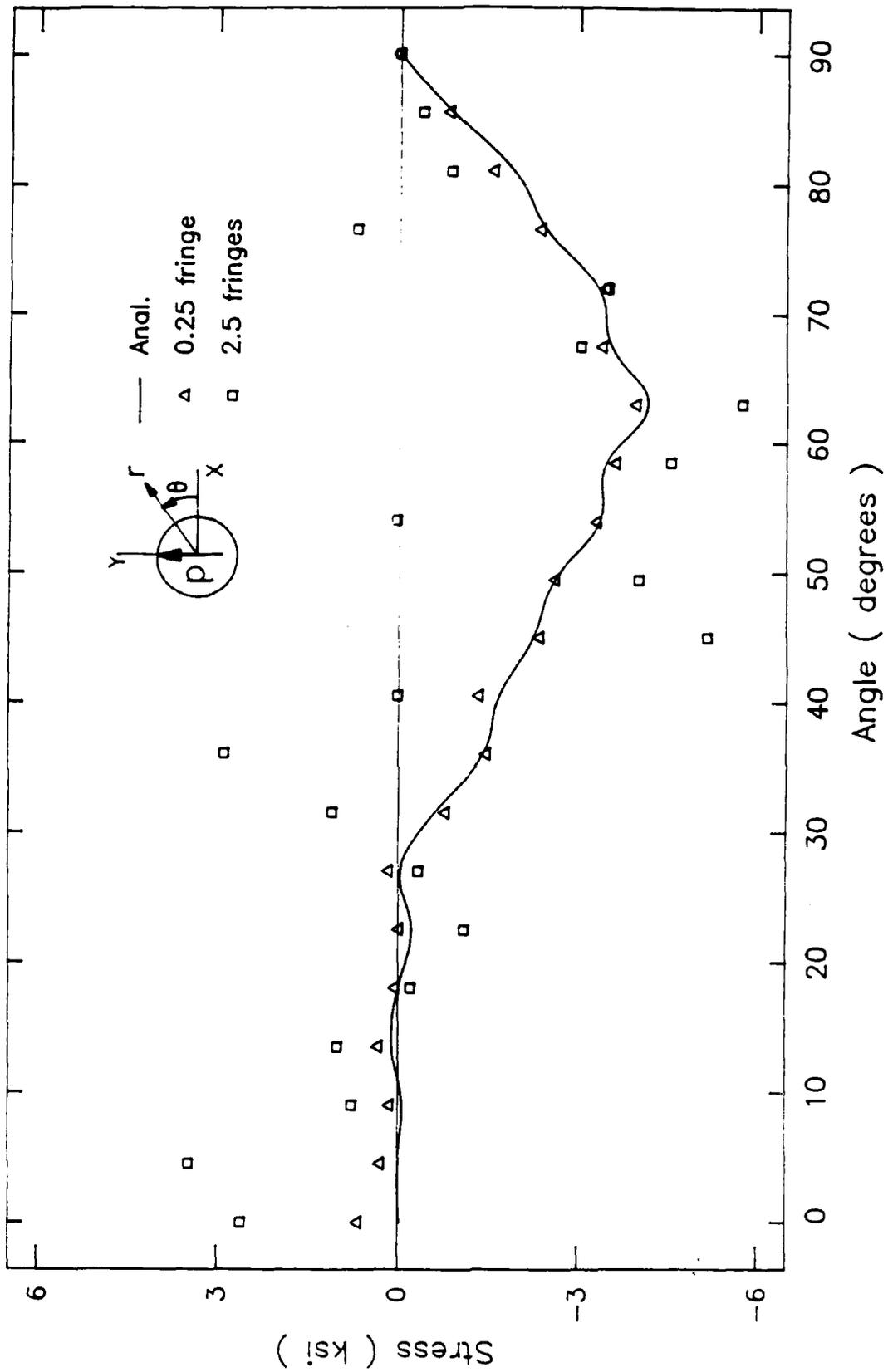
Fig. 17. Comparison of shear stresses determined from the load input
case and a displacement input case with random errors of maximum value
corresponding to one quarter fringe order. Input data were adjusted to
give a peak shear stress 5 ksi.
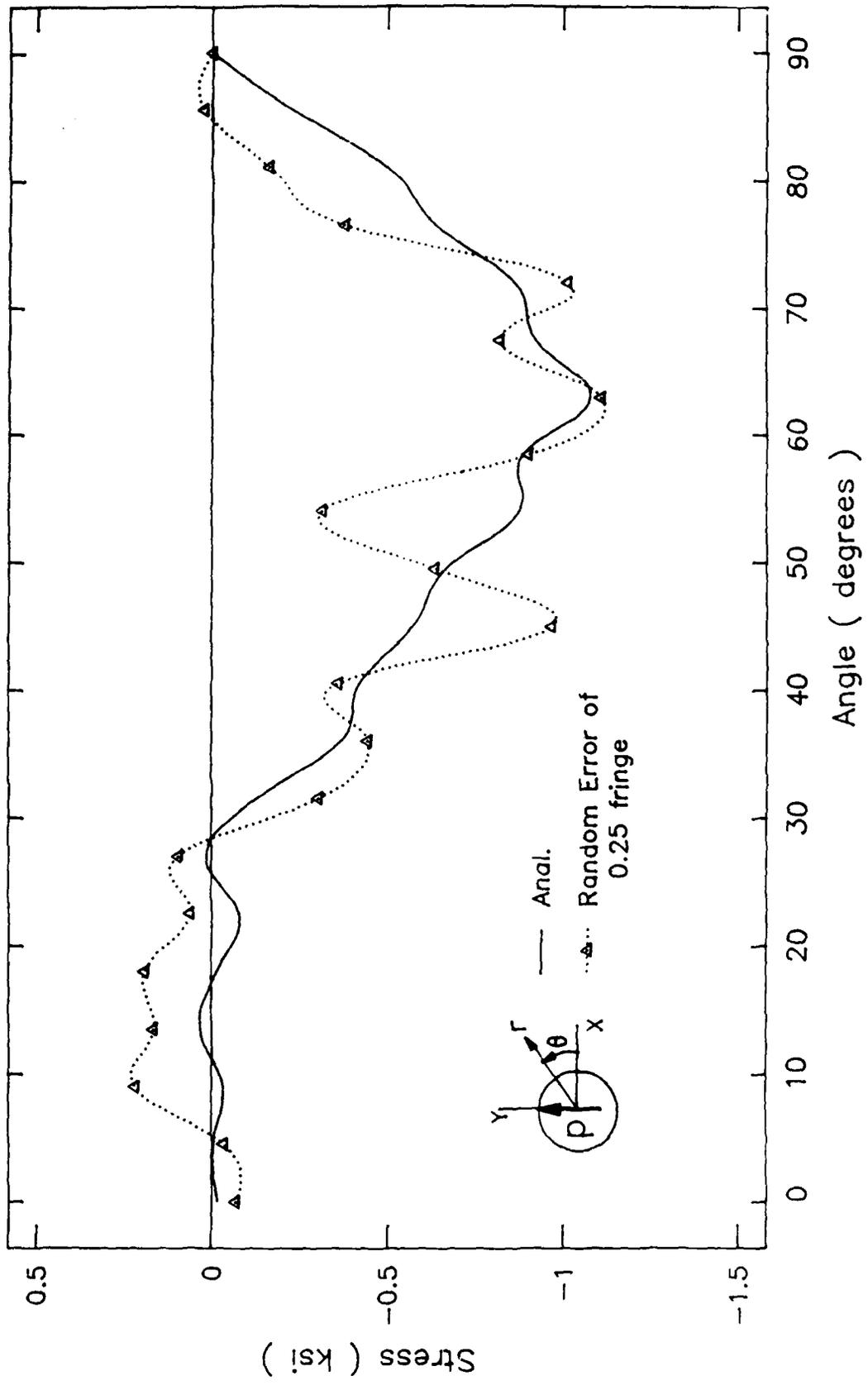
Fig. 18. Comparison of shear stresses determined from the load iput case and a displacement input case with random errors of maximum value corresponding to one quarter fringe order. Input data were adjusted to give a peak shear stress 1 ksi.
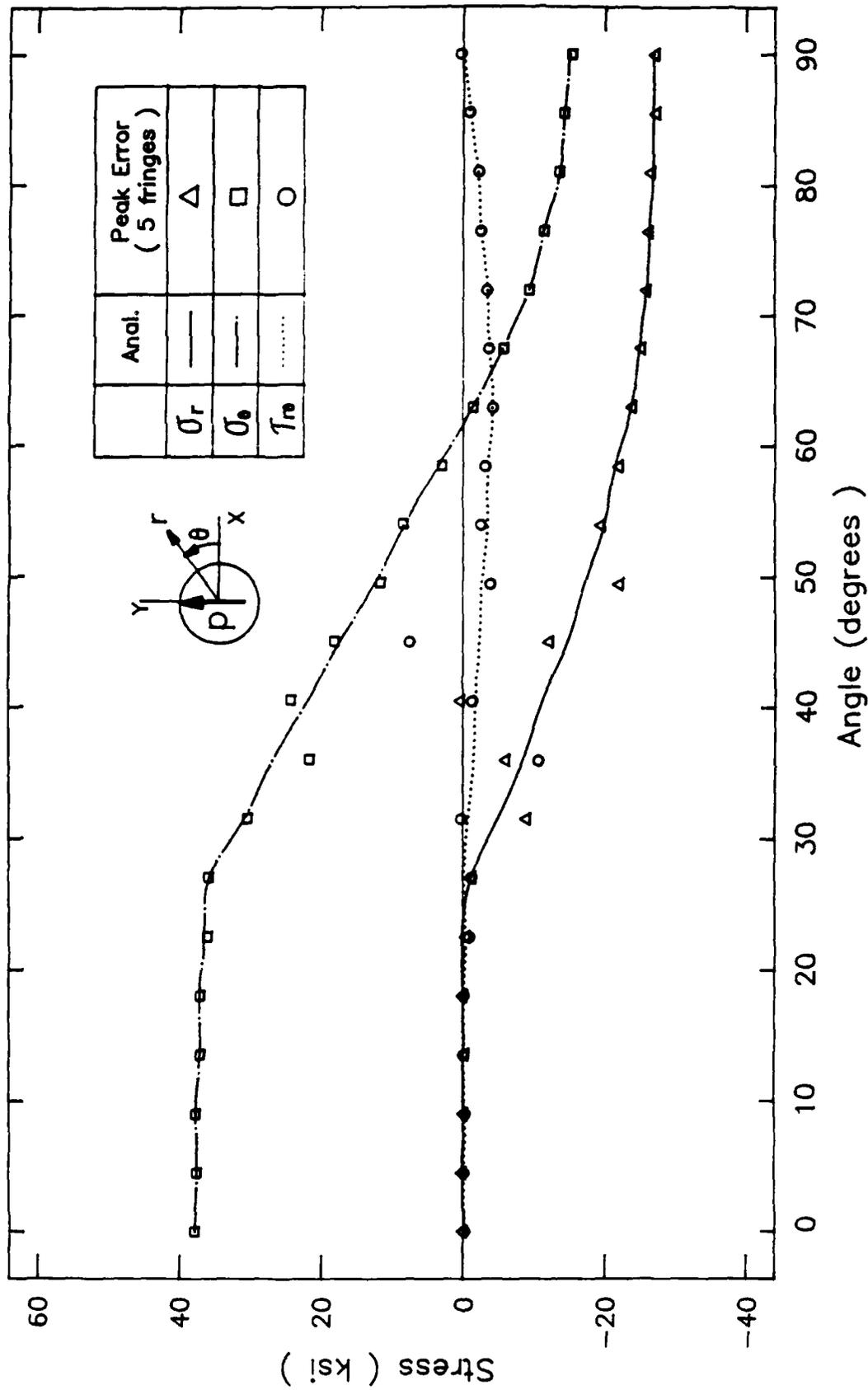
Fig. 19. Comparison of stresses for the load input case and a displacement input case with a localized peak error corresponding to 5 fringe orders.

74
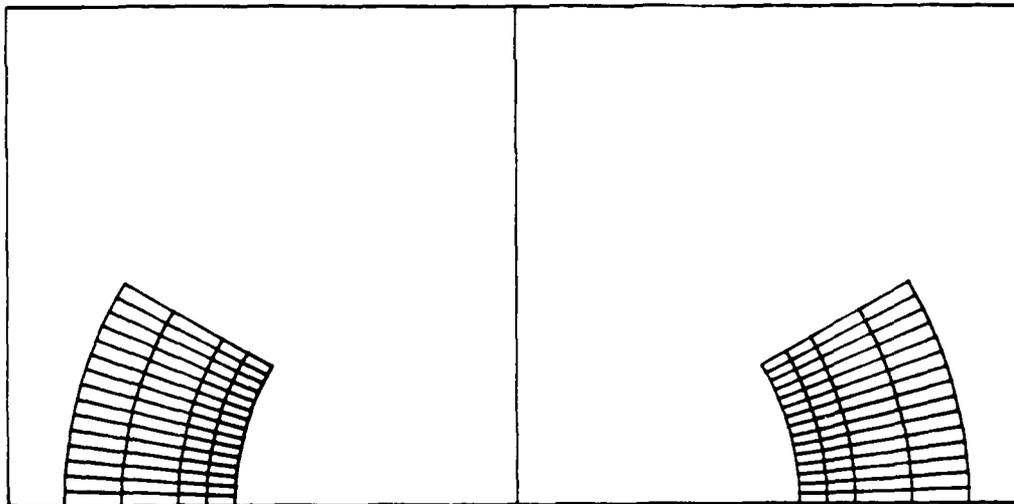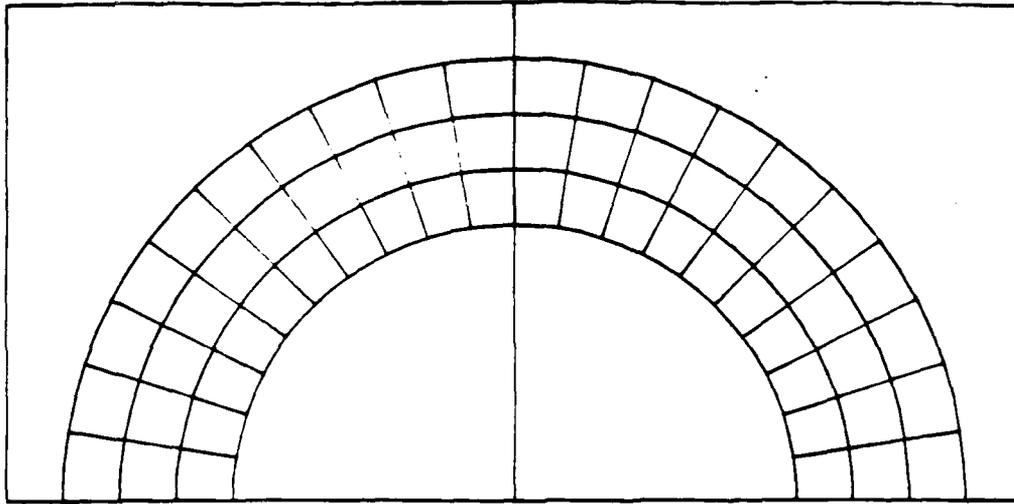
Fig. 20.  Meshes used for the localized hybrid analysis of the aluminum plate.
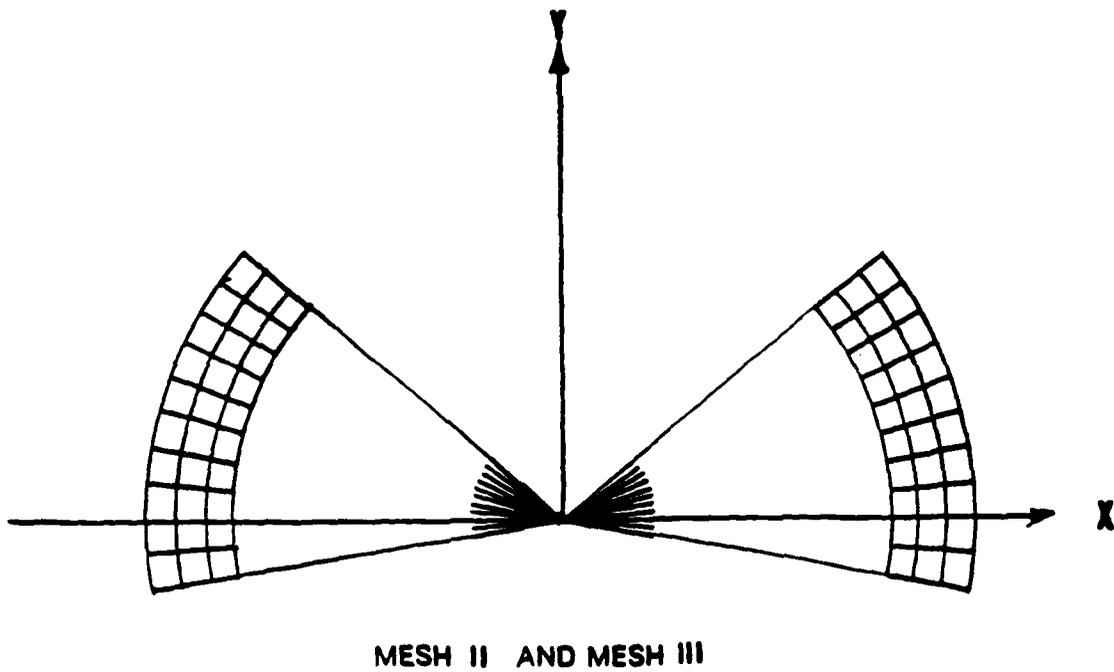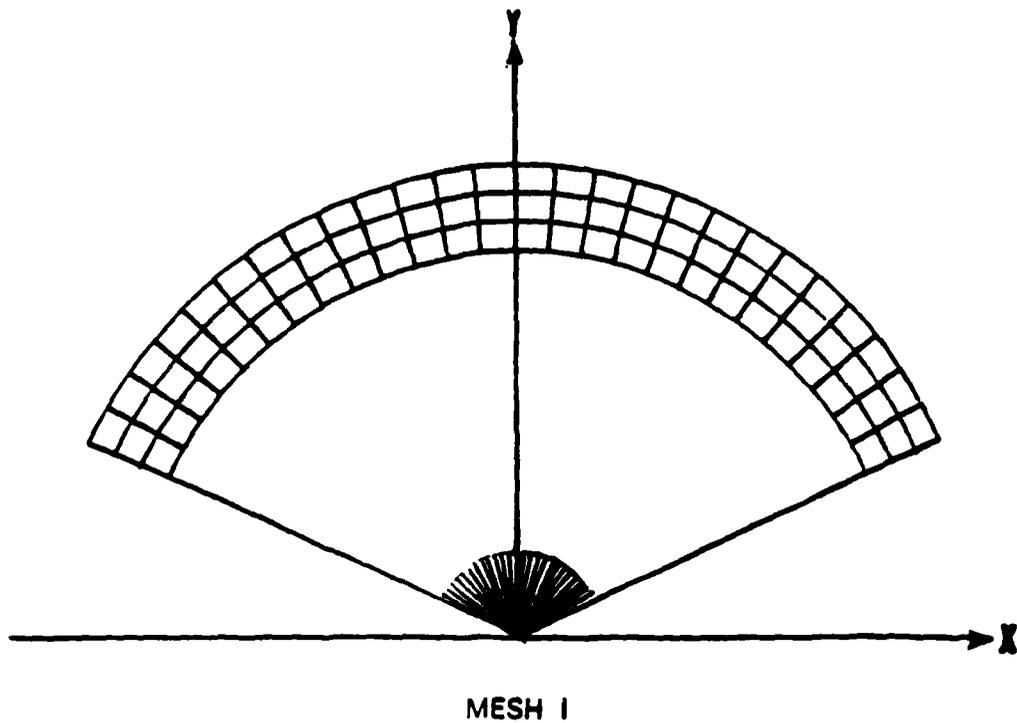
Fig. 21.  Meshes used for the localized hybrid analysis of the composite
plate.
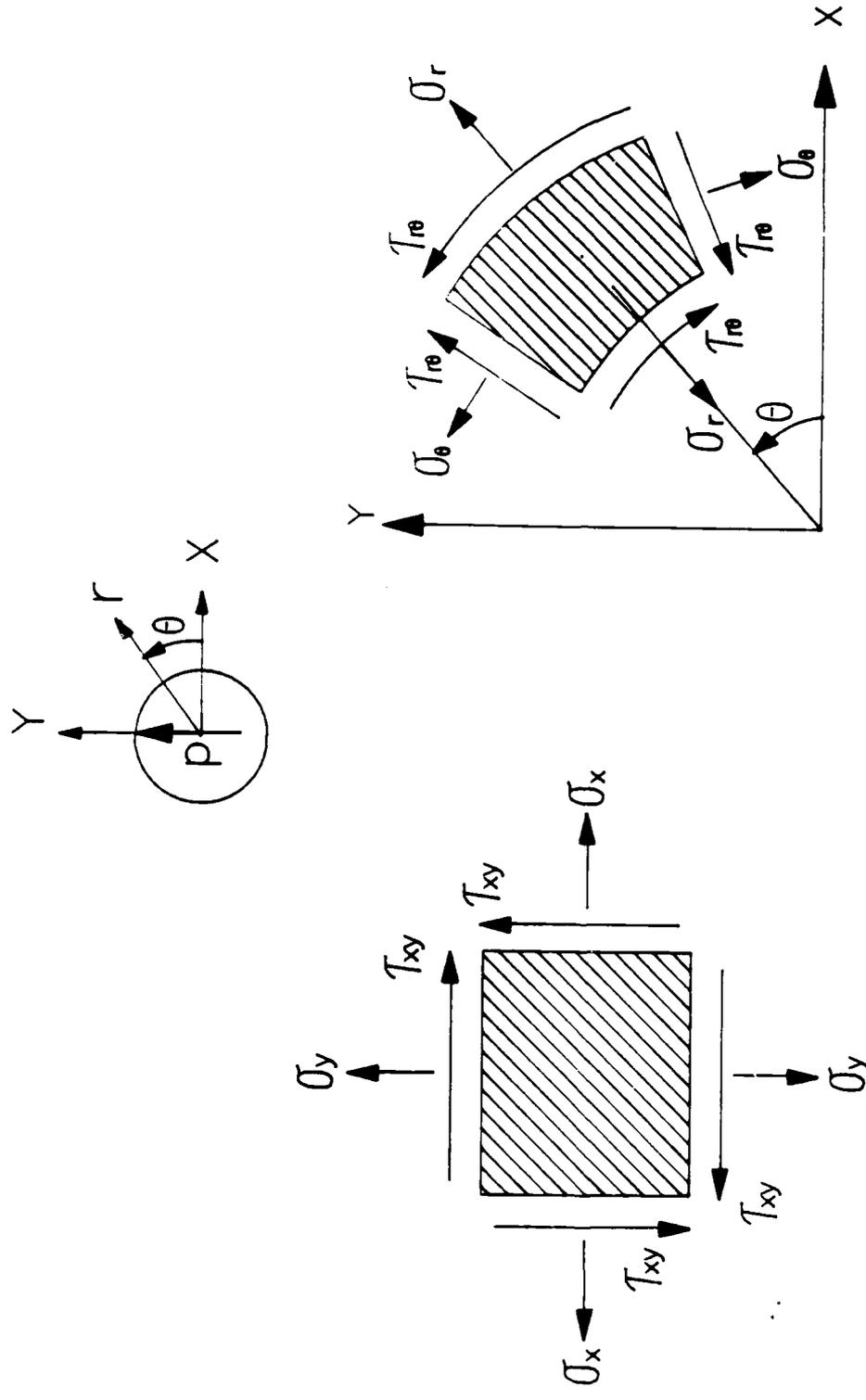
Fig. 22. Sign conventions for the angular coordinate system and shear stress.
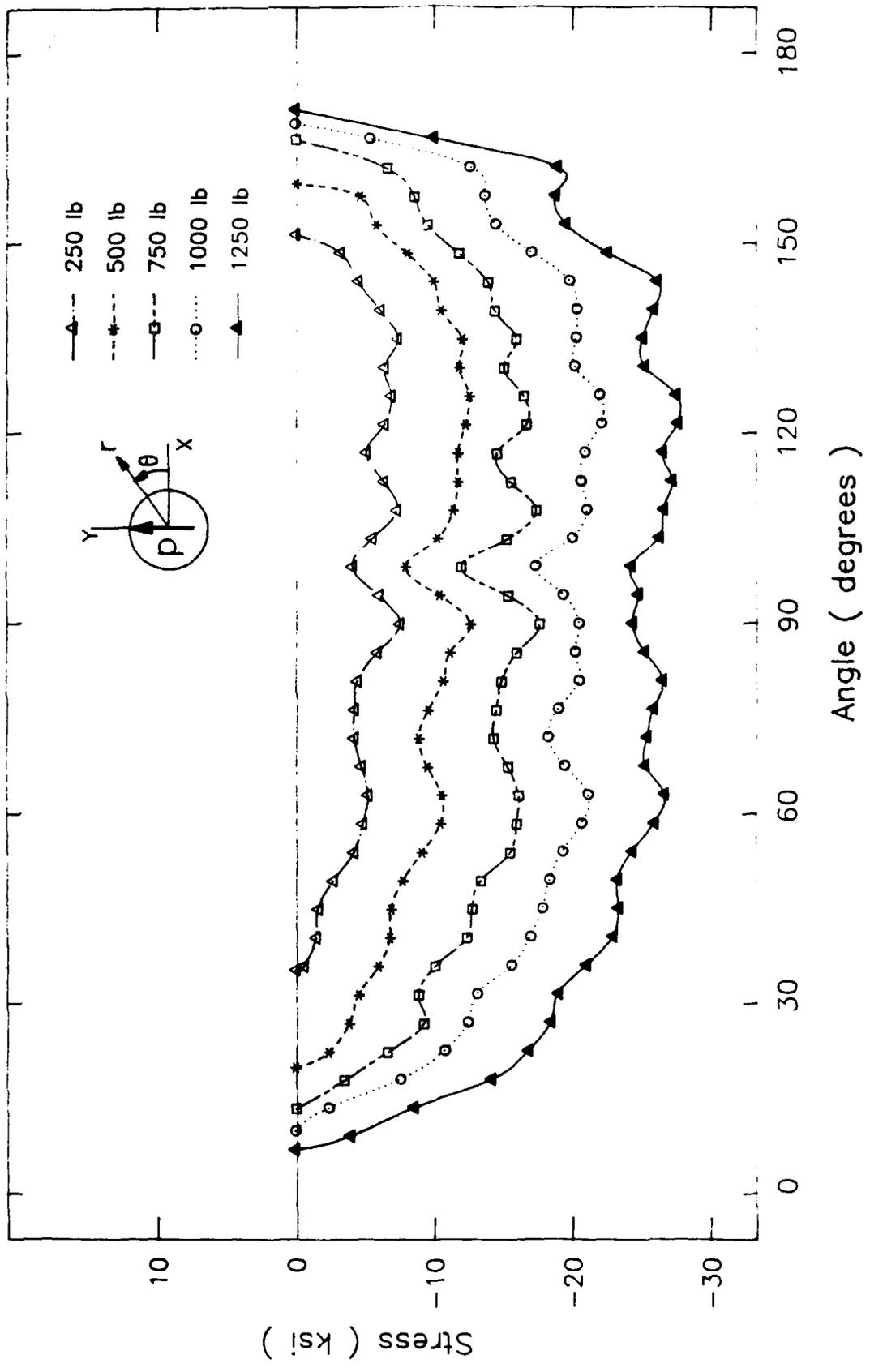
Fig. 23. Radial stress distributions for the aluminum specimen on the load increasing phase. These were calculated using the localized hybrid approach.
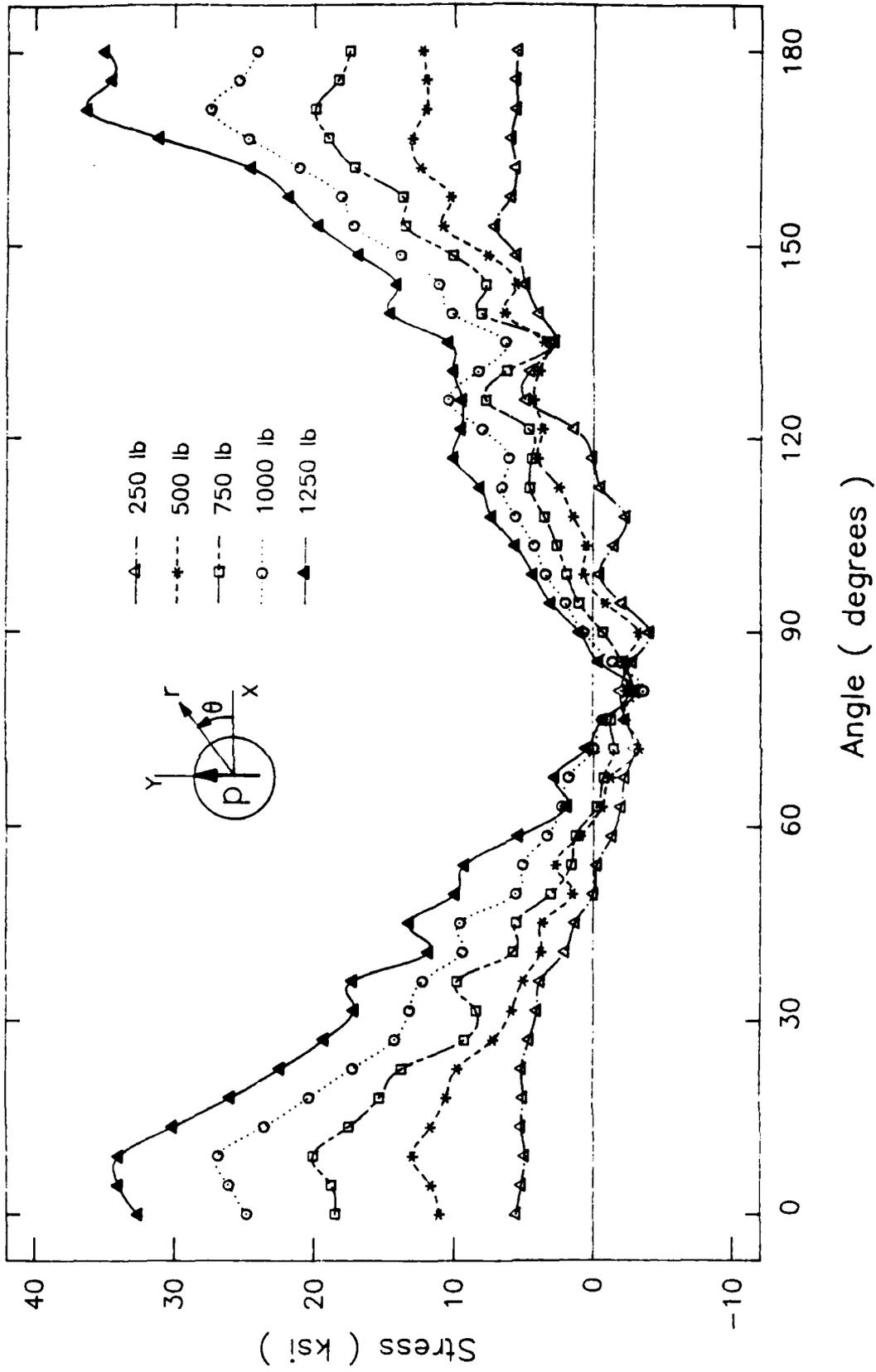
Fig. 24. Hoop stress distributions for the aluminum specimen on the load increasing phase.
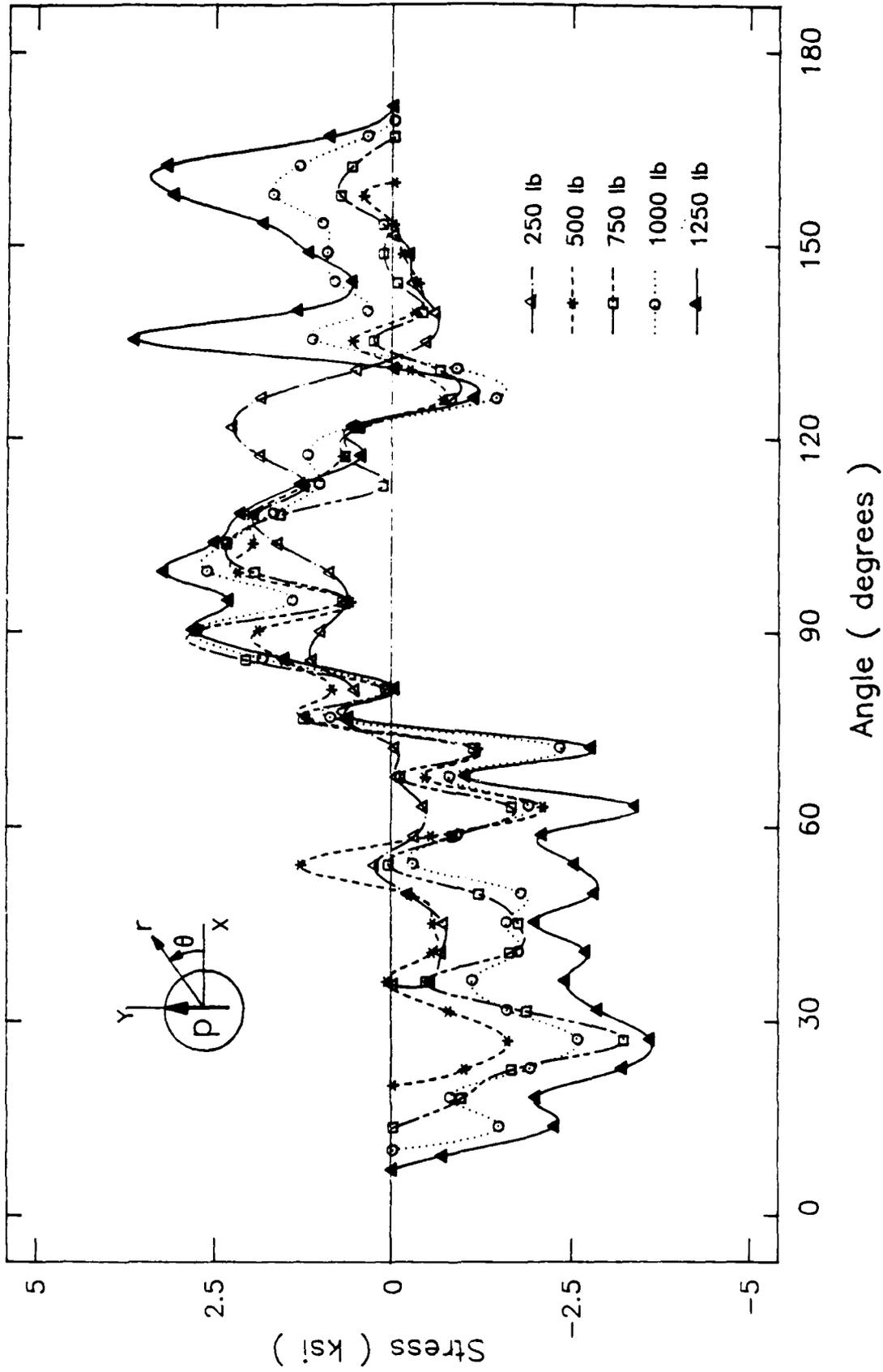
Fig. 25. Shear stress distributions for the aluminum specimen on the load-increasing phase.
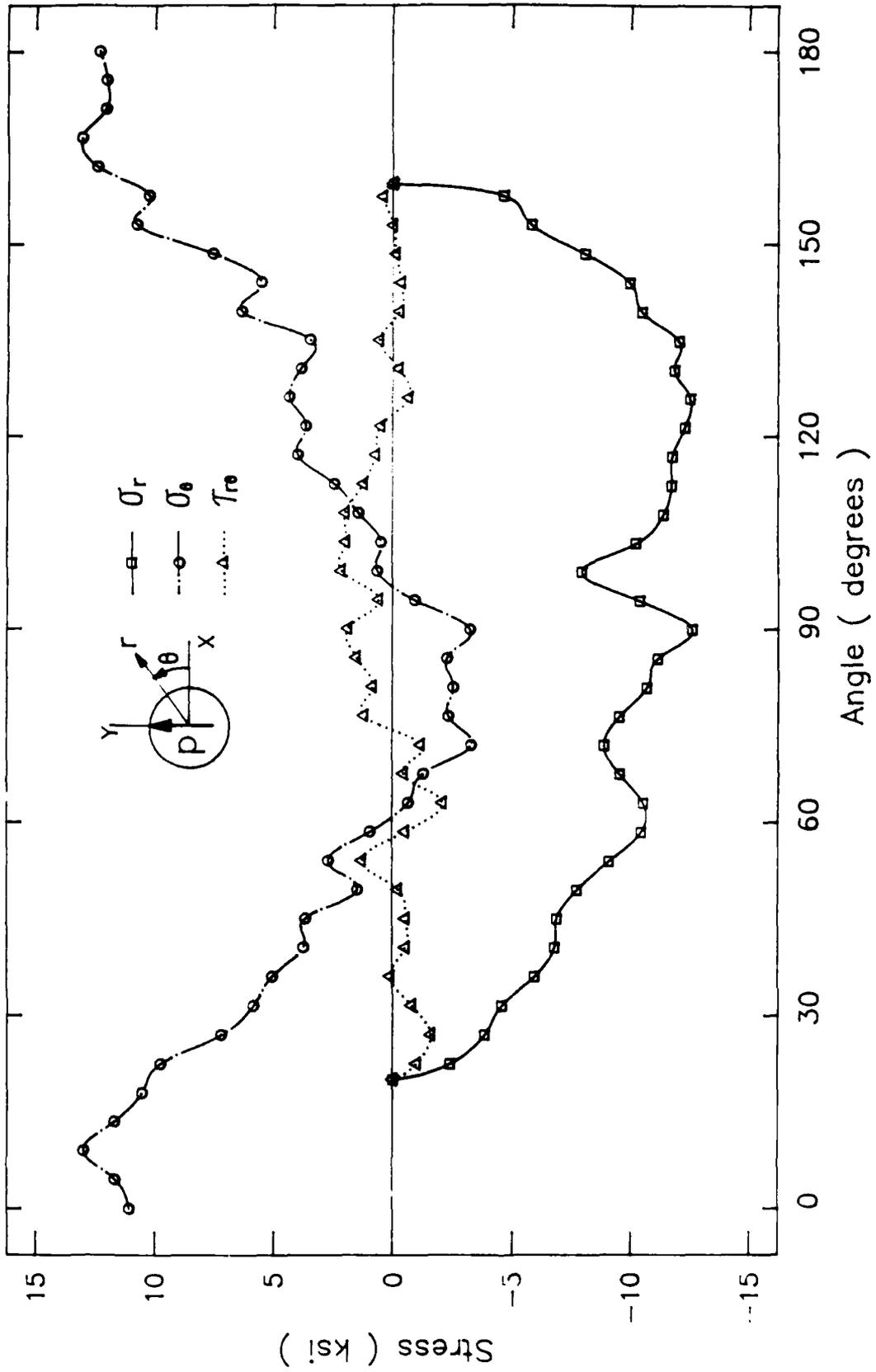
Fig. 26. Stress components for the aluminum specimen at a load of 500 lb. on the load increasing phase.
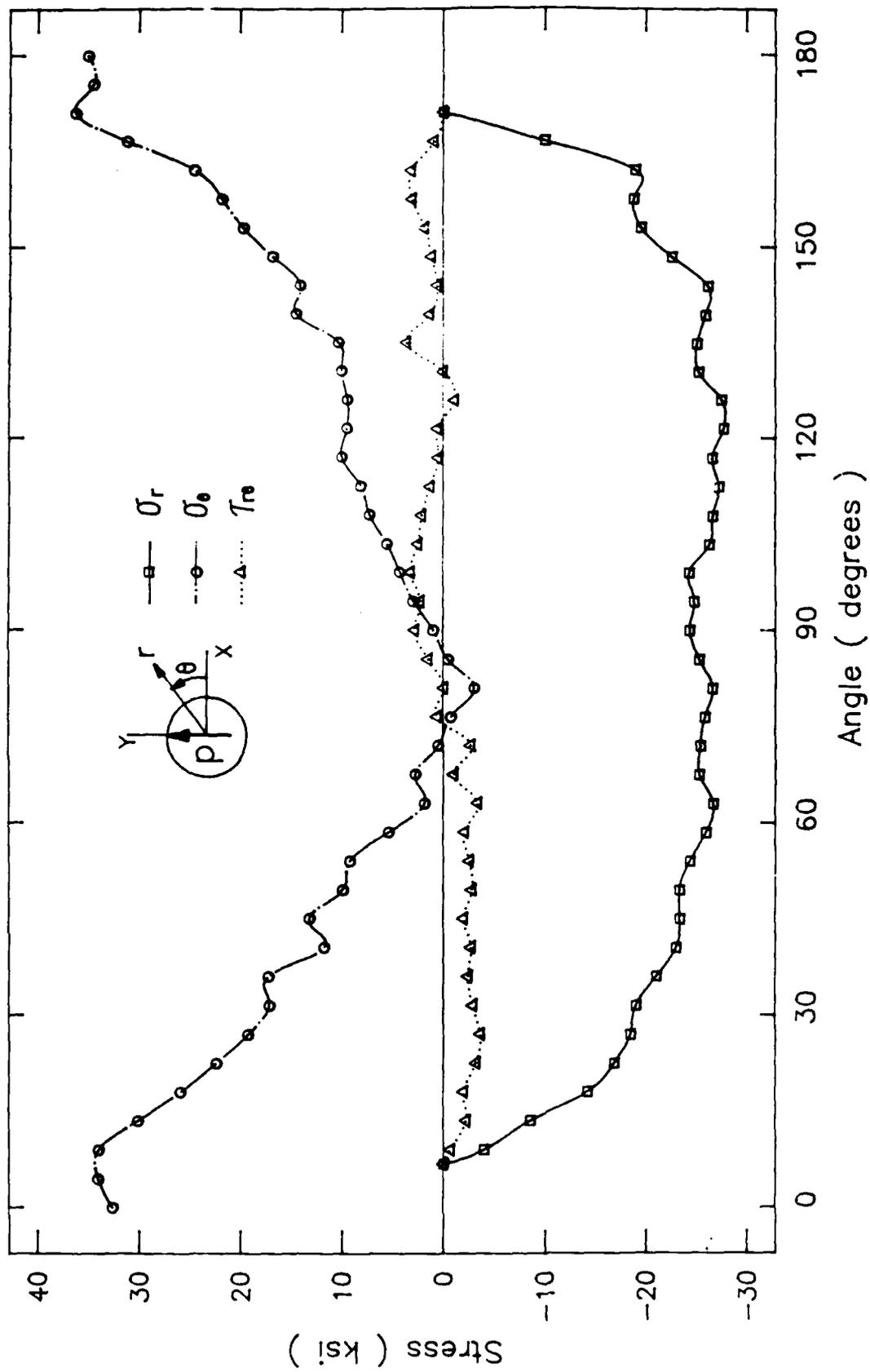
Fig. 27. Stress components for the aluminum specimen at a load of 1250 lb.
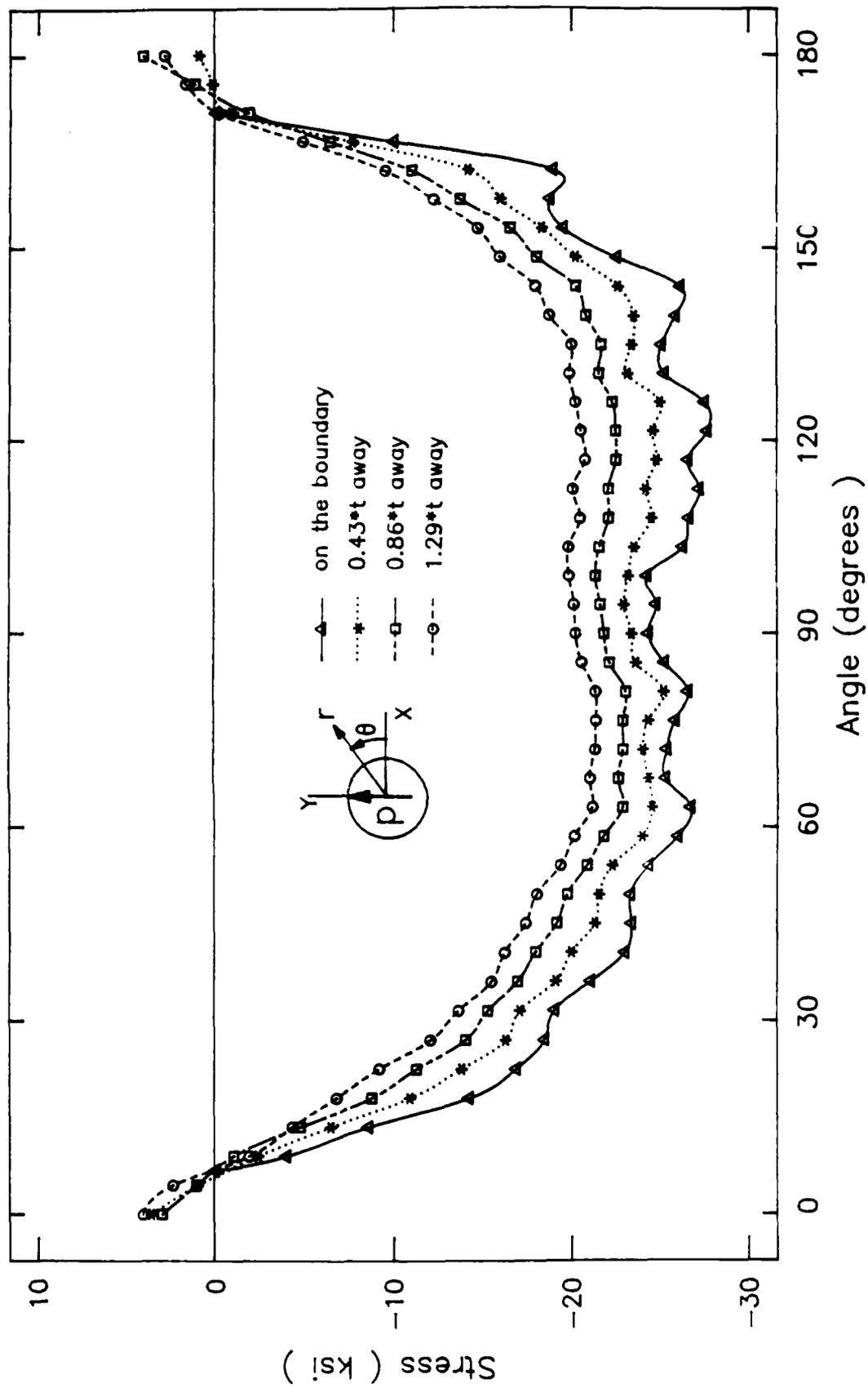
Fig. 28. Radial stress distributions for various locations on and near
the contact boundary, for the aluminum specimen with a load of 1250 lb.
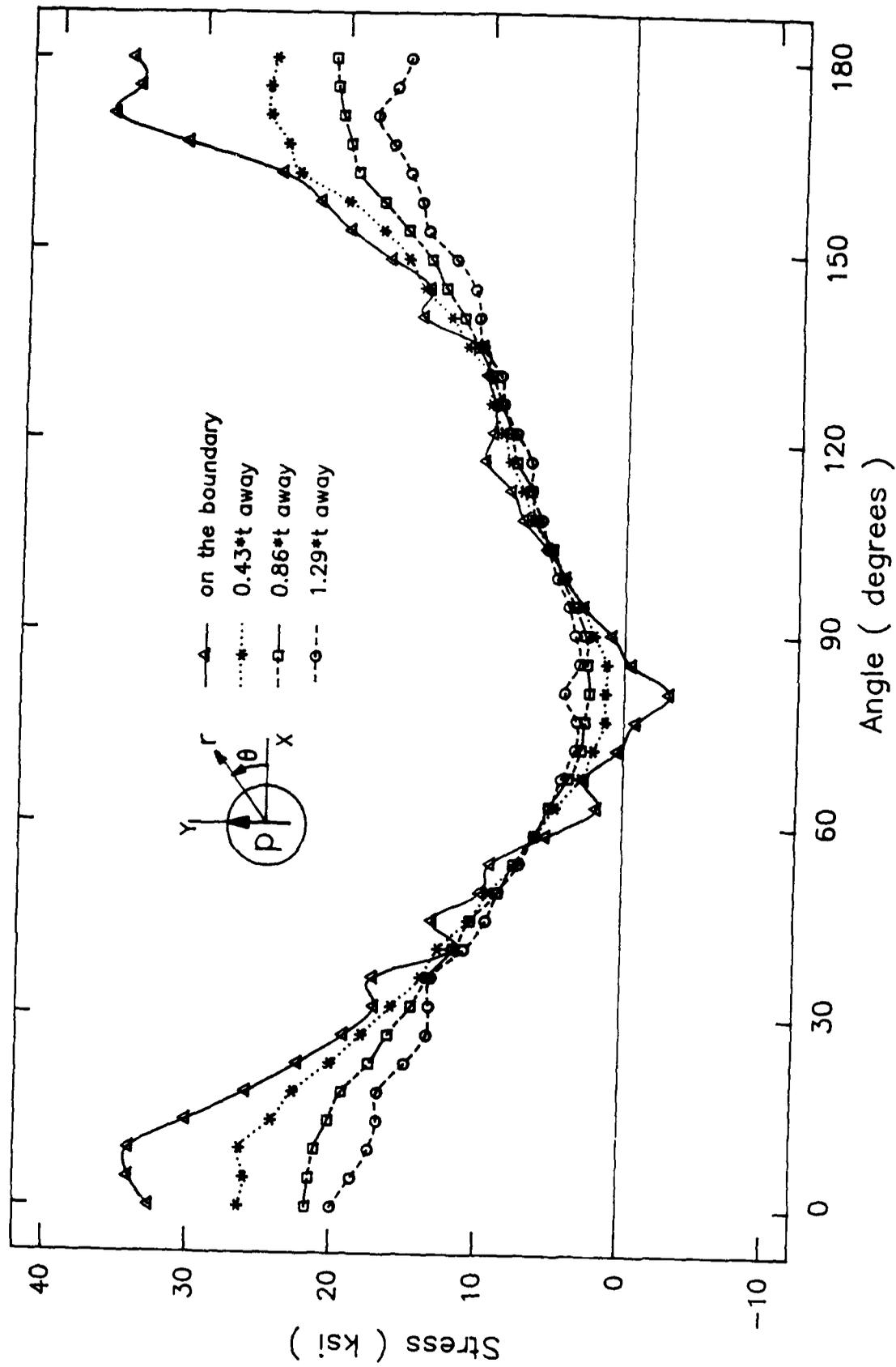
Fig. 29. Hoop stress distributions for various locations on and near the contact boundary, for the aluminum specimen with a load of 1250 lb.
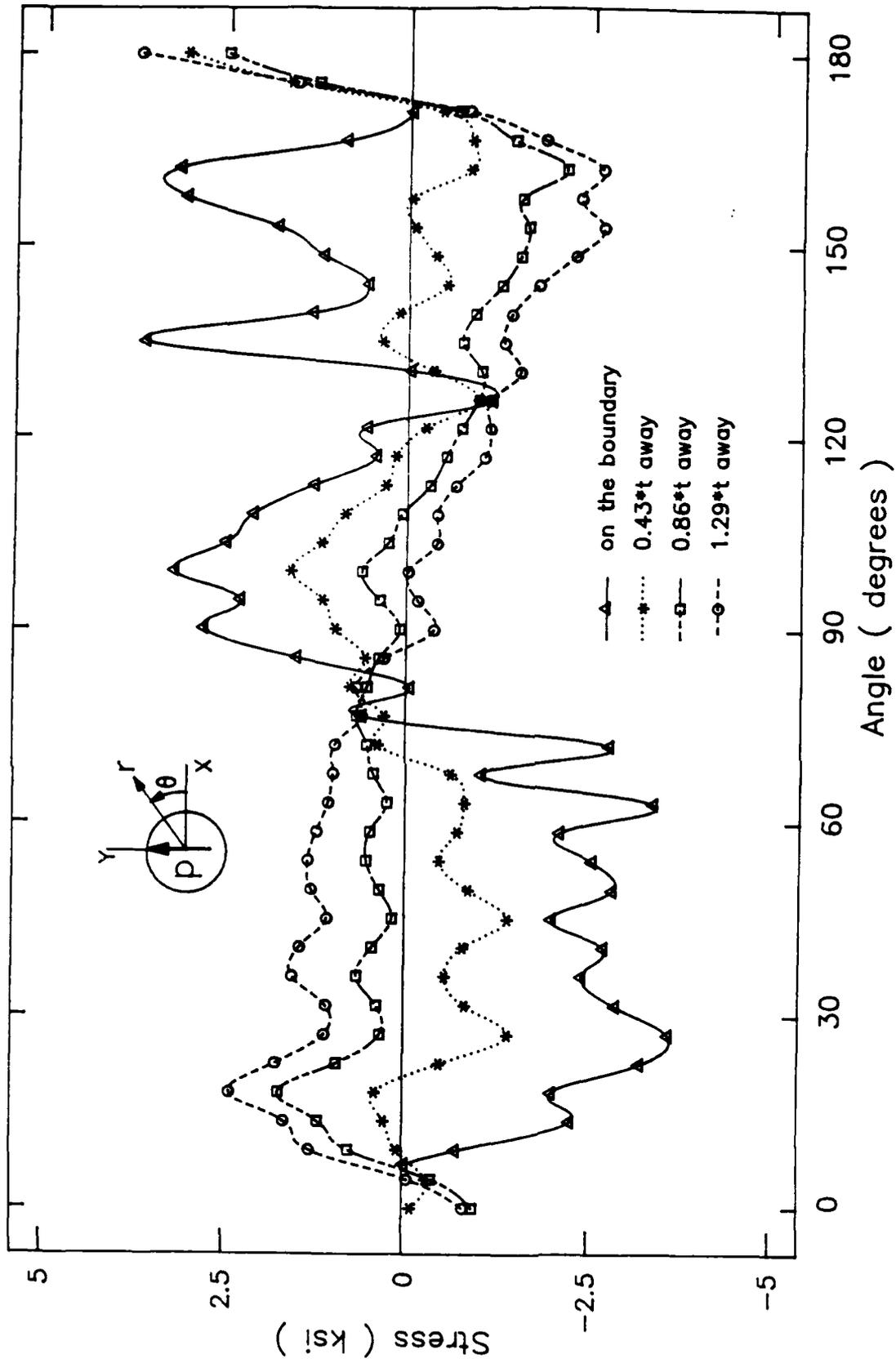
Fig. 30. Shear stress distributions for various locations on and near the contact boundary, for the aluminum specimen with a load of 1250 lb.

85
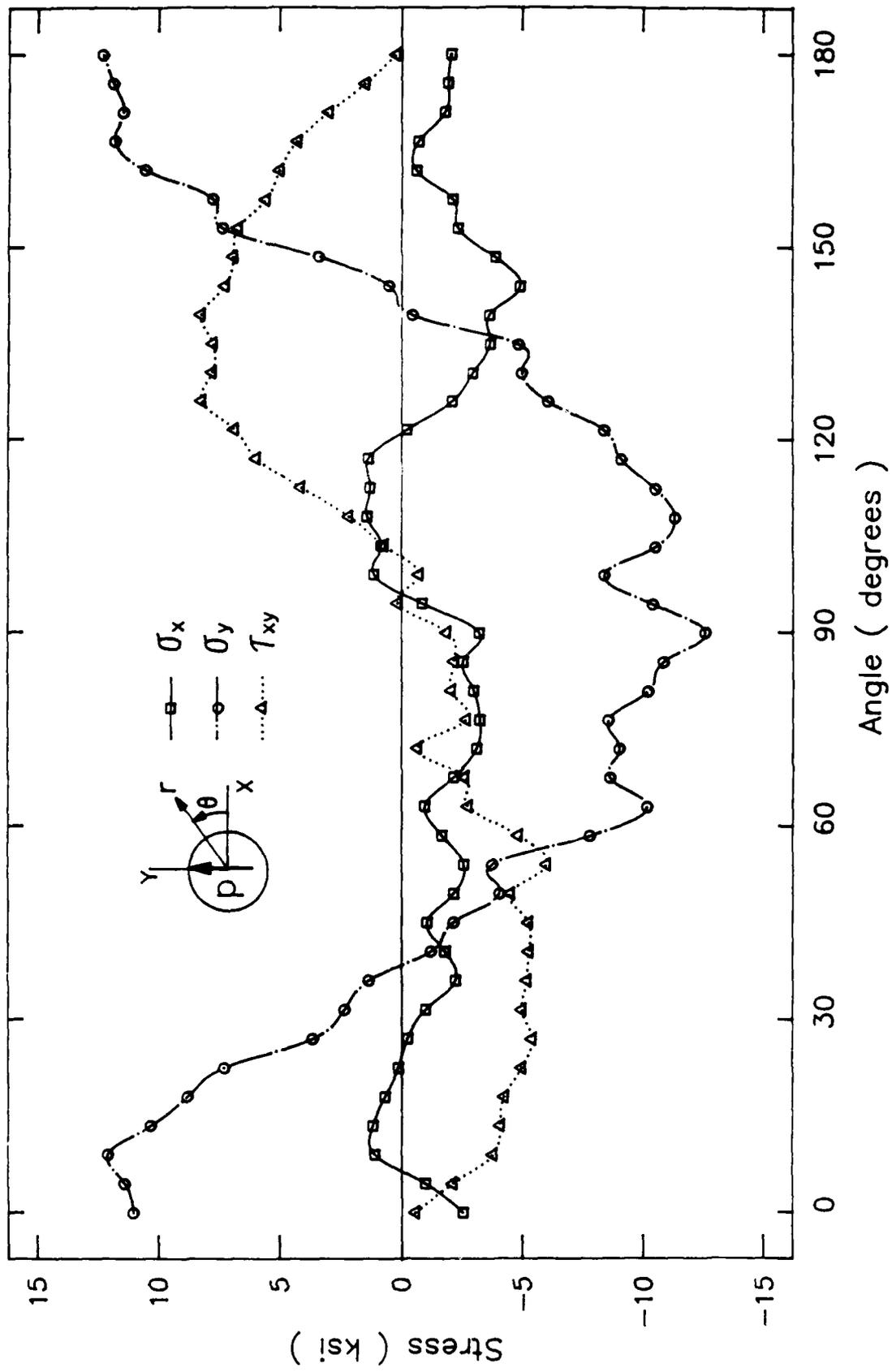
Fig. 31. Cartesian components of stress at the contact boundary; for the aluminum specimen with a load of 500 lb.
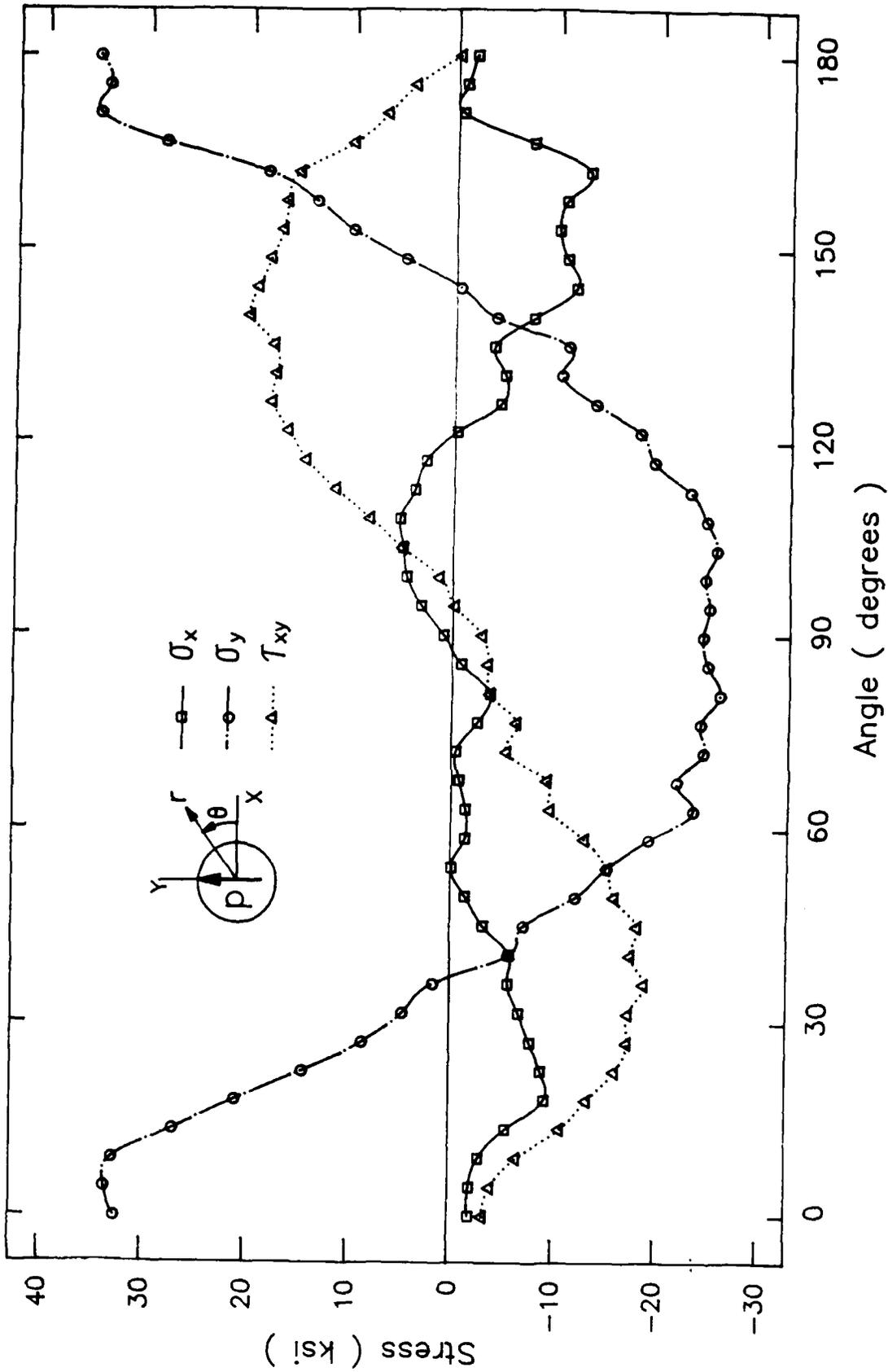
Fig. 32 Cartesian components of stress at the contact boundary; for the aluminum specimen with a load of 1250 lb.
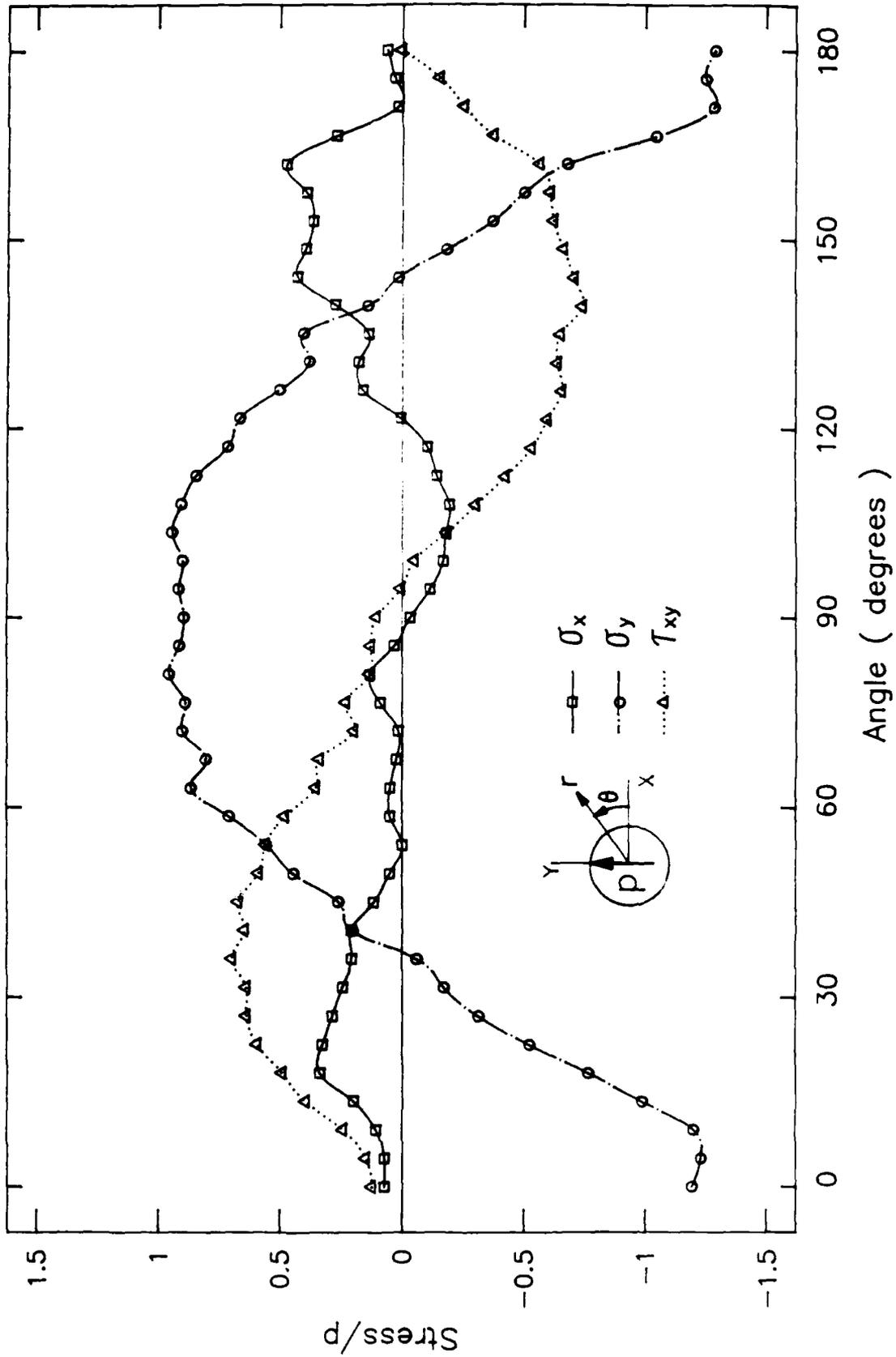
Fig. 33. Cartesian stress components, normalized with respect to the bearing stress, for the aluminum specimen with a load of 1250 lb.
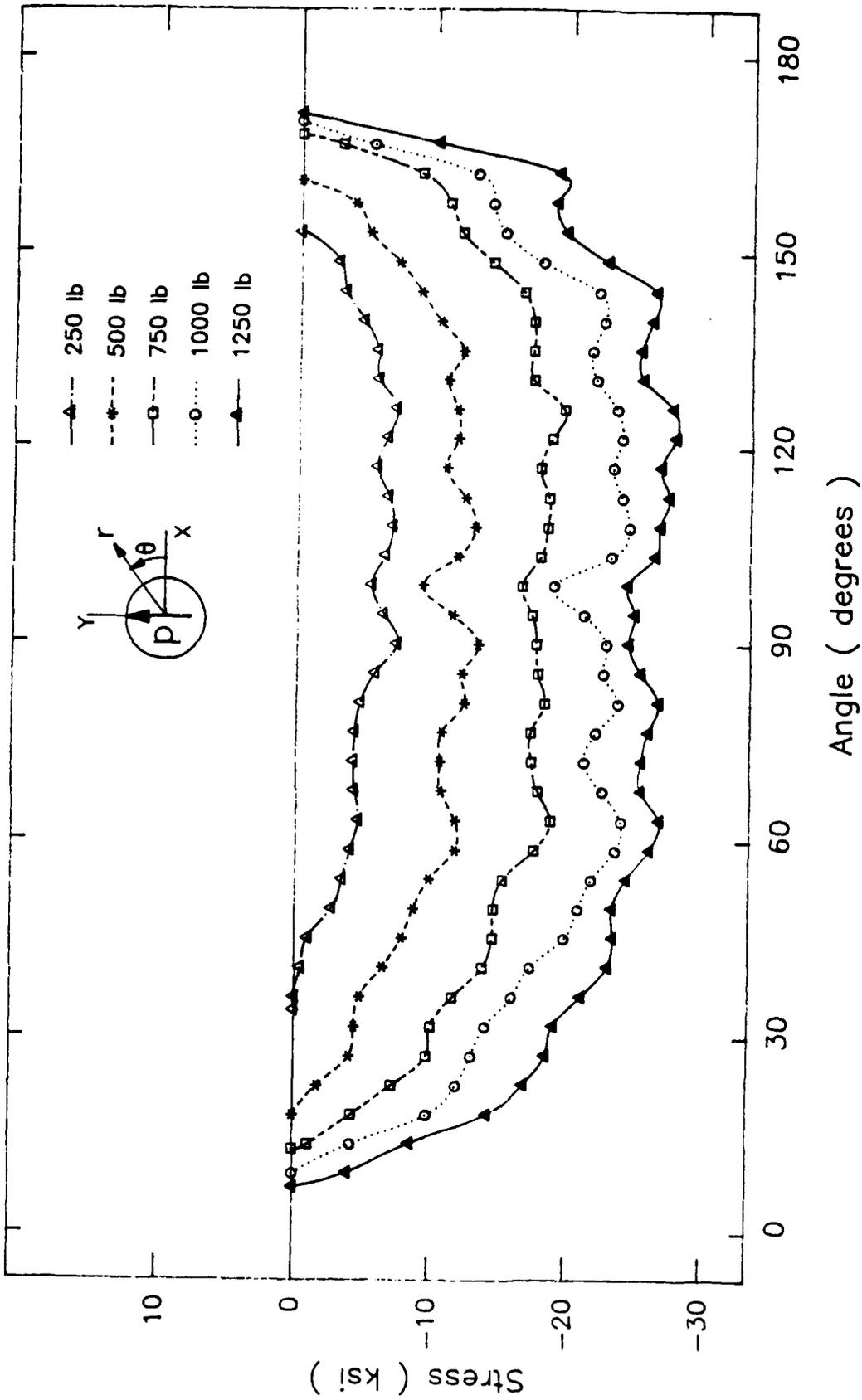
Fig. 34. Variation of the radial contact stress component for the aluminum specimen with angle for the load decreasing phase.

89
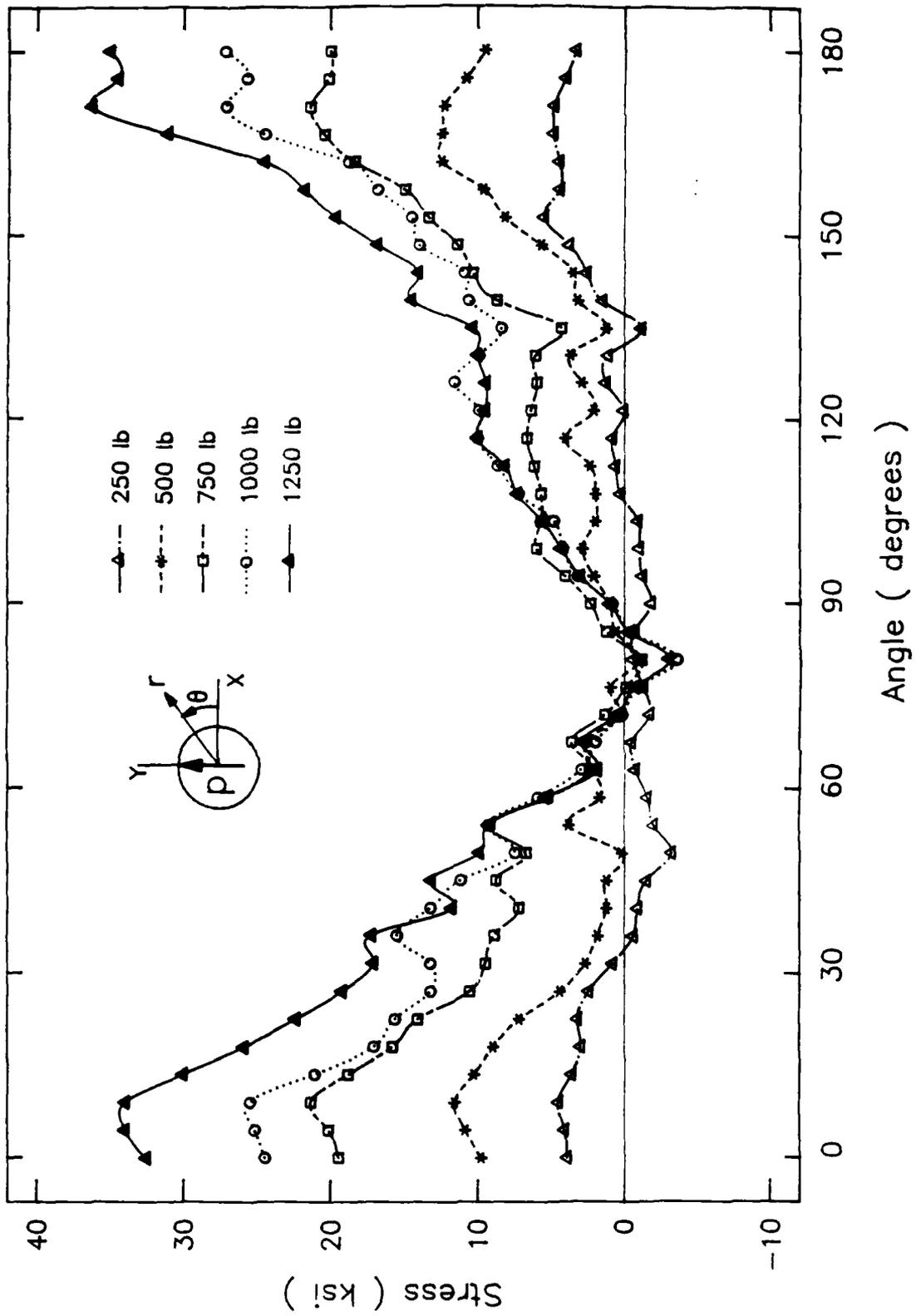
Fig. 35. Variation of the hoop contact stress component for the aluminum specimen with angle for the load decreasing phase.

90
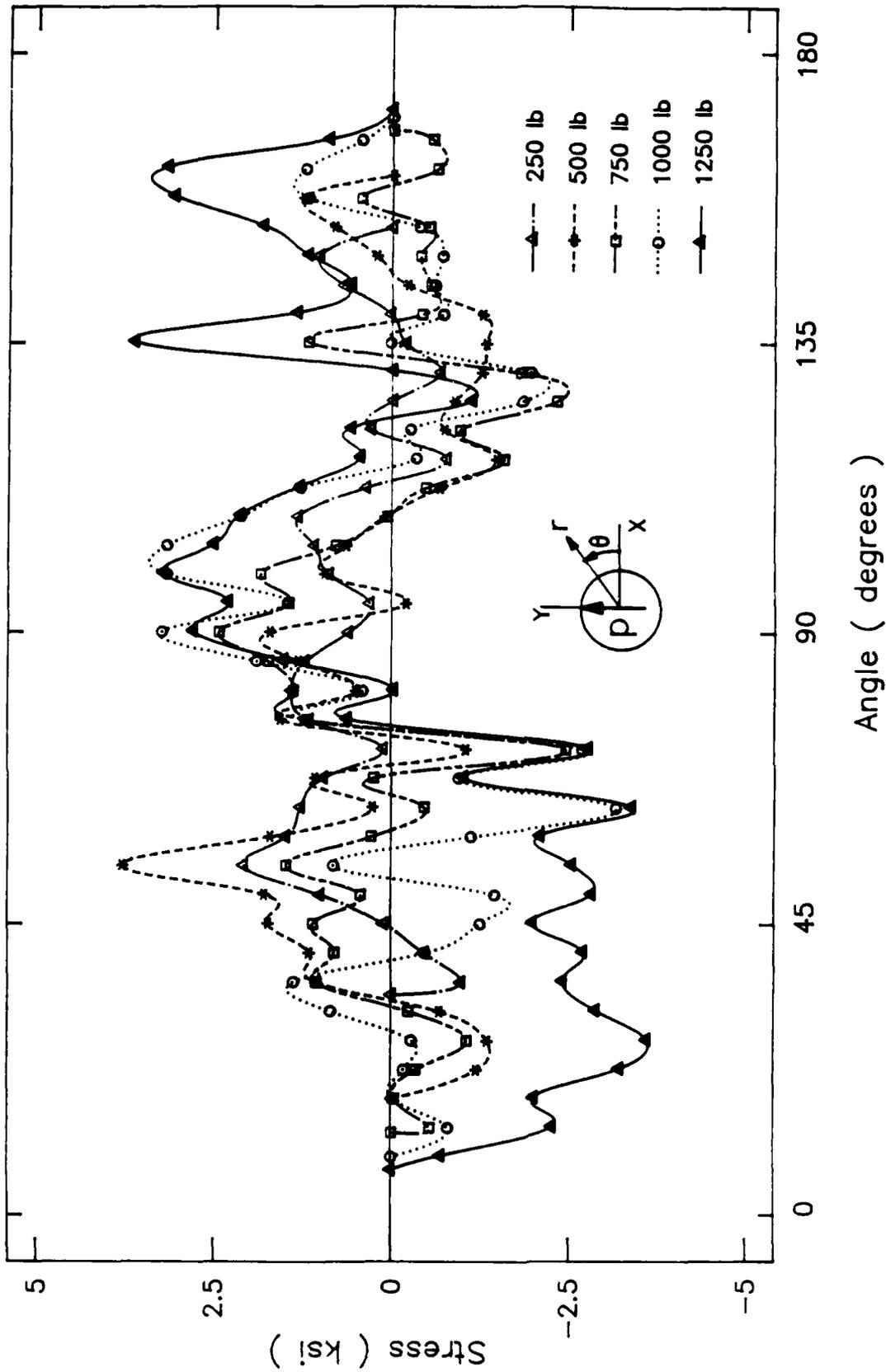
Fig. 36. Variation of the shear contact stress component for the aluminum specimen with angle for the load decreasing phase.
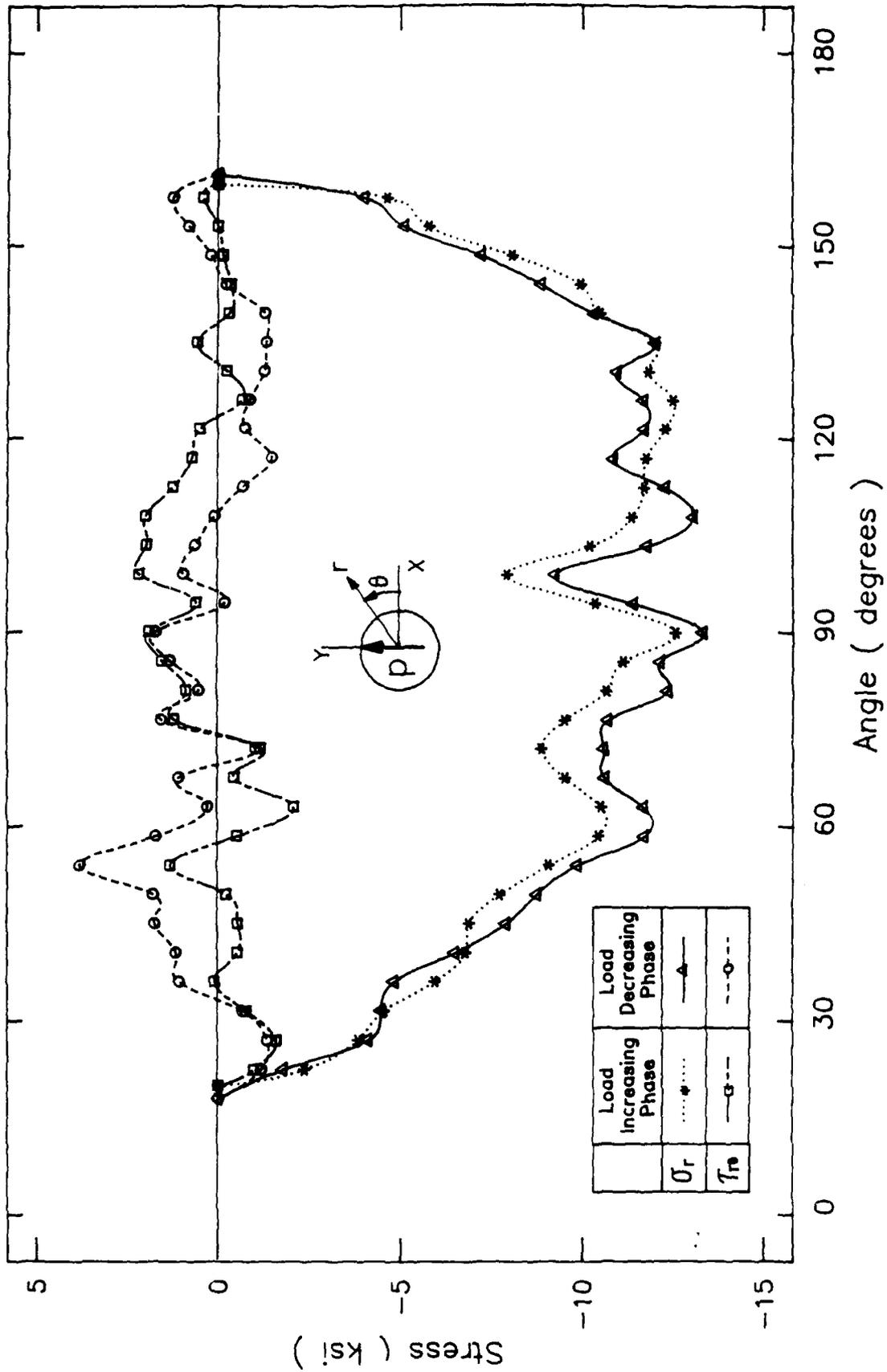
Fig. 37. Comparison of radial and shear stresses for the load
increasing and decreasing phases, for the aluminum specimen with a load
of 500 lb.
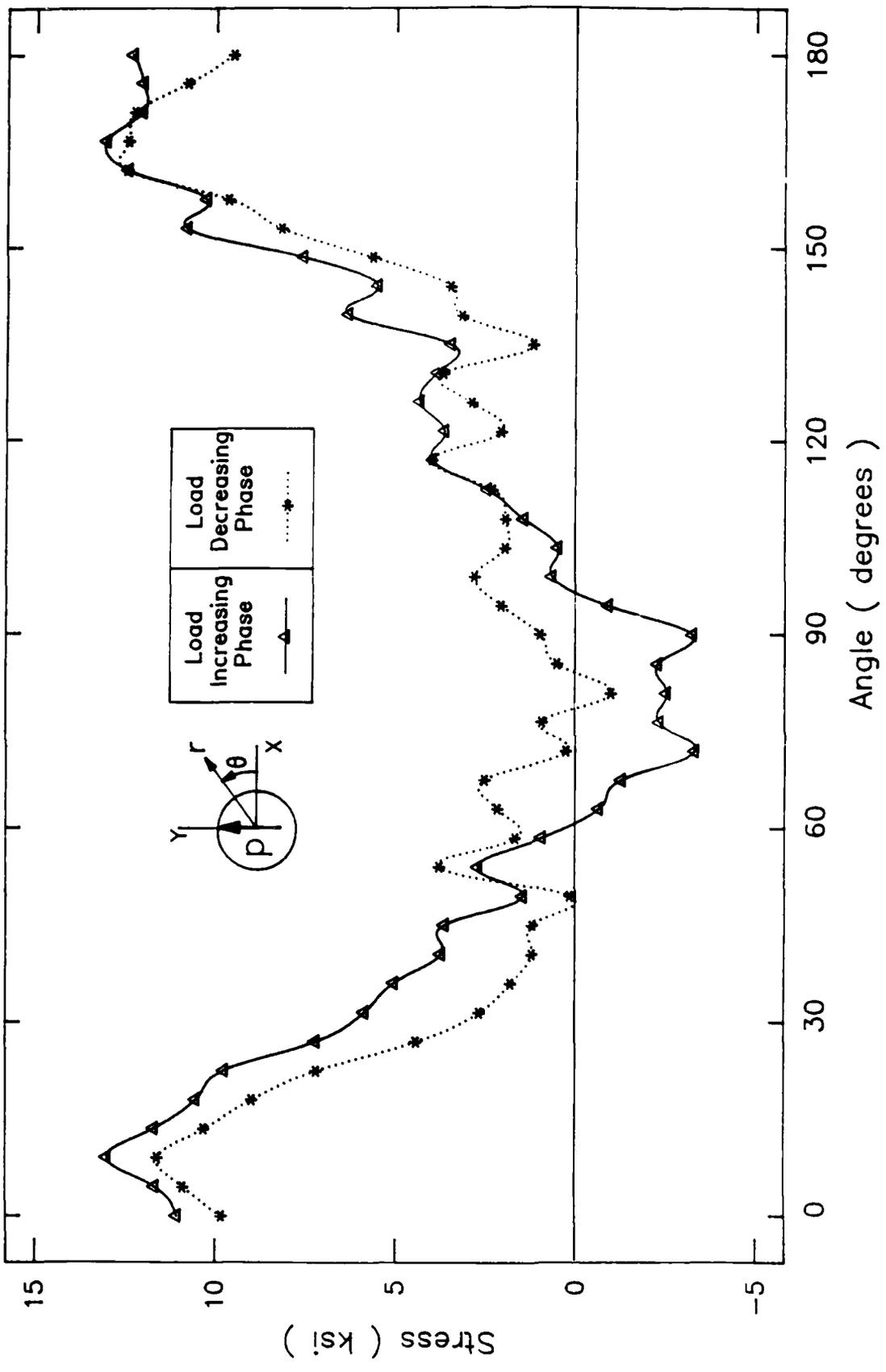
Fig. 38. Comparison of the hoop stresses for the load increasing and decreasing phases, for the aluminum specimen with a load of 500 lb.

93
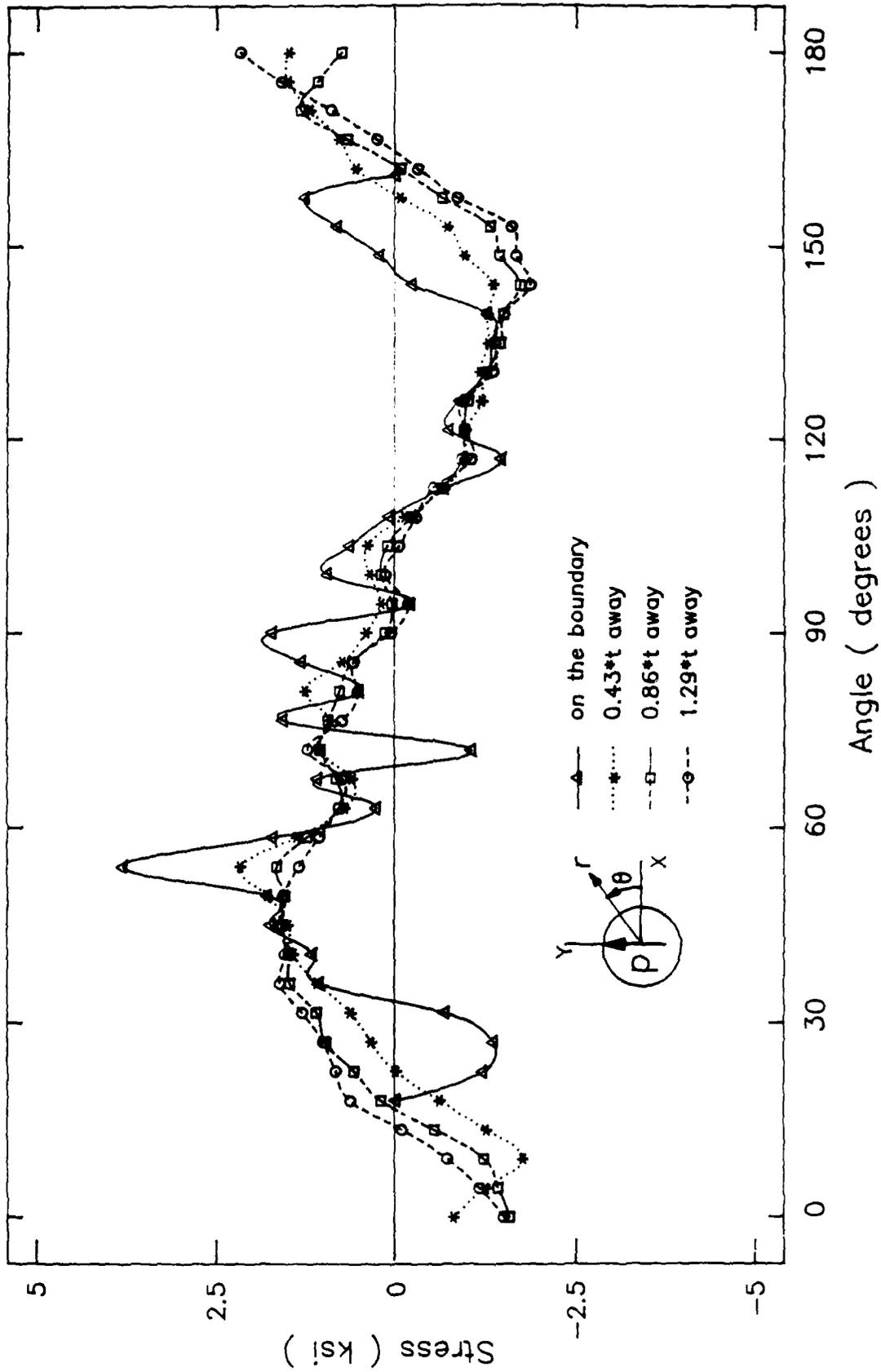
Fig. 39. Shear stress distributions on the load decreasing phase for the aluminum specimen with a load of 500 lb. The effect of distance from the contact boundary is illustrated.
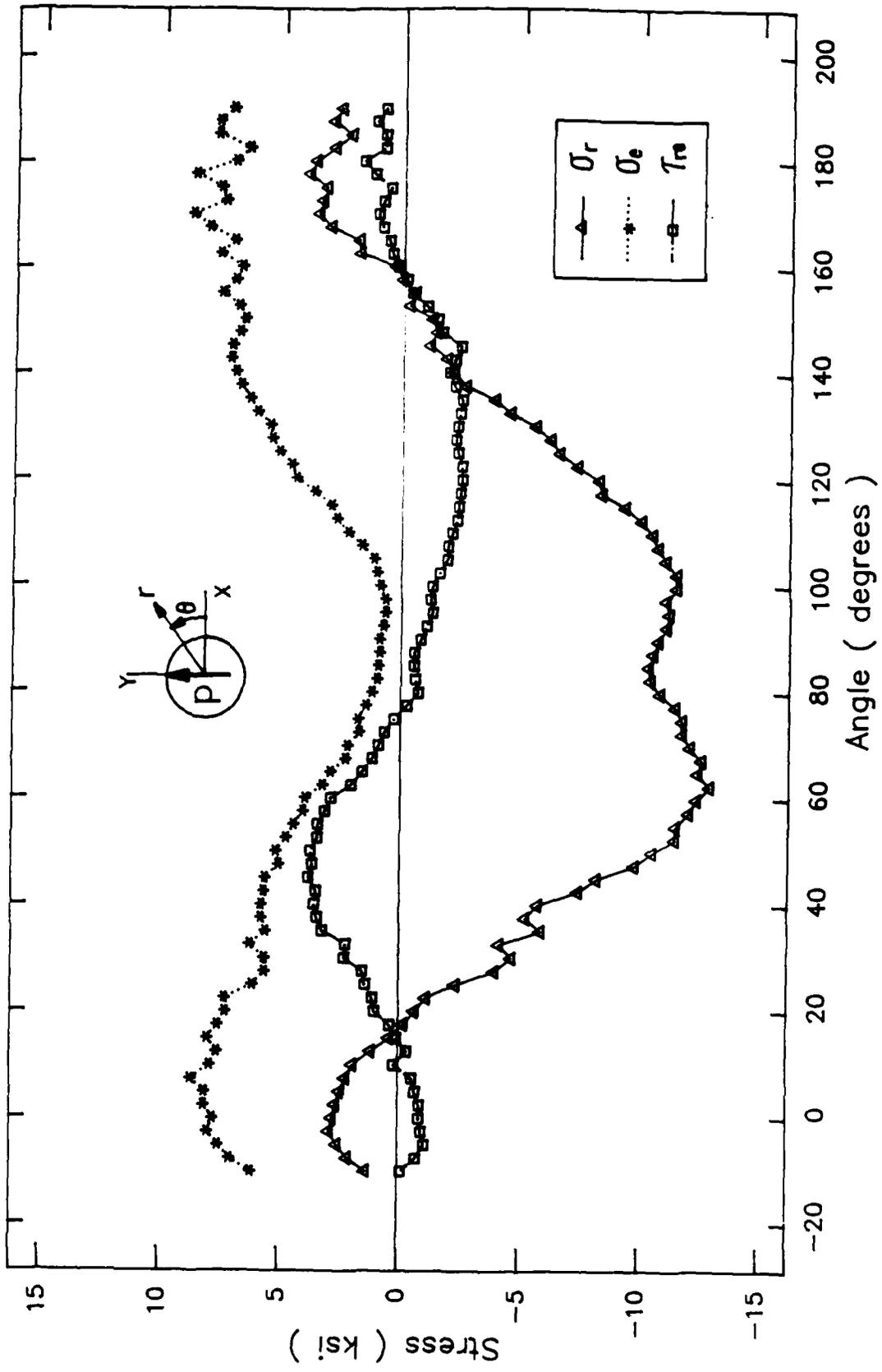
Fig. 40. Polar stress components for the pin-loaded graphite-epoxy plate under a load of 400 lb. The stresses are those on a circular arc 1.55 thicknesses from the contact boundary.
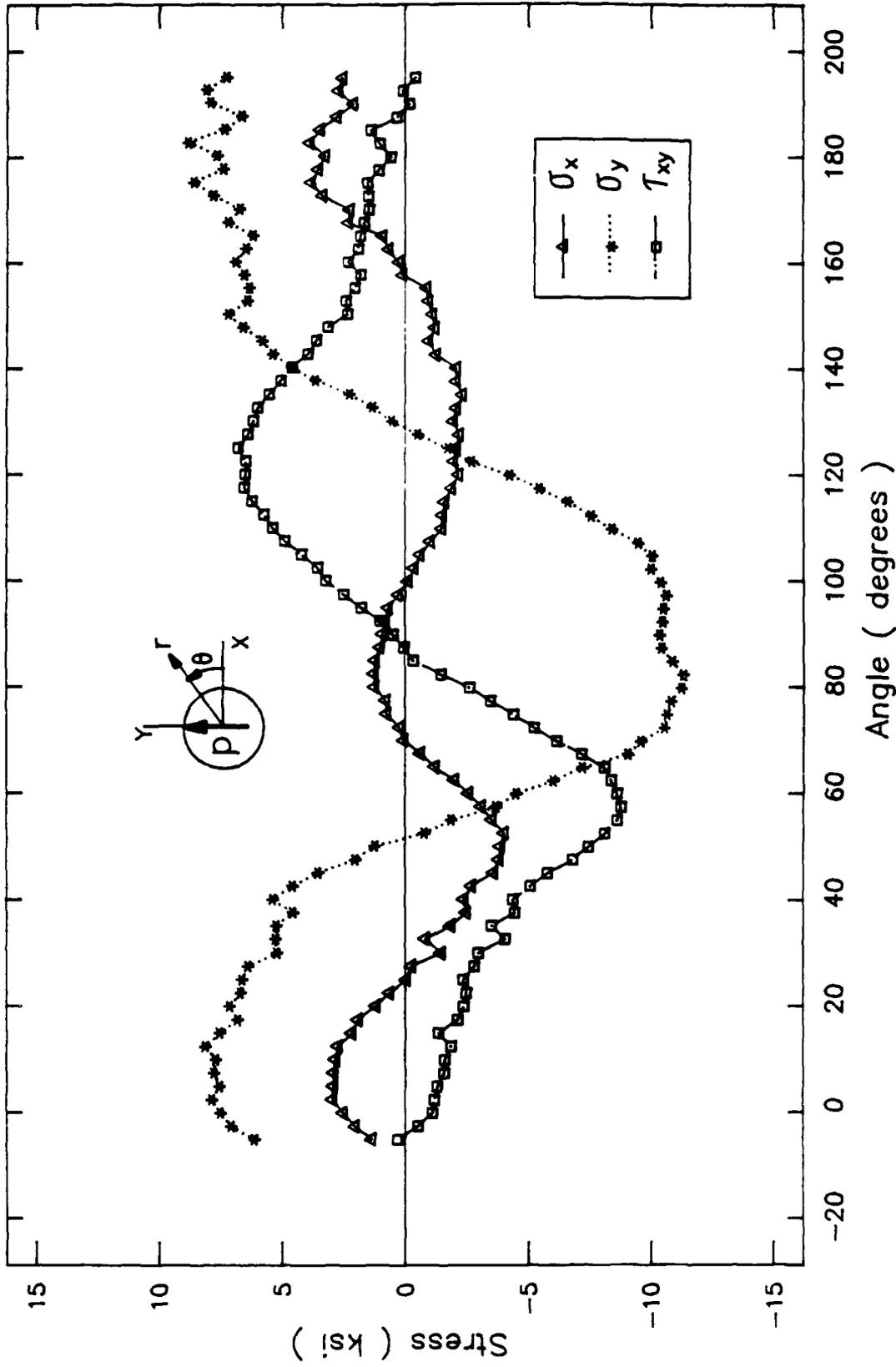
Fig. 41. Cartesian stress components for the pin-loaded graphite-epoxy plate under a load of 400 lb. The stresses are those on a circular arc 1.55 thicknesses from the contact boundary.
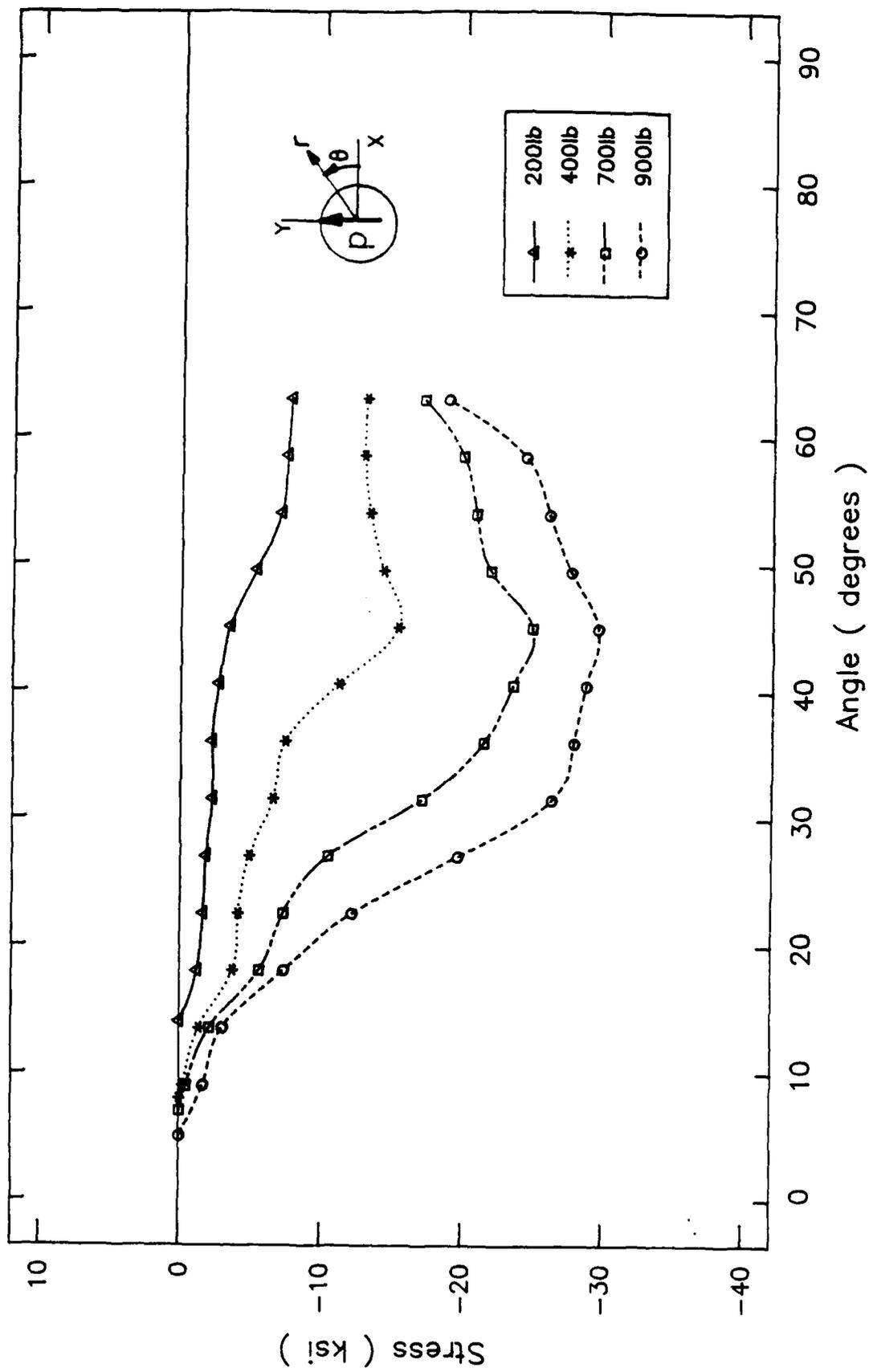
Fig. 42. Radial contact stress distributions for the graphite-epoxy plate.
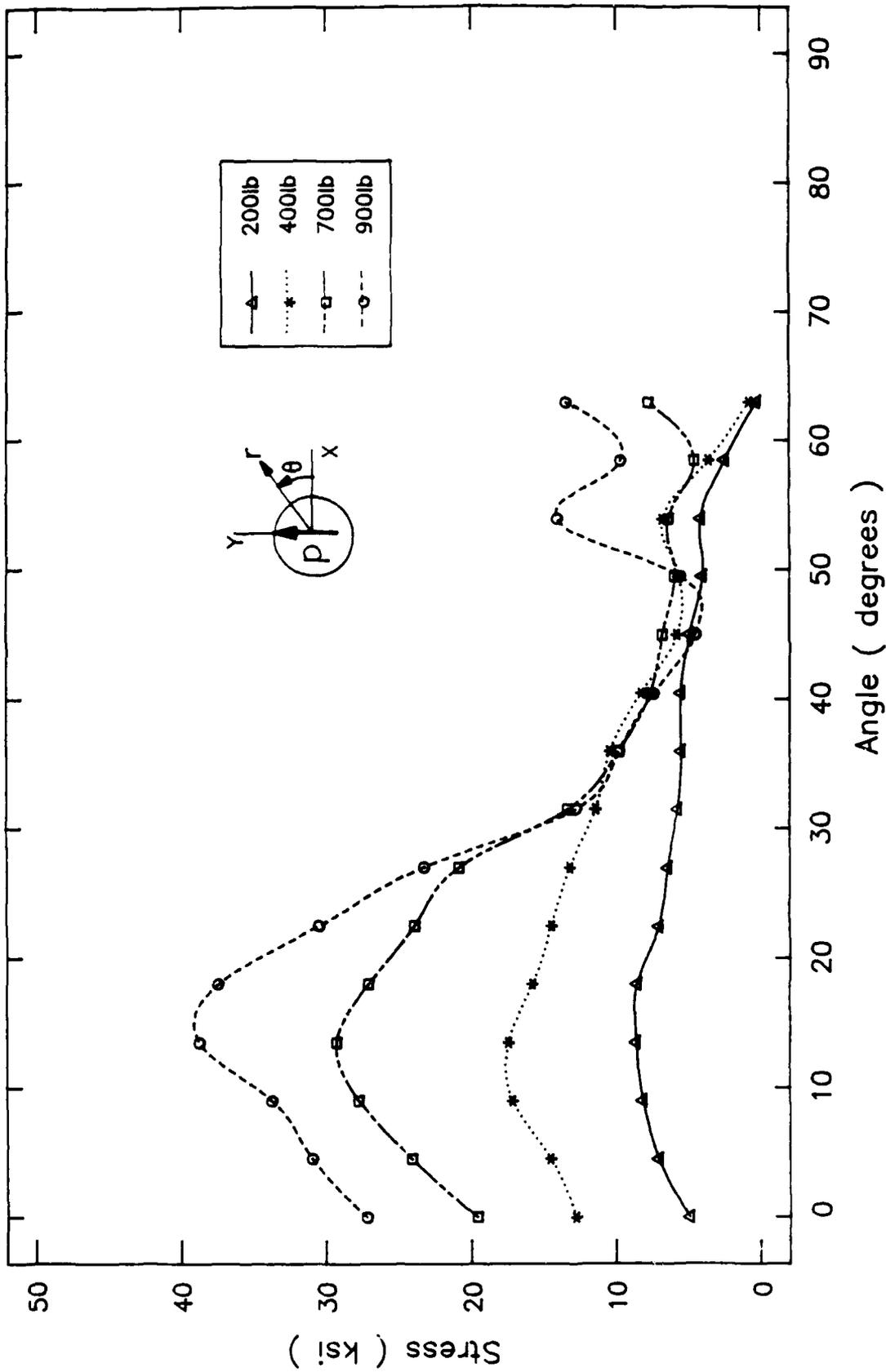
Fig. 43. Hoop contact stress distributions for the graphite-epoxy plate.

98
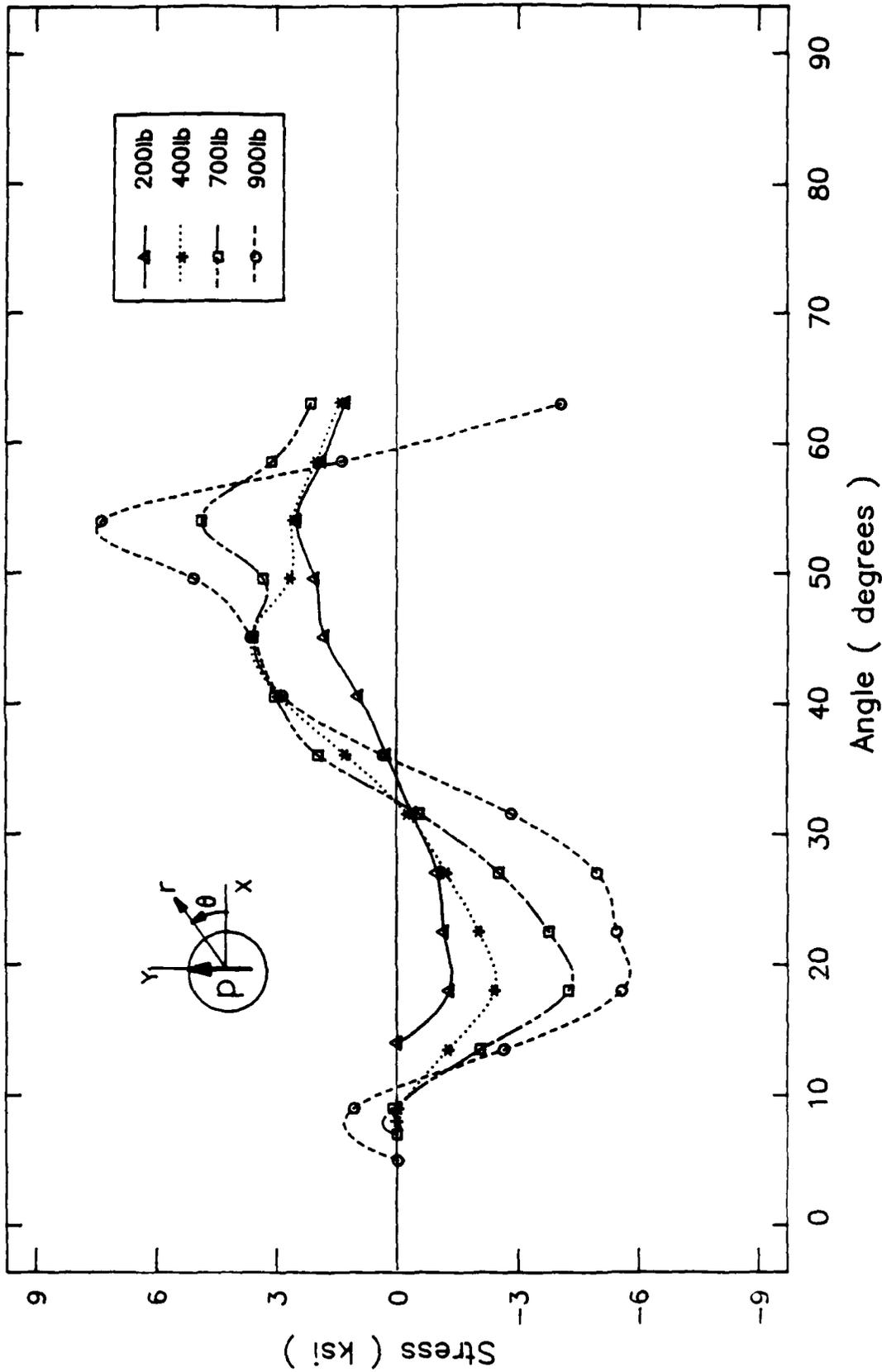
Fig. 44. Shear contact stress distributions for the graphite-epoxy plate.

99
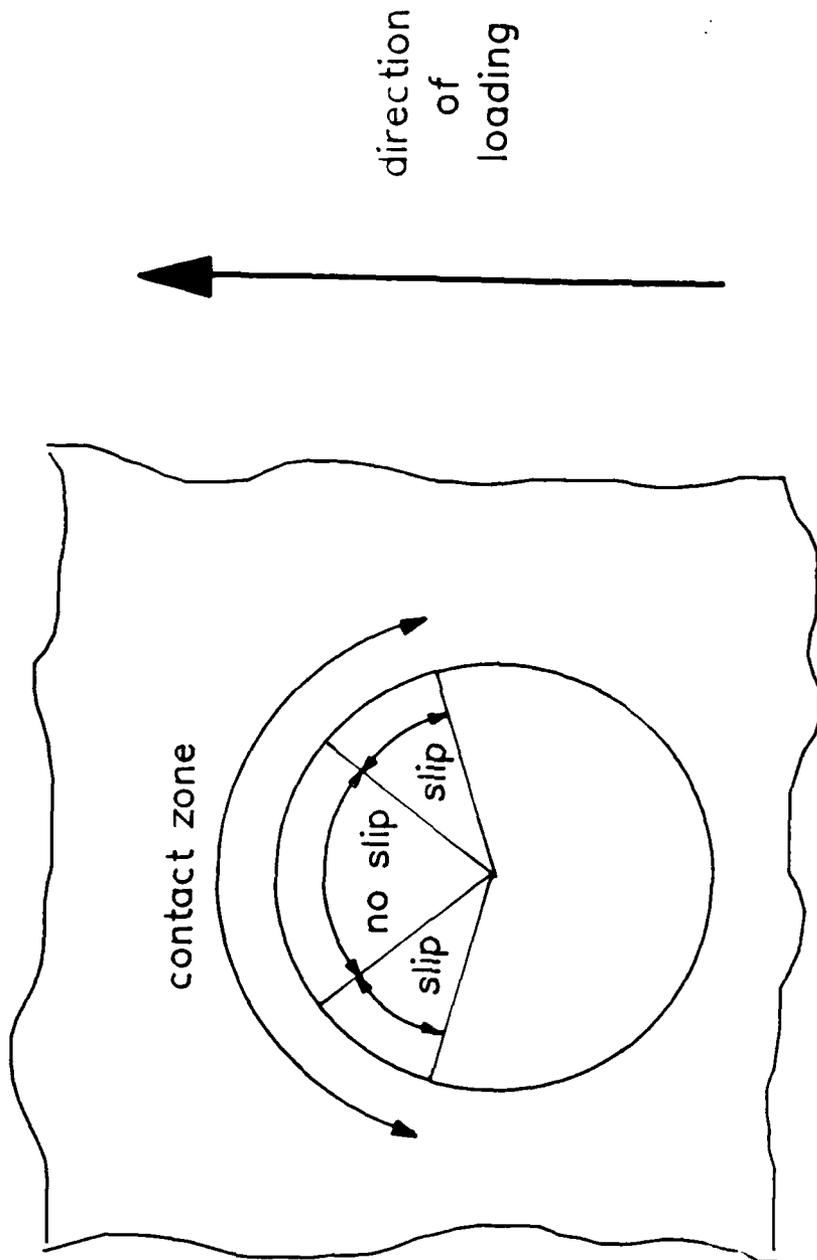
Fig. 45. Schematic of important zones in a pin-plate contact.
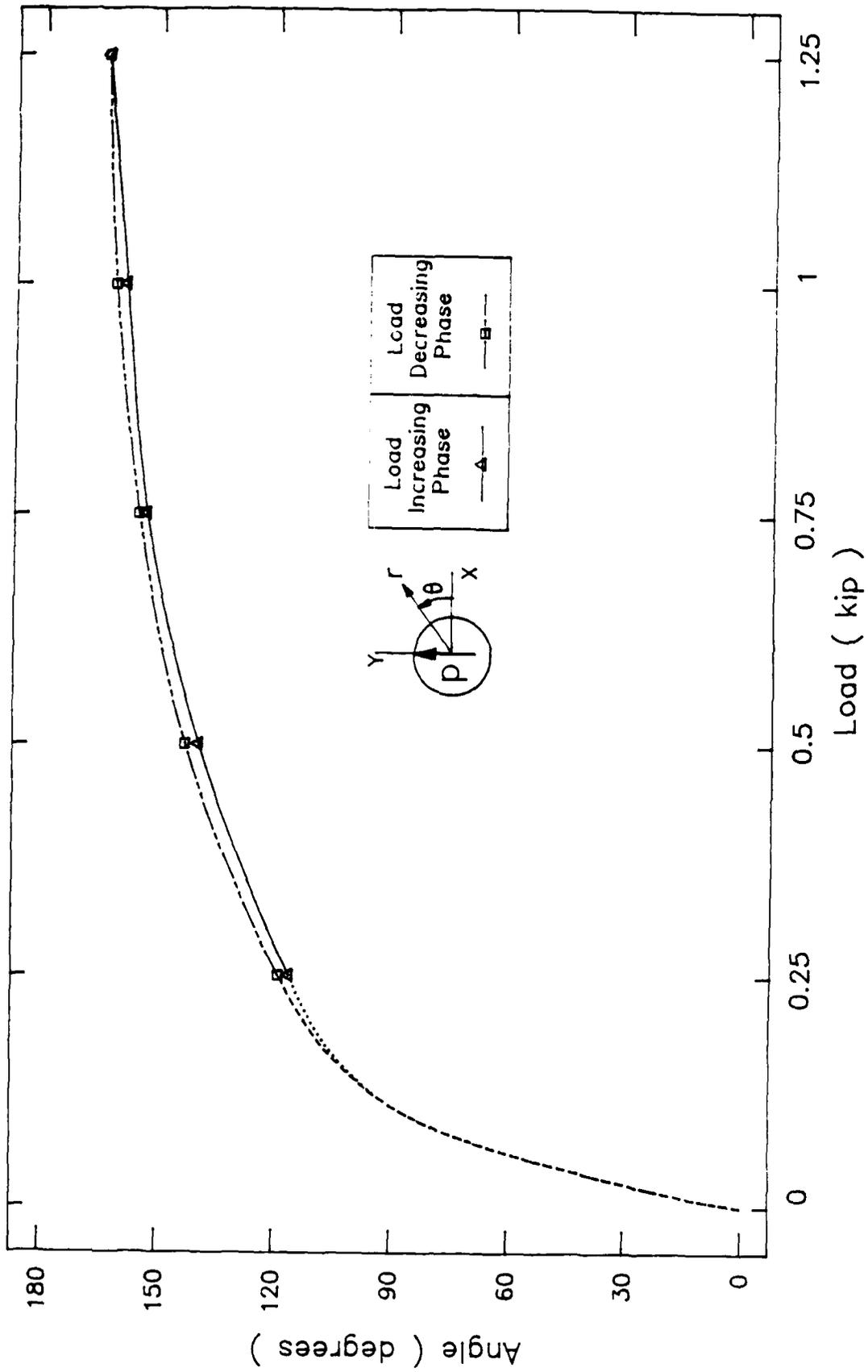
Fig. 46. Variation of contact angle with applied load for the aluminum plate.
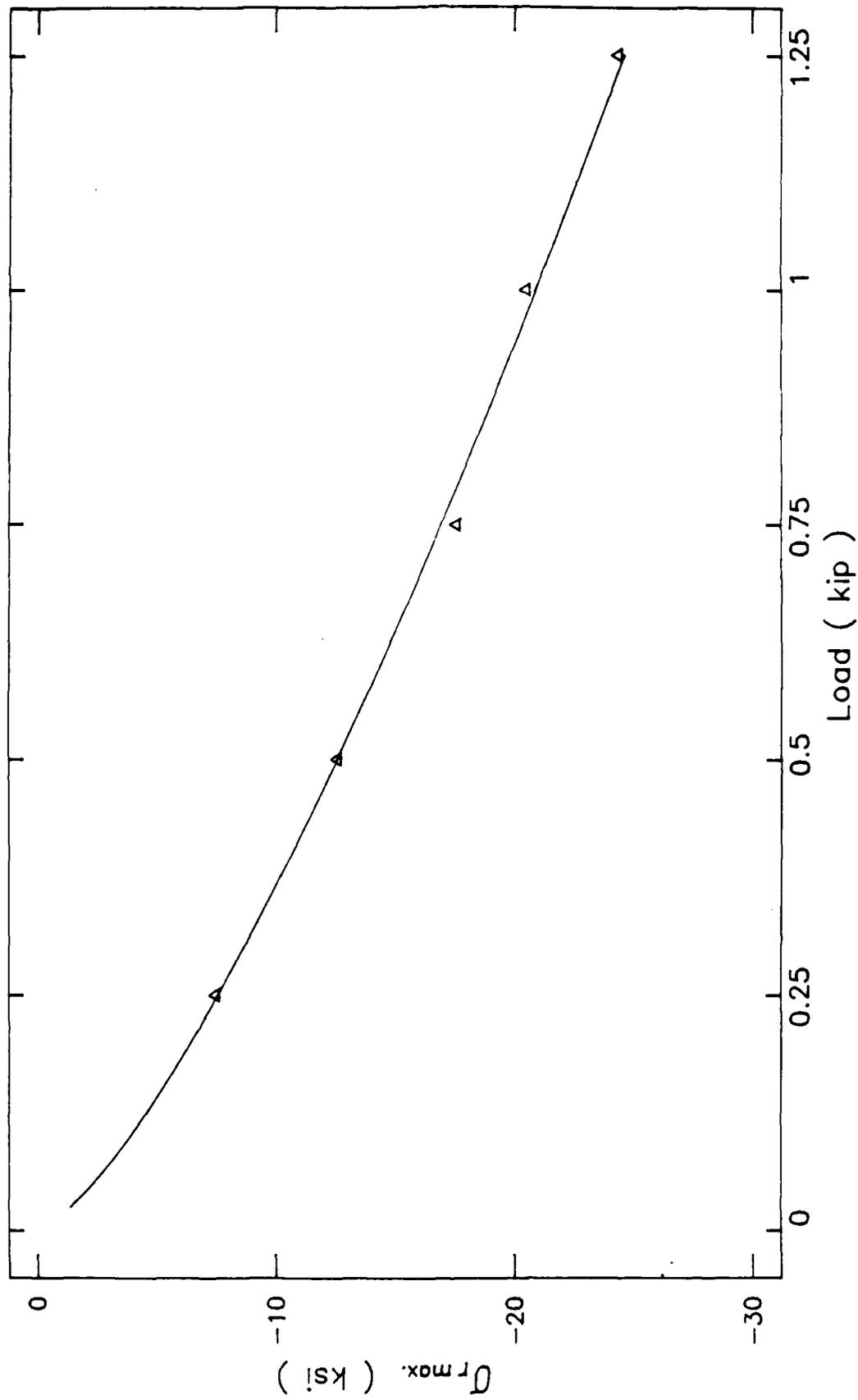
Fig. 47. Variation of the maximum radial contact stress with applied load for the aluminum plate.
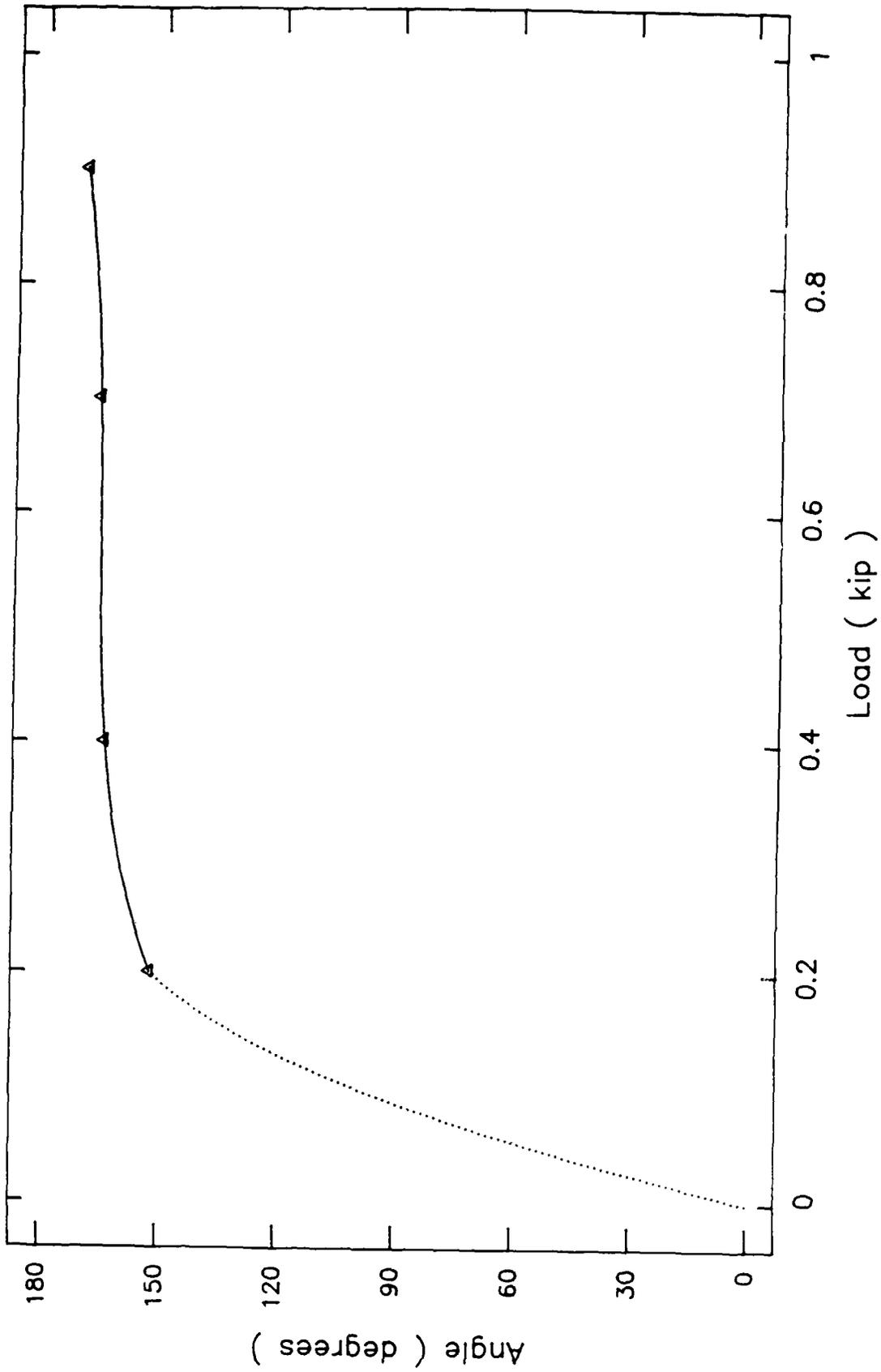
Fig. 48. Variation of contact angle with applied load for the graphite-epoxy plate.
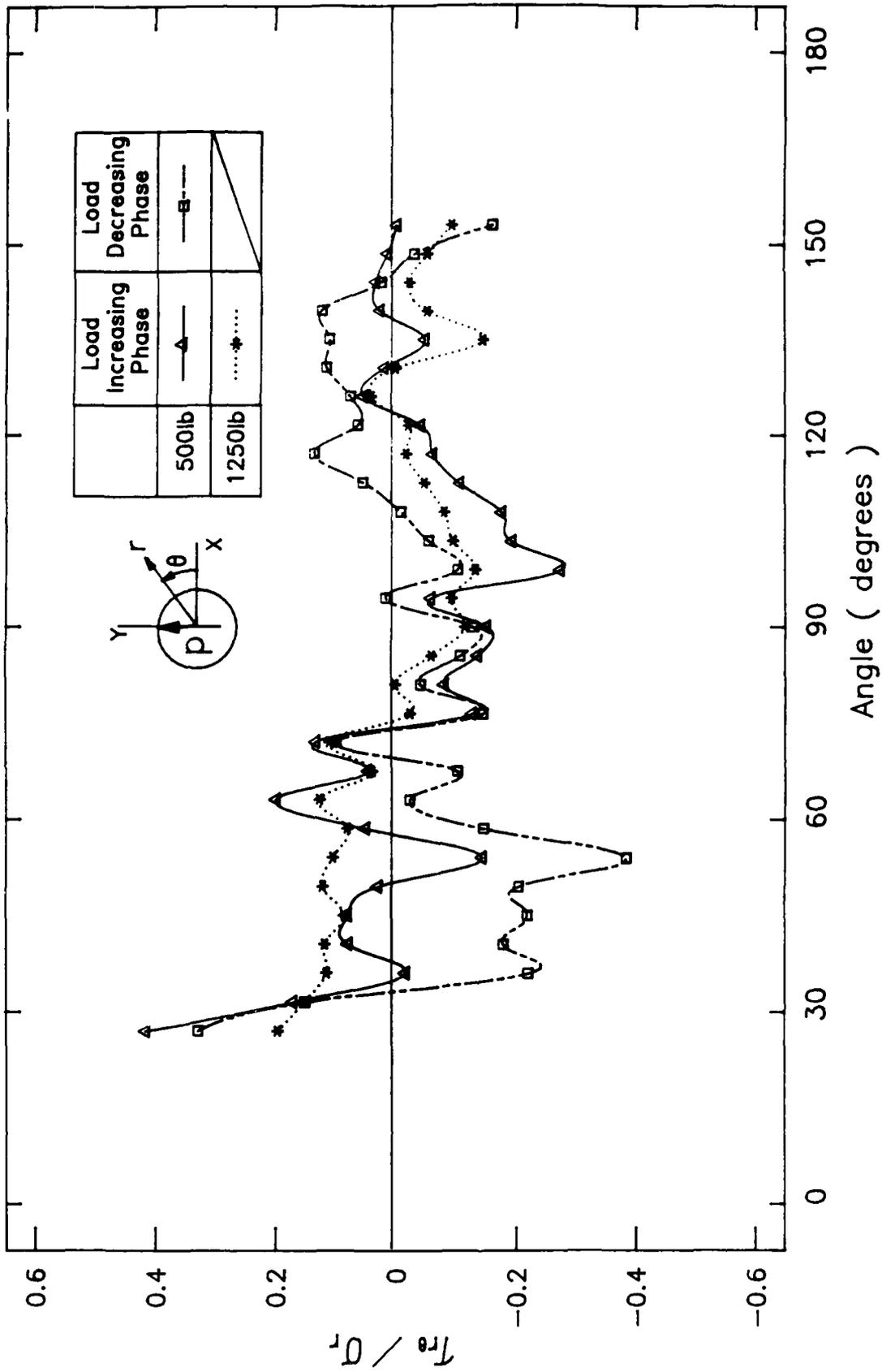
Fig. 49. Ratio of shear stress to radial stress on the load increasing and decreasing phases for the aluminum plate.
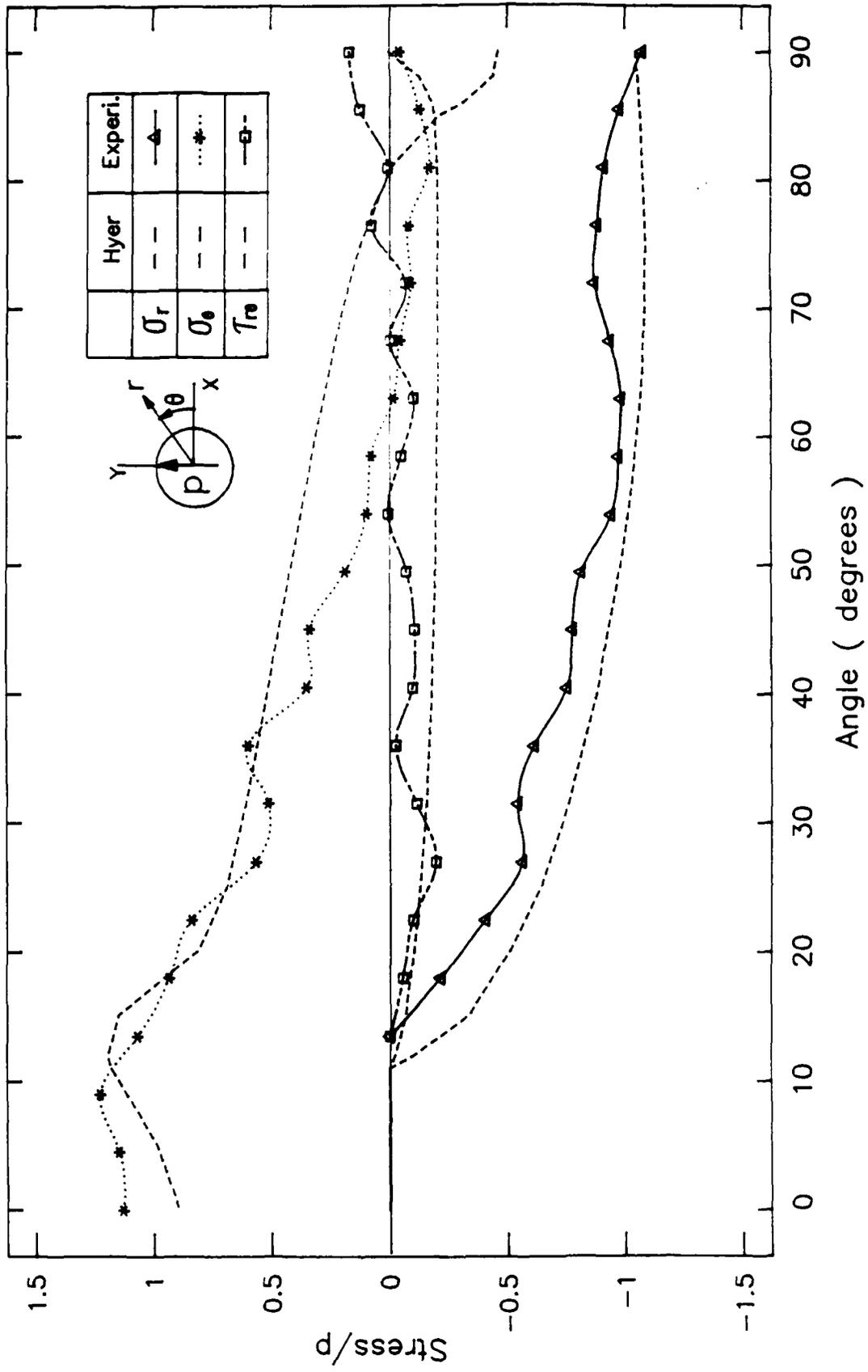
Fig. 50. Comparison of experimental stress distributions (load = 750 lb.) for the aluminum plate, with analytical results from Hyer and Klang [10].
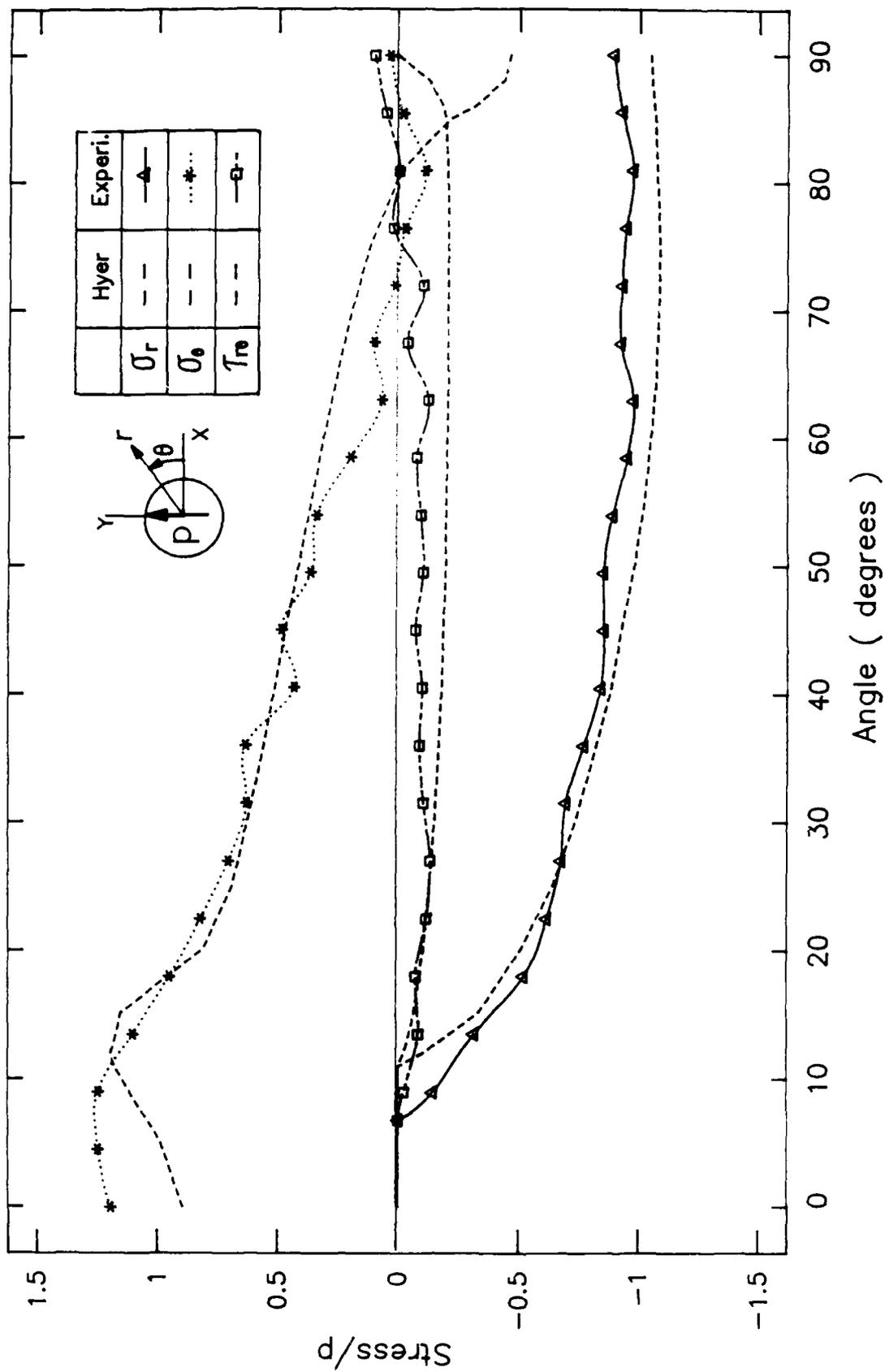
Fig. 51. Comparison of experimental stress distributions (load = 1250 lb.) for the aluminum plate, with analytical results from Hyer and Klang [10].
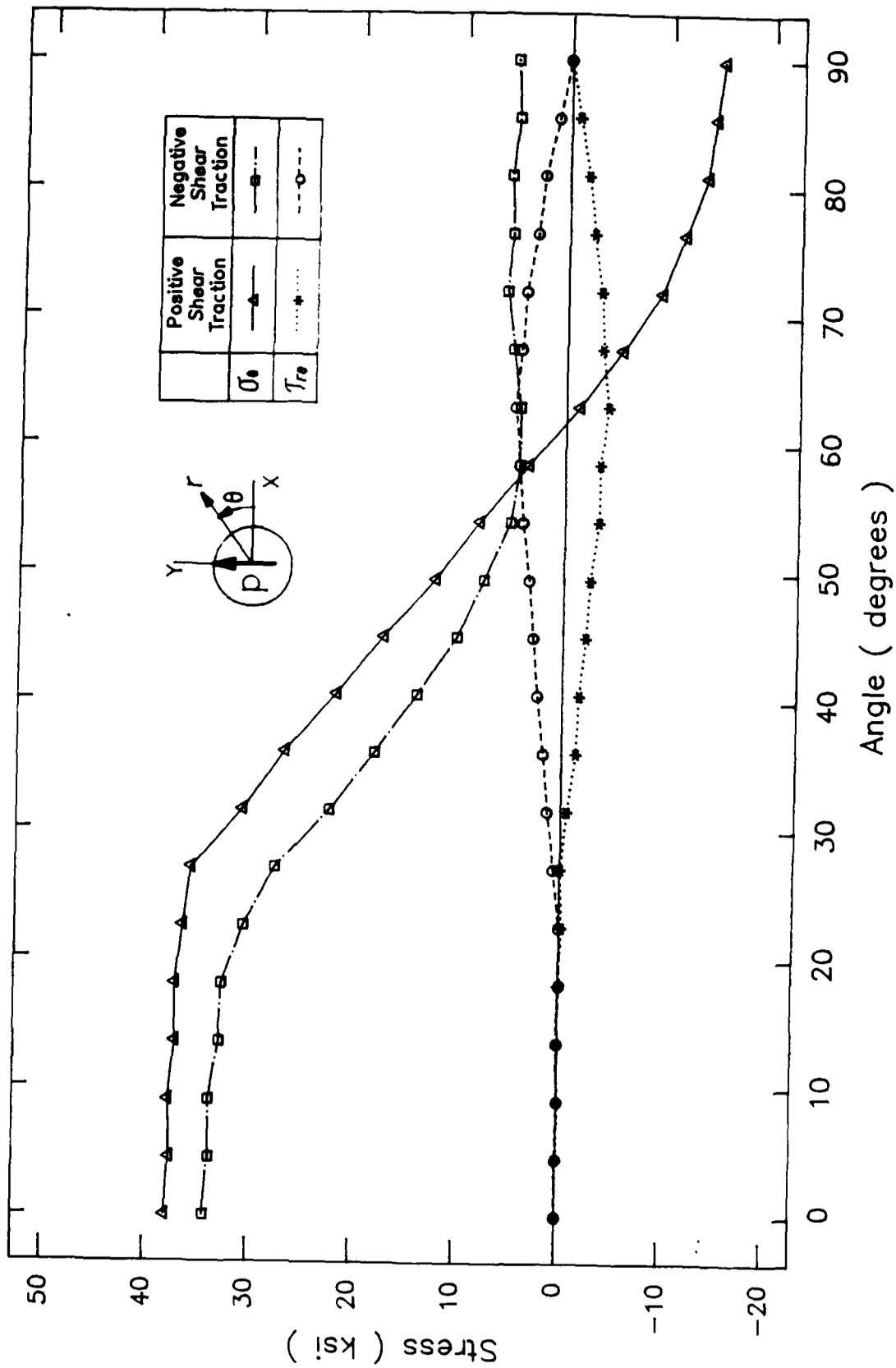
Fig. 52. Numerical illustration of effect of sign of frictional
tractions upon the sign of hoop stress near the point of first contact.
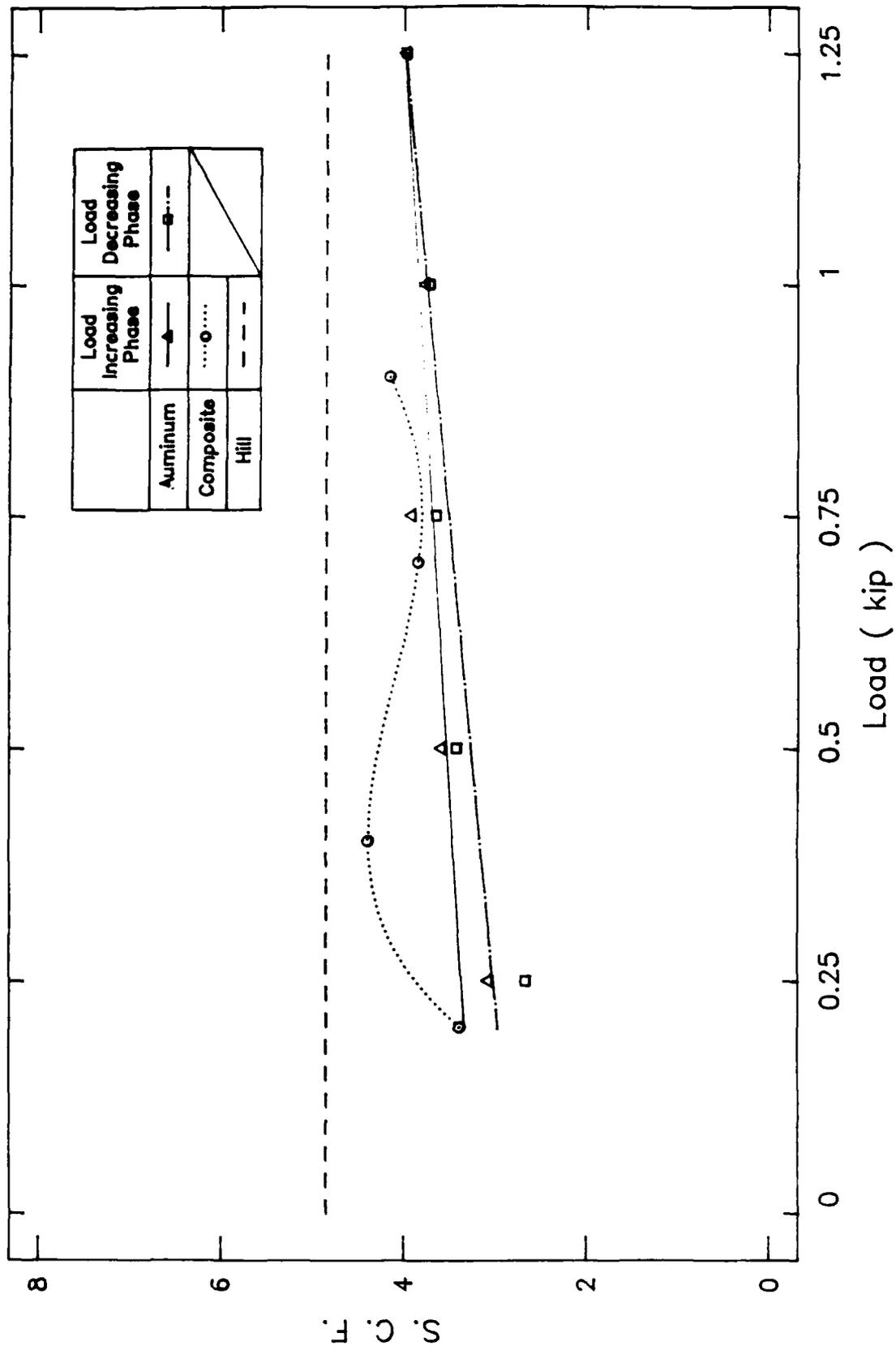
Fig. 53. Variation of stress concentration factors for the aluminum and composite plates. A value from Frocht and Hill [11] is also shown.
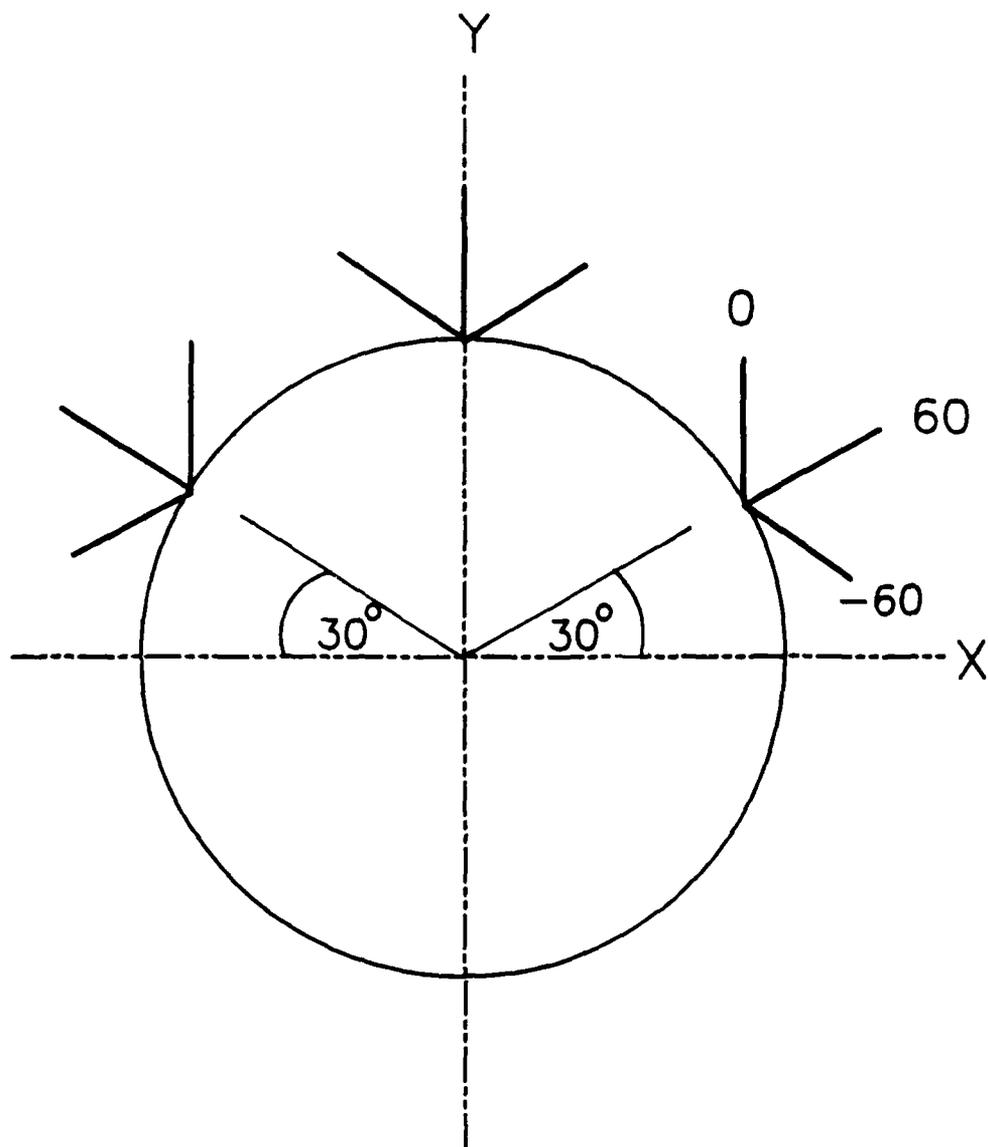
Fig. 54. Schematic of the fiber directions in the graphite-epoxy plate.

bearing failure

matrix tension failure
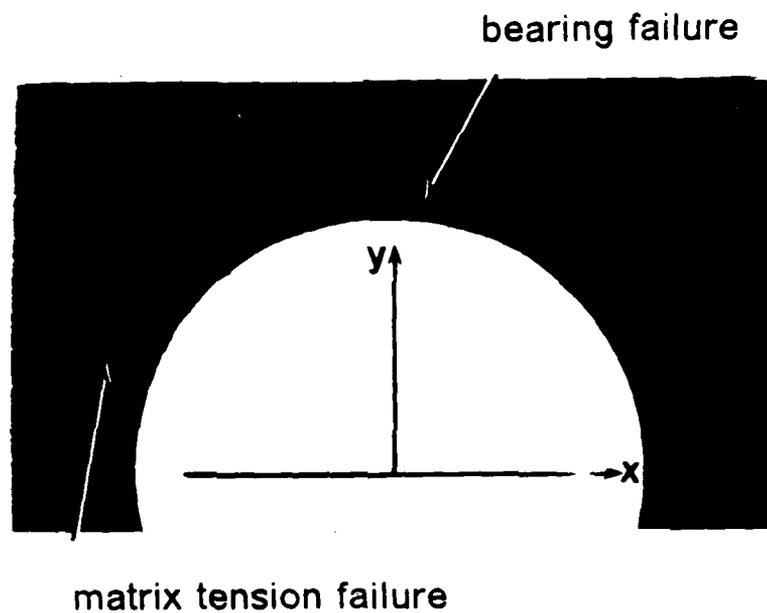
Fig. 55. Radiograph showing matrix cracking and some bearing failure in the composite plate after unloading.

**delamination**
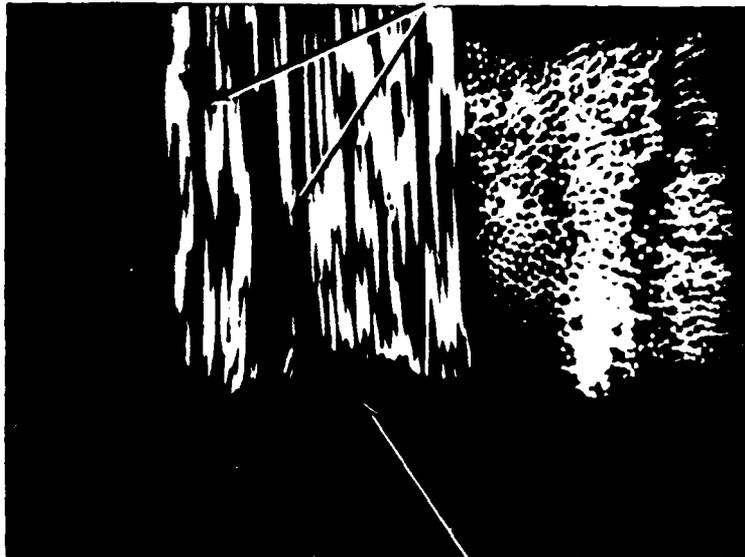
**fiber kinking failure**

Fig. 56. Micrograph showing fiber kinking (bearing) failure in the composite plate.
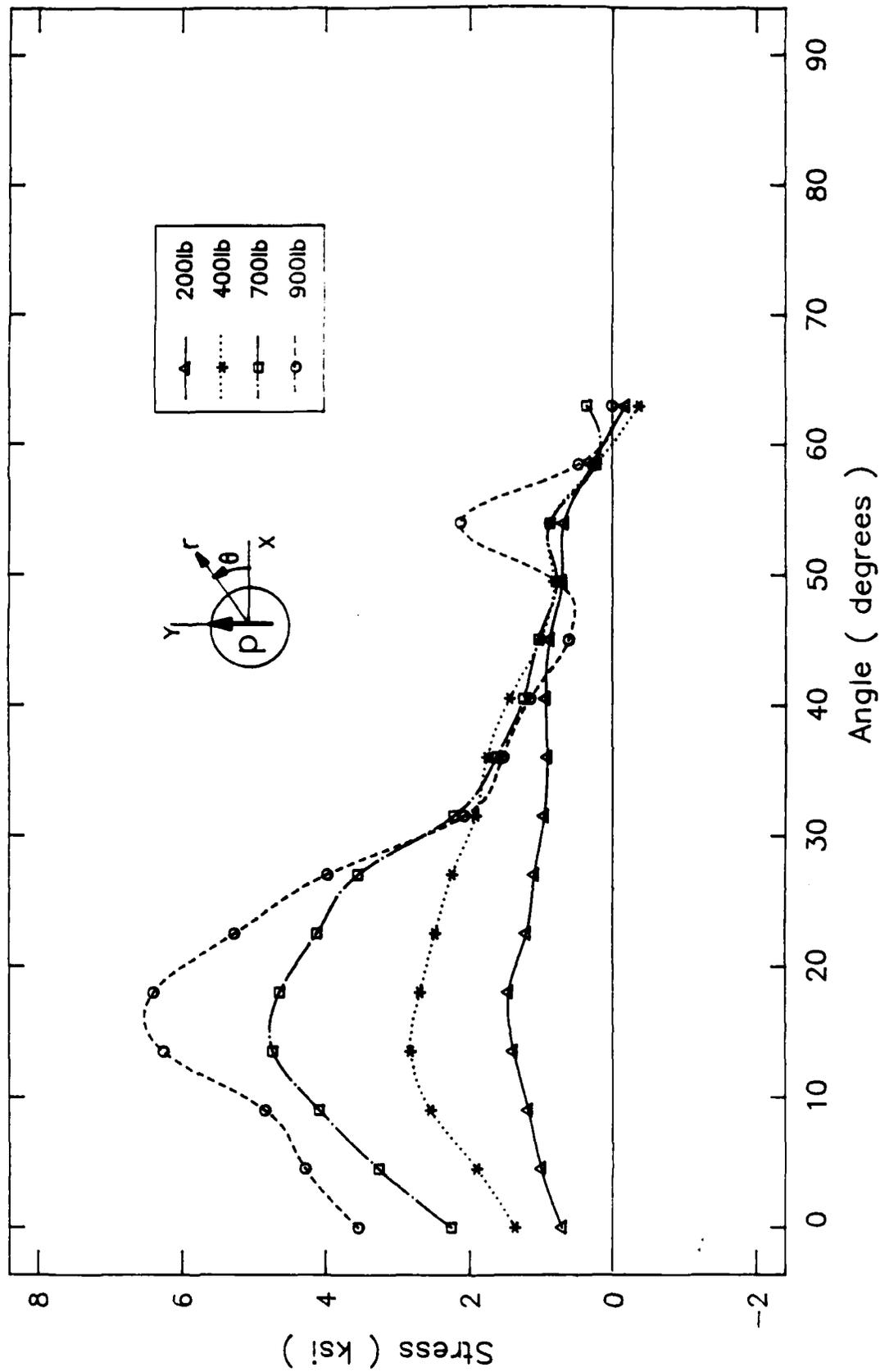
Fig. 57. 60° Ply stresses normal to the fiber direction in the composite plate.
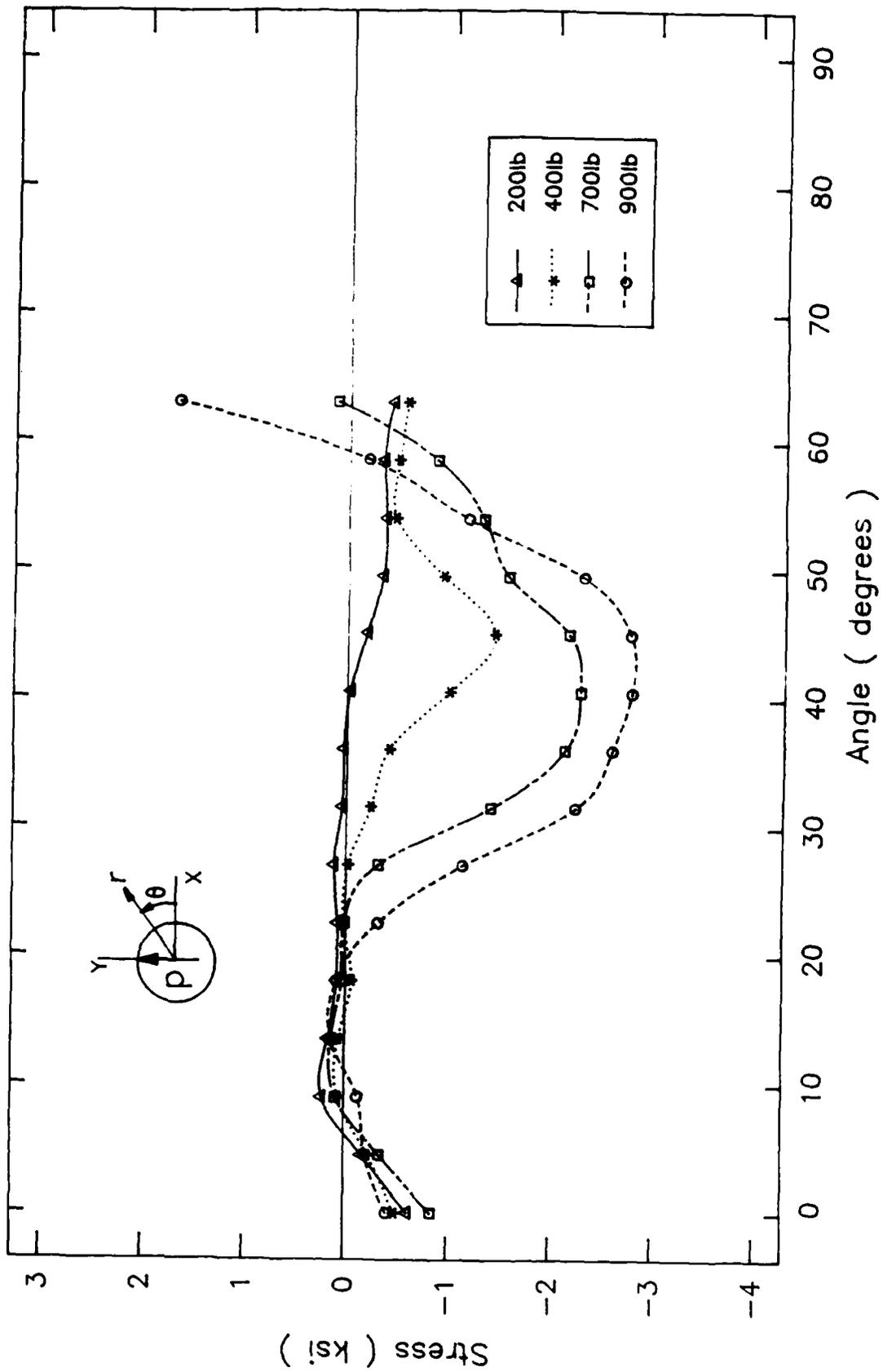
Fig. 58. 0° Ply stresses normal to the fiber direction in the composite plate.

113
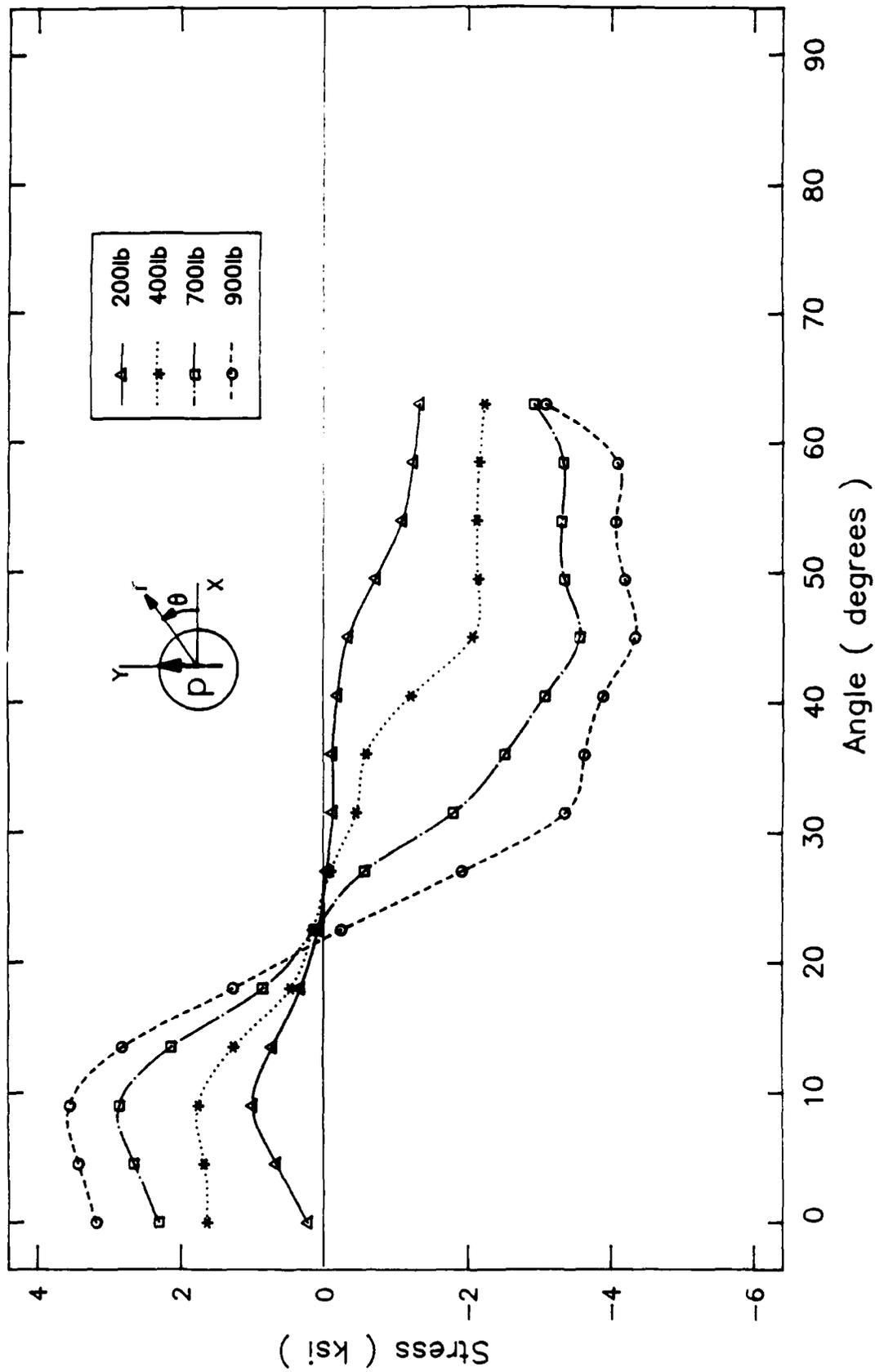
Fig. 59. -60° Ply stresses normal to the fiber direction in the composite plate.

114

# FURTHER REFINEMENT AND APPLICATIONS OF THE MIXED
# COMPUTATIONAL ALGORITHM FOR PLANE ELASTIC CONTACT PROBLEMS

E. Yogeswaren[*] and J. N. Reddy[‡]
Department of Engineering Science and Mechanics
Virginia Polytechnic Institute and State University
Blacksburg, VA  24061

## ABSTRACT

The mixed finite element scheme developed earlier has been further
studied in order to improve the model characteristics and operation as
well as to explore further applications with regards to mechanical
joints.  One of the important modifications that has been implemented in
the present study is the utilization of a dynamic as well as a static
coefficient of friction for the evaluation of contacting surface
behavior instead of a single friction coefficient as used in the
previous study.  This has improved the model behavior and involved a
substantial reorganization of program methodology.  Other refinements
include the incorporation of a modified solution technique that allows
the solution of the indefinite stiffness equation system which is formed
in the first iteration of the first load step, and the usage of a finer
mesh.  The new solution technique also avoids the halt of execution of
the program whenever small elements are introduced in the leading
diagonal due to contact loss.

The case of the pin-loaded aluminum plate has been studied again to
obtain better correlation with experimental results; and a pin-loaded
orthotropic plate behavior as predicted by an analytical solution is
compared with the present model predictions.  The hybrid technique has
been used to estimate the static and dynamic coefficients of friction of
the aluminum pin/plate system.

An elastic-plastic analysis based failure model of pin-loaded
laminates is illustrated by examples which indicate when bearing,
shearout and tensile failure occur in the laminate mechanical joints.
Finally, some improvements that could be carried out on the present
model to predict severe deformation and fracture behavior are discussed.

---

[*]Graduate Research Assistant

[‡]Clifton C. Garvin Professor of Engineering Science and Mechanics

# 1. INTRODUCTION

The updated Lagrangian formulation based on a mixed variatonal statement and the associated finite element model developed earlier [1] gave results in good agreement with the analytical solutions for most contact problems studied there. However, the numerical results obtained for the pin-loaded aluminum plate showed poor correlation with the experimental results of Joh [2]. The poor correlation can be attributed to both theoretical and experimental models used. It was also discovered that the need for a better solution technique existed since the program operation was disrupted whenever certain contact node pairs were about to lose contact thus creating very small terms in the leading diagonal. The work reported here is largely based on the subsequent research carried out to improve the accuracy of the results by modifying and refining the computational procedure developed earlier. Applications of the refined model to the pin-loaded plate problem and other contact problems such as a mechanical joint in filamentary composite laminates are presented.

Factors responsible for the discrepancy between the theoretical and experimental results can be many and may include the non-ideal conditions under which the experiment was conducted. An attempt is made in the present study to see if closer agreement between the theoretical and experimental results can be achieved by refining the computational model. Indeed, the study showed that it is possible if a dynamic coefficient of friction ($\mu_d$) and a static coefficient of friction ($\mu_s$) are used in the analysis instead of a single coefficient of friction, as was done in the earlier work. This approach is more realistic since this comes closer to the continuously varying friction coefficient

116

observed in practice. The basis for the values of $u_d$ and $u_s$ is provided by the hybrid technique study conducted with the experimental values of displacements along the hole boundary.

It was reported in [1] that the first node of the finite element mesh was selected as to be constrained in both directions which enables the use of a conventional banded solver. This is due to the fact that the leading diagonal terms in $[K^{11}]$ (see [1]) will be zero in the first iteration of the first load increment, thus giving an indefinite system of equations. Although this simple solution worked for problems with carefully chosen mesh numbering, it breaks down when leading diagonal terms become small due to loss of contact between pairs of nodes. Hence, the earlier solution scheme was discarded in favor of the technique suggested by Mirza [3].

In addition to the above modifications, which are mainly remedial in nature, some applications of the refined model were also conducted particularly with respect to failure in mechanical joints of composites. The advantages and pitfalls of the technique are also outlined in the section on applications.

Finally, an alternative kinematic description is suggested for severe deformations and cracks encountered in contact systems. This model when incorporated in the present scheme can lead to economical analyses of large deformation problems with fracture by avoiding the remeshing techniques normally used in these cases. No attempt is made to implement the computational procedure in the present study.

117

## 2. PRESENT STUDY

### 2.1 Contact Stress Evaluation

Evaluation of the kinematical relations and tractions at the contacting surface is a significant factor in the analysis of contact problems. One of the main advantages accrued from mixed formulation is that the normal and tangential surface tractions can be calculated directly from the nodal stress values obtained in the mixed model. A practical way of treating contact surfaces is to assume that the forces are transferred only at the nodal points as concentrated forces resulting from the integrated effect of contact stresses up to and including the contactor node. In the earlier work [1] a segment of triplet nodes were considered on the contactor body, with the node in consideration as the middle node, and by integrating the tractions on the contactor surface the nodal forces were obtained. In the present study a more direct and simple algorithm is adopted to reduce calculations involved and by using a finer mesh it is made certain that the accuracy of the model is not compromised.

In the present analysis the contact status of any contact segment of the target body containing a node of the contactor is decided by the normal and tangential nodal forces at the given node. If the tangential force at a node is more than the frictional capacity then the node is under sliding contact. The limiting frictional resistance that can be sustained by a stationary node K is given by,

$$\begin{pmatrix} \text{Static} \\ \text{Frictional} \\ \text{Capacity} \end{pmatrix}_K = \begin{pmatrix} \text{Static Coefficient} \\ \text{of friction } \mu_s \end{pmatrix} \times \begin{pmatrix} \text{Normal Force} \\ \text{Component} \\ \text{at node K} \end{pmatrix}. \quad (2.1)$$

However, if there is already slip occurring in the last load increment, the frictional capacity is given by

$$\begin{pmatrix} \text{Dynamic} \\ \text{Frictional} \\ \text{Capacity} \end{pmatrix}_K = \begin{pmatrix} \text{Dynamic Coefficient} \\ \text{of Friction } \mu_d \end{pmatrix} \times \begin{pmatrix} \text{Normal Force} \\ \text{Component} \\ \text{at Node K} \end{pmatrix}. \quad (2.2)$$

Although the above concept was discussed in [1], it was left to the current study to implement this into the program. Thus as a first step, the direct path discussed in this section was chosen to check the usefulness of this notion. It should be noted here that Sections 3.3.4 and 3.3.5 of [1] are made obsolete by the present approach. But, implementation of $\mu_s$ and $\mu_d$ in the integration process outlined in these sections will be carried out if the present method is found to be unsatisfactory in later applications.

Sticking contact occurs if the frictional capacity as determined by Eq. (2.1) or Eq. (2.2) exceeds the tangential force at node K. The conditions of contact from the last load increment determines whether Eq. (2.1) or Eq. (2.2) is used. Any free target segment that comes in contact will have a sticking contact since the tangential force is zero along the free surface. This is also true when a segment re-establishes contact after a separation. However, when the friction coefficient is very low the frictional capacity may be so low that sliding may occur at initial contact itself.

Sliding condition is brought about when the nodal tangential force exceeds the frictional capacity of the segment given by the appropriate equation (2.1) or (2.2). The node is constrained to move only in the tangential direction and the frictional resistance opposes the relative motion of the bodies. The dynamic frictional resistance opposing the motion changes continuously as a function of the relative magnitude of the tangential and normal forces acting at a given node. As a first-order approximation, the value of the resistance at the beginning of the

119

load increment is assumed to be opposite to the direction of motion. It is to be noted that the global nodal forces are the external forces acting on every element to balance the forces due to the stresses. Frictional forces are externally applied at the contactor nodes in the direction of tangential force and are given by,

$$(\text{External Frictional Forces})_< = \text{sign}\left(\begin{array}{c}\text{tangential}\\\text{nodal force}\end{array}\right)_K \times u_d \times \left(\begin{array}{c}\text{normal}\\\text{nodal}\\\text{force}\end{array}\right)$$

(2.3)

if and only if

$$\left|\begin{array}{c}\text{Normal}\\\text{Nodal Force}\end{array}\right| \leq \left|\begin{array}{c}\text{Tangential}\\\text{Nodal Force}\end{array}\right|. \qquad (2.4)$$

The frictional force is determined at all equilibrium configurations and applied along the target surface.

When the coefficient of friction is very small the frictional capacity of all the segments under contact is identically zero at all times. The contactor nodes follow the fixed target surface and since the target surface need not be parallel to the global axes, a local coordinate system is defined with constraint of movement along one axis.

Separation occurs when the reactive contact forces act in the negative direction of the unit outward normal to the contact surface. However, if the forces as evaluated at the end of an equilibrium configuration become positive, then there is no contact force betwen the contacting bodies, and the segment containing the node has separated. This node is considered to be free and once again is a potential contactor node and checked for contact overlap in subsequent load increments.

120

## 2.2 Modified Solution Technique

The finite element equations resulting from the mixed formulation can be written as,

$$
\begin{bmatrix}
[K^{11}] & [K^{12}] \\
[K^{12}]^T & [K^{22}]
\end{bmatrix}
\begin{Bmatrix}
u \\
S
\end{Bmatrix}
=
\begin{Bmatrix}
F \\
0
\end{Bmatrix}
\tag{2.5}
$$

where

$$
K^{11}_{ij} = \int_{\Omega} \left[ \tau_{xx} \frac{\partial \psi_i}{\partial x} \frac{\partial \psi_j}{\partial x} + \tau_{xy} \left( \frac{\partial \psi_i}{\partial x} \frac{\partial x_j}{\partial y} + \frac{\partial \psi_i}{\partial y} \frac{\partial \psi_j}{\partial x} \right) + \tau_{yy} \frac{\partial \psi_i}{\partial y} \frac{\partial \psi_j}{\partial y} \right] dxdy
$$

$$
\tag{2.6}
$$

Thus it can be seen from Eq. (2.6), for the first iteration of the first load increment, that $[K^{11}] = 0$ because $\tau_{xx} = \tau_{xy} = \tau_{yy} = 0$, thus resulting in an indefinite system of equations. Although Eq. (2.5) can be solved for this condition, by first solving for stress and then for displacements, a more direct way has been given by Mirza [3]. He suggested that premultiplying both sides of the equation by the transpose of the global stiffness matrix, one can obtain a positive-definite system of equations. For example, if Eq. (2.5) can be written as

$$
[K][\delta] = [P]
\tag{2.6}
$$

where

$$
[K] =
\begin{bmatrix}
[0] & [K^{12}] \\
[K^{12}]^T & [K^{22}]
\end{bmatrix}, \quad
\{\delta\} =
\begin{Bmatrix}
u \\
S
\end{Bmatrix} \times P =
\begin{Bmatrix}
F \\
0
\end{Bmatrix},
$$

then a positive definite system is given by

$$
[K]^T [K]\{\delta\} = [K]\{P\},
\tag{2.7}
$$

and the solution of Eq. (2.7) gives the results of Eq. (2.6).

This technique has been extended in the present study by reforming Eqs. (2.5) into the type given by Eq. (2.6) whenever leading diagonal terms are small and then carrying out the operations described above.

## 3. LITERATURE REVIEW

### 3.1 Overview

The earlier work [1] contains and discusses a number of references on the finite element analyses of contact problems and the present review is intended to be within the scope of the present study. The major aspects of contact problems have been discussed in detail in [1] and it would be appropriate here to concentrate on how the model can be improved by modifications based on an Eulerian-Lagrangian formulation as discussed in [4-6], and to examine some of the work that has been carried out on the failure of mechanical joints in composites.

Mixed formulations of contact problems can be further enhanced by incorporating a form of kinematic description, addressed in [4] as an Eulerian-Lagrangian displacement model. The conventional Lagrangian description uses a fixed reference material configuration to formulate equilibrium equations where a certain reference quantity of material is "followed" throughout its physical behavior. Conversely, the material can be allowed to "flow" across a fixed spatial reference and physical measurements can be referred to the fixed frame. The total Lagrangian description uses initial configuration as the reference whereas the updated Lagrangian description refers to the current deformed state. But the General Lagrangian description and Eulerian-Lagrangian description are more flexible in that the configurations used to measure spatial variables and to define the strain measure need not be the same. Thus, this allows material flow across the meshes thus enabling

122

large deformations in contact and fracture to be captured within an initial mesh rather than employing mesh redefining techniques. The application of this technique is illustrated in [5] for contact problems and in [6] for dynamic fracture problems.

Calculation of the strength and failure mode of a composite laminate containing a pin-loaded hole requires the knowledge of the load distribution inside the surface of the hole. Frequently, a cosine load distribution is assumed since such a load distribution greatly simplifies the calculations. The stresses inside the laminate calculated by a cosine load distribution may differ significantly from those which actually arise in the structure. As a result, those failure criteria which require an accurate knowledge of the stress distributions near the surface of the hole, will predict failure inaccurately when used in conjunction with cosine load distribution. Work on composite bolted joints has been extensive with early studies concentrating on empirical design and gradually progressing to analytical methods for stress analysis (see [7-14]) and the search for appropriate failure criteria (see [15-20]). Empirical design methods proved too costly and time consuming since the large number of variables in joint design require huge data bases for each material and class of laminates. Thus analytical techniques have been attractive, although this requires vigilance on the part of the designer towards the pitfalls normally encountered.

## 3.2 Eulerian-Lagrangian Description for Severe Deformation and Fracture

This section reviews the updated Lagrangian scheme used in the present study, and outlines the Eulerian-Lagrangian formulation for an easier and accurate modelling of contact and fracture. However, the latter scheme is not implemented on the computer during the present research.

The modified functional with the Lagrange multiplier for the updated Lagrangian formulation is given by (see [1]),

$$\pi_L = \int_{V_1} \frac{1}{2} {}_1C_{ijrs} \, {}_1e_{rs} \, {}_1e_{ij} dv + \int_{V_1} {}^1\tau_{ij}({}_1e_{ij} + {}_1\eta_{ij}) dv - {}^1F$$

$$- \int_{V_1} {}_1S_{ij}[{}_1e_{ij} - \frac{1}{2}(\frac{\partial u_i}{\partial x_j} + \frac{\partial u_j}{\partial x_i})] dv \tag{3.1}$$

Since $\quad {}_1S_{ij} \, {}_1e_{ij} = U_o^* + \frac{1}{2} C_{ijk\ell} \, {}_1e_{ij} \, {}_1e_{k\ell} \tag{3.2}$

Eq. (3.1) can be expressed as

$$\pi_L = \int_{V_1} [\pi_{ij}(e_{ij} + {}_1\eta_{ij}) + \frac{1}{2} {}_1S_{ij}(\frac{\partial u_i}{\partial x_j} + \frac{\partial u_j}{\partial x_i}) - U_o^*] dv - {}^1F \tag{3.3}$$

where $U_o^*$ the complementary strain energy density,

$$U_o^* = \frac{1}{2} D_{ijk\ell} \, {}_1S_{ij} \, {}_1S_{k\ell} \tag{3.4}$$

By imposing stationarity on $\pi_L$ in Eq. (3.3), we obtain the following two approximate equilibrium equations which form the basis of the mixed finite-element model:

$$\int_{V_1} {}^1\tau_{ij}\delta({}_1\eta_{ij}) dv + \int_{V_1} {}_1S_{ij}\delta u_{i,j} dv = \delta({}^1F) = \int_{V_1} {}^1\tau_{ij}\delta({}_1e_{ij}) dv \tag{3.5}$$

$$\int_{V_1} u_{i,j}\delta({}_1S_{ij}) dv = \int_{V_1} D_{ijk\ell} \, {}_1S_{k\ell}\delta({}_1S_{ij}) dv = 0 . \tag{3.6}$$

124

Approximating the displacements and stresses by

$$u_i(x_1, x_2) = \sum_{j=1}^{n} u_i^j \psi_j(x_1, x_2) \tag{3.7}$$

$$_1 S_{ij}(x_1, x_2) = \sum_{k=1}^{n} {_1}S_{ij}^k \psi_k(x_1, x_2) \tag{3.8}$$

and substituting Eqs. (3.7) and (3.8) into Eqs. (3.5) and (3.6), we obtain the mixed finite element model,

$$\begin{bmatrix} [K^{11}] & [K^{12}] \\ [K^{12}]^T & [K^{22}] \end{bmatrix} \begin{Bmatrix} u \\ S \end{Bmatrix} = \begin{Bmatrix} \{F\}^L \\ 0 \end{Bmatrix} - \begin{Bmatrix} \{F\}^{NL} \\ 0 \end{Bmatrix}, \tag{3.9}$$

where the details of the element matrices are given in [1].

A similar approach with the Eulerian-Lagrangian model would give,

$$\pi_L = \frac{1}{2} \int_{V^R} ({_1}\tau_{ij} + {_1}S_{ij})({_1}e_{ij} + {_1}\eta_{ij}) \tilde{J} dV_R$$

$$- \int_{V^R} {_1}S_{ij} [{_1}e_{ij} - \frac{1}{2}(\frac{\partial u_i}{\partial x_k^R}\tilde{J}_{kj} + \frac{\partial u_j}{\partial x_k^R}\tilde{J}_{ki})]\tilde{J} dV_R \tag{3.10}$$

where

$$\tilde{J}_{kj} = \frac{\partial x_k^R}{\partial X_j} \quad \text{and} \quad \tilde{J} = |\tilde{J}_{ij}| .$$

Similar manipulations as for the updated Lagrangian formulation lead to,

$$\begin{bmatrix} [K'_{11}] & [K'_{12}] & [K'_{13}] \\ [K'_{21}] & [K'_{22}] & [K'_{23}] \\ [K'_{31}] & [K'_{32}] & [K'_{33}] \end{bmatrix} \begin{Bmatrix} \{u\} \\ \{U\} \\ \{S\} \end{Bmatrix} = \begin{Bmatrix} \Delta R'_1 \\ \Delta R'_2 \\ \Delta R'_3 \end{Bmatrix} \tag{3.11}$$

where $\{u\}$ is the Lagrangian incremental displacement, $\{U\}$ is the Eulerian incremental displacement, and $\{S\}$ is the incremental stress vector. The total incremental displacement is given by

$$\{U_T\} = \{u\} - \{U\} \tag{3.12}$$

The details of the Eulerian-Lagrangian method and its application in the present context can be found in [4] for the contact model and in [6] for the fracture model, although References 4 and 6 consider only the displacement formulations.

## 3.3 Failure analysis of Mechanical Joints in Composites

Stress analysis, a failure criterion and a strength model are the basic components of a joint failure analysis (or a strength analysis). The three basic failure modes associated with bolted joints in composites are the bearing failure, the shearout failure and the net tensile failure (see [15-23]). It has been found that the shearout and the net tensile failure can be adequately modelled by a plane elastic stress analysis, with a point stress failure hypothesis and a macroscopic failure model such as the maximum stress or the maximum strain criterion.

Recently, there is a trend towards studies incorporating ply-by-ply failure analysis of bolted joints, in order to assess the damage to individual plies (see Reddy and Pandey [24]). This requires some form of macroscopic criterion such as the Tsai-Hill or Hoffman's criterion to predict failure.

An altogether different approach has been adopted towards failure by Hyer et al. ([7],[8]), who have used the maximum radial and circumferential stresses as indicators of the capacity of a bolted joint in order to study the effects of pin elasticity, pin fit-interference and friction on the capacity of a joint. They concluded that all three factors are detrimental to the capacity of the bolted joint.

126

## 4. APPLICATIONS

### 4.1 A Pin-Loaded Aluminum Plate

Three different meshes were used to model the aluminum plate. All meshes took advantage of the symmetry of the problem and modelled only half the plate. Further simplification was carried out on Mesh A (Fig. 1), where only a quarter of the pin was modelled as was discussed in the earlier study [1]. However, both Mesh B and Mesh C did not adopt this simplification and they modelled half the pin as shown. The contact nodal locations of Mesh A are reiterated here for completeness. These locations are the following (degrees): 0.0, 1.0, 2.0, 4.0, 6.0, 8.0, 10.0, 12.5, 15.0, 20.0, 25.0, 30.0, 35.0, 40.0, 45.0, 54.0, 63.0, 72.0, 90.0, 99.0, 108.0, 117.0, 126.0, 135.0, 144.0, 153.0, 162.0, 171.0 and 180.0. In Mesh B these locations were spaced at 9° intervals and in Mesh C these were at 2.5° intervals for the first 90° and at 9° intervals for the second 90° as shown in Fig. 2 and 3 respectively. The number of elements and the nodes in the meshes are given as follows:

Mesh A:   236 elements, 286 nodes,

Mesh B:   332 elements, 391 nodes,

Mesh C:   452 elements, 540 nodes.

All nodes along the line of symmetry were constrained to move only in the lengthwise direction and the center of the pin (numbered 1) in all three meshes was constrained in both directions. The load applied was distributed along the shorter edge away from the pin, in the lengthwise direction. A dynamic coefficient of friction $u_d = 0.25$ and a static coefficient of friction $u_s = 0.35$ were used in the analysis with these numerical values having been estimated from the hybrid technique.

127

The load was applied in 14 steps following closely the experimental loading values. In the load increasing phase the values of load were 20, 23, 520, 1240, 1460, 1670 and 1980 lbs. respectively with the decreasing phase values being 1800, 1600, 1210, 1070, 535, 210 and 40 respectively giving 14 load steps. The number of iterations required for each load increment were 3, 8, 3, 3, 3, 1, 2, 2, 2, 3, 2, 3, 3, and 3 for the case illustrated in Fig. 6, where Mesh A was used and results are plotted for load step 4, where the total load is at a value of 1240 lbs.

The case shown in Fig. 5 was analyzed with the modified computational procedure discussed in Section 2. The results show a closer agreement with the experimental results of Joh [2], than the results shown in Fig. 4, which were obtained using the original procedure of [1]. It is interesting to note that a constant value of friction coefficient of 0.15 gives a closer agreement in Fig. 4 than the constant friction coefficient of 0.30, these values being chosen arbitrarily. It is possible here to be misled easily to conclude that a better choice of value of friction coefficient might be 0.15 than 0.30 unless the full picture is revealed by Fig. 5, which indicates that better results are given by a dynamic/static friction model. Indeed it is possible to conclude here that yet better modelling can be achieved by a continuous friction coefficient variation such as that given by a power law although the implementation of this may be more cumbersome. It can also be seen that the angle of contact is more realistic in Fig. 5 (after the modification) than in Fig. 4 (before the modification).

The load decreasing phase results shown in Fig. 6 compare favorably with the experimental results, despite some 66% difference in the values

of $\tau_{r\theta}$ from 40° to 75°. This can be considered fair compared to the results given by the method before modification, which gave identical results to the load increasing phase without any negative values for $\tau_{r\theta}$.

## 4.2  A Pin-Loaded Ortrotropic Plate

An analytical solution to the problem of pin-loaded composite laminate has been obtained by Hyer et al. ([7],[8]) based on a complex Fourier series method and a collocation technique which enforced boundary conditions at discrete locations around the hole boundary. Results were obtained by this analytical method for infinite orthotropic plates loaded by pins. These results were chosen to be compared with the finite element results since both methods capture the idealized conditions of the model to the same degree.

The mesh shown in Fig. 7 was selected to idealize the infinite plate and the pin, with 426 elements and 509 nodes. The nodes along the line of symmetry were constrained to move only in the lengthwise direction in the same way as the nodes along the longer boundary whereas the nodes along both shorter boundaries were constrained to move along the y-direction. Normalized circumferential, radial and shear stresses along the hole boundary were plotted against the radial angle and found to compare well with the analytical results (Figs. 8 and 9).

## 4.3  Application of the Hybrid Technique to Estimate Static, and Dynamic Coefficients of Friction

This technique basically consists of applying the loading, prescribing the displacements from moire analysis to the hole boundary and prescribing other boundary conditions as before. Thus only the plate is discretized for this analysis, without the pin, and the mesh

129

used is shown in Fig. 10. The stresses along the boundary are obtained
from the analysis and are shown in Figs. 11 and 12 plotted against the
radial angle. Thus the shear stress $\tau_{r\theta}$ and the radial stress $\sigma_{rr}$ show
remarkable resemblence to the stresses given by Joh [2] at a load level
of 1840 lbs.

In order to assess the friction coefficient values, to be used for
the regular finite element analysis, $\tau_{r\theta}/\sigma_{rr}$ ratio was plotted against
the radial angle for load increasing and decreasing phases and the
result is given in Fig. 13. In the load increasing phase nearly all
contact is associated with slip and the maximum ratio of $\tau_{r\theta}/\sigma_{rr}$ cannot
exceed the dynamic friction coefficient and thus $\mu_d = 0.25$ is a rational
choice. The negative ratio is maximum between 55° and 60°, where the
transition from slip to stick occurs and thus $\mu_s = 0.35$ is chosen to be
the static friction coefficient.

## 4.4 Analysis of Failure in Mechanical Joints

A composite laminate $(0°/\pm45°/90°)_s$ with laminae of the following
properties has been used for these studies:

| | | |
|---|---|---|
| $E_1 = 19.1 \times 10^3$ ksi | $X_T = 229.4$ ksi | $T = 17.3$ ksi |
| $E_2 = 2.0 \times 10^3$ ksi | $Y_T = 10.1$ ksi | |
| $G_{12} = 0.9 \times 10^3$ ksi | $X_C = 252.1$ ksi | |
| $\nu_{12} = 0.3$ | $Y_C = 32.0$ ksi | |

It has been established that certain configurations favor certain modes
of failure [18]. This fact has been used in determining the plate
configurations for studying bearing failure (Mesh F, Fig. 14), shearout
failure (Mesh G, Fig. 15) and tensile failure (Mesh H, Fig. 16).

The analysis has been carried out and normalized radial and
circumferential strain curves have been produced for each failure

mode. Failure is indicated by the increased strains given by a nonlinear model incorporating Tsai-Hill criterion as compared to a linear elastic model. Results are shown in Figure 17 for bearing failure, Fig. 18 for shearout failure and Fig. 19 for tensile failure. The Tsai-Hill criterion used in this study is,

$$(\frac{\sigma_1}{X})^2 + (\frac{\sigma_2}{Y})^2 + (\frac{\sigma_3}{Z})^2 - (\frac{1}{X^2} + \frac{1}{Y^2} - \frac{1}{Z^2})\sigma_1\sigma_2 - (\frac{1}{Y^2} + \frac{1}{Z^2} - \frac{1}{X^2})\sigma_2\sigma_3$$

$$- (\frac{1}{Z^2} + \frac{1}{X^2} - \frac{1}{Y^2})\sigma_1\sigma_3 + (\frac{\sigma_4}{R})^2 + (\frac{\sigma_5}{S})^2 + (\frac{\sigma_6}{T})^2 \geq 1$$

where X, Y are either compressive ($X_c$, $Y_c$) or tensile ($X_T$, $Y_T$) strengths and T is the shear strength in the xy plane.

## 5. SUMMARY AND CONCLUSIONS

The mixed finite element model developed in [1] has been modified by incorporating a realistic interface friction conditions and a solution procedure. A dynamic as well as a static friction coefficient were used to analyze a pin-loaded plate problem for which experimental results are available. The new solution algorithm not only provides flexibility in numbering the nodes but also avoids the halt of computation due to the appearance of small terms on the leading diagonal, during the analysis. An accurate contact stress analysis is essential in some applications such as the study of failure in bolted joints of laminated composites and some example problems have been studied in this area.

It is possible to extend the capabilities of the present model even further by adopting an Eulerian-Lagrangian formulation. This will simplify the analysis of problems, such as cracks emanating from bolted joints by several orders of magnitude.

## REFERENCES

1. Heyliger, P. R. and Reddy, J. N., "A Mixed Computational Algorithm for Plane Contact Problems," Computers & Structures, Vol. 26, No. 4, pp. 621-653, 1987.

2. Joh, D., "An Experimental Study of Frictional Phenomena Around the Pin Joints of Plates Using Moire Inferometry," Ph.D. Dissertation, Department of Engineering Science and Mechanics, Virginia Polytechnic Institute and State University, Blacksburg, VA, 1986.

3. Mirza, F. A., "A Solution Technique for Indefinite Systems of Mixed Finite Elements," International Journal of Numerical Methods in Engineering, Vol. 20, pp. 1555-1561, 1981.

4. Haber, R. B., "A Mixed Eulerian-Lagrangian Displacement Model for Large-Deformation Analysis in Solid Mechanics," Computer Methods in Applied Mechanics and Engineering, Vol. 43, pp. 277-292, 1984.

5. Haber, R. B. and Hariandja, B. H., "An Eulerian-Lagrangian Finite Element Approach to Large-Deformation Frictional Contact," Computers and Structures, Vol. 20, No. 1-3, pp. 193-201, 1985.

6. Koh, H. M. and Haber, R. B., "Elastodynamic Formulation of the Eulerian-Lagrangian Kinematic Description," Journal of Applied Mechanics, Vol. 53, pp. 839-845, December 1986.

7. Hyer, M. W. and Klang, E. C., "Contact Stresses in Pin-Loaded Orthotropic Plates," Report No. CCMS 84-02 and VPI-E-84-14, Virginia Polytechnic Institute and State University, Blacksburg, VA, April 1984.

8. Hyer, M. W., Klang, E. C. and Cooper, D. E., "The Effects of Pin Elasticity, Clearance and Friction on the Stresses in a Pin-Loaded Orthotropic Plate," Journal of Composite Materials, Vol. 21, pp. 190-206, March 1987.

9. Mangalgiri, P. D., "Pin-Loaded Holes in Large Orthotropic Plates," AIAA Journal, Vol. 22, pp. 1478-1484, October 1984.

10. Mangalgiri, P. D. and Dattaguru, B., "Elastic Analysis of Pin Joints in Composite Plates," Aeronautics Research and Development Board, Govt. of India, New Delhi, Rept. ARDB-STR-5014, Nov. 1980.

11. Oplinger, D. W. and Gandhi, K. R., "Analytical Studies of Structural Performance in Mechanically Fastened Composite Plates," Army Materials and Mechanics Research Center, Watertown, MA, Report M574-8, pp. 221-240, 1974.

12. Oplinger, D. W., "On the Structural Behavior of Mechanically Fastened Joints in Composites Materials," Proceedings of the Conference of Fiber Composites in Structural Design, California, pp. 575-502, 1978.

13. Lekhnitskii, S. G., *Anisotropic Plates*, Translated from Russian, Gordon and Breach Science Publishers, New York, 1968.

14. Mushkhelishvili, N. I., *Some Basic Problems of the Mathematical Theory of Elasticity*, Translated from Russian by J. R. M. Radok, Noordhoff, Groningen, Netherlands, 1963.

15. Chang, F. K., Scott, R. A. and Springer, G. S., "Strength of Mechanically Fastened Composite Joints," University of Michigan, AFWAL-TR-82-4095, July 1982.

16. Collings, T. A., "On the Bearing Strengths of CFRP Laminates," *Journal of Composite Materials*, Vol. 13, No. 3, pp. 241-252, 1982.

17. Garbo, S. P. and Ognowski, M., "Effect of Variances and Manufacturing Tolerances on the Design Strength and Life of Mechanically Fastened Composite Joints," McDonnell Douglas, AFFDL-TR-81-3041, St. Louis, MO, April 1981.

18. York, J. L., Wilson, D. W. and Pipes, R. B., "Analysis of the Net Tension Failure Mode in Composite Bolted Joints," *Journal of Reinforced Plastics and Composites*, Vol. 1, April 1982.

19. Whitney, J. M. and Nuismer, R. J., "Stress Fracture Criteria for Laminated Composites Containing Stress Concentrations," *Journal of Composite Materials*, Vol. 8, pp. 253-265, July 1974.

20. Wilson, D. W. and Pipes, R. B., "Analysis of the Shearout Failure Mode in Composite Bolted Joints," *Proceedings of the International Conference on Composite Structures*, Marshall I. H. (Ed.), Applied Science Publishers, 1981.

21. Tsiang, T. H., "Damage Development in Fiber Composites due to Bearing, Sc.D. Thesis, Department of Materials Science and Engineering, MIT Cambridge, MA, February 1983.

22. Tsiang, T. H. and Mandell, J. F., "Bearing/Contact for Anisotropic Materials, *AIAA Journal*, pp. 1273-1277, August 1985.

23. Tsiang, T. H. and Mandell, J. F., "Damage Development in Bolt Bearing of Composite Laminate," *AIAA Journal*, pp. 1570-1577, October 1985.

24. Reddy, J. N. and Pandey, A. K., "A First-Ply Failure Analysis of Composite Laminates," *Computers & Structures*, Vol. 25, No. 3, pp. 371-393, 1987.

Number of nodes = 286

Number of elements = 236   (linear)

$E_1$ = 10,400 ksi

$E_2$ = 10,400 ksi

$G_{12}$ = 3,910 ksi

$\nu_{12}$ = 0.33

Radius of the hole = 0.375 in.

Radius of the pin = 0.3745 in.

a = 1.495 in., b = 7.005 in.,

c = 1.5 in., plate thickness = 0.06 in.
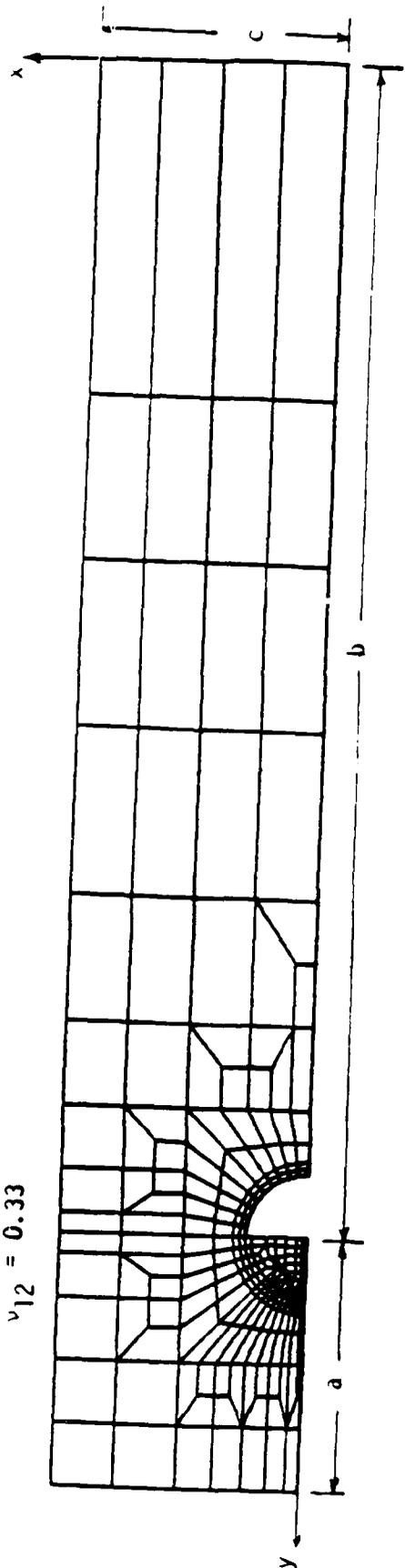
Figure 1.  Mesh A for the pin-loaded aluminum plate (pin is also made of aluminum).

134
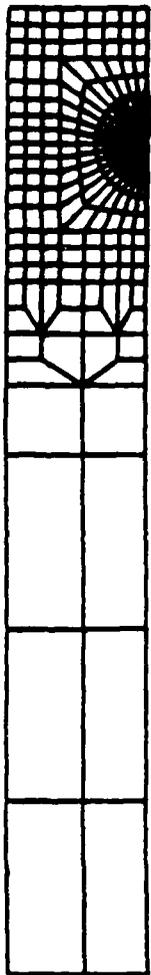
Number of nodes = 391

Number of elements = 332 (linear)
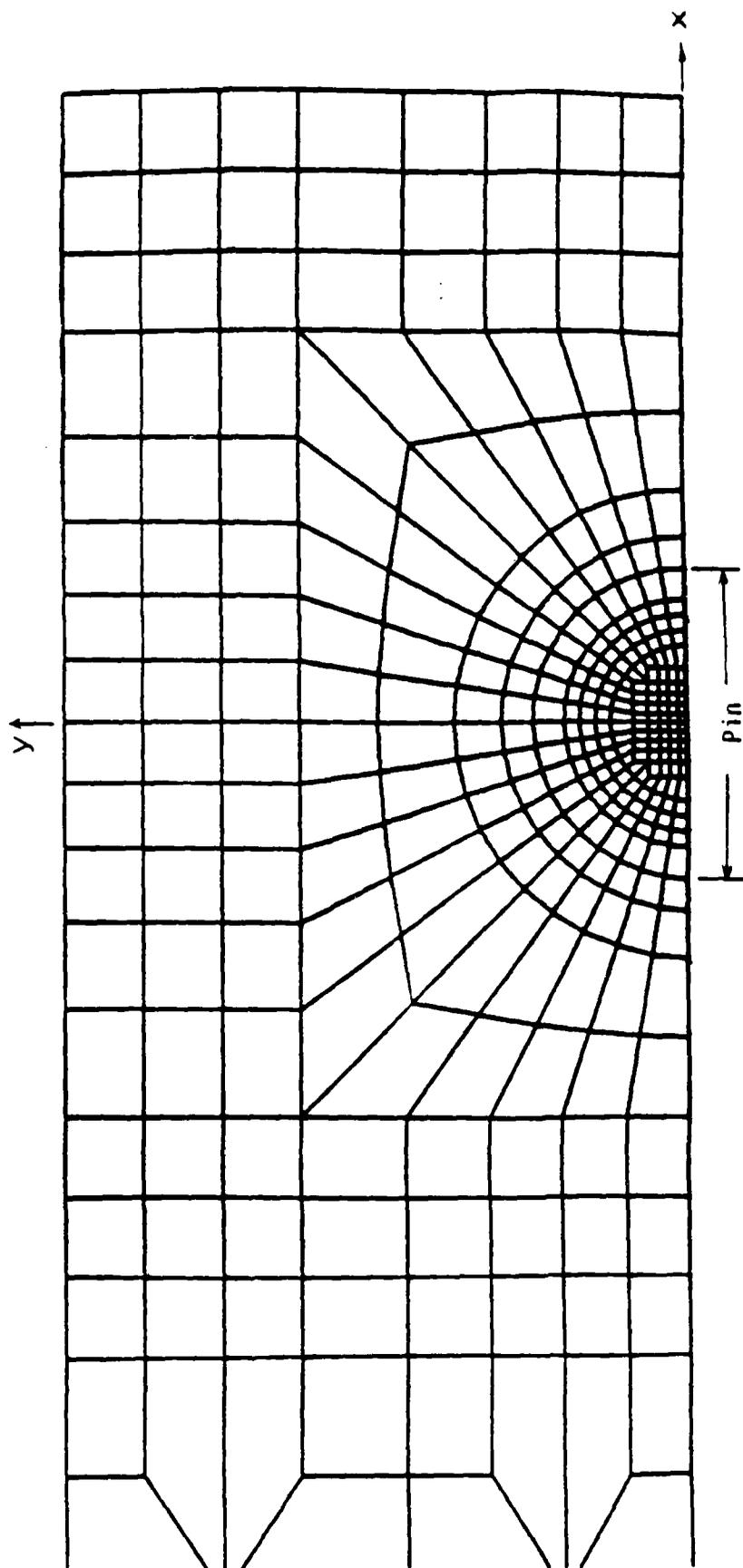
Figure 2. Mesh B for the pin-loaded aluminum plate.

135
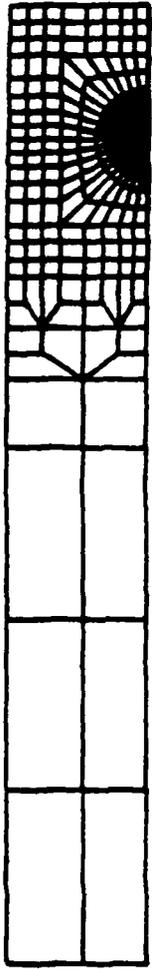
Number of elements = 540

Number of nodes = 452
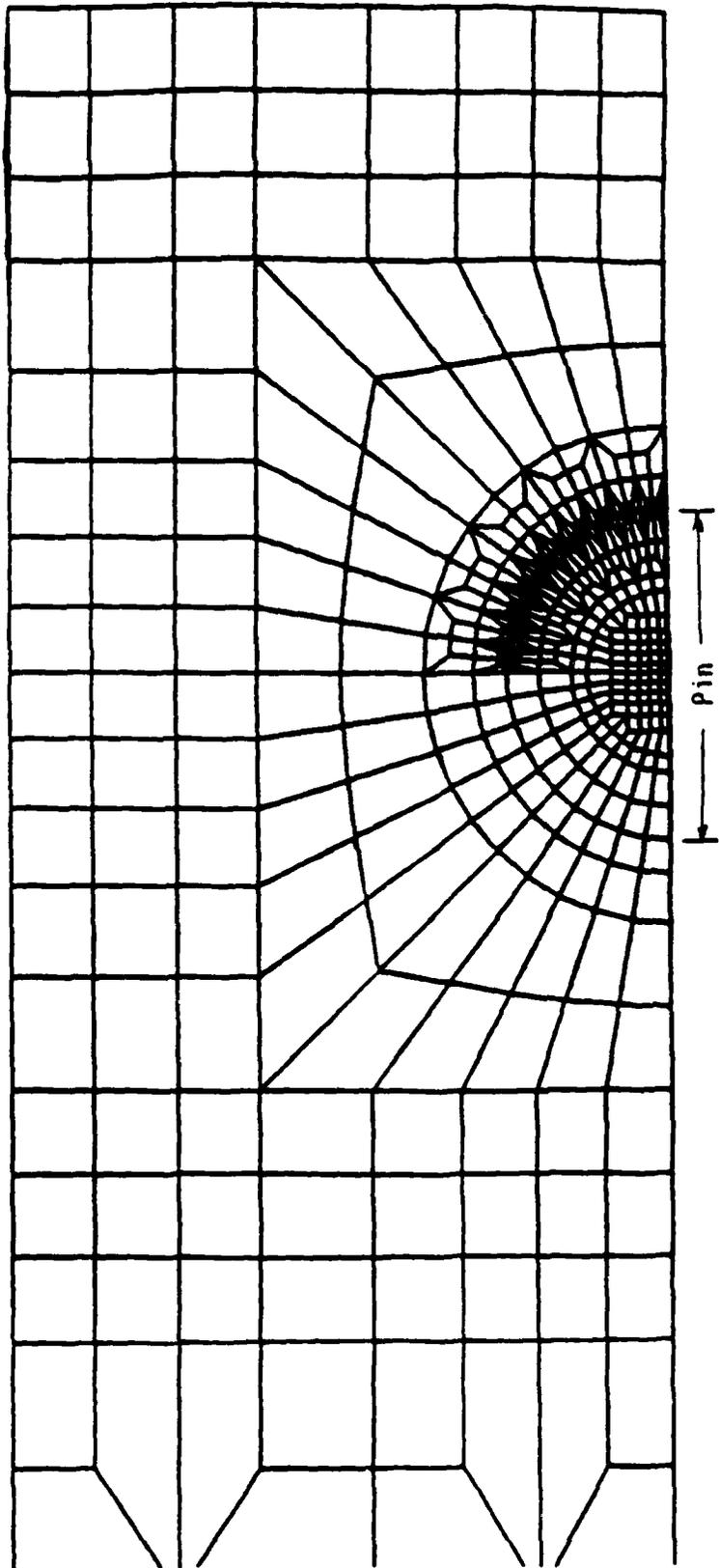
Figure 3. Mesh C for the pin-loaded aluminum plate

Pin

136
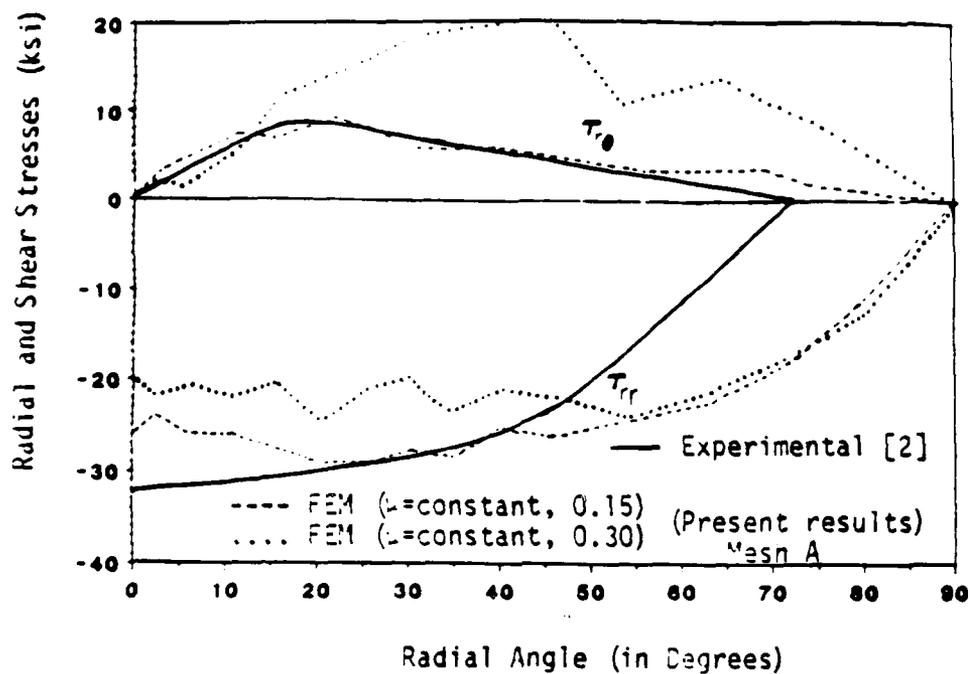
Figure 4. Comparison of the experimental and finite element
results for load-increasing phase at load level 1240 lbs.
(the FEM scheme used is that originally developed in [1]).

137
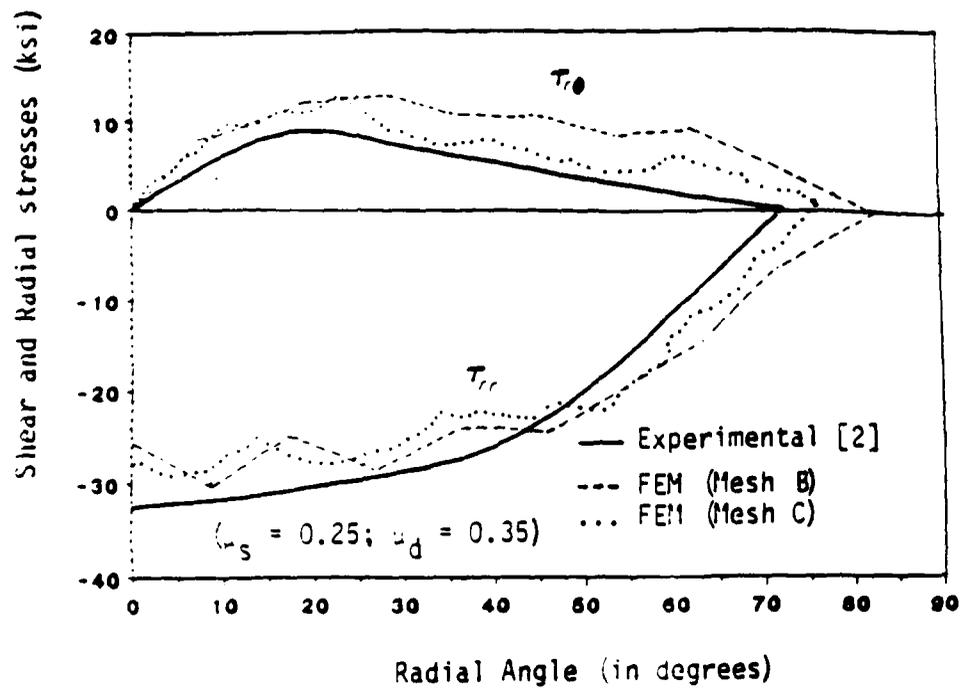
Figure 5. Comparison of the experimental and finite element results (the FEM scheme used is the modified version of the scheme developed in [1]; Load increasing phase at load level 1240 lbs.).

138
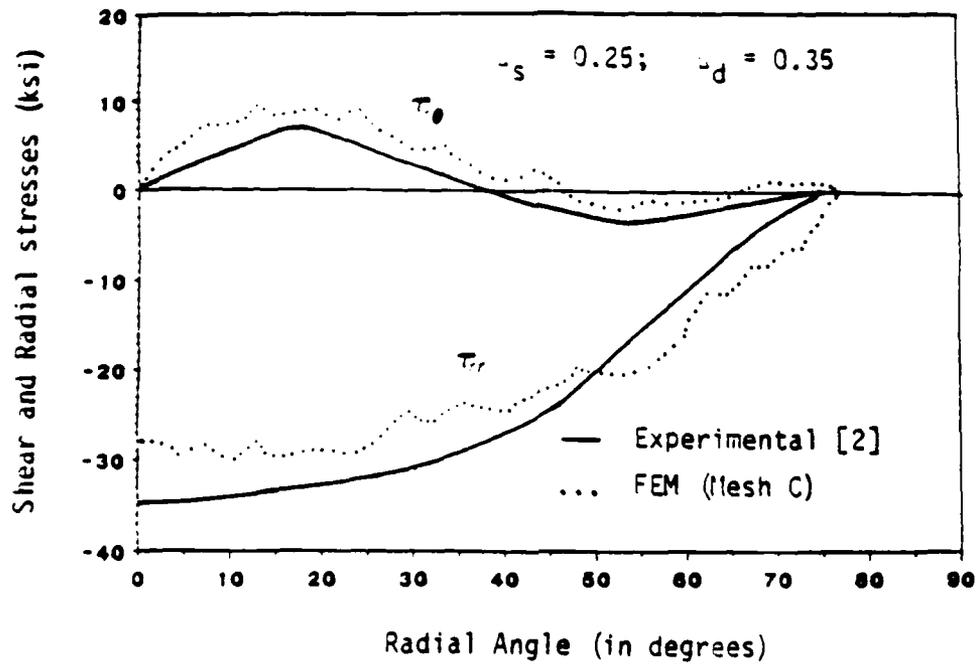
Figure 6. Comparison of the experimental and finite element
results (the FEM scheme is the modified version)
for the load decreasing phase at load level 1210 lbs.

139

Plate
properties:

$E_1 = 12,400$ ksi

$E_2 = 3,730$ ksi

$G_{12} = 3,210$ ksi

$\nu_{12} = 0.66$

Radius of plate hole = 1 in.
Radius of pin = 1 in.

a = 4 in., b = 2 in., thickness of plate = 1 in.

Pin is made of steel

Number of nodes = 509
Number of elements = 426
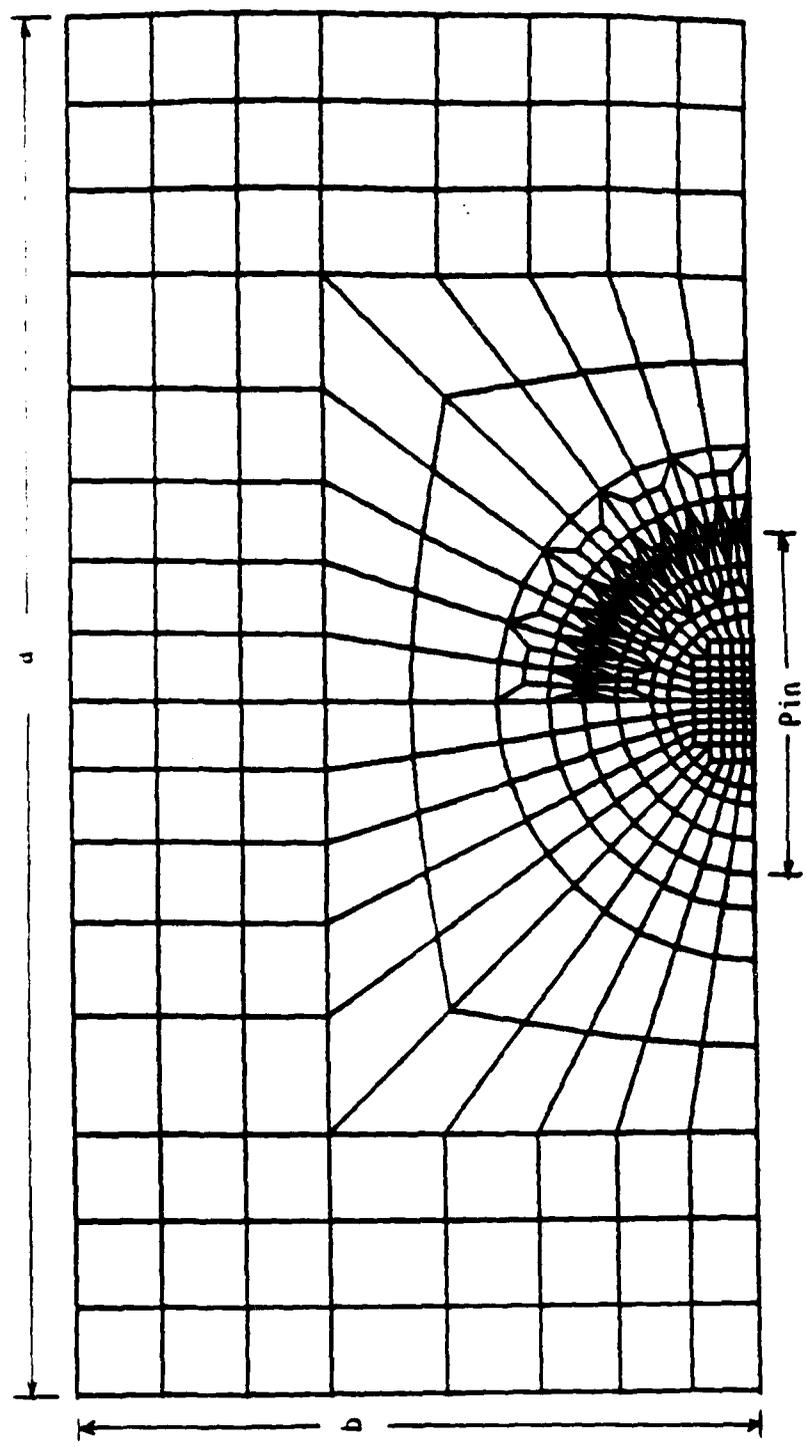


Figure 7. Mesh D for the pin-loaded orthotropic plate.

140
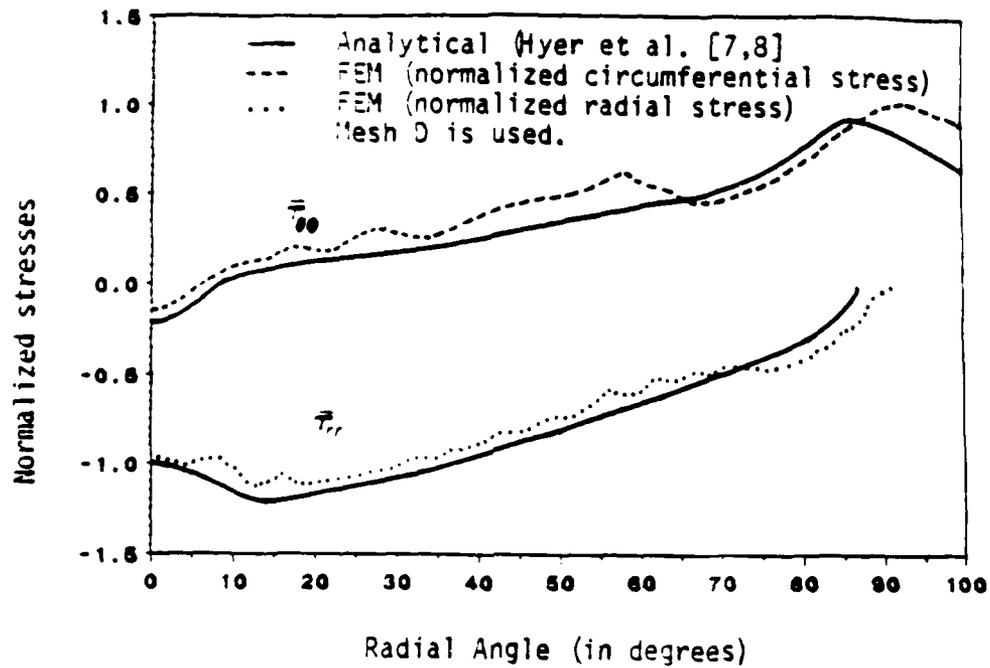
Figure 8. Comparison of the analytical and finite element results for the pin-loaded orthotropic plate. The stress is normalized with respect to the average bearing stress (81.9 ksi).

141
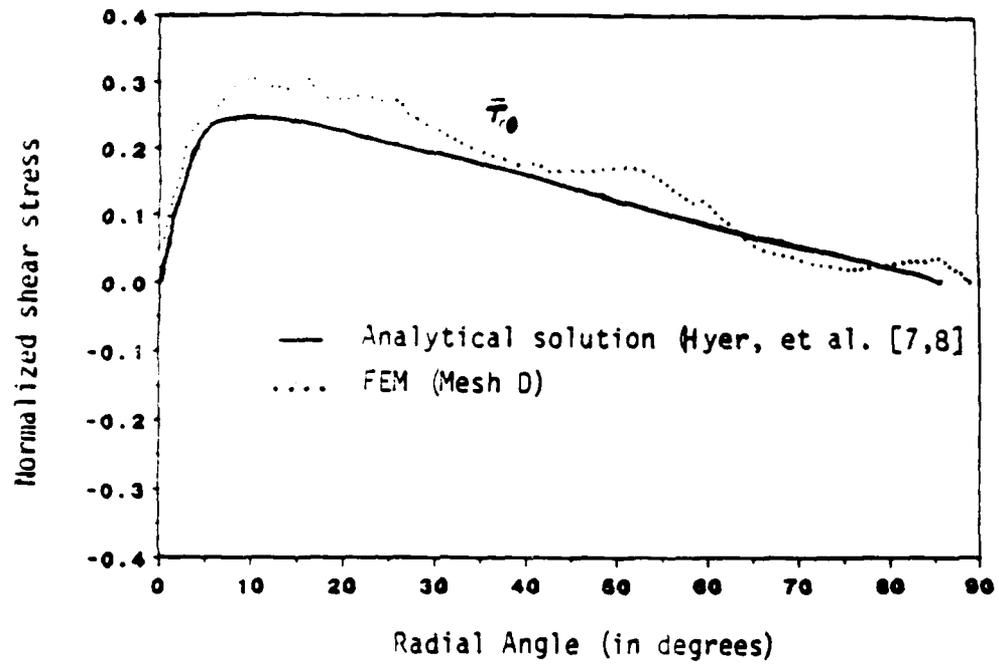
Figure 9. Comparison of the analytical and finite element solutions for the pin-loaded orthotropic plate (stress is normalized with respect to the average bearing stress, 81.9 ksi.).

142
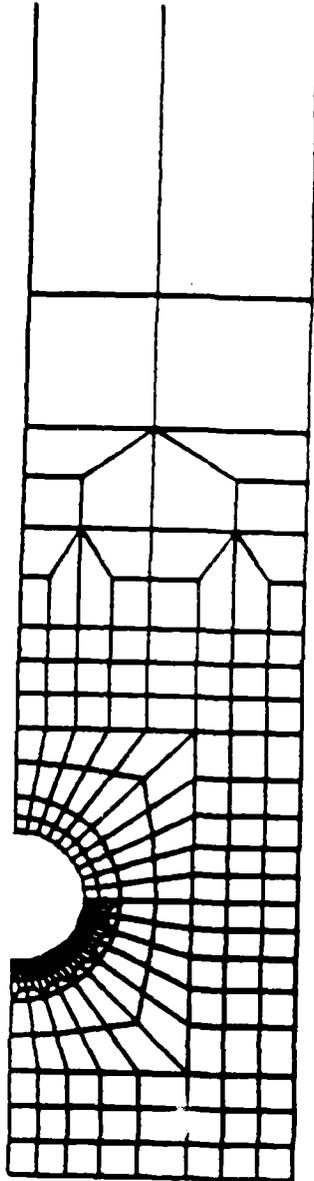
Figure 10. Mesh E used for hybrid (experimental/numerical) study of the pin-loaded plate problem.
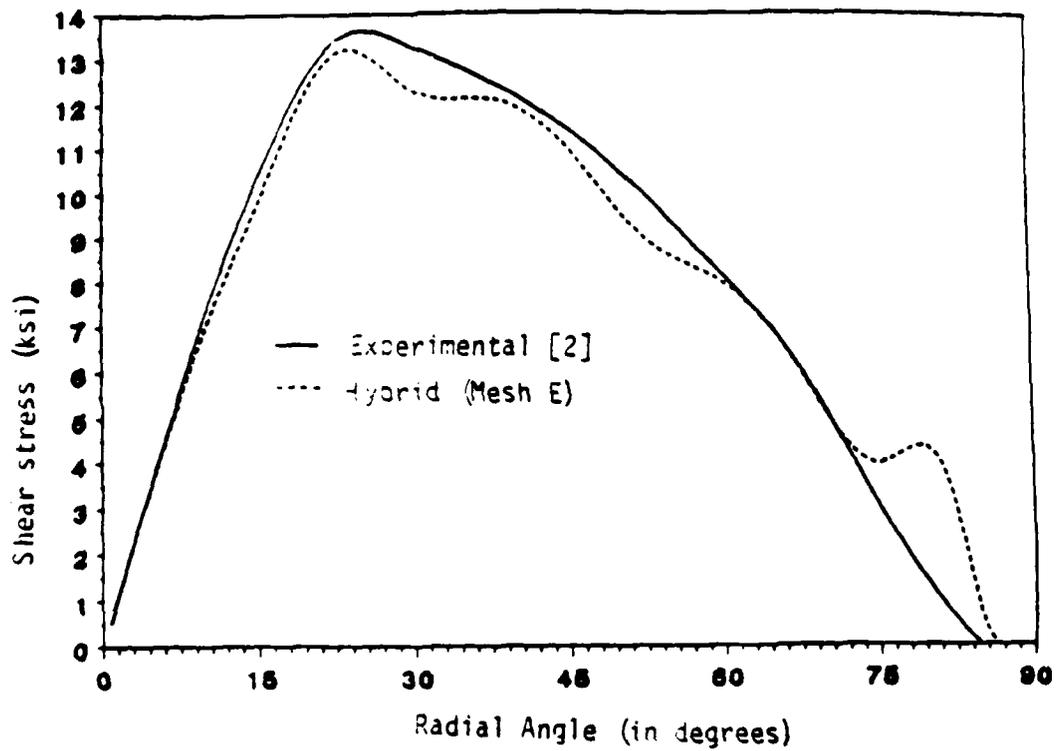
Figure 11. Comparison of the shear stress distributions
obtained in the experiment and hybrid analysis
of the pin-loaded aluminum plate (load increasing
phase at load level 1840 lbs).

144
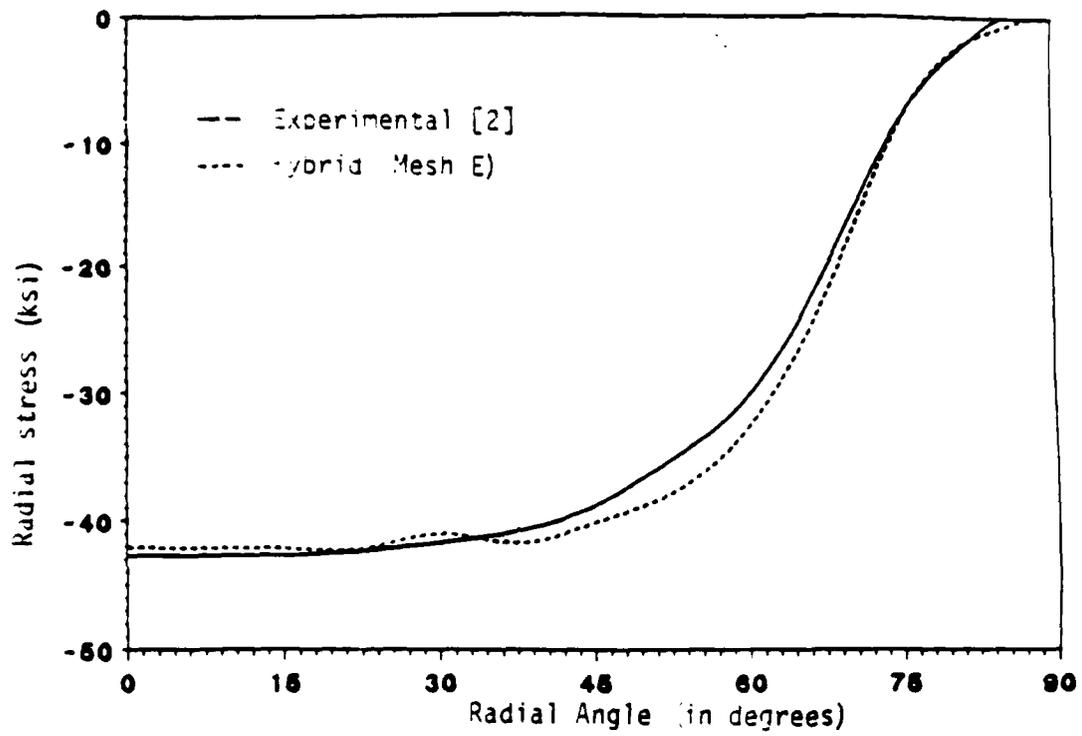
Figure 12. Comparison of the radial stress distributions obtained in the experiment and hybrid analysis of the pin-loaded aluminum plate (load=1840 lbs).
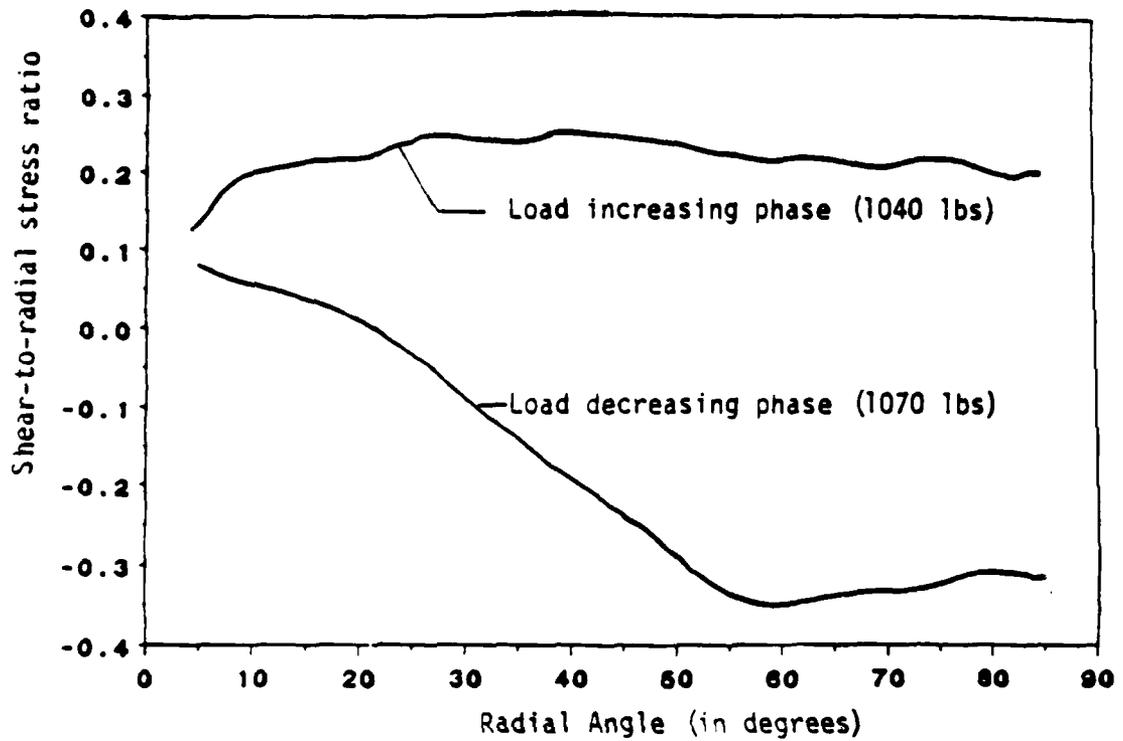
Figure 13. Variation of the ratio of shear stress-to-radial stress for load increasing and load decreasing phases of the pin-loaded aluminum plate (results obtained using the hybrid technique).
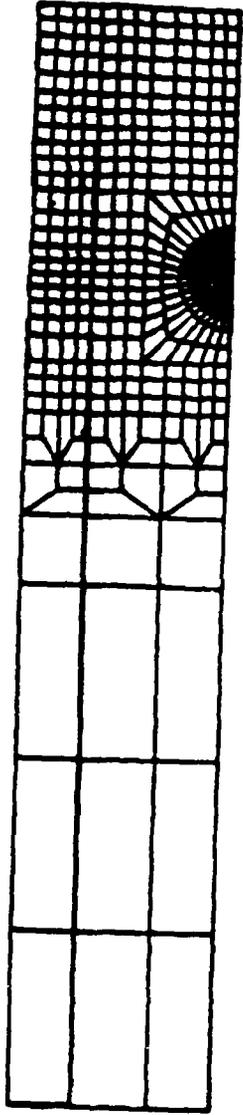
Figure 14. Mesh used for the bearing failure in a mechanical joint.
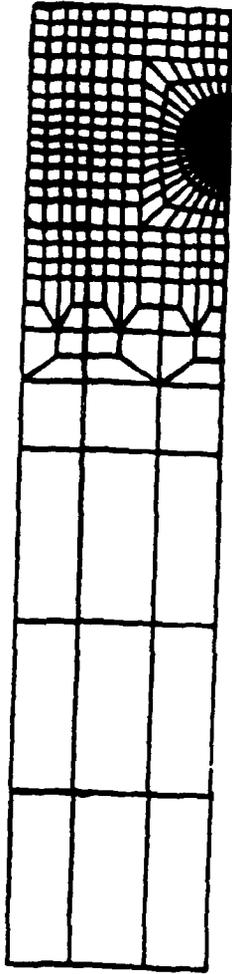
Figure 15. Finite element mesh G used for shearout and bearing failure in composite joints.

Figure 16. Finite element mesh H used in tensile failure of composite joints.
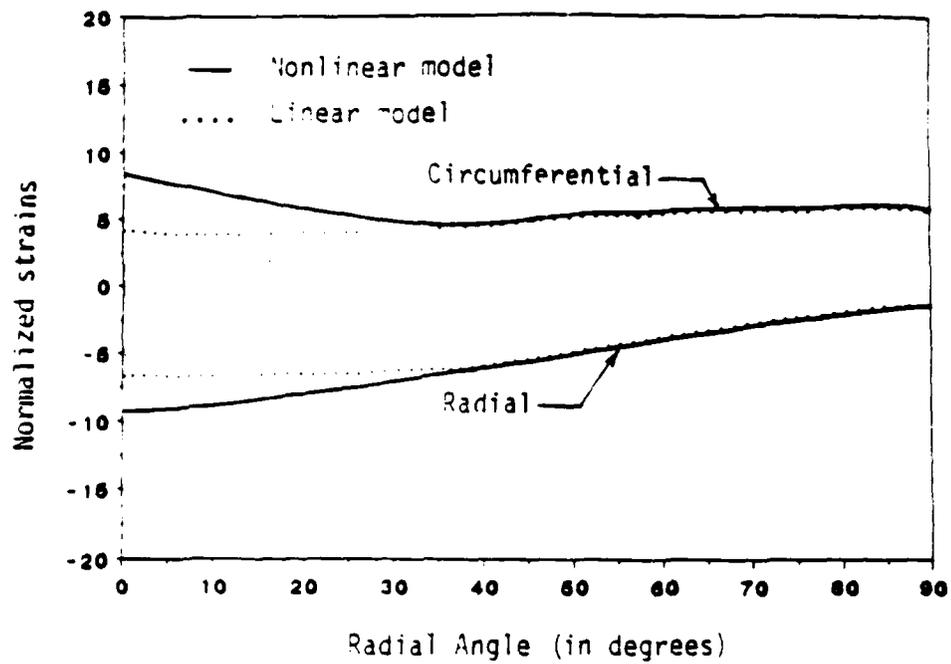
Figure 17. Radial and cicumferential strains in an orthotropic
plate (the linear and nonlinear models show separation
indicating bearing failure from $\theta=0°$ to $\theta=35°$).

148
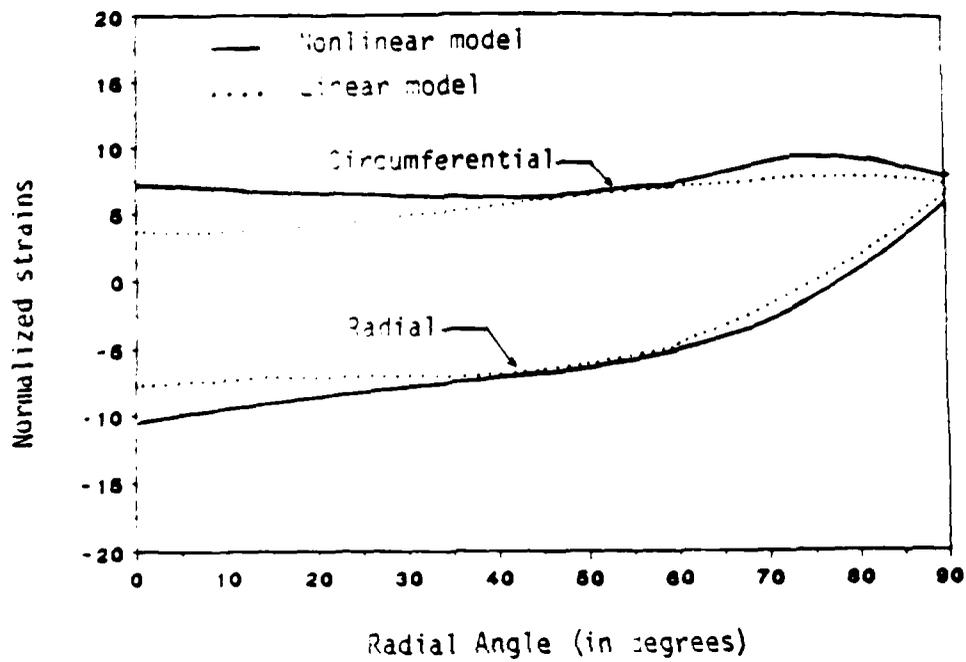
Figure 18. Radial and circumferential strains in an orthotropic plate ( bearing failure: =0° to 35°; shearout failure: = 60° to 80°).

# GENERAL SUMMARY AND CONCLUSIONS

The initial experiments on the aluminum plate provided essential information for the development and refinement of the general numerical analysis of plane elastic contact problems. Specifically, the experiments provided coefficients of friction and stress distributions for comparative purposes. Displacement data were also combined with the finite element method to produce a hybrid solution for the pin-loaded aluminum plate. From these interactions of experimental and numerical studies a general algorithm for plane elastic contact problems has emerged. This now includes the provision for both static and dynamic coefficients of friction. The path has also been paved for the analysis of problems involving severe deformation and fracture in anisotropic materials.

Two new experiments have been performed on the aluminum plate and a graphite-epoxy composite. The second aluminum specimen was tested to provide a closer approximation to the two-dimensional stress state required in the analysis. A further innovation, which allowed closer study of the stresses at the contact boundary, was the use of a zero-thickness gratings. In conjunction with a localized hybrid analysis, comprehensive stress distributions have been obtained for the loading and unloading parts of the load cycle. Certain analytically predicted behavior has been confirmed and some surprisingly large stress gradients have been discovered.

Ideally, a comparison of the new experimental results and those predicted from the refined algorithm should be made. Time and resource limitations prevent a comprehensive comparison. However, the radial and shear stresses obtained using Mesh B in Fig. 5 for a load of 1240 lb

(with $u_x = 0.25$ and $u_d = 0.35$) have been compared with those from the second experiment on the aluminum plate in Fig. A. It may be seen that the radial stresses are in close agreement near the point of first contact. The agreement is less good near the end of the contact zone. The shear stresses appear to be overestimated in the numerical analysis. This may be a direct result of assuming values of $u_s$ and $u_d$ which were larger than those operating in the second experiment. The lack of agreement in the peak shear stresses and the departure of the radial stresses away from the point of first contact is consistent with and a consequence of the overestimate of the shear stresses in the numerical analysis.

The experiment on the quasi-isotropic composite plate highlighted important differences between it and the isotropic aluminum. Most surprising was the difference in the shear stress distribution at the surface of contact. Analytical studies do not predict such differences but other experimental studies of lesser sensitivity than moire interferometry indicate similar inconsistencies.

The study of the composite plate included a failure analysis which used the experimentally determined displacement and stress distributions to identify and locate the failure modes. This experiment provides potentially ideal data for validation and assessment of the new Eulerian-Lagrangian algorithm presented in this report.
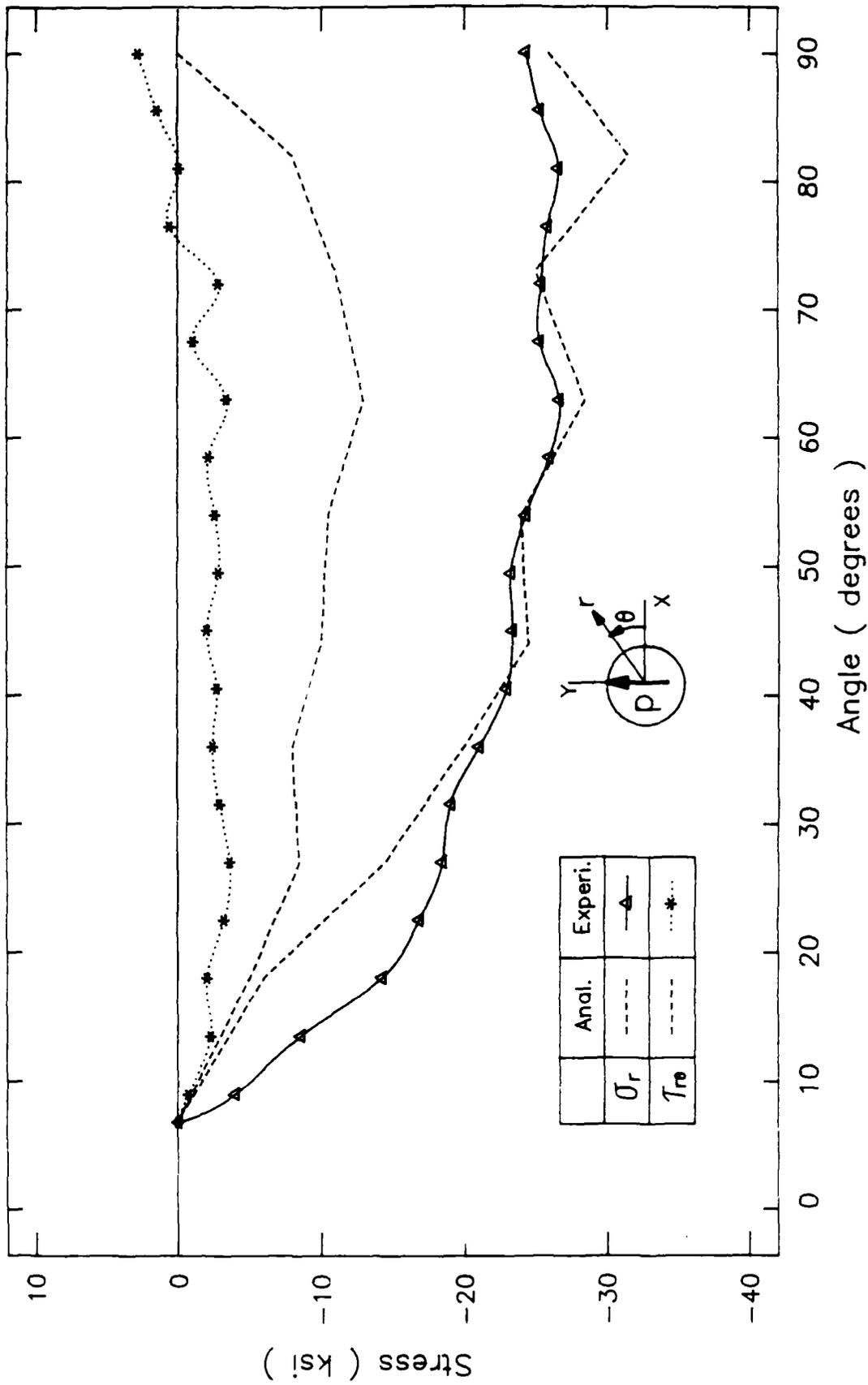
Fig. A. Comparison of updated numerical results and those of the aluminum experiment. The numerical results are based upon assumed values of $\mu_s = 0.35$ and $\mu_d = 0.25$.

APPENDIX A

Fringe patterns for the aluminum specimen

1) U-field, load increasing phase, P = 25 lb

154

2) V-field, load increasing phase, P = 25 lb

3) U-field, load increasing phase, P = 250 lb
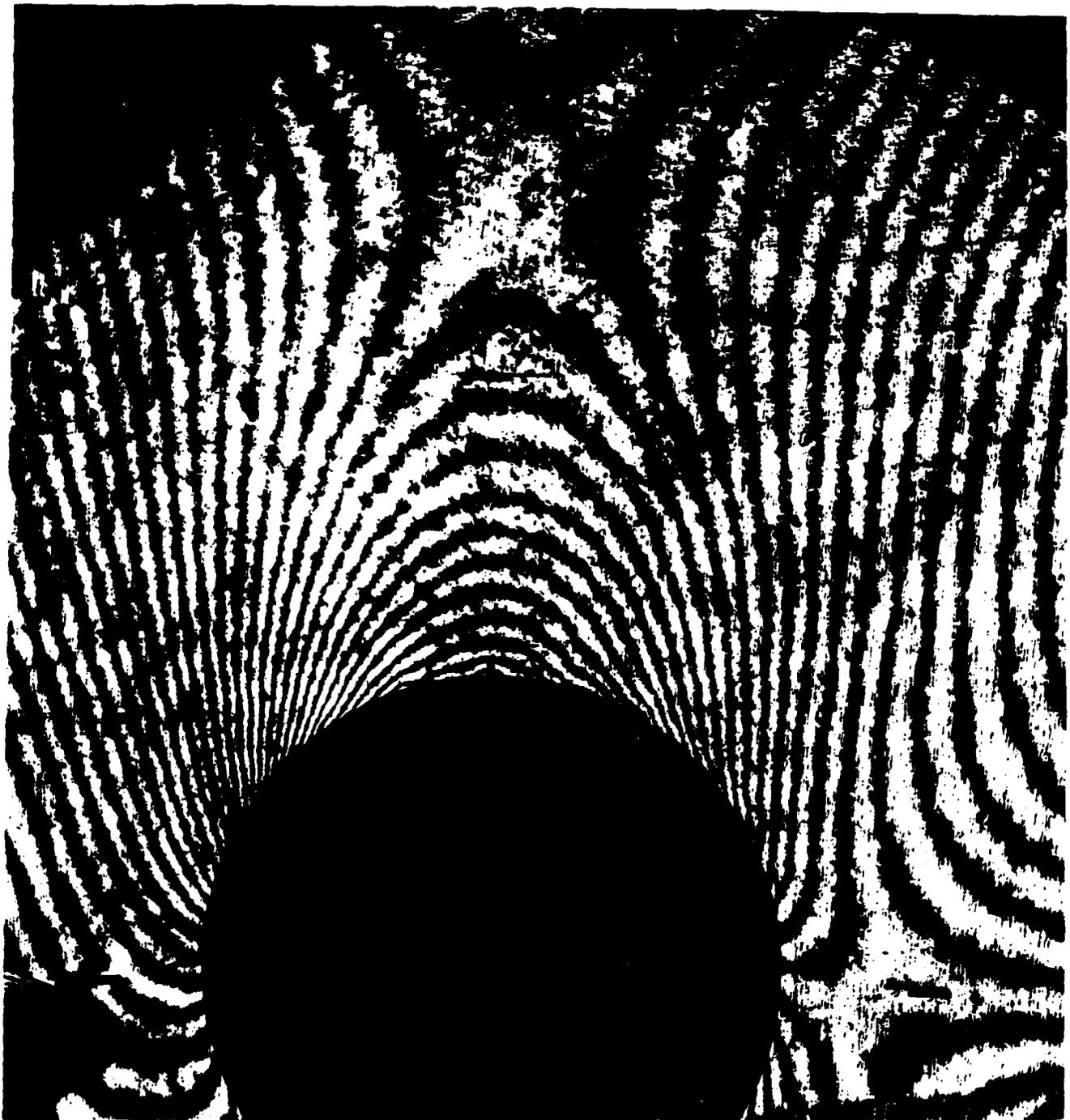
4) V-field, load increasing phase, P = 250 lb

5)  U-field, load increasing phase, P = 500 lb

158

6) V-field, load increasing phase, P = 500 lb

159

7) U-field, load increasing phase, P = 750 lb

8)  V-field, load increasing phase, P = 750 lb

161
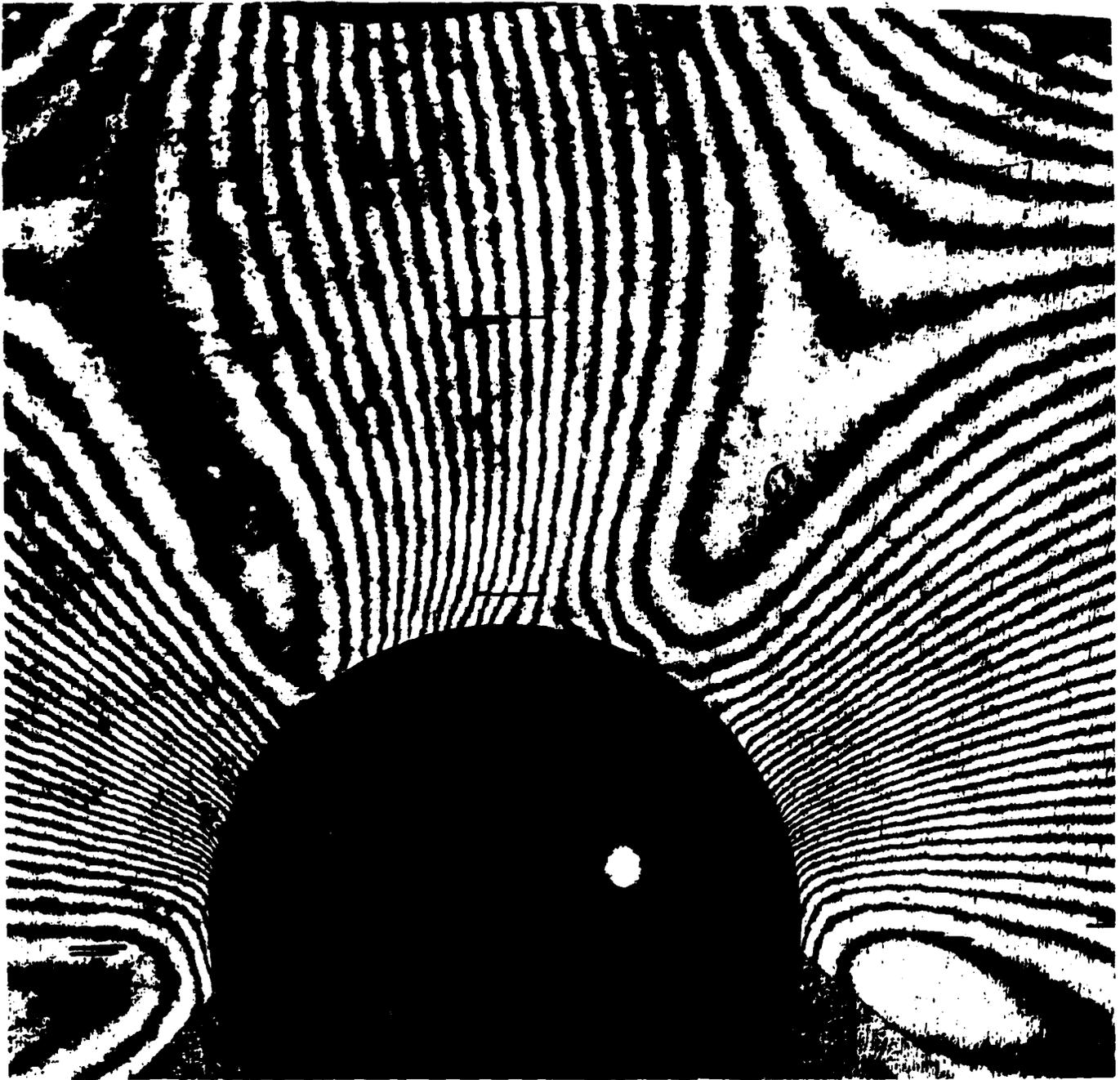
9) U-field, load increasing phase, P = 1000 lb

10) V-field, load increasing phase, P = 1000 lb

11) U-field, load increasing phase, P = 1250 lb

164
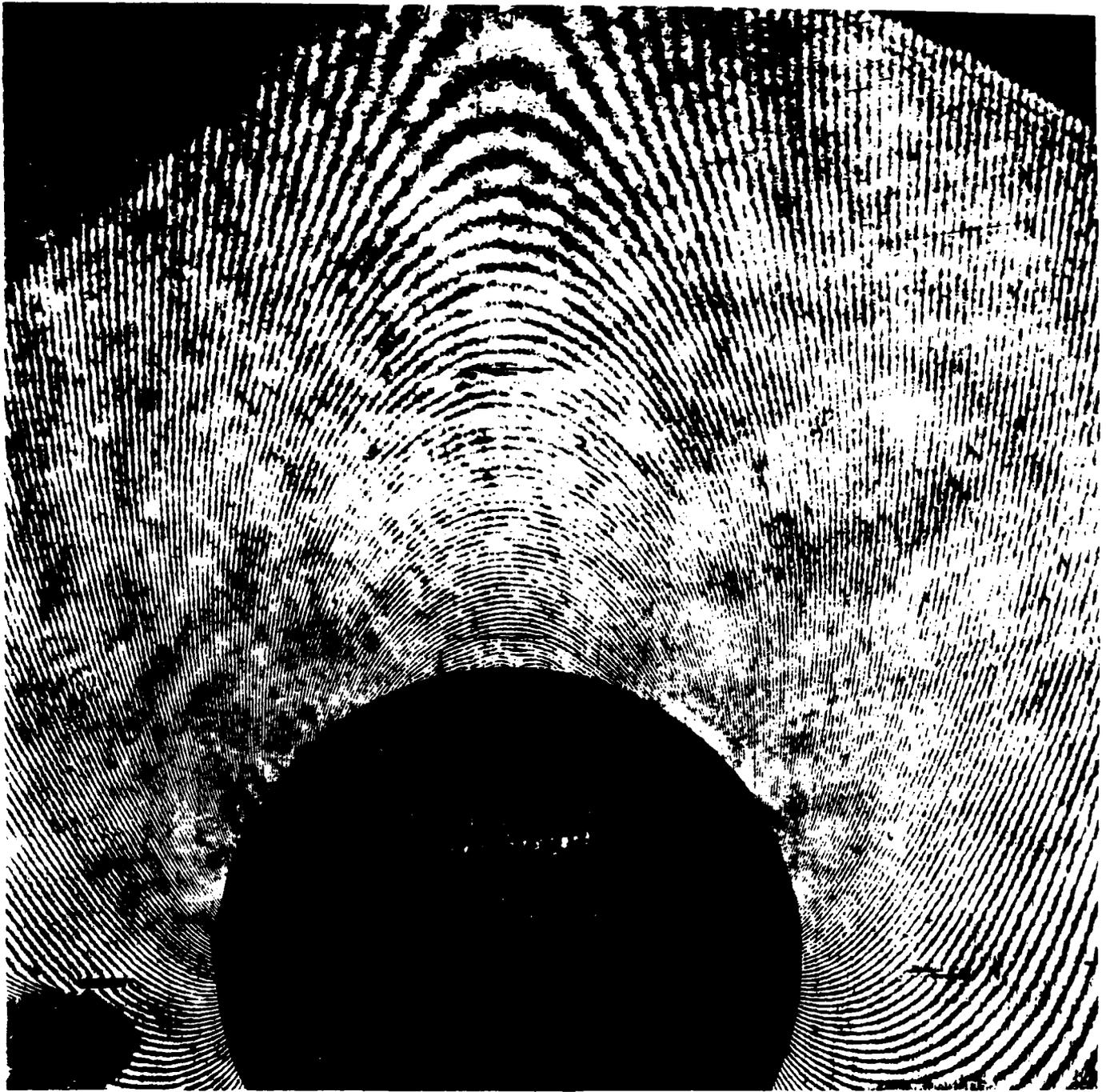
12) V-field, load increasing phase, P = 1250 lb
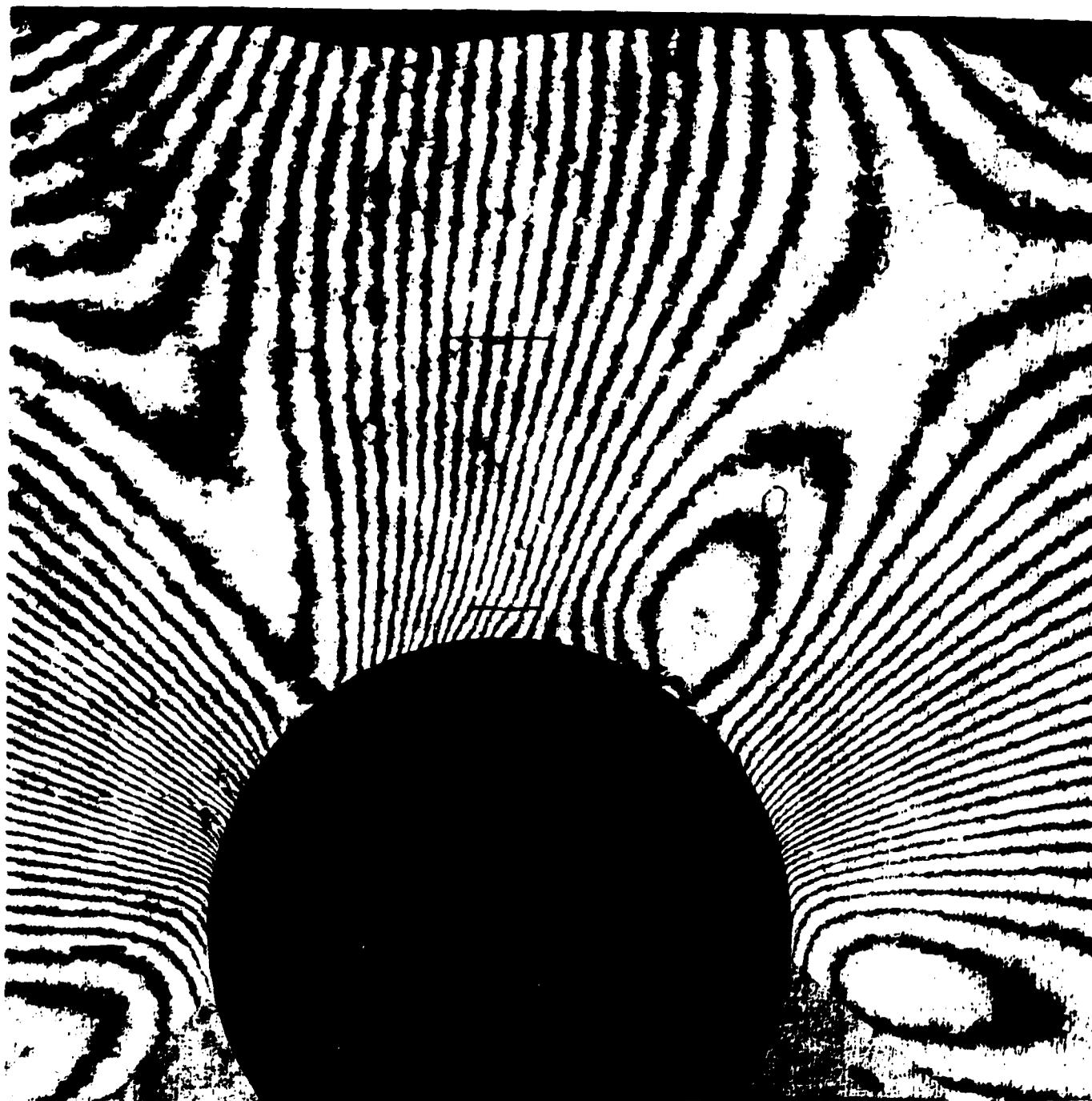
13) U-field, load decreasing phase, P = 1000 lb
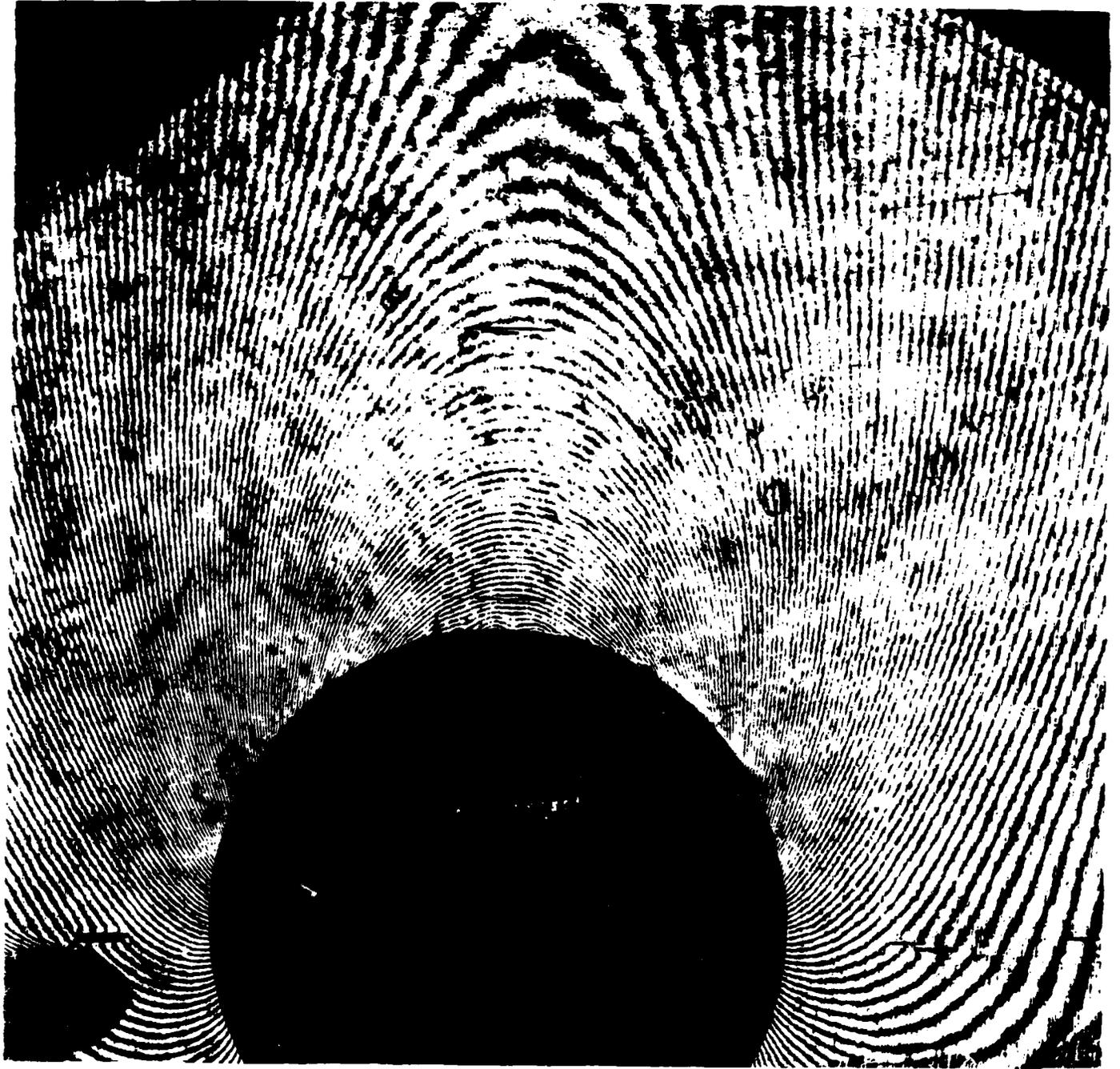
14) V-field, load decreasing phase, P = 1000 lb
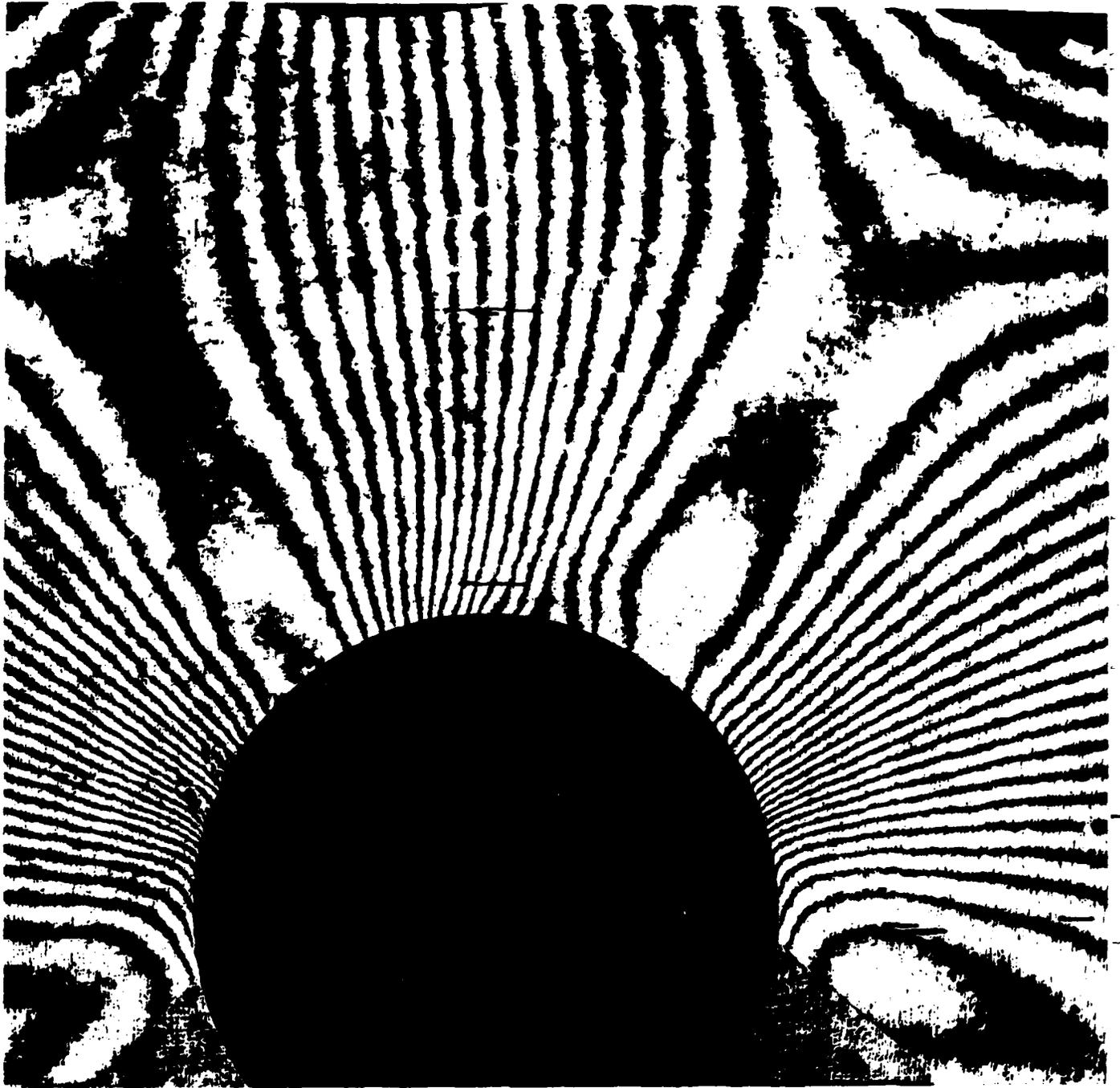
15)  U-field, load decreasing phase, P = 750 lb

168
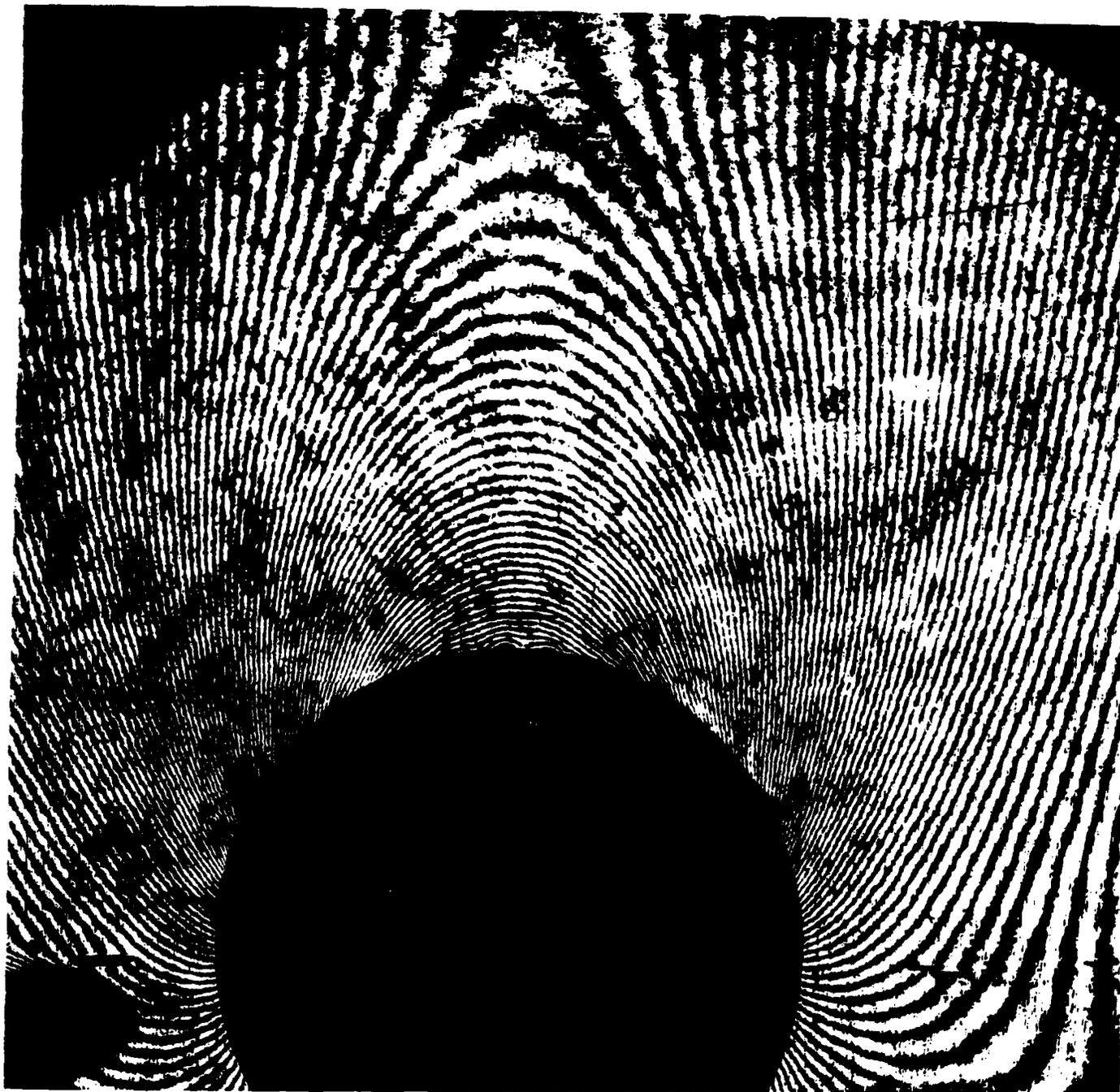
16) V-field, load decreasing phase, P = 750 lb
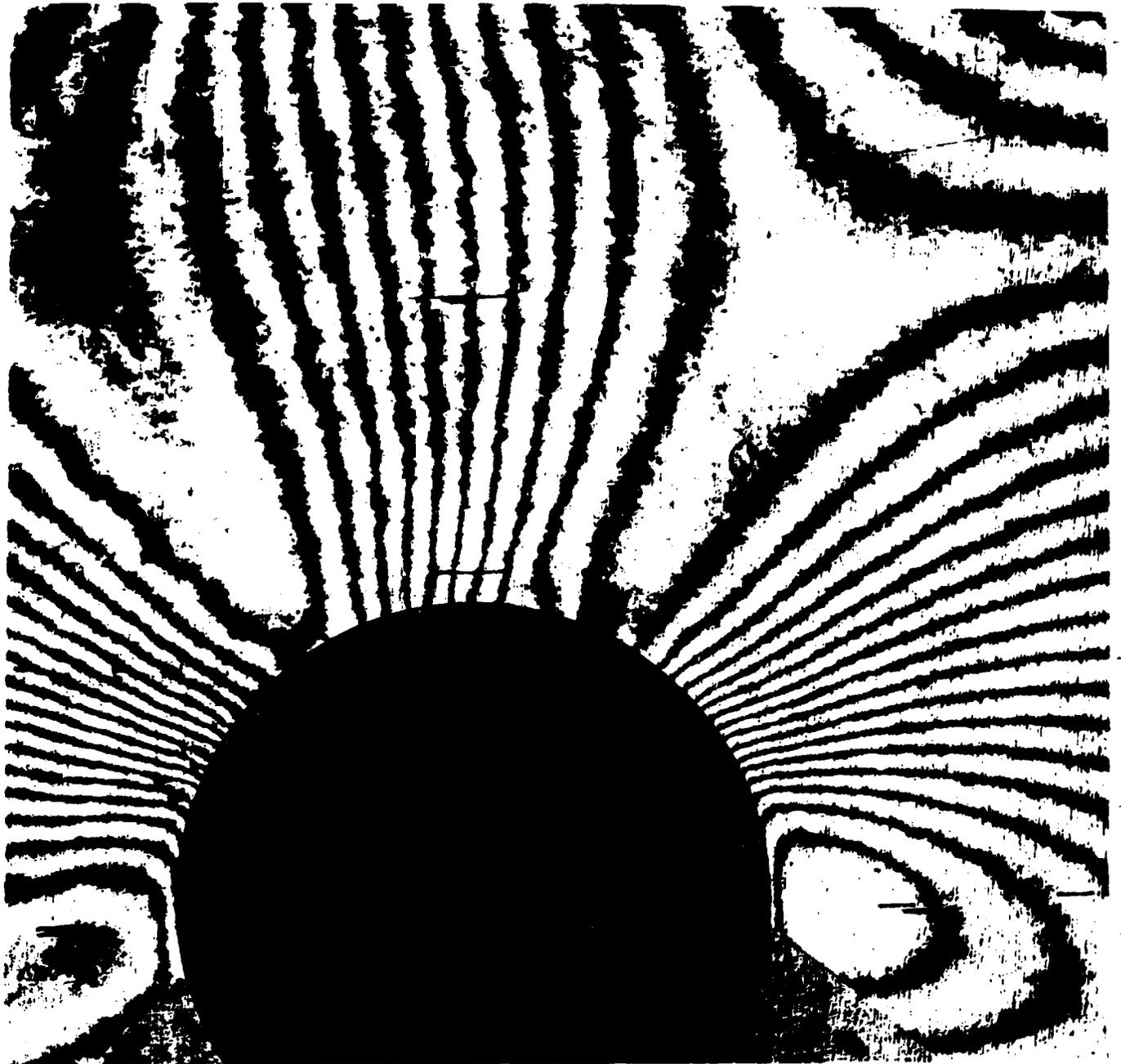
17) U-field, load decreasing phase, P = 500 lb

18) V-field, load decreasing phase, P = 500 lb

171
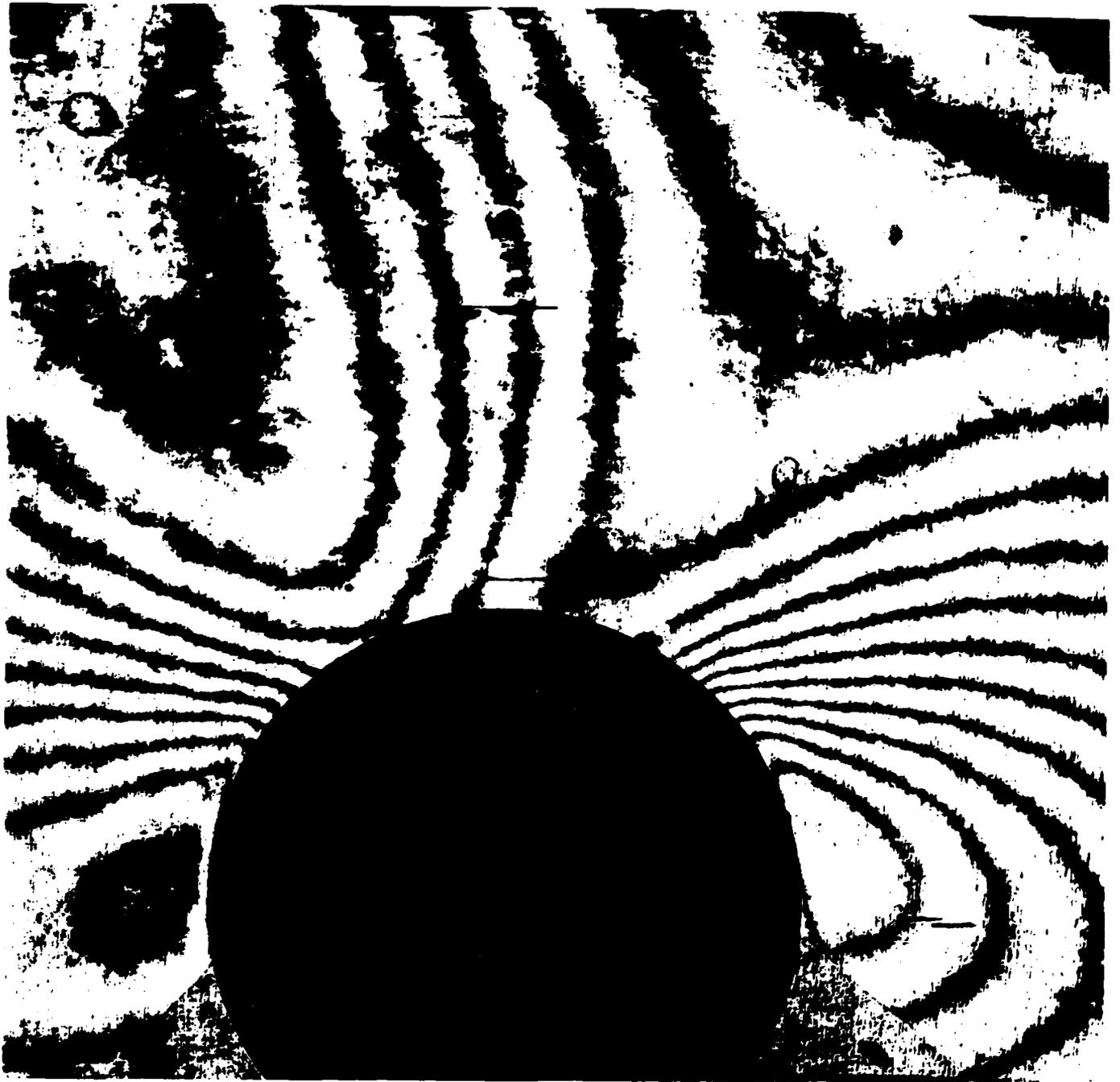
19) U-field, load decreasing phase, P = 250 lb

20) V-field, load decreasing phase, P = 250 lb

21) U-field, load decreasing phase, P = 25 lb

22) V-field, load decreasing phase, P = 25 lb

175

## APPENDIX B

Fringe patterns for the graphite-epoxy plate

1)  U-field, load increasing phase, P = 20 lb

2) V-field, load increasing phase, P = 20 lb

3) U-field, load increasing phase, P = 100 lb
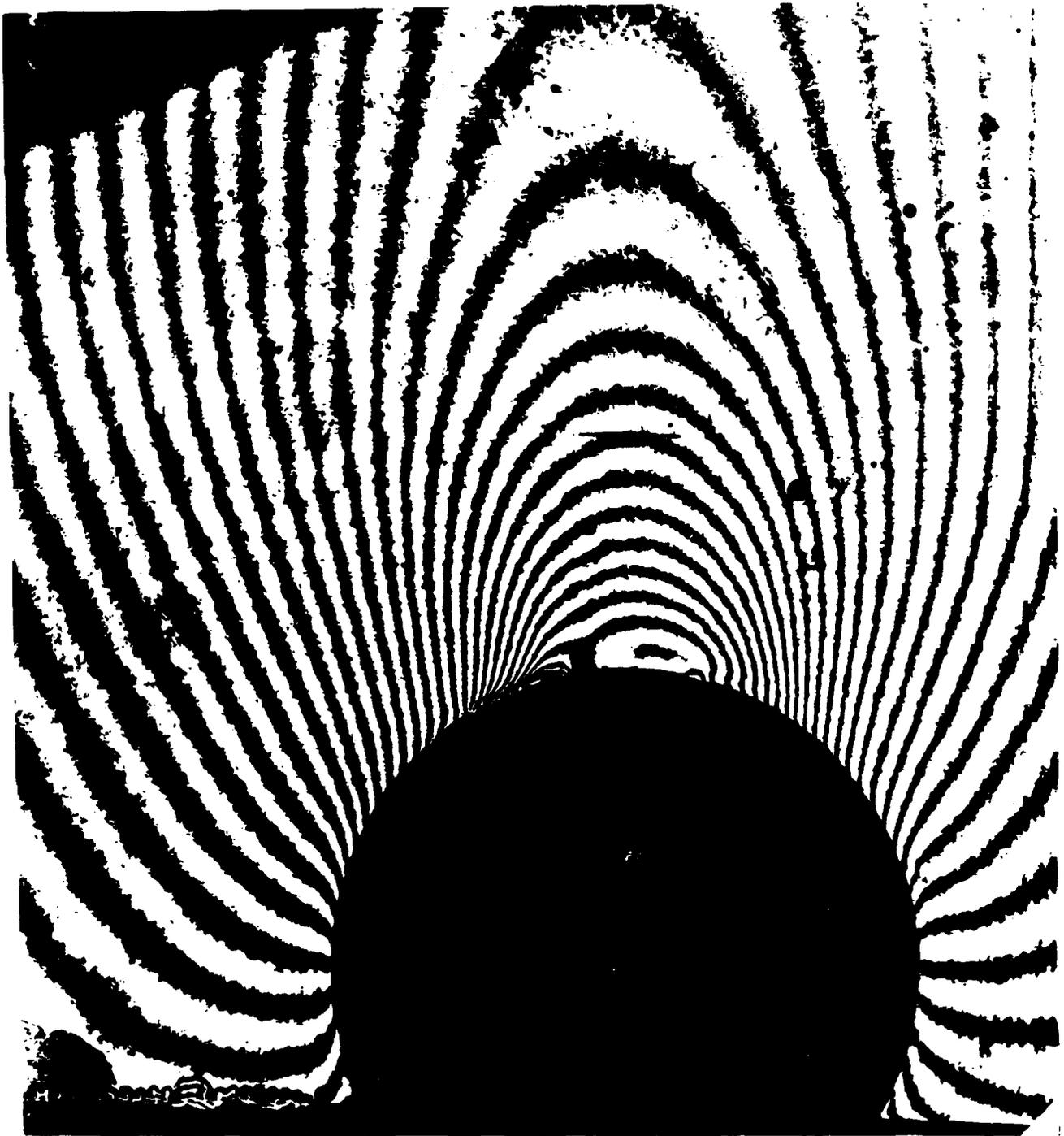
4) V-field, load increasing phase, P = 100 lb
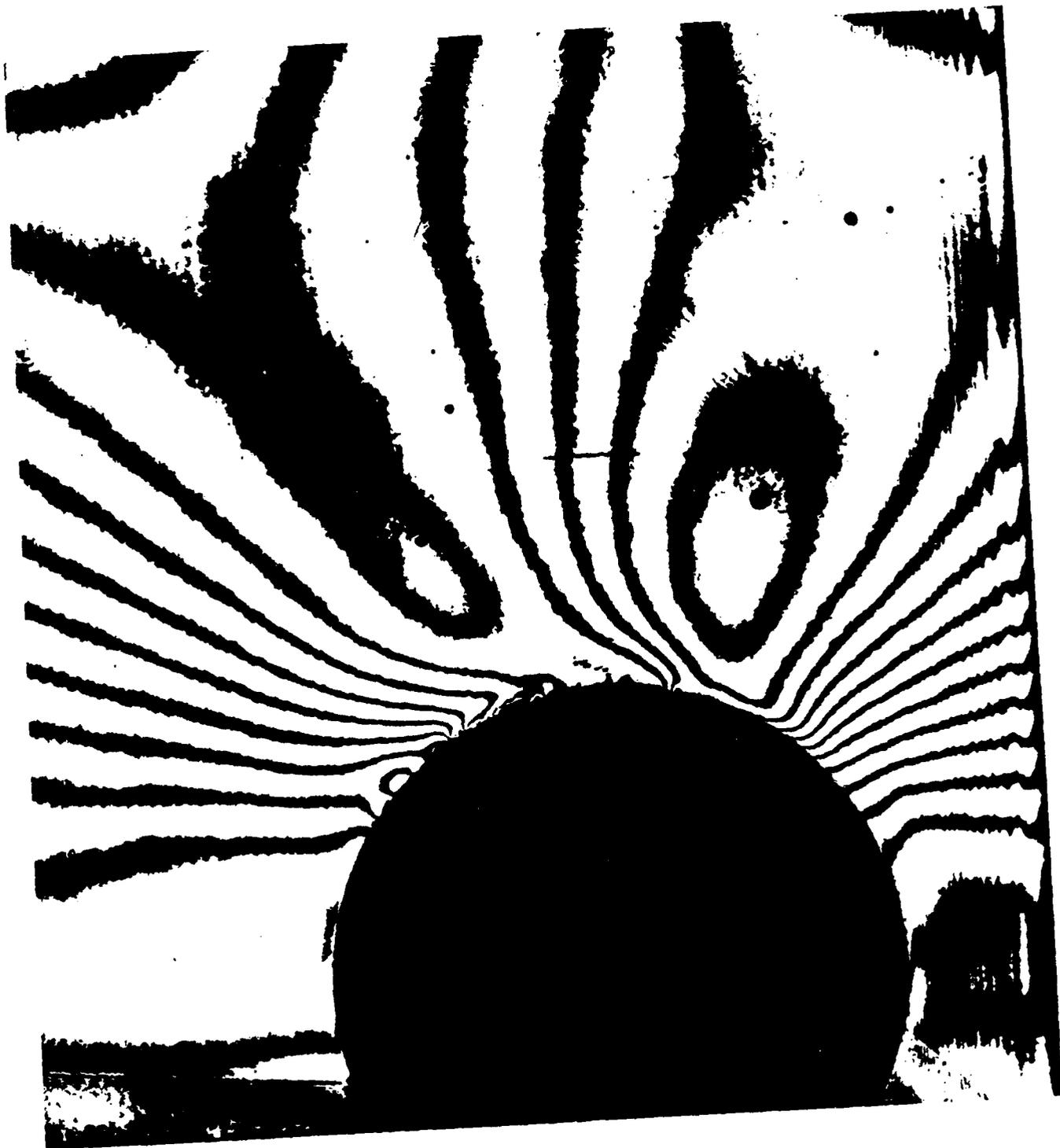
5) U-field, load increasing phase, P = 200 lb

6) V-field, load increasing phase, P = 200 lb

182
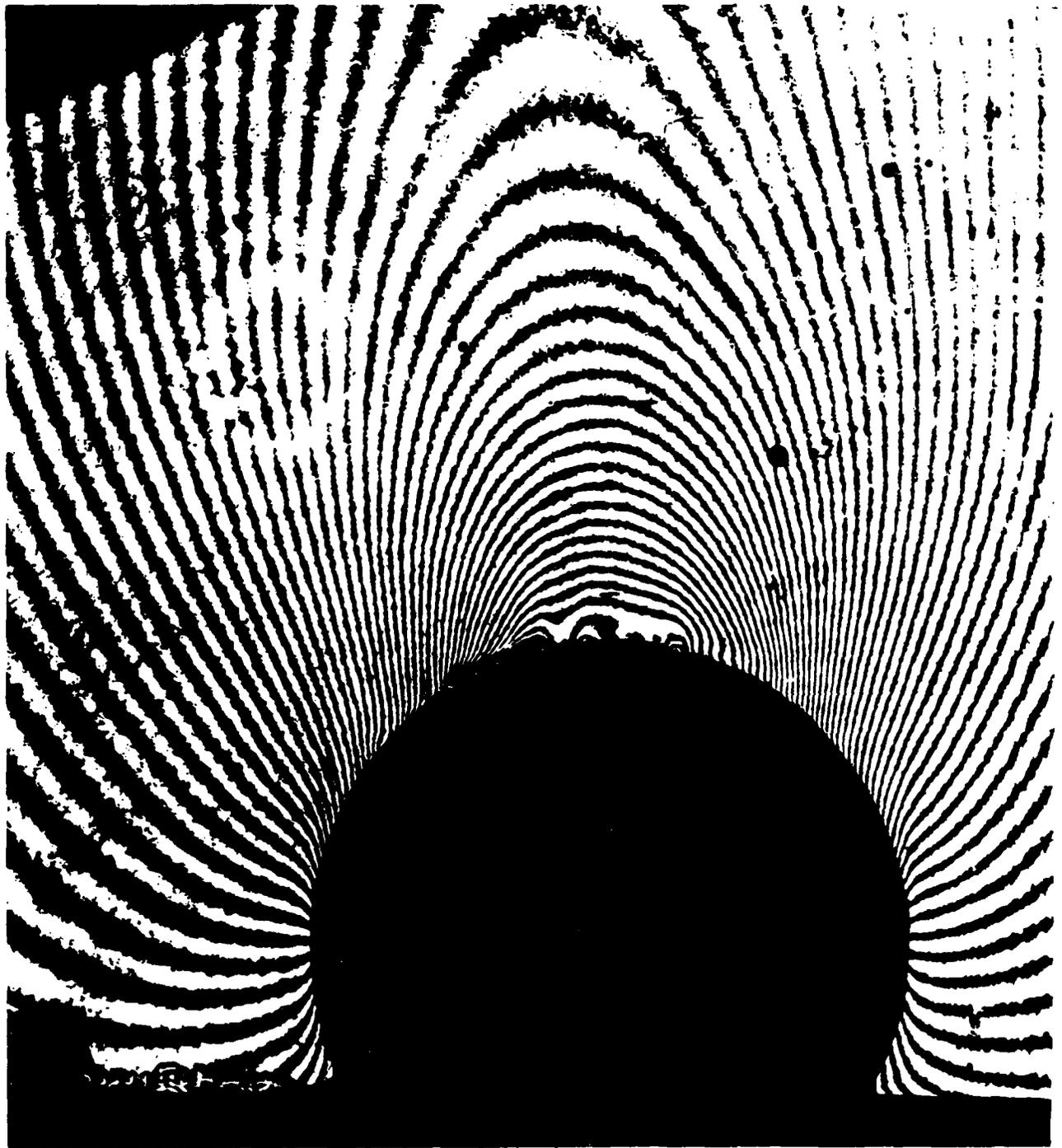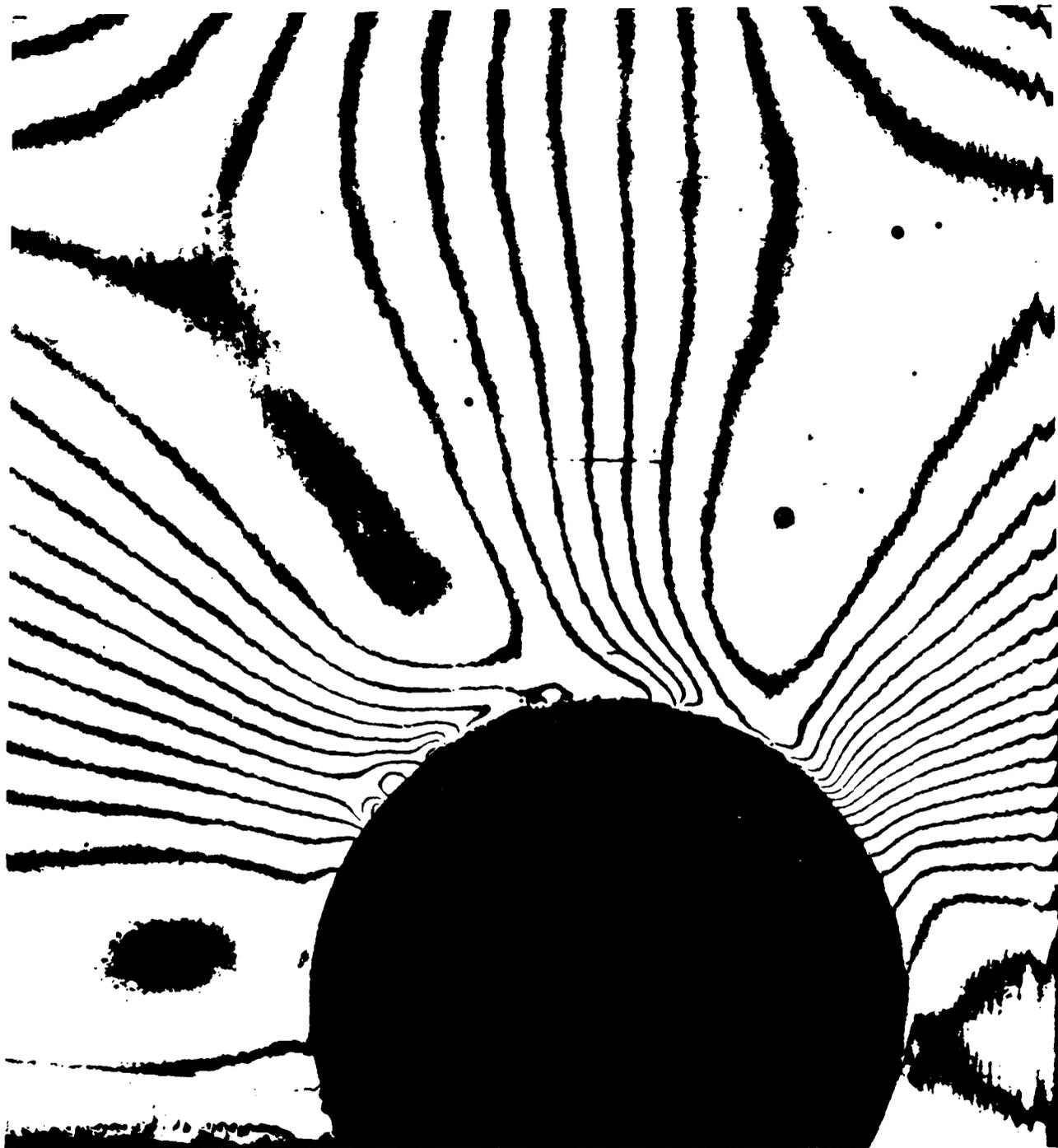
7)  U-field, load increasing phase, P = 300 lb

8) V-field, load increasing phase, P = 300 lb

9) U-field, load increasing phase, P = 400 lb
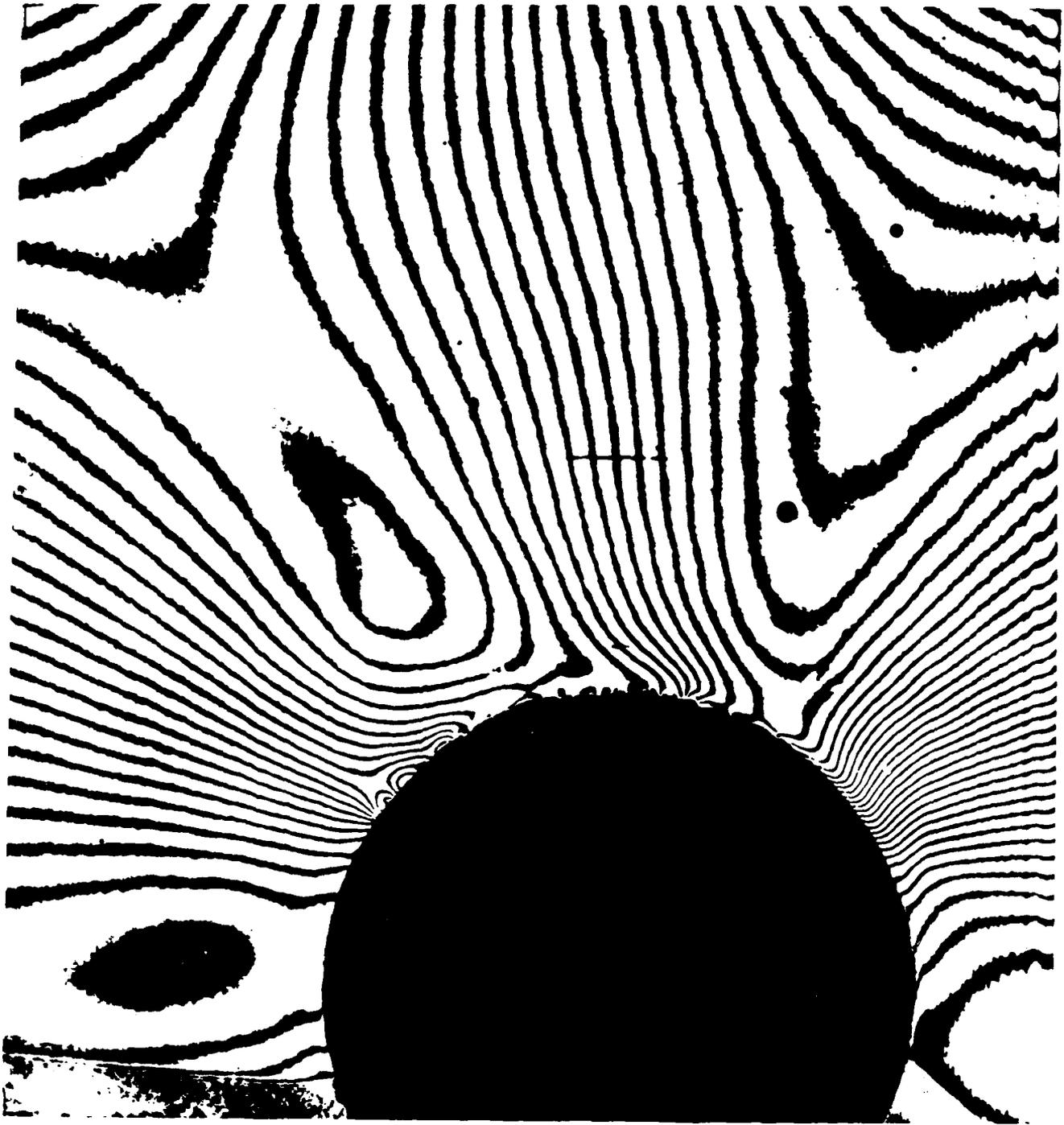
185

10)  V-field, load increasing phase, P = 400 lb

186

11) U-field, load increasing phase, P = 500 lb

187

12) V-field, load increasing phase, P = 500 lb

188

13) U-field, load increasing phase, P = 700 lb

189

14) V-field, load increasing phase. P = 700 lb

190
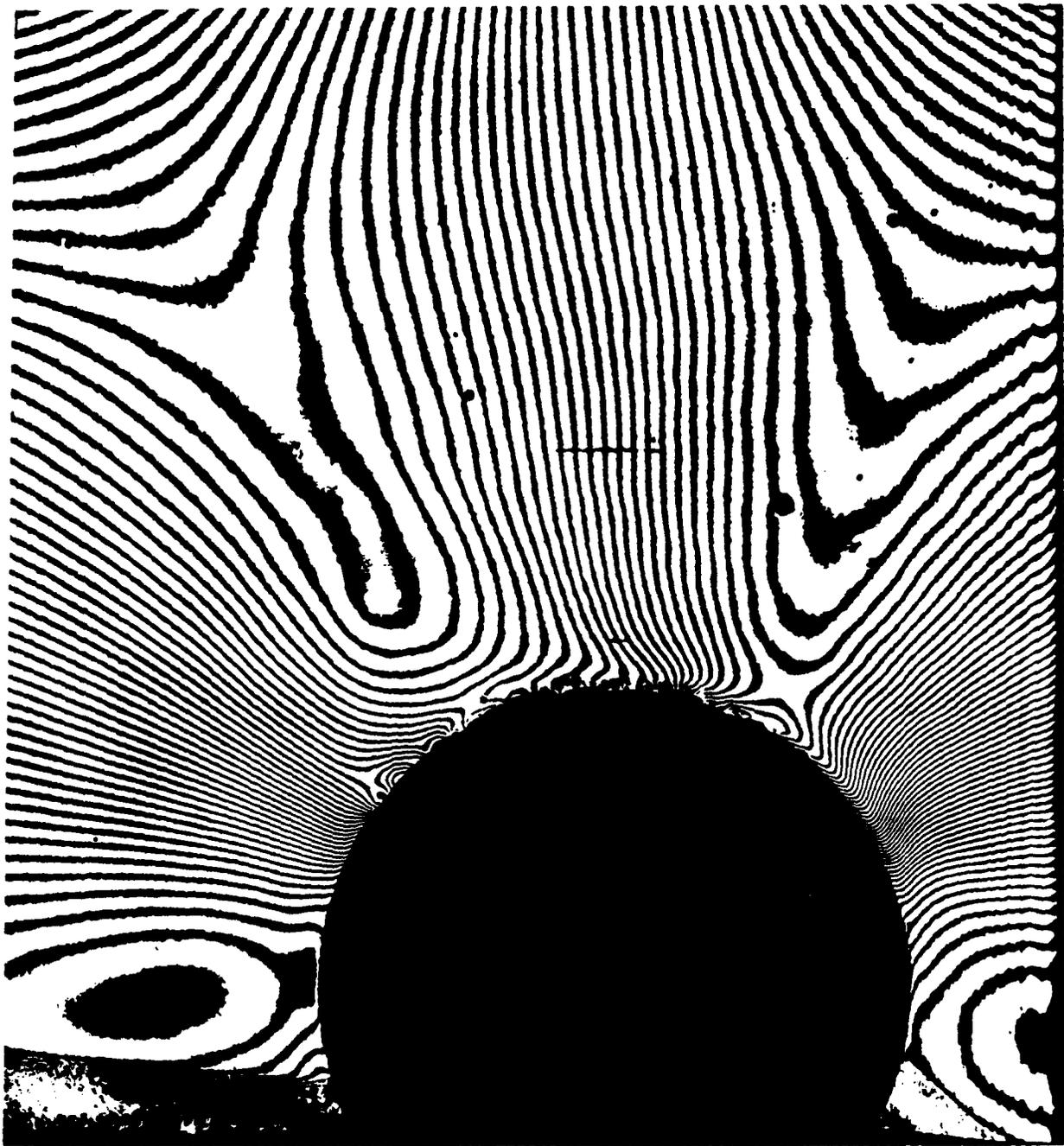
15) U-field, load increasing phase, P = 900 lb

191

16) V-field, load increasing phase, P = 900 lb

192

17) U-field, load increasing phase. P = 1200 lb

(8) V-field, load increasing phase, $P = 1200$ lb

194

19) U-field, load increasing phase, P = 1500 lb

195
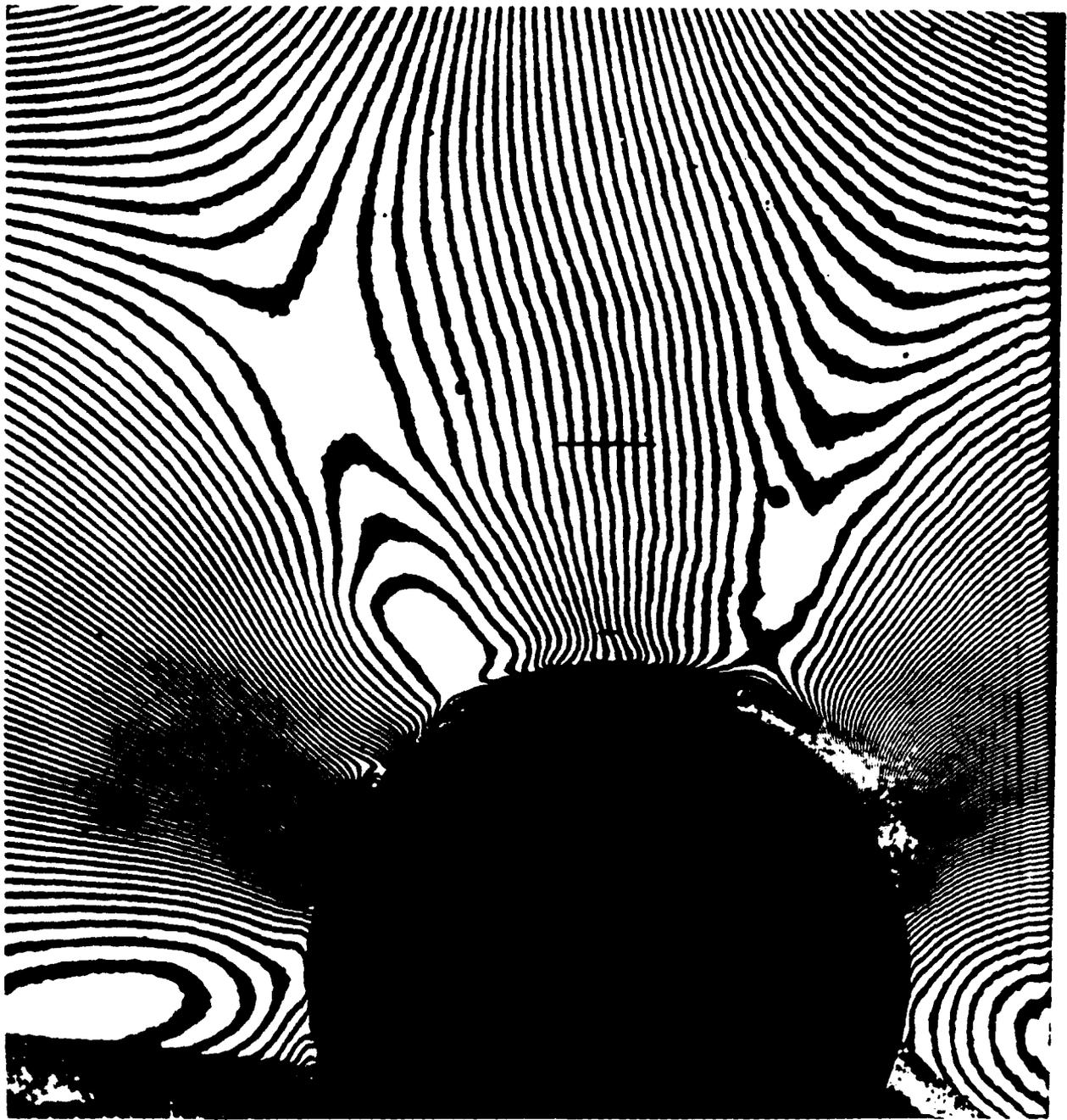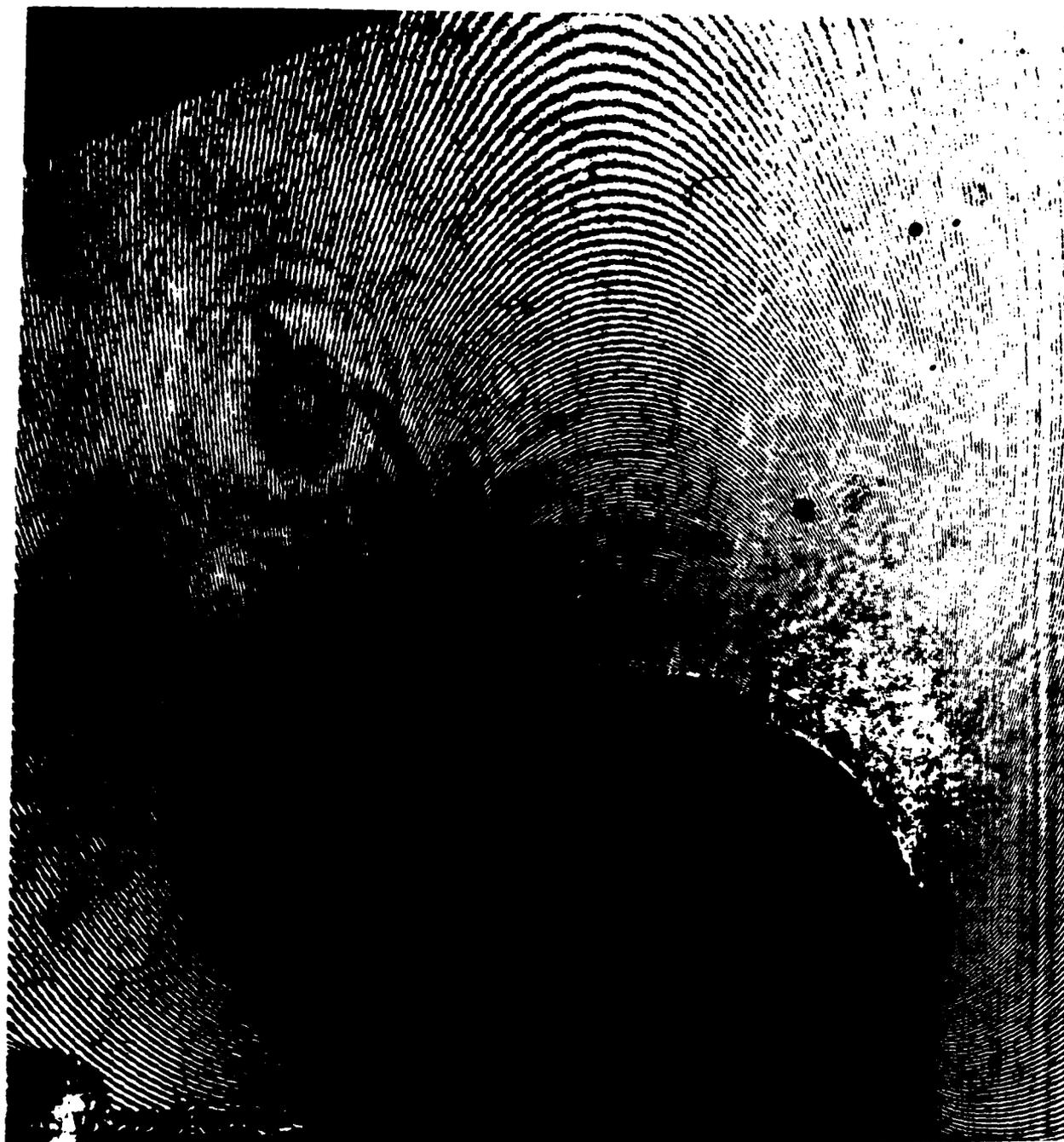
20) V-field, load increasing phase, P = 1500 lb
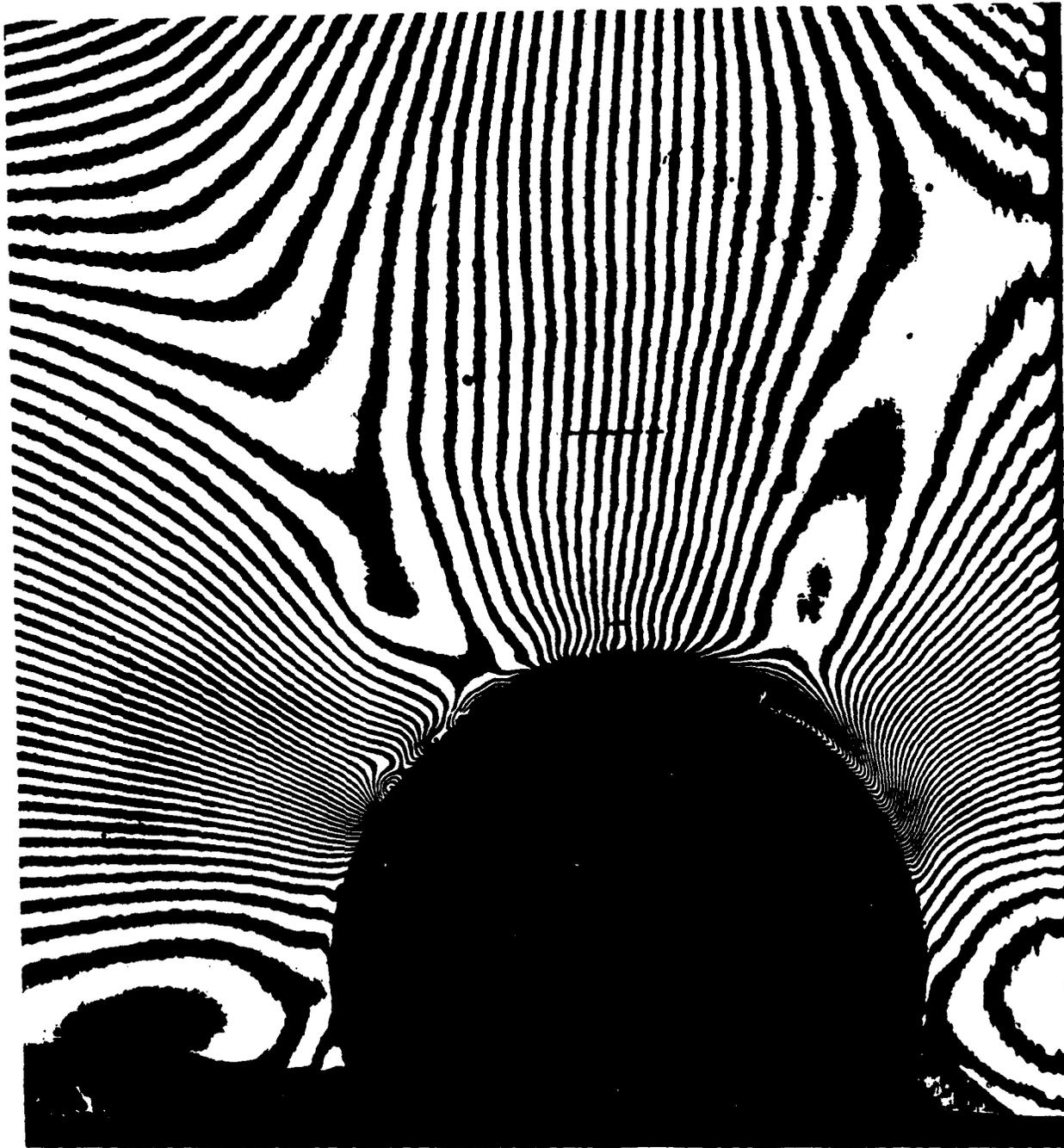
21) U-field, load decreasing phase, P = 700 lb

22) V-field, load decreasing phase, P = 700 lb

23) U-field, load decreasing phase, P = 20 lb

241) V-field, load decreasing phase, t = 2? s

## Acknowledgements